Title of Thesis

Experimental Investigation and CFD Simulation of Mixture Formation and Combustion in Hydrogen Direct Injection Spark-Ignition Engine

March 2018

Kazi Mostafijur Rahman

Graduate School of Natural Science and Technology,
Division of Industrial Innovation Sciences
(Doctoral Programme)

Okayama University, Japan

Experimental Investigation and CFD Simulation of Mixture Formation and Combustion in Hydrogen Direct Injection Spark-Ignition Engine

A dissertation submitted in partial fulfillment of the requirements
for the degree of Doctor of Philosophy
(Major: Mechanical Engineering)

By

Kazi Mostafijur Rahman
(B.Sc. in Mechanical Engineering,
Khulna University of Engineering and Technology, Bangladesh, 2007)
(M.Sc. in Mechanical Engineering, Okayama University, Japan, 2015)

Under the supervision of

Professor Eiji TOMITA

Co-supervised by

Professor Shinichiro YANASE

Professor Akihiko HORIBE

&

Professor Nobuyuki KAWAHARA

Graduate School of Natural Science and Technology
Okayama University, Japan

TO WHOM IT MAY CONCERN

We hereby certify that this is a typical copy of the original Doctoral dissertation of

Mr. **Kazi Mostafijur Rahman**

Thesis Title

Experimental Investigation and CFD Simulation of Mixture Formation and Combustion in Hydrogen Direct Injection Spark-Ignition Engine

Seal of supervisor

Professor Eiji TOMITA

Official Seal

Professor Kenji TOMIOKA
Dean, Graduate School of Natural
Science and Technology
Okayama University, Japan

Abstract

Depletion of fossil fuel, stringent emission regulation and environmental concern have led to the research and development of alternative fuel powered internal combustion (IC) engines. Hydrogen has long been considered as one of the most promising energy carriers and investigated as a fuel for internal combustion engines (ICEs) due to its potential for high engine efficiency and greenhouse gas reduction. Much research has focused on hydrogen direct-injection spark-ignition (DISI) engines. A major challenge in the use of H2-DI is in-cylinder hydrogen-air mixing. It is critical to understand the physical process of mixing between the injected fuel and the air within the cylinder to optimize the overall performance of the direct injection engine. The local equivalence ratio near the spark plug at the time of the spark discharge is particularly important for successful ignition. In addition, the mixture distribution around the spark plug, together with fluid motion, strongly influences the combustion initiation, which subsequently affects the engine performance, efficiency, and emissions. Thus, a fundamental understanding of mixture formation processes is necessary to optimise DI-H2 ICE operation.

In this study, mixture formation process in jet guided direct injection hydrogen spark ignition engine is investigated through simultaneous application of high speed visualization and spark-induced breakdown spectroscopy (SIBS). Spectroscopic analysis of spark-plasma emission and high-speed visualization of spark behavior with different air-excess ratio are conducted simultaneously in a compression-expansion machine (CEM) designed and fabricated by Heat Power Laboratory, Okayama University. Spark-induced breakdown spectroscopy (SIBS) technique is employed as a diagnostic tool for quantitative measurements of local fuel concentration in a direct-injection hydrogen spark-ignition research engine developed at Tokyo City University for the first time. A new sensor with an optical fibre housed in the centre electrode of the spark plug is developed from a commercially available M12-type spark plug with no major modification to the electrodes, leading to stable spark formation. Exposure duration for spectroscopic measurement of spark plasma is optimized to obtain better atomic emission intensity of Hα (656nm) and N (745nm). Results from CEM clearly indicate that with presence of relatively higher hydrogen

concentration near spark gap region, breakdown voltage became higher which made spark discharge difficult to sustain over a long time and; both continuum background emission (i.e. emission from spark plasma) and atomic emission intensity of the spectral distribution declines. As expected, lower the preset air excess ratio, resulted in higher intensity ratio of Hα/N due to presence of higher concentration of hydrogen fuel compared to that of nitrogen. However, with a hydrogen density above a certain level, emission intensity ratio does not show a linear relationship and it is considered that there is a limit to the amount of hydrogen atoms that can be excited. Therefore, a change in the discharge energy lead to a corresponding change in the relationship between atomic emission intensity ratio and excess air ratio.

For SIBS measurements in hydrogen research engine, we sought to characterise the effects of ambient pressure at ignition timing on spectral line emissions and to improve the accuracy of SIBS measurements by taking into account the pressure dependency of atomic emissions. A linear relationship (calibration line) is demonstrated between air excess ratio and intensity ratio for both IH/IN and IH/IO over all pressure values at different spark timing. A significant effect of the corresponding pressure at ignition timing was observed on SIBS measurements and emission line characteristics. Retarded spark timing (i.e. higher ambient pressure at the ignition site), resulted in lower spectral line intensities as well as weaker background emissions. This indicates the variation in spark discharge behaviour and plasma formation with variation in ambient pressure inside the engine cylinder during spark timing variation. At relatively higher pressures, the cooling of the expanding plasma was quicker due to collisional processes with the surrounding gas, leading to both a weaker broadband continuum and atomic emissions. A calibration MAP, representing the correlation of air excess ratio with both intensity ratio and pressure at ignition timing, was developed by taking into account the effect of the corresponding pressure at ignition timing on spectral line intensity for quantitative measurements of local air excess ratio in a research engine. Local stratification of the fuel mixture in the vicinity of the spark gap location associated with direct injection strategies was confirmed using the newly developed spark plug sensor. The COV of local air excess ratio was considerably smaller for measurements made through the calibration map. This indicates that the accuracy of measurements of local air excess ratio

through the spark plug sensor can be improved significantly when the pressure dependency of atomic emissions is taken into account.

Multidimensional CFD simulation is carried out over a range of global air-excess and different injection strategies, by using commercial 3D-CFD software ANSYS Forte, to obtain better insight on hydrogen jet characteristics and mixture formation process in hydrogen direct-injection engines. Simulation confirmed that with retarded injection during compression stroke, fuel jet experience higher pressure immediately upon exiting from the nozzle tip. This high ambient pressure hinders the gas diffusion into the ambient air and consequently reduce the jet penetration. The G-equation model, mathematically known as the level-set method, is used to track the location of the flame front, independent of mesh resolution, with a highly efficient numerical technique. As the flame expanded, the flame front rippled, and buckled due to the stratification of the fuel/air mixture and turbulence conditions in the cylinder. It is found that, with late injection most of the fuel mass exist within a small volume (typically near the spark plug region in jet guided combustion system) in space and once the ignition is initiated by the spark-discharge, flame surface rapidly engulfed the fuel-air mass leading to higher mass fraction burned (MFB) and rapid combustion. Very good agreements were achieved between predicted pressure profiles with experimental data. To validate the experimental results (i.e. SIBS data), local fuel concentration at electrode gap during ignition timing was extracted from simulation results. The claim to achieve higher accuracy in SIBS measurement by taking into account the pressure dependency of atomic emissions, was confirmed through CFD simulation data of local equivalence ratio. The predicted λ_{local} values from simulation matched quite well with experimentally measured values. To reach up-to this level of agreements, it is required to specify initial and boundary conditions accurately; do very fine tuning of several important parameters namely, turbulent flame speed ratio, flame stretching factor, flame development co-efficient etc. These demonstrate that the simulation carried out in this study was successful in predicting the mixture formation process as well as combustion phenomenon in a hydrogen engine.

TABLE OF CONTENTS

List of Figures

List of Tables

ACKNOWLEDGEMENTS

First and foremost, all Glory and Praise be to ALLAH, the Almighty, the Creator, the Cherisher and Sustainer of the heavens and universe.

I would like to appreciate my employer Khulna University of Engineering and Technology (KUET), Bangladesh for approving the study leave and allowing me to pursue higher studies at Okayama University, Japan; and acknowledge the contributions of Ministry of Education, Culture, Sports, Science and Technology (MEXT), Japan in providing me the scholarship (MONBUKAGAKUSHOU) which together made this study possible.

I would wish to express my sincerest gratitude to my supervisor, Professor Eiji TOMITA, for his valuable advice, encouragement and the fruitful exchange of knowledge that helped me sort out the technical details of my work. I have been amazingly fortunate to have an advisor who has supported me throughout whole study and allowed to me explore my ideas.

I am deeply grateful to my co-supervisor Associate Professor Nobuyuki KAWAHARA, who gave me the freedom to explore on my own and at the same time provided the guidance to recover when my steps faltered. His insightful comments and constructive criticisms at different stages of my research were thought-provoking and helped me to grow as a researcher.

I like to thank the members of my Ph.D. jury board, in particular Professor Dr. Shinichiro YANASE (Fluid Dynamics, Okayama University) and Professor Dr. Akihiko HORIBE (Heat Transfer Engineering, Okayama University), for their valuable time and enthusiasm in accepting the task.

Lots of appreciation goes to Assistant Professor Kazuya TSUBOI. I would wish to extend my appreciation and gratefulness to Mrs. Hanako OZAWA for her continuous support and cooperation regardless of the matter whether its personal or official. Special thanks to Isao YAMANE for his technical assistance during various stages of this research.

I am indebted to the members of the *Heat Power Engineering. Laboratory* specially my co-workers Mr. Daichi MATSUNAGA, Mr. Mizuki KAMEDA and Mr. Yuki KASAHARA with whom I have interacted during the course of my doctoral program. They have provided me with valuable support in many aspects of this work.

I would also like to thank Dr. Yungjin Kim (Post-doctoral fellow), Dr. Tasyrif Bin Abdul Rahman (University of Malaysia Perlis) and my PhD colleagues, Mr. Alireza Valipour, Mr. Cagdas Aksu with whom I have shared more than just our office. It was a great pleasure to work with them in the same laboratory and I wish them all the very best!

I would like to thank my mother Mazeda Begum, my in-laws, my brothers and sisters and, most of all, my father Kazi Momtaz Uddin. I wish, we can share the joy of the moment of this big achievement, together as a family! My heartfelt appreciation goes to my beloved wife Khaleda Akter "MILY" for her understanding, unconditional support and encouragement over the years and I could not ask for more. Special apology to my son "ANON" and daughter "AFIFA" for being away from them. I feel so lucky to have them in my life and just watching them smile makes me realize how beautiful my life is!

CHAPTER: 1

Introduction

1.1 Research Background and Motivation

Hydrogen has long been considered as one of the most promising energy carriers and investigated as a fuel for internal combustion engines (ICEs) due to its potential for high engine efficiency and greenhouse gas reduction [1-5]. There are some initiatives in Japan to move towards the "dream of a hydrogen-based society" and to accelerate the installation of hydrogen stations for fuel-cell vehicles that run on electricity, generated by burning hydrogen. Today, various governments, especially in Europe, the United States, Canada, and Japan, are taking leading roles in establishing and promoting low carbon electricity generation through cogeneration systems. Until now, hydrogen-fuelled cogeneration has been dominated by fuel cell applications, and the high cost of these systems has been a limiting factor for hydrogen's viability as a fuel for stationary power applications [6-9]. However, reciprocating hydrogen-fuelled engines that can offer an economic proposition comparable to natural gas and diesel could establish hydrogen-fuelled cogeneration system as a viable alternative. Obara et al. investigated a hybrid cogeneration system (HCGS) by combining a solid polymer membrane-type fuel cell (PEM-FC) and a hydrogen mixture gas engine (NEG) [10]. They reported improvement in power generation efficiency and reduction in carbon dioxide emission.

Much research has focused on hydrogen direct-injection spark-ignition (DISI) engines due to their high volumetric efficiency and potential to avoid knock, preignition, and backfiring, which have detrimental effects on engine performance and emissions [11-14]. Optimisation of spark timing, injection timing, and injection pressure, are important aspects of the development of hydrogen DISI engines [15] and can suppress backfiring and knocking, especially at higher engine loads. Oikawa et al. reported a "plume ignition combustion concept" (PCC) for hydrogen DISI engines, denoting the ignition of a rich mixture plume during or right after an injection event [16]. In their study, the injector was mounted close to the spark plug to achieve jet-guided combustion with the jet being directed towards the spark plug using high injection pressures (200 bar). This PCC combustion with late injection strategy was shown to substantially reduce NOx emissions at high speed and under high load conditions while maintaining high thermal efficiency and power. A major challenge in the use of H2-DI is in-cylinder hydrogen-air mixing. It is critical to understand the physical process of mixing between the injected fuel and the air within the cylinder to optimize the overall performance of the direct injection engine. The high-pressure injector used for the direct-injection engines usually have multiple holes in the nozzle tip to ensure an even distribution of fuel and promote proper mixing. This results in the formation of multiple under-expanded jets in the cylinder, which interact with each other and with the in-cylinder boundaries to form the fuel-air mixture before combustion. Almost in all cases, fluid fuel injection flow is three-dimensional and turbulent. This flow can be measured and calculated to some limited degree of accuracy using reasonable assumptions. In continuous system whose combustion chamber are usually large, fuel injection may be assumed to be represented by a turbulent free gas jet discharging into surrounding air.

The local equivalence ratio near the spark plug at the time of the spark discharge is particularly important for successful ignition, because the jet-guided system generates a stratified fuel concentration near the spark plug in a DISI engine. In addition, the mixture distribution around the spark plug, together with fluid motion, strongly influences the combustion initiation, which subsequently affects the engine performance, efficiency, and emissions. Thus, a fundamental understanding of mixture formation processes is necessary to optimise DI-H2 ICE operation. To better understand how to both achieve an optimal local mixture and control the large-scale stratification, a diagnostic tool for providing information on the mixture distribution in practical engines should be developed. Instantaneous fuel concentration measurements in production engines will greatly aid in engine design and optimisation.

There are several approaches to studying fuel concentrations in an SI engine, including infrared (IR) absorption, planar laser induced fluorescence (PLIF), Raman scattering, laser-induced breakdown spectroscopy (LIBS) and spark-induced breakdown spectroscopy (SIBS) or spark emission spectroscopy. A 3.392-μm He-Ne laser was used to obtain fuel concentrations for combustion diagnostics [17-26]. One of the members of our group was the first to investigate the possibility of measuring fuel concentration near the spark plug in a test engine [21]. Subsequently, Tomita et al. used an optical sensor with a pair of sapphire rods to pass laser light through the combustion chamber of a practical engine; they also discussed several of the factors that affected measurement accuracy [22,23]. Their sensor has also been applied to practical SI engines and direct-injection gasoline engines [24]. We developed an optical spark-plug sensor with a double-pass measurement length using an

infrared absorption technique for measuring hydrocarbon fuel concentrations [25,27]. LIF measurements have been used widely because the LIF signal is relatively strong and provides two-dimensional fuel concentration information at a specified time [28-30]. Tomita et al. [28] applied the PLIF method to study the fuel concentration distribution in a transient hydrogen jet. Results showed that each transient hydrogen jet had different configurations and concentration distributions. Kaiser and White [30] performed an optical study of mixture preparation in a hydrogen-fuelled engine using a PLIF technique; their report favoured increased injection pressure and careful nozzle design. Ferioli et al. [31] used LIBS on engine exhaust gas to illustrate the ability of this technique to measure the equivalence ratio of SI engines, using the ratios of C/O and C/N atomic peaks derived from the measured spectra. Phuoc [32] used a laser-induced spark to measure the ignition and fuel-to-air ratio of CH4-air and H2-air combustible mixtures simultaneously using the measured spectral peak ratio Hα (656 nm)/O (777 nm). Shudo and Oba [33] measured the mixture formation characteristic with a hydrogen jet in a nitrogen-filled constant-volume chamber using LIBS techniques. We have also tried to measure the equivalence ratio using LIBS and discussed the accuracy of spatially, temporally, and spectrally resolved measurements [34,35]. However, IR absorption is not suitable for measuring the hydrogen/air ratio due to the lack of absorption bands at visible and infrared wavelengths. PLIF and LIBS require major engine modifications including optical access, which limit their application to production engines. Quantitative measurements of the cycle-to cycle variations in the mixture strength at or near the ignition site are comparatively rare for practical hydrogen SI engines.

With SIBS, the signal detection and spectroscopy are similar to LIBS; however, spark generation occurs between two electrodes, in which the spark itself is used as the light source to estimate the equivalence ratio in the spark plug. SIBS can therefore be used in a combustion chamber with no engine modifications, because the plasma excitation can be implemented using a conventional spark plug. Spark-emission spectroscopy has been applied to measure the equivalence ratio in a DISI engine [36-38]. Ando and Kuwahara [37], and Fansler et al. [38] reported individual measurements of the equivalence ratio at the spark gap using the ratio of CN (388 nm) emission intensity and OH (306 nm) radical intensity from the spark that initiates combustion. They determined the cycle-resolved local fuel–air ratio in the spark gap, controlled the large-scale stratification, and evaluated the utility of SIBS as an engine diagnostic tool. However, it is difficult to detect the equivalence ratio under lean mixture conditions due to lack of the linearity of CN/OH emission intensity ratio. All of these studies require engine modification for optical access to the combustion chamber from outside. Kawahara et al. [39] used the SIBS technique to measure the local equivalence ratio in a laminar premixed flame of a CH4/air mixture. Spectrally resolved emission spectra of plasma generated by a spark plug were investigated for their potential to measure local fuel concentrations in a premixed mixture. The spectrum was measured through an optical fibre housed in the centre electrode of the spark plug, which makes this technique suitable for measuring the equivalence ratio in the spark gap at ignition timing, in production engines without engine modification. Roy et al. [40] further improved the spark-plug sensor to measure the local fuel–air concentration in the spark gap at the time of ignition in a fired, jet-guided hydrogen SI-engine operated under stratified-charge conditions using SIBS. Tasyrif et al. [41] investigated the mixing process of a hydrogen jet in

a constant-volume vessel and characterised the spatial distribution of the equivalence ratio across the jet and along its axis. Later, they reported the effects of the ambient pressure on fuel concentration measurements for a jet of hydrogen injected into a nitrogen environment with different ambient pressures; also, local concentrations were measured at various spark locations in a constant-volume vessel [42].

On the other hand, due to the difficulty in modeling the complex physical phenomena and the massive computational need, numerical simulations of direct-injection hydrogen engines are relatively rare. There have been some studies on DI gas engines; however, better insight of the fundamental characteristics of high pressure hydrogen injection, ignition process and combustion event in a Hydrogen DISI engine are also necessary.

1.2 Objectives of the present study

The experimental works described in this thesis are conducted by using a compression-expansion machine (CEM) designed and fabricated by Heat Power Laboratory, Okayama University; and a direct-injection hydrogen spark-ignition research engine developed at Tokyo City University. Both RCEM and research engine allow optical access for the visual investigation of jet penetration, mixture formation and flame propagation.

The primary objective of this study is to investigate mixture formation process in jet guided direct injection hydrogen spark ignition engine through simultaneous application of high speed visualization and spark-induced breakdown spectroscopy (SIBS). Spark-induced breakdown spectroscopy (SIBS) technique is employed as a diagnostic tool for local fuel concentration measurements in a direct-injection hydrogen research engine for the first

time. A new spark plug sensor is developed from a commercially available spark plug embedded with an optical fiber. Experimental investigations are carried out first in a compression expansion machine (CEM) and then in a hydrogen production engine.

In the present work, we sought to characterise the effects of in-cylinder pressure during ignition event on spectral line emissions and to improve the accuracy of SIBS measurements by taking into account the pressure dependency of atomic emissions.

For experiment in CEM, time series spectroscopic analysis of spark discharge plasma emission is conducted, and exposure duration is optimized to obtain better atomic emission intensity of Hα (656nm) and N (745nm). Visualization of hydrogen flame and local air excess ratio measurement are carried out simultaneously.

For experiment in a hydrogen production engine, first, the correlation between the air excess ratio (relative air/fuel ratio) and atomic emission intensity ratio (also known as a calibration curve) is examined for different ignition timing under port injection conditions. A calibration MAP representing the correlation of air excess ratio (air/fuel) with both intensity ratio and in-cylinder pressure during ignition event is generated by considering the effect of in-cylinder pressure on spectral line intensity. The calibration curve and calibration MAP are subsequently used for quantitative measurements of the local air excess ratio for both port injection and direct injection strategies.

A second objective of the present work is to obtain a deepened understanding of mixture formation and subsequent combustion in hydrogen IC engine by the application of three-dimensional numerical simulation. The goal is also to establish a basis for recommendations

regarding an optimisation of the combustion concept. Commercial 3D-CFD software ANSYS Forte is employed to examine different types of turbulence models in single-cylinder engine simulations in order to estimate the suitability of a predictive computation of the hydrogen-air mixing and combustion process of premixed, partially premixed and non-premixed combustion modes that occur in hydrogen direct-injection engines. The software incorporates proven Chemkin-Pro solver technology which is the gold standard for use in chemical kinetic simulation. ANSYS Forte includes state-of-the-art Automatic Mesh Generation (AMG), including Solution Adaptive Mesh Refinement (SAM) and geometry-based adaptive mesh refinement (AMR) features.

To evaluate the influence of injection timing (i.e. start of injection) relative to spark timing on hydrogen jet structure and mixture formation, experimental data of both CEM and research engine are validated by means of numerical results obtained from ANSYS Forte CFD package.

1.3 Thesis outline

The thesis is organized in 7 chapters as follows:

Chapter 1 briefly presents the introduction and background of the study. It also highlights the motivation and objectives of the current research. The discussion involves the global initiatives taken to introduce hydrogen energy to meet current challenges and energy demand, literature on hydrogen direct injection spark ignition engines, shortcomings of the existing approaches to study mixture formation process, and implementation of spark-

induced breakdown spectroscopy (SIBS) as a diagnostic tool to investigate local fuel concentration in hydrogen direct-injection spark-ignition engines.

Chapter 2 discusses the combustion characteristics of hydrogen fuel, prospects of using hydrogen as a fuel for internal combustion engines (ICE), and global R&D efforts on the development of hydrogen direct injection spark ignition(DISI) engine and their challenges. The DISI engine can operate fundamentally in two modes: the homogeneous (early injection) and the stratified-charge modes (late injection). Internal mixture formation, or direct injection, can eliminate many of the combustion abnormalities associated with external mixture formation strategies. A comprehensive survey on the state-of-the-art techniques to study mixture formation process such as Infrared (IR) absorption, Planar laser induced fluorescence (PLIF), Raman scattering, Ion current, Laser-induced breakdown spectroscopy (LIBS) and Spark-induced breakdown spectroscopy (SIBS) is presented.

Chapter 3 presents visualization of jet structure through help of a high-speed video camera for hydrogen injected in a constant volume vessel with different ambient pressures. A high-speed camera, able to capture the evolution of hydrogen jet over time, was used along with an Ar-ion laser and metal halide lamp as the light sources to illuminate the hydrogen jet at the nozzle exit. This allow the study of jet structure in addition to other physical processes resulting from hydrogen gas injection. Time-series images show that jet plume appears to penetrate faster when hydrogen is injected with higher injection pressure into a chamber of comparatively lower ambient pressure as velocity of the jet or total momentum supplied to the fuel jet at the injector exit was higher for increasing the injection pressure. Therefore, the injected fluid with additional momentum could accelerate more readily by pushing aside

the ambient fluid though density of chamber medium was considerably higher than the injected gas. On the other hand, higher ambient pressure resulted in considerably shorter jet tip penetration along with wider jet angle which is caused by the higher inertia of the fluid elements that the injected fluid must accelerate and push aside.

Chapter 4 introduces the development of new sensor with an optical fibre housed in the centre electrode of the spark plug for SIBS measurement. This sensor is developed from a commercially available M12-type spark plug with no major modification to the electrodes, leading to stable spark formation. Spectroscopic analysis of spark-plasma emission and high-speed visualization of spark behavior with different air-excess ratio was studied simultaneously in a compression expansion machine (CEM). Exposure duration for spectroscopic measurement of spark plasma is optimized to obtain better atomic emission intensity of Hα (656nm) and N (745nm). When hydrogen concentration was relatively higher, both continuum background emission (i.e. emission from spark plasma) and atomic emission intensity of the spectral distribution declines. Results clearly indicates that presence of higher fuel concentration in the vicinity of spark gap leads to higher discharge energy as the magnitude of both breakdown voltage and current increase though duration of spark event becomes shorter with lower air excess ratio. Influence of different injection timing on local fuel concentration near spark gap region is characterized in detail. It is found that the with late injection the mixture at spark gap region become more stratified which ultimately lead to rapid combustion and heat release.

Chapter 5 explains the experimental work for investigation of mixture formation process in a hydrogen direct injection production engine. The test engine and its specifications,

configurations and basics of engine operation are discussed. An in-house developed common rail injector is used for high pressure hydrogen injection directly into the combustion chamber. Retarded spark timing (i.e. higher ambient pressure at the ignition site) resulted in lower spectral line intensities as well as weaker background emissions. It is well established that with relatively higher pressure and density of atoms or molecules, the cooling of expanding plasma accelerates, and the collision probability increases, leading to both a weaker broadband continuum and atomic emissions. A "calibration MAP" representing the correlation of air excess ratio (relative air/fuel ratio) with both intensity ratio and pressure at ignition timing is generated and subsequently used for quantitative measurements of local fuel concentrations for both port injection and direct injection strategies to demonstrate and explore the effects of pressure dependency of atomic emission on the accuracy of the SIBS measurements. Local stratification of the fuel mixture in the vicinity of the spark gap location associated with direct injection strategies is confirmed; the coefficient of variation of the local air excess ratio is relatively small for measurements made using the calibration map. This demonstrates that the measurement accuracy of local fuel concentrations through a spark plug sensor can be improved significantly when the pressure dependency of atomic emissions is taken into account.

Chapter 6 presents the numerical simulation performed over a range of global air-excess and ratio different injection strategies, through commercial 3D-CFD software ANSYS Forte to obtain a deepened understanding of hydrogen jet characteristics and mixture formation in hydrogen direct-injection engines. Governing equations for 3D-CFD modeling of internal combustion engine (ICE), basic of turbulence modeling and wall treatment, setting the initial

and boundary conditions is discussed to best describe the physical model. Concept of inflow boundary condition at the nozzle exit was successfully utilized to introduce gaseous hydrogen directly into the combustion chamber. G-equation model, mathematically known as the level-set method, was used to track the location of the flame front, independent of mesh resolution, with a highly efficient numerical technique. CFD simulation data of local equivalence ratio supported the claim that accuracy of SIBS measurement can be improved significantly by taking into account the pressure dependency of atomic emissions.

Chapter 7 summarizes the conclusions drawn from this study.

References

[1] Karim G. Hydrogen as a spark ignition engine fuel. Int J Hydrogen Energy 2003;28(5):569-77.

[2] Verhelst S. Recent progress in the use of hydrogen as a fuel for internal combustion engines. Int J Hydrogen Energy 2014;39(2):1071-85.

[3] Frolov SM, Medvedev SN, Basevich VY, Frolov FS. Self-ignition of hydrocarbon-hydrogen-air mixtures. Int J Hydrogen Energy 2013;38(10):4177-84.

[4] Wang Z, Naterer GF. Integrated fossil fuel and solar thermal systems for hydrogen production and CO2 mitigation. Int J Hydrogen Energy 2014;39(26):14227-33.

[5] Salvi BL, Subramanian KA. Experimental investigation on effects of compression ratio and exhaust gas recirculation on backfire, performance and emission characteristics in a hydrogen fuelled spark ignition engine. Int J Hydrogen Energy 2016;41(13):5842-55.

[6] Briguglio N, Ferraro M, Brunaccini G, Antonucci V. Evaluation of a low temperature fuel cell system for residential CHP. Int J Hydrogen Energy 2011;36:8023e9.

[7] Hwang JJ, Zou ML. Development of a proton exchange membrane fuel cell cogeneration system. J Power Sources 2010;195:2579e85.

[8] Onovwiona HI, Ugursal VI. Residential cogeneration systems: review of the current technology. Renew Sust Energ Rev 2006;10:389-431.

[9] Lipman TE, Edwards JL, Kammen DM. Fuel cell system economics: comparing the costs of generating power with stationary and motor vehicle PEM fuel cell systems. Energ Policy 2004;32:101-25.

[10] Obara S, Tanno I. Study on capacity optimization of PEM fuel cell and hydrogen mixing gas-engine compound generator. Int J Hydrogen Energy 2007;32(17):4329-4339.

[11] White CM, Steeper RR, Luts AE. The hydrogen-fueled internal combustion engine: a technical review. Int J of Hydrogen Energy 2006;31(10):1292-305.

[12] Mohammadi A, Shioji M, Nakai Y, Ishikura W, Tabo E. Performance and combustion characteristics of a direct injection SI hydrogen engine. Int J Hydrogen Energy 2007; 32(2):296-304.

[13] Rottengruber H, Berckmu¨ ller M, Elsa¨ sser G, Brehm N, Schwarz C. Direct-injection hydrogen SI-engine – operation strategy and power density potential. SAE paper no. 2004-01- 2927; 2004.

[14] White CM. A qualitative evaluation of mixture formation in a direct-injection hydrogen-fuelled engine. SAE Paper No. 2007-01-1467. 2007.

[15] Duan J, Liu F, Sun B. Backfire control and power enhancement of a hydrogen internal combustion engine. Int J Hydrogen Energy 2014;39(9):4581-9.

[16] Oikawa M, Ogasawara Y, Kondo Y, Sekine K, Takagi Y, Sato Y. Optimization of hydrogen jet configuration by single hole nozzle and high speed laser shadowgraphy in high pressure direct injection hydrogen engines. Int J Automotive Engineering 2012;3:1-8.

[17] Hall MJ, Koenig M. A fiber-optic probe to measure precombustion in-cylinder fuel-air ratio fluctuations in production engines. Proc Combust Inst 1996;26(2):2613-8.

[18] Koenig M. and Hall MJ. Measurements of Local In-Cylinder Fuel Concentration Fluctuations in a Firing SI Engine. SAE Paper No.971644. 1997.

[19] Koenig M. and Hall MJ. Cycle-Resolved Measurements of Pre-Combustion Fuel Concentration Near the Spark Plug in a Gasoline SI Engine. SAE Paper No.981053. 1998.

[20] K. Kawamura, T. Suzuoki, A. Saito, T. Tomoda, M. Kanda, Development of instrument for measurement of air–fuel ratio in vicinity of spark-plug (application to DI gasoline engine), JSAE Rev. 19 (1998) 305–310.

[21] S. Yoshiyama, Y. Hamamoto, E. Tomita, K. Minami, Measurement of hydrocarbon fuel concentration by means of infrared absorption technique with 3.39 μm He–Ne Laser, JSAE Rev. 17 (1996) 339-345.

[22] E. Tomita, N. Kawahara, M. Shigenaga, A. Nishiyama, R.W. Dibble, In Situ measurement of hydrocarbon fuel concentration near a spark plug in an engine cylinder by 3.392 μm infrared laser absorption method: discussion of applicability with a homogeneous methane–air mixture, Meas. Sci. Technol. 14 (2003) 1350–1356.

[23] E. Tomita, N. Kawahara, A. Nishiyama, M. Shigenaga, In Situ measurement of hydrocarbon fuel concentration near a spark plug in an engine cylinder by 3.392 μm infrared laser absorption method: application to actual engine, Meas. Sci. Technol. 14 (2003) 1357-1363.

[24] E. Tomita, N. Kawahara, S. Yoshiyama, A. Kakuho, T. Itoh, Y. Hamamoto, In-Situ fuel concentration measurement near spark-plug in spark-ignition engines by 3.39 μm infrared laser absorption method, Proc Combust Inst 2002;29(1):735-741.

[25] A. Nishiyama, N. Kawahara, E. Tomita, In-Situ Fuel Concentration Measurement near Spark Plug by 3.39 μm Infrared Absorption Method (Application to Spark Ignition Engine). SAE Paper No.2003-01-1109. 2003.

[26] Kawahara N, Tomita E, Kadowaki T, Honda T, Katashiba H. In situ fuel concentration measurement near a spark plug in a spray-guided direct-injection spark-ignition engine using infrared absorption method, Exp Fluids 2010;49(4):925-36.

[27] N. Kawahara, E. Tomita, K. Hayashi, M. Tabata, K. Iwai, R. Kagawa, Cycle-resolved measurements of the fuel concentration near a spark plug in a rotary engine using an in situ laser absorption method, Proc Combust Inst 2007;31(2):3033-3040.

[28] Tomita E, Hamamoto Y, Yoshiyama S, Toda H. Measurement of fuel concentration distribution of transient hydrogen jet and its flame using planar laser induced fluorescence method. JSAE Rev 1998;19(4):329-35.

[29] Blotevogel T, Hartmann M, Rottengruber H, Leipertz A. Tracer-based laser-induced fluorescence measurement technique for quantitative fuel/air-ratio measurements in a hydrogen internal combustion engine. Appl Opt 2008;47(35):6488-96.

[30] Kaiser S, White CM. PIV and PLIF to evaluate mixture formation in a direct-injection hydrogen-fuelled engine. SAE Paper No.2008-01-1034. 2008.

[31] F. Ferioli, P.V. Puzinauskas, S.G. Buckley, Laser-induced breakdown spectroscopy for on-line engine equivalence ratio measurements. Appl Spectro 2003;57(9):1183-1189.

[32] Phuoc TX. Laser-induced spark for simultaneous ignition and fuel-to-air ratio measurements. Opt Lasers Eng 2006;44(6):520-34.

[33] Shudo T, Oba S. Mixture distribution measurement using laser induced breakdown spectroscopy in hydrogen direct injection stratified charge. Int J Hydrogen Energy 2009;34(5):2488-93.

[34] N. Kawahara, J.L. Beduneau, T. Nakayama, E. Tomita, Y. Ikeda, Spatially, temporally and spectrally resolved measurement of laser induced plasma in air. Appl. Phys., B Laser Opt. 2007;86(4):605-614.

[35] Y. Ikeda, A. Nishiyama, N. Kawahara, T. Nakayama, E. Tomita, Local Equivalence Ratio Measurement of CH4/air and C3H8/air Laminar Flames With and Without Flame Front by LIBS. Sect. 5, LIBS2006, 2006.

[36] R.M. Merer, J.S. Wallace, Spark Spectroscopy for Spark Ignition Engine Diagnostics. SAE Paper No. 950164. 1995.

[37] K. Kuwahara, H. Ando, Diagnostics of in-cylinder flow, mixing and combustion in gasoline engines. Meas. Sci. Technol. 2000;11:95-111.

[38] T.D. Fansler, B. Stojkovic, M.C. Drake, M.E. Rosalik, Local fuel concentration measurements in internal combustion engines using spark-emission spectroscopy. Appl. Phys., B Laser Opt. 2002;75(4):577-590.

[39] N. Kawahara, E. Tomita, S. Takemoto, Y. Ikeda. Fuel concentration measurement of premixed mixture using spark-induced breakdown spectroscopy. Spectro Acta Part B 2009;64(10):1085-1092

[40] Roy MK, Nobuyuki K, Tomita E, Fujitani T. Jet-guided combustion characteristics and local fuel concentration measurements in a hydrogen direct-injection spark-ignition engine. Proc Combust Inst 2013;34:2977-84.

[41] Abdul Rahman MT, Kawahara N, Tsuboi K, Tomita E. Visualization and concentration measurement of a direct injection hydrogen jet in a constant-volume vessel using spark-induced breakdown spectroscopy. Int J Hydrogen Energy 2014;39(31):17896-17905.

[42] Abdul Rahman MT, Kawahara N, Tsuboi K, Tomita E. Effect of ambient pressure on local concentration measurement of transient hydrogen jet in a constant-volume vessel using spark-induced breakdown spectroscopy. Int J Hydrogen Energy 2015;40(13):4717-4725.

CHAPTER: 2

Hydrogen as a fuel for IC engine

2.1 Hydrogen as alternative fuel

Research on alternate fuel is gaining more attention in recent years but which fuel or fuels will emerge and to what extent they will replace the use of conventional fuel are remain to be answered. A shift to zero-carbon emission hydrogen systems could fundamentally resolve these energy supply and environmental problems. Hydrogen can be obtained from natural gas, gasoline, coal-gas, methanol, propane, landfill gas, biomass, anaerobic digester gas, other fuels containing hydrocarbons, and water. Obtaining hydrogen from water is an energy intensive process called electrolysis, while hydrocarbons require a more efficient reforming process. Hydrogen is a universal fuel that could power automobiles, aircraft, spacecraft, power plants and appliances, including gas stoves that can operate on mountain-tops. The use of hydrogen as a fuel for transportation and stationary applications is receiving much favorable attention as a technical and policy issue. Hydrogen fueled engines tend to be more energy efficient because of their complete combustion.

The major challenge in using hydrogen as an automotive fuel is storing it safely and efficiently on-board vehicles. Although it is possible to store hydrogen as a high-pressure gas in steel containers, disadvantages exist because of the weight of the storage containers and the safety hazard in the event of an accident. Other methods of storage for hydrogen include solid or liquid hybrids, low temperature cryogenic liquids, or a combination of the two.

2.1.1 Characteristics of hydrogen as a fuel for IC engine

Table 2-1 Properties of Hydrogen and hydrocarbon fuels

Properties	**Hydrogen**	**Gasoline**	**Methane**
Molecular weight, (g/mol)	2.016	~107	16.043
Density, (kg/m^3)	0.08	~750	0.65
Mass diffusivity in air, (cm^2/s)	0.61	0.05	0.16
Kinematic viscosity, (mm^2/s)	110	1.18	17.2
Stoichiometric volume fraction, (in air)	29.5	1.65	9.5
Minimum ignition energy, (mJ)	0.02	0.25	0.28
Minimum quenching distance, (mm)	0.64	~2.0	2.03
Flammability limits in air, (vol%)	4-75	1.0-7.6	5-15
Flammability limits, (φ)	0.1-7.1	0.7-3.0	0.5-1.67
Burning velocity at NTP air, (cm/sec)	265-325	37-43	45
Auto-ignition temperature, (K)	858	501-744	813
Adiabatic flame temperature, (K)	2390	~2275	2225
Normalized flame emissivity, (200K, 1atm)	1.0	1.7	1.7
Stoichiometric air-to-fuel ratio, (kg/kg)	34.2	14.7	17.1
Lower heating value, (MJ/kg)	120	45	50
Higher heating value, (MJ/kg)	142	48	55.5

Hydrogen has significantly different properties compared to the more traditional fuels. Table 2.1 lists the most important physical and combustion-related properties [1-4] as a reference for the discussion in the following. Hydrogen molecule is very light and mobile (high mass diffusivity), and shows a very low density at atmospheric conditions. It has wide flammability limits, with flammable mixtures from as lean as $\lambda = 10$ to as rich as $\lambda = 0.14$ (0.1

< φ <7.1) which allows smooth engine operation and a wide range of engine power output. The flammability limits widen with increasing temperature, with the lower flammability limit dropping to 2 vol% at 300^{o}C (equivalent to λ = 20/ φ = 0.05) [18]. The lower flammability limit increases with pressure [5], with the upper flammability limit having a fairly complex behavior in terms of pressure dependence [6] but of lesser importance to engines. Engine efficiency increases remarkably by de-throttling and lean operation at low engine loads. Homogeneous operation with λ > 2 reduces combustion temperatures below the formation temperature of thermal nitric oxides, resulting in virtually zero combustion emissions. There is a limit to how lean the engine can be run, as lean operation can significantly reduce the power output due to a reduction in the volumetric heating value of the air/fuel mixture.

Further to the flammability limits, the laminar burning velocities of hydrogen remarkably differ from those of hydrocarbon fuels. Taking atmospheric conditions (p = 1.013 bar, T = 293.15 K) as reference, the laminar flame speed of stoichiometric hydrogen-air mixtures (u_l = 265 cm/s to 325 cm/s) is about seven times higher than the laminar flame speed of gasoline and methane (u_l = 37 cm/s to 45 cm/s). Even at lean conditions, the flame speed is high enough to prevent efficiency losses caused by delayed combustion. In case of high-pressure hydrogen direct-injection an additional gain of the effective burning velocity due to an increased turbulence level can be obtained. In addition, its high burning velocity may contribute to a relatively high thermal efficiency with a shorter combustion period at the ignition timing close to top dead center (TDC) [7].

The amount of energy needed to ignite hydrogen is about one order of magnitude less than that required for gasoline. This enables hydrogen engines to ignite lean mixtures and ensures prompt ignition. The easy ignitability of hydrogen-air mixtures shows a considerable reduction of cycle-to-cycle variation coefficients compared to gasoline engines enabling efficiency-optimized spark-timing settings. Unfortunately, the low ignition energy means that hot gases and hot spots on the cylinder can serve as sources of ignition, creating problems of premature ignition and flashback. Preventing this is one of the challenges associated with running an engine on hydrogen.

The auto-ignition temperature of hydrogen can be seen to exceed the values for methane and gasoline. This makes hydrogen particularly suited for spark ignition operation and unsuited for compression ignition.

2.2 Hydrogen engine technology and current development

Current researches have focused on high pressure hydrogen injection directly into the engine combustion chamber with spark discharge as ignition source [8-11], due to their high volumetric efficiency and potential to avoid preignition and backfiring, which are the main problems in hydrogen-fueled IC engines. The ability for hydrogen engines to burn cleanly and operate efficiently is owed to the unique combustion characteristics of hydrogen that allow ultra-lean combustion with dramatically reduced NO*x* production and efficient low-engine load operation. In contrast, the same combustion characteristics impose technical challenges at high engine-loads due to an increased propensity to preignite the hydrogen–air mixture and increased NO*x* production.

Due to the challenges of onboard hydrogen storage, current hydrogen-powered internal combustion engine vehicles have a limited range and in some cases reduced trunk space available compared to their conventional-fuel counterparts. Numerous hydrogen engine-powered vehicles ranging from two-wheelers to passenger cars, pickup trucks to buses and off-road equipment have been designed, built and tested over the last few decades.

2.2.1 Overview of R&D projects worldwide

Japan, USA, EU has taken initiatives to shift towards a hydrogen-based transportation system. Whether hydrogen will be used in combustion engines or fuel cells in the future depends decisively on the extent to which both concepts meet the existing customer requirements with regard to driving performance, procurement and operating costs. It is believed that the utilization of hydrogen as a fuel for transportation is more likely to be expected in internal combustion engines than in fuel cells at least for some decades [12].

2.2.1.1 In Japan

In Japan's National Basic Energy Plan, the government has stated that the aim of the policy includes the establishment of a hydrogen society ahead of other countries, starting in 2014. They developed a roadmap that specifies expansions in popularization efforts for household and industrial fuel cells, cost reductions for hydrogen fuel and FCVs, and the establishment of a large-scale hydrogen supply chain that includes transport of hydrogen by sea. The introduction of hydrogen power generation for industrial purposes is a priority goal and policies are being developed to position hydrogen energy as a central secondary energy source for other applications as well.

In Japan, Professor Furuhama at the Musashi Institute of Technology (currently Tokyo City University) began his research on hydrogen IC engine since 1970. In 1974, he demonstrated the drive of "Musashi No. 1," the first 2000 cc hydrogen engine vehicle in Japan, which was developed by modifying a Nissan Junior 2-ton truck. Major improvements were made later and vehicle No. 10, namely, "Musashi No. 10," was exhibited at the COP3 meeting held in Kyoto in 1997.

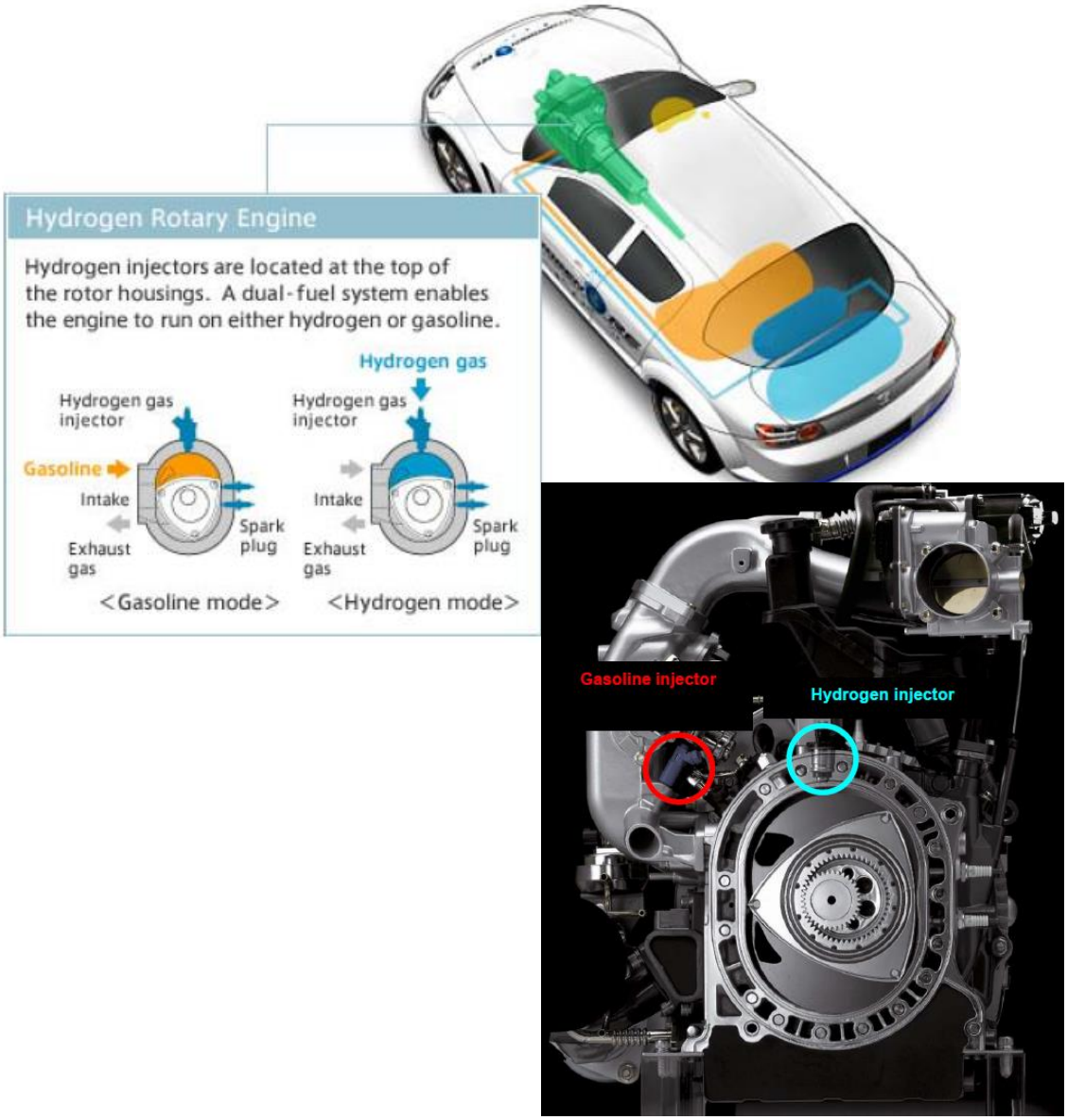

Fig.2.1 RX-8 Hydrogen RE (Source Mazda Motor)

Since the announcement of the Mazda HR-X, the first hydrogen rotary engine vehicle, at the 1991 Tokyo Motor Show, Mazda has been promoting research and development of hydrogen rotary engines. The RX-8 Hydrogen RE (see Fig.2.1) and the Premacy Hydrogen RE Hybrid (see Fig.2.2) are equipped with a dual-fuel system, so the vehicles can run on gasoline if there is no hydrogen available. The RX-8 Hydrogen RE is equipped with two compressed hydrogen tanks with an operating pressure of up to 350 bar, giving the vehicle a range of approximately 100 km in hydrogen operation plus an additional 550 km on gasoline. A combination of lean and stoichiometric hydrogen combustion operation results in a 23% improvement in fuel economy compared to gasoline operation, but at the cost of significant reductions in power and range. The performance of the vehicle is reduced from 154 kW in gasoline mode, to 80 kW in hydrogen operation, with a torque of 140 Nm [92]. The maximum speed is reduced from 234 kph to 169 kph. In 2007 Mazda signed a 'memorandum of understanding' to provide around 30 RX-8 Hydrogen RE's to HyNor – a national development project of Norway which promotes the use of hydrogen in the transport sector, with the ultimate plan being a roadway stretching 580km from Oslo to Stavanger, complete with hydrogen fueling stations along the route [93]. In 2007, Mazda unveiled the Mazda Premacy RE hybrid which incorporates a hybrid system that improves energy efficiency, delivering improved acceleration. As in the hydrogen RX-8, the on-board RENESIS rotary engine can burn either gasoline or hydrogen, however in the Premacy, the rotary engine does not move the vehicle directly; it instead powers a generator that charges a small lithium-ion battery pack which helps power an 110kW electric motor. The vehicle can accelerate to 60 mph in around ten seconds and reach a top speed of more than 100 mph. Driving range is about 200km using hydrogen, with the additional 400km from the gasoline. The hydrogen tank

with 110 litres at 350 bar stores up to 2.4 kg hydrogen. The Premacy Hydrogen RE Hybrid with a driving range of 200 km.

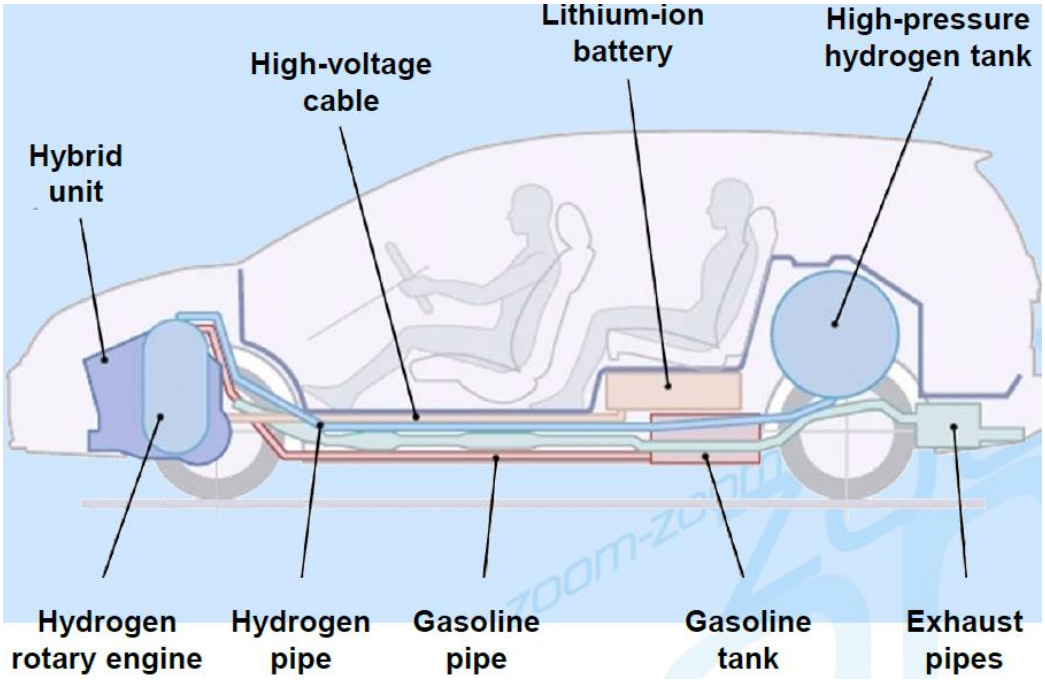

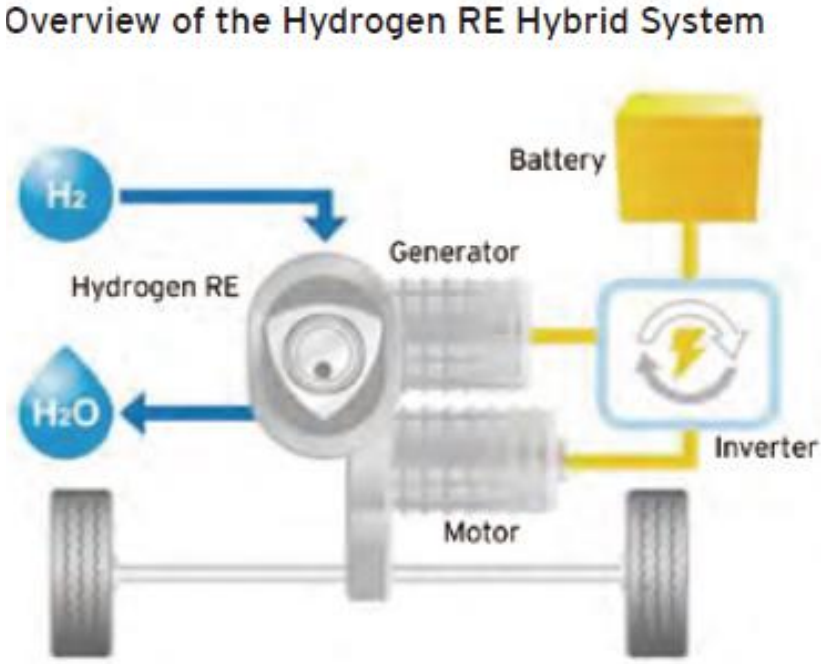

Fig.2.2 Premacy Hydrogen RE (Source Mazda Motor)

Next-generation Environmentally Friendly Vehicle Development and Commercialization Project (EFV21) of the Japanese Ministry of Land, Infrastructure, and Transport (MLIT) ran in two terms between 2005 and 2010; and was coordinated by the National Traffic Safety & Environment Laboratory (NTSEL). It aimed at reducing CO2 emissions from heavy duty engines and focused on H_2ICEs as opposed to FCVs or BEVs in order to obtain high specific power outputs. It resulted in the development of DI injectors, mapped combustion strategies in single cylinder engines (metal and optical), evaluated a multi-cylinder engine towards the project target power output and looked at different ways of reaching NOx emission standards [11,13-16].

Fig.2.3 Hybrid light duty truck equipped with a 4 L 91 kW hydrogen engine

Fig.2.4 Microbus equipped with a 4.7 L 105 kW hydrogen engine

Parallel to the work performed within the NTSEL project, Tokyo City University was also involved in research leading to the demonstration of 2 hydrogen vehicles. Iwasaki et al. [17] report the conversion of 2 engines to turbocharged PFI operation on hydrogen. These were used in a light duty truck with a hybrid powertrain (with the electric drive used to fill in low speed torque), see Fig. 2.3, and a 'microbus' (19 passengers, see Fig. 2.4), with the latter serving for over 2 years and covering more than 15000 km within the year 2014 (it was put

out of service in March 2013-personal comm.). Lean operation was used to avoid the formation of NOx, so that after-treatment was not necessary; and turbocharging recovered most of the power loss due to the lean mixtures. Both vehicles were tested on the JE05 test cycle and emitted NOx emissions far below the Japan Post New Long-Term Regulation. The authors devoted much work to devising measures for avoiding abnormal combustion (backfire in particular), primarily through changes in the ignition system.

2.2.1.2 In USA

In the U.S., between 2004 and 2011 the Office of Energy Efficiency and Renewable Energy of the Department of Energy's FreedomCAR and Vehicle Technologies Program sponsored work at the Argonne and Sandia National Laboratories targeted at reaching specific peak and part load efficiencies, and NOx emissions. In order to reach these targets, experimental work was undertaken on metal and optical single cylinder engines supported by numerical work (CFD simulations) [18-29].

2.2.1.3 In EU

In Europe, a three-year (2004-2007) Integrated Project called HyICE [30] resulted in the demonstration of engine concepts exceeding a specific power output of 100 kW/l and a peak efficiency of 42%. The project was funded in the 6th Framework Programme of the European Commission and coordinated by BMW. The consortium consisted out of industrial and academic partners and investigated hydrogen's potential on single and multi-cylinder engines, with DI as well as cryogenic PFI; developed 1D and CFD modeling tools; DI injectors, and looked at optical measurement techniques to elucidate the particularities of hydrogen

combustion in engines. Other regional activities in Europe resulted in the conversion of passenger cars [31,32] and a fork lift truck to H2ICE operation [33], in the framework of demonstration programs.

2.2.2 Mixture formation strategies for hydrogen engine

The proper design of the mixture formation process is crucial for achieving high engine efficiencies while meeting more and more stringent emissions targets. Similar to conventionally fueled engines, hydrogen engines have gone through continuing improvement and refinement in terms of mixture formation strategies. The main classification of mixture formation strategies is based on the location of the formation of the hydrogen and conventional fuel mixture: External mixture formation refers to where hydrogen is introduced outside the combustion chamber (usually within the intake manifold), which contrasts with internal mixture formation, where the hydrogen is introduced directly into the combustion chamber. Modern hydrogen combustion engines almost exclusively use electronically controlled fuel-injection systems; however, the requirements and specifications for these systems change widely based on the injection location and the temperature of the injected fuel. Generally, hydrogen injection systems for external mixture formation are operated at lower injection pressures (2-8 bar) compared to systems for hydrogen direct injection (5-250 bar). Also, the exposure of injectors to in-cylinder temperatures and pressure in combination with increased injection pressures for internal mixture formation systems still requires further injector development to reach production standards in terms of durability [34]. Research and development have also been performed on external mixture formation concepts with cryogenic hydrogen [35-40] posing

challenges to the injection system due to extremely low temperatures (boiling temperature of hydrogen is approximately 253°C) and related issues, for example, injector icing.

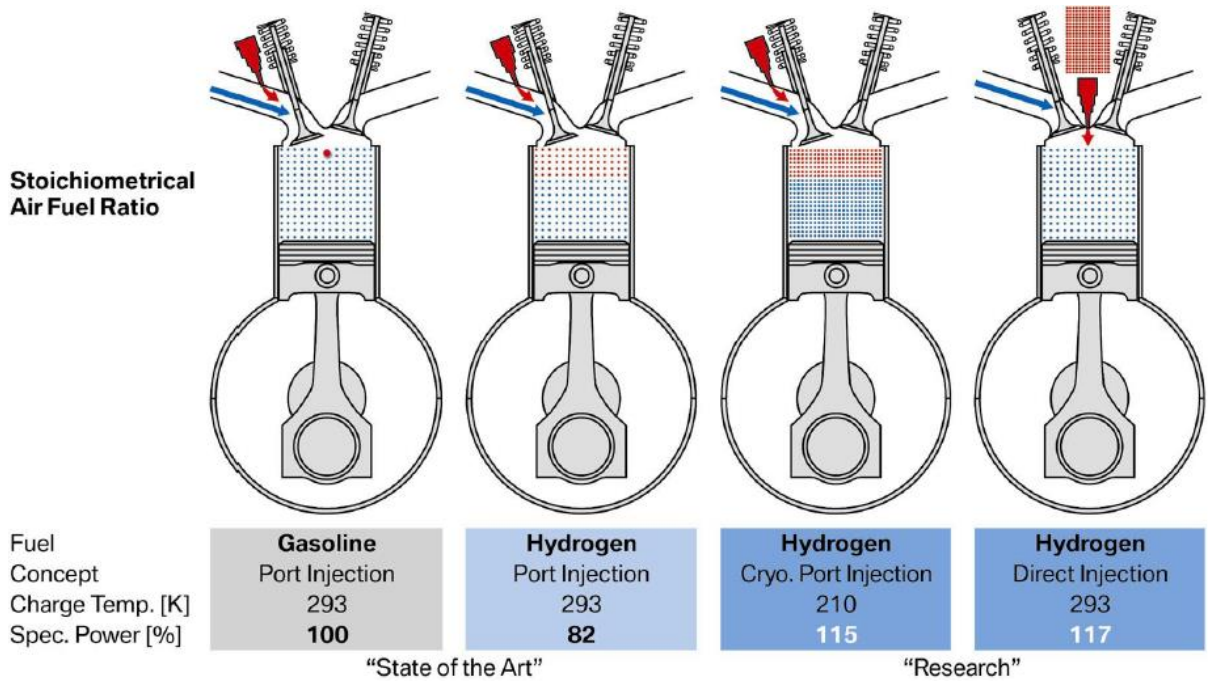

Fig.2.5 Potential of specific power of various engine concepts

2.2.2.1 External mixture formation

Initial implementation of hydrogen fuel technologies included the usage of external mixture formation by either injecting hydrogen into an intake manifold or near the intake valve with port fuel injection (PFI) [41,42]. External mixture formation by means of port fuel injection (PFI) has been demonstrated to result in higher engine efficiencies, extended lean operation, lower cyclic variation and lower NOx production compared to internal mixture formation

through direct injection (DI) [43,44]. This is the consequence of the higher mixture homogeneity due to longer mixing times for PFI as well as decreased mixing for DI as the intake generated turbulence contributes less to the mixing. Additionally, the cost and complexity are significantly lower for PFI than for DI [45] and retrofitting an existing engine is possible. On the other hand, the power output of an external mixture formation hydrogen engine is limited because of the decrease in volumetric efficiency: due to the low density of hydrogen and small air requirement for stoichiometric mixtures, the cylinder volume taken up by the hydrogen in a stoichiometric mixture amounts to 29.5%. Assuming a constant fuel-to-air equivalence ratio of 0.5 ($\lambda = 2$) results in a theoretical maximum power output of the hydrogen engine that is only about 50% of a regular gasoline engine in stoichiometric operation (see Fig.2.6). Thus researchers have investigated the potential of using supercharging in combination with constant lean air–fuel ratio operation to mitigate the significant power loss [46,47]. An effective way to limit the power loss compared to gasoline or diesel engines is by running hydrogen port-injection engines at stoichiometric air–fuel ratios. However, stoichiometric port-fuel injection operation is prone to combustion anomalies and also requires an aftertreatment system to reduce the level of oxide of nitrogen emissions. As shown in Fig.2.6, stoichiometric H_2 PFI operation results in a theoretical power density of approximately 86% compared to gasoline. The mixture formation concepts employing hydrogen port injection result in compromises either in terms of power density with lean air–fuel ratio approaches or engine efficiency with stoichiometric concepts. However, the most serious problem with PFI is the high possibility of pre-ignition and backfire, especially with rich mixtures.

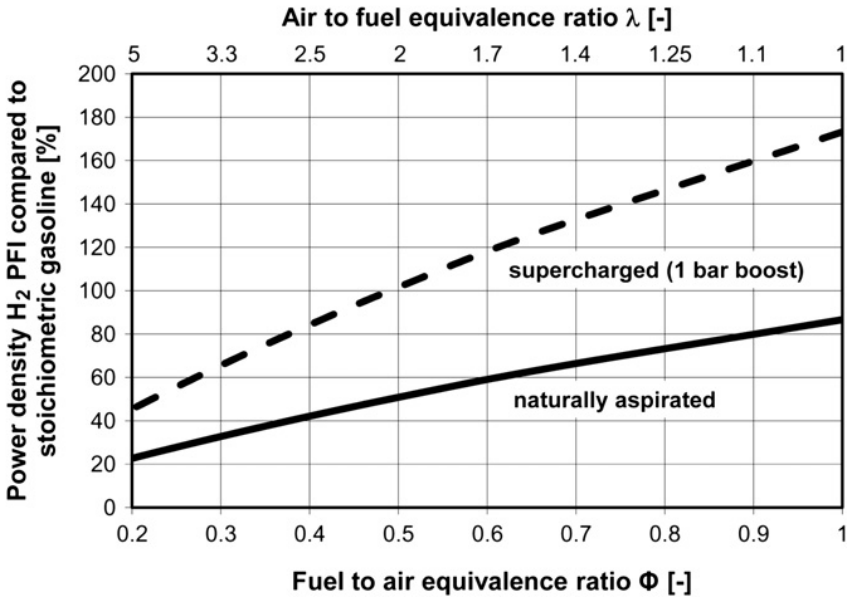

Fig.2.6 Theoretical power density of a PFI H2 engine compared to stoichiometric gasoline operation as a function of equivalence ratio and charging strategy

Pre-ignition is a problem much more serious in hydrogen engines then in other internal combustion engines because of the lower ignition energy of hydrogen–air mixtures, wider range of flammability and smaller quenching distance of hydrogen. Here, preignition is defined as combustion prior to spark discharge, and in general, results from surface ignition at engine hot spots, such as spark electrodes, valves or engine deposits. The limiting effect of preignition is that a preignition event will advance the start of combustion and produce an increased chemical heat release rate. In turn, the increased heat-release rate results in a rapid pressure rise, higher peak cylinder pressure, acoustic oscillations and higher heat rejection that leads to higher in-cylinder surface temperatures. The latter effect can advance the start of combustion further, which in turn can lead to a runaway effect, and if left unchecked will lead to engine failure [2]. It is therefore a necessity for practical application

that preignition is avoided. The second combustion anomaly backfire or backflash occurs when the fresh charge is ignited before the intake valve is closed and results from the hydrogen mixing with hot residual gases that remain in the cylinder after combustion. The appearance of backfire is difficult to predict. Generally, backfire arises at high thermal loads. Possible adaptations to prevent backfire are:

1. The use of cold-rated spark plugs, in order to have low surface temperatures on the tip. A waste spark ignition system has to be avoided. Using an ignition coil with grounding will avoid residual voltage on the spark plug.

2. The use of cooled exhaust valves (e.g. sodium cooled exhaust valves)

3. A cooling system designed to provide uniform coolant flow rates.

2.2.2.2 Internal mixture formation

Direct injection of hydrogen has long been viewed as one of the most attractive options for advanced H_2ICE to avoid combustion anomalies and increase the power density or volumetric efficiency while achieving near-zero emissions. Similar to common classifications for gasoline engines, hydrogen DI mixture formation strategies have also been grouped in jet-guided, wall-guided, and air-guided concepts (see Fig.2.7) [48]. Based on the start of injection (SOI), one can differentiate early DI and late DI operation; however, no clear threshold between these two categories has been defined. Fig.2.8 shows a schematic of different hydrogen DI strategies and their respective injection timings. In order to avoid

displacement of fresh charge by hydrogen of low density, the start of injection even for early injection is usually set after intake valve closing.

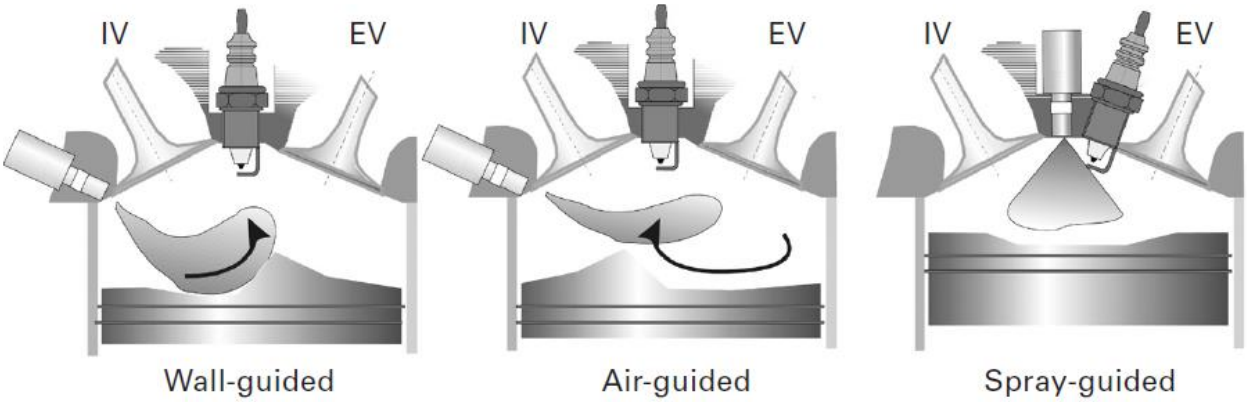

Fig.2.7 Wall, air and spray-guided combustion concepts

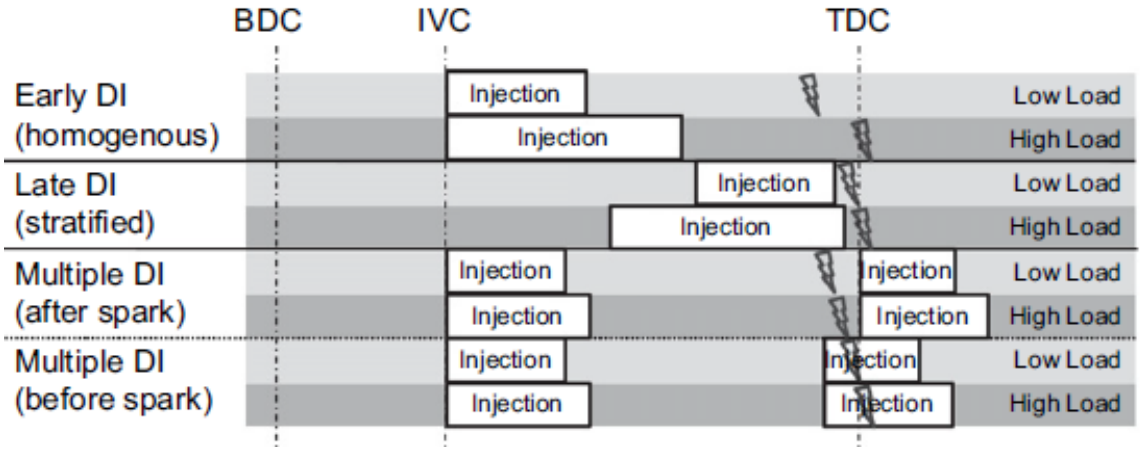

Fig.2.8 Schematic of injection strategies for DI [223].

The preignition problem is controlled by timing injection to both minimize the residence time that a combustible mixture is exposed to in-cylinder hot-spots (i.e., late injection) and allow for improved mixing of the intake air with the residual gases. The improved volumetric

efficiency (equal to PFI gasoline or higher) and the higher heat of combustion of hydrogen compared to gasoline provides the potential for DI-H2ICE power density to be approximately 115% that of the identical engine operated on gasoline [49]. The challenge with DI-H2ICE operation is that in-cylinder injection requires hydrogen–air mixing in a very short time. For early injection (i.e., coincident with IVC) maximum available mixing times range from approximately 20–4 ms across the speed range 1000–5000 rpm, respectively. In practice, to avoid preignition, start of injection (SOI) is retarded with respect to IVC, and mixing times are further reduced.

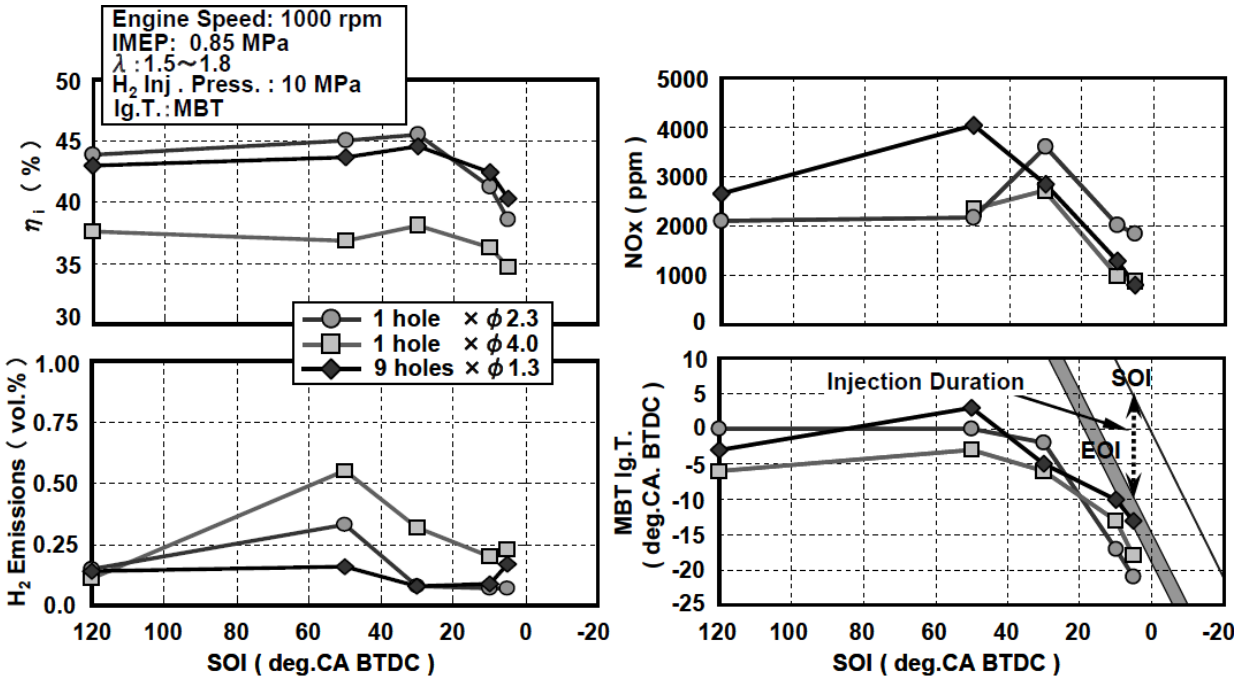

Fig.2.9 Effect of injection timing (SOI) on engine performance

Given the high probability of incomplete mixing with late injection, much effort has been devoted to understanding the effect of injection timing on DI-H2ICE properties. The effect of SOI on NO*x* emissions has been investigated by Homan et al. [50], Glasson and Green [51]

and Eichlseder et al. [49] where it is observed that the effect of SOI on NO*x* emissions is not simple: NO*x* emissions increase with retard of SOI in several data sets, and decrease in others. Oikawa et al. reported a "plume ignition combustion concept" (PCC) for hydrogen DISI engines, denoting the ignition of a rich mixture plume during or right after an injection event [9]. In their study, the injector was mounted close to the spark plug to achieve jet-guided combustion with the jet being directed towards the spark plug using high injection pressures (200 bar). This PCC combustion with late injection strategy was shown to substantially reduce NOx emissions at high speed and under high load conditions while maintaining high thermal efficiency and power as shown in Fig.2.9.

2.3 Fuel Concentration Measurement Techniques

The local equivalence ratio near the spark plug at the time of the spark discharge is particularly important for successful ignition, because the jet-guided system generates a stratified fuel concentration near the spark plug in a DISI engine. In addition, the mixture distribution around the spark plug, together with fluid motion, strongly influences the combustion initiation, which subsequently affects the engine performance, efficiency, and emissions. Thus, a fundamental understanding of mixture formation processes is necessary to optimise DI-H2 ICE operation. To better understand how to both achieve an optimal local mixture and control the large-scale stratification, a diagnostic tool for providing information on the mixture distribution in practical engines should be developed. Instantaneous fuel concentration measurements in production engines will greatly aid in engine design and optimisation.

There are several approaches to studying fuel concentrations in an SI engine, including infrared (IR) absorption, planar laser induced fluorescence (PLIF), Raman scattering, laser-induced breakdown spectroscopy (LIBS) and spark-induced breakdown spectroscopy (SIBS) or spark emission spectroscopy.

2.3.1 Planar laser induced fluorescence (PLIF)

Laser diagnostics are widely used in fundamental combustion science, research, and development to investigate transient phenomena without influencing the system under study by inserting probes and surfaces. LIF measurements have been used widely because the LIF signal is relatively strong and provides two-dimensional fuel concentration information at a specified time. Figure 2.10 shows the simplified PLIF experimental facility.

Tomita et al. [52] applied the PLIF method to study the fuel concentration distribution in a transient hydrogen jet. Results showed that each transient hydrogen jet had different configurations and concentration distributions. Kaiser and White [18] performed an optical study of mixture preparation in a hydrogen-fuelled engine using a PLIF technique; their report favoured increased injection pressure and careful nozzle design. Volker et al. [53,54] reported potential adverse effects that added tracers might have on mixture formation, and combustion. In his study quantitative equivalence ratio maps are estimated for the fuel injection event within a single cycle in a direct-injection spark-ignition engine. Spray velocities determined from the moving fuel cloud are in good agreement with previous particle image velocimetry measurements. However, these optical methods require changes in the engine combustion chamber design because of the need for optical windows. Therefore, these methods are difficult to apply to commercial engines.

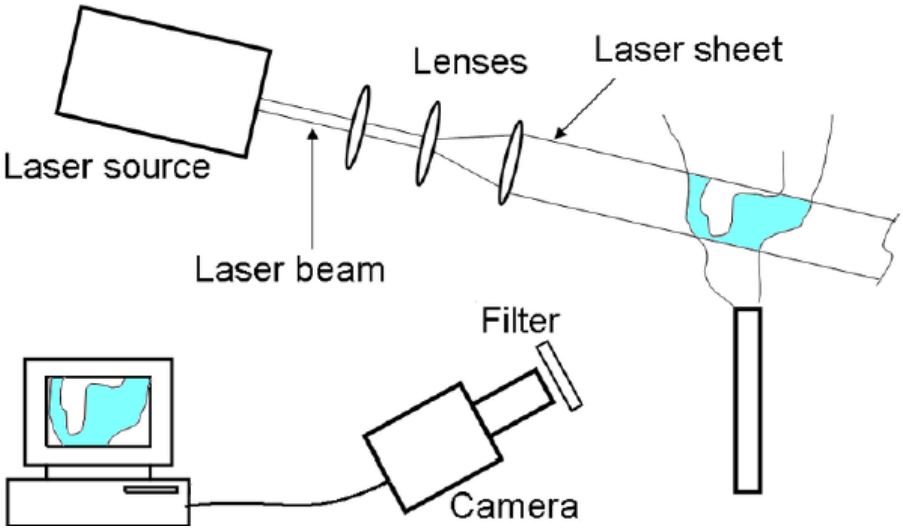

Fig.2.10 Experimental set-up for PLIF measurement

2.3.2 Infrared (IR) absorption technique

A 3.392-μm He-Ne laser was used for in-situ measurements of fuel concentrations for combustion diagnostics [55-26]. The research group at Heat power engineering laboratory of Okayama University was the first to report the possibility of measuring fuel concentration near the spark plug in a test engine [59]. Figure 2-10 shows the optical sensor installed in a spark plug. This sensor was developed by modifying a commercially available spark plug which makes it possible to install it in a practical engine and measure the fuel concentration near the spark plug under firing conditions. Subsequently, Tomita et al. used an optical sensor with a pair of sapphire rods to pass laser light through the combustion chamber of a practical engine; they also discussed several of the factors that affected measurement accuracy [60,61]. Their sensor has also been applied to practical SI engines and direct-

injection gasoline engines [62]. We developed an optical spark-plug sensor with a double-pass measurement length using an infrared absorption technique for measuring hydrocarbon fuel concentrations [63,65]. The results show that during the compression stroke, the characteristics of the mixture formation near the spark plug differed according to the injection timing. Laser infrared absorption technique indicates higher measurement uncertainty even in lean mixture conditions. However, the mixture is ignited near the spray plume or the vapour mixture around the spray in a spray-guided DISI engine, so it is important to measure the equivalence ratio at the spark point. It is very difficult to measure the fuel/air ratio inside an engine cylinder, even using the absorption technique, due to the lack of absorption bands at visible and infrared wavelengths.

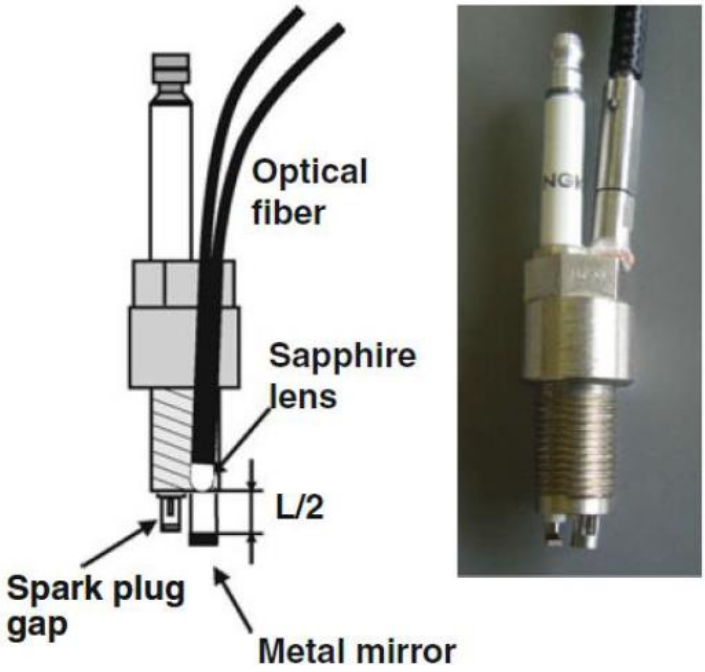

Fig.2.11 Schematic diagram and photograph of an IR spark plug sensor

2.3.3 Raman scattering

Raman spectroscopy is a spectroscopic technique based on inelastic scattering of monochromatic light, usually from a laser source. Inelastic scattering means that the frequency of photons in monochromatic light changes upon interaction with a sample. Photons of the laser light are absorbed by the sample and then reemitted. Frequency of the reemitted photons is shifted up or down in comparison with original monochromatic frequency, which is called the Raman Effect. This shift provides information about vibrational, rotational and other low frequency transitions in molecules. A Raman photon is emitted if a molecule then undergoes a transition to a higher vibrational energy state than its original state (Stokes-Raman) to a lower energy vibrational state (Anti-Stokes Raman). Figure 2.12 shows the difference in energy or wavelength of a scattered light from a material is characteristic for a particular bond in its molecular structure. The various energy shifts associated with different molecular vibrations leads to a Raman spectrum which is unique for each molecule and provides a precise spectral fingerprint. Raman spectroscopy can be used to study solid, liquid and gaseous samples. In recent years, several papers have been published in which Raman scattering was used for the investigation of mixture formation processes, exhaust gas recirculation, and cold start phenomena of conventional [66] or propane fired spark ignition engines [67,68]. When applying Raman scattering for the investigation of engines with direct fuel injection, the occurrence of droplets is an additional source of disturbance, because the elastically scattered light from fuel droplets can generate signal intensities which are up to 20 orders of magnitude larger than the Raman signals.

Linear Raman scattering has been used for the investigation of the mixture formation inside an optically accessible gasoline direct injection spark ignition engine [69]. The concentrations of O2, N2, H2O, and isooctane have been measured simultaneously and cycle resolved along a line of nearly 1 cm at three different locations inside the combustion chamber. By means of polarization-resolved detection optics, it was possible to separate the highly polarized Raman signals from unpolarized contributions from light emissions by stray light from surfaces, background luminescence, or laser-induced fluorescence. However, this measurement technique provides very small signal intensities, so its careful adaptation to the particularity of the test object is very important for successful utilization.

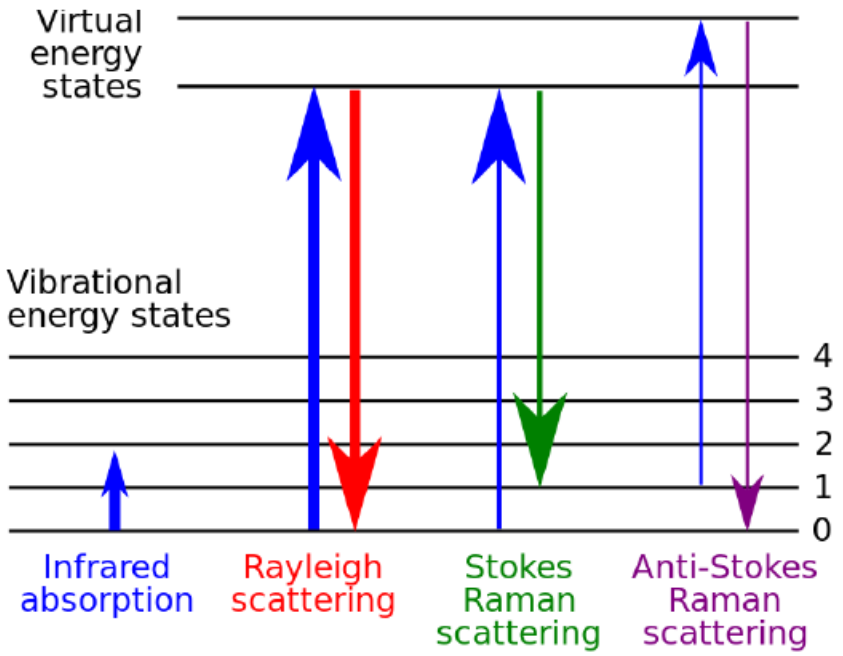

Fig.2.12 Energy-level diagram showing the states involved in Raman signal. The line thickness is roughly proportional to the signal strength from the different transitions

2.3.4 Laser-induced breakdown spectroscopy (LIBS)

Laser-induced breakdown spectroscopy (LIBS) (or laser-induced plasma spectroscopy, LIPS) has advanced dramatically due to the availability of online real-time information on a surrogate material with no sample preparation. LIBS of gases are possible using high power laser pulses. When a short-pulse laser is focused into air or other gases, the laser beam creates localized plasma. The collection and spectral analysis of the plasma emissions allows the qualitative identification of atomic species. Ferioli et al. [70] used LIBS on engine exhaust gas to illustrate the ability of this technique to measure the equivalence ratio of SI engines, using the ratios of C/O and C/N atomic peaks derived from the measured spectra. Phuoc [71] used a laser-induced spark to measure the ignition and fuel-to-air ratio of CH4-air and H2-air combustible mixtures simultaneously using the measured spectral peak ratio Hα (656 nm)/O (777 nm). Shudo and Oba [72] measured the mixture formation characteristic with a hydrogen jet in a nitrogen-filled constant-volume chamber using LIBS techniques. Kawahara et al. [73,74] also report measurements of equivalence ratio using LIBS technique and discussed the accuracy of spatially, temporally, and spectrally resolved measurements. Figure 2.13 shows the Schematic diagram of experimental apparatus for Laser Induced Breakdown Spectroscopy (LIBS) [73].

However, IR absorption is not suitable for measuring the hydrogen/air ratio due to the lack of absorption bands at visible and infrared wavelengths. PLIF and LIBS require major engine modifications including optical access, which limit their application to production engines. Quantitative measurements of the cycle-to cycle variations in the mixture strength at or near the ignition site are comparatively rare for practical hydrogen SI engines.

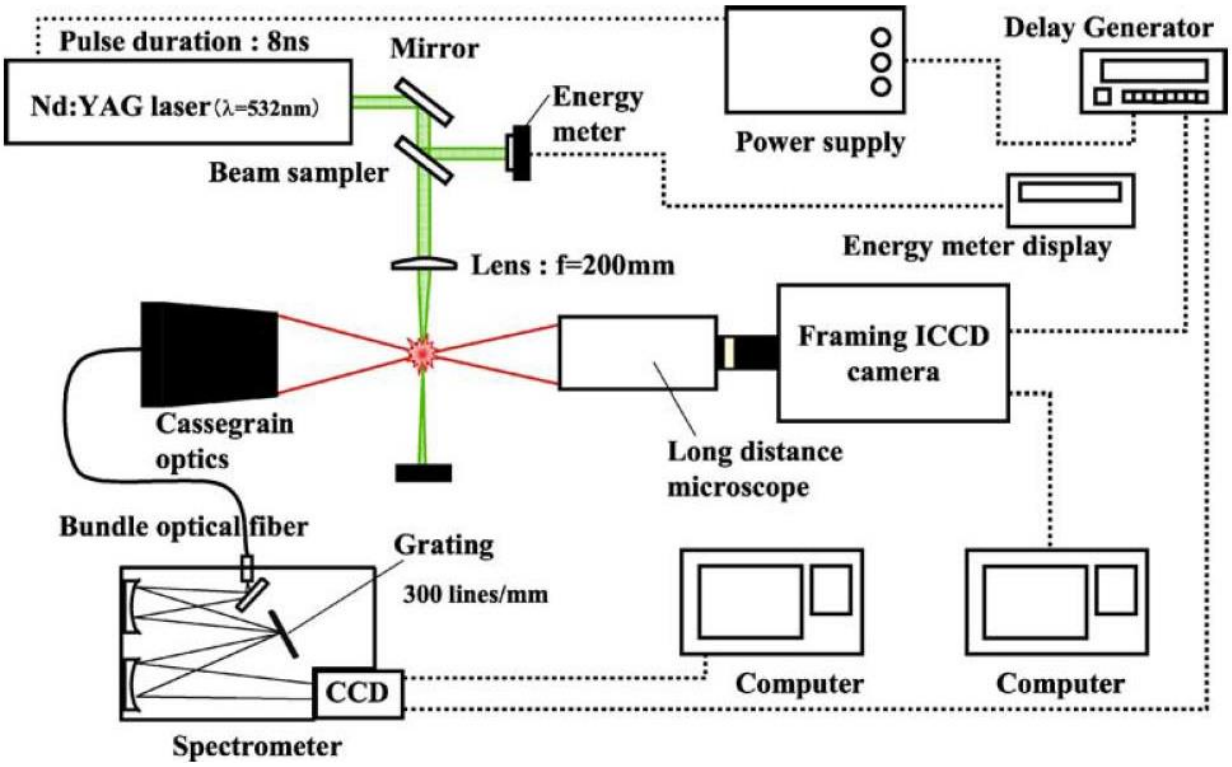

Fig.2.13 Schematic diagram of experimental apparatus for Laser Induced Breakdown Spectroscopy (LIBS)

2.3.5 Spark-induced breakdown spectroscopy (SIBS)

With SIBS, the signal detection and spectroscopy are similar to LIBS; however, spark generation occurs between two electrodes, in which the spark itself is used as the light source to estimate the equivalence ratio in the spark plug. SIBS can therefore be used in a combustion chamber with no engine modifications, because the plasma excitation can be implemented using a conventional spark plug. Spark-emission spectroscopy has been

applied to measure the equivalence ratio in a DISI engine [75-77]. Merer et al. [75] observed the light emissions from a spark discharge by inserting a fiber optic cable through the centre electrode of a spark plug, to investigate the possibility of determining the fuel-air ratio in the spark gap at ignition with spectroscopy. He observed the total broadband light emission from the spark and the light emission centred at 385 nm from the cyanogen radical (chemical formula CN) for varied f and residual gas concentrations. Ando and Kuwahara [76], and Fansler et al. [77] reported individual measurements of the equivalence ratio at the spark gap using the ratio of CN (388 nm) emission intensity and OH (306 nm) radical intensity from the spark that initiates combustion. They determined the cycle-resolved local fuel–air ratio in the spark gap, controlled the large-scale stratification, and evaluated the utility of SIBS as an engine diagnostic tool. However, it is difficult to detect the equivalence ratio under lean mixture conditions due to lack of the linearity of CN/OH emission intensity ratio. Letty et al. [78] analyzed emission spectra from electrical and laser sparks in flowing methane–air mixtures of various compositions and discussed the differences and similarities between the electrical and laser sparks in the context of their emission. The emission spectra from the laser spark were characterized by a weak continuum, onto which several strong atomic lines and some molecular bands were superimposed, in contrast to the spectra of electrical spark where a strong continuum, few atomic lines and several strong molecular bands were evident. All of these studies require engine modification for optical access to the combustion chamber from outside. Kawahara et al. [79] used the SIBS technique to measure the local equivalence ratio in a laminar premixed flame of a CH4/air mixture. Spectrally resolved emission spectra of plasma generated by a spark plug were investigated for their potential to measure local fuel concentrations in a premixed mixture. The spectrum was measured

through an optical fibre housed in the centre electrode of the spark plug, which makes this technique suitable for measuring the equivalence ratio in the spark gap at ignition timing, in production engines without engine modification. Roy et al. [80] further improved the spark-plug sensor to measure the local fuel–air concentration in the spark gap at the time of ignition in a fired, jet-guided hydrogen SI-engine operated under stratified-charge conditions using SIBS. Tasyrif et al. [81] investigated the mixing process of a hydrogen jet in a constant-volume vessel and characterised the spatial distribution of the equivalence ratio across the jet and along its axis. Later, they reported the effects of the ambient pressure on fuel concentration measurements for a jet of hydrogen injected into a nitrogen environment with different ambient pressures; also, local concentrations were measured at various spark locations in a constant-volume vessel [82].

2.4 Summary

Shifting to hydrogen energy can have a profound positive impact on the Earth's biological systems. The wide-flammability limits, the fast fuel conversion, the reliable ignition behavior and the carbon-free combustion make hydrogen an ideal fuel for internal combustion engine applications. Advanced hydrogen-engine concepts are based on direct-injection (DI) fuel systems. In contrast to port-injection, DI not only avoids loss of power due to low volumetric efficiency, but also can mitigate combustion problems such as knock, backfire, and pre-ignition, which have detrimental effects on engine performance and emissions. An area of necessary research and development is the improvement of the hydrogen injectors for DI. The exposure of injectors to in-cylinder temperatures and pressure in combination with increased injection pressures for internal mixture formation systems still requires further

injector development to reach production standards in terms of durability. Extent of benefit from DI depends in great degree on the injection strategy and the subsequent mixture formation. The local equivalence ratio near the spark plug at the time of the spark discharge is particularly important for successful ignition; in addition, the mixture distribution around the spark plug, together with fluid motion, strongly influences the combustion initiation, which subsequently affects the engine performance, efficiency, and emissions. Therefore, understanding the details of injection and mixing is an imperative step to improve the efficiency of future hydrogen engines. To better understand how to both achieve an optimal local mixture and control the large-scale stratification, a diagnostic tool for providing information on the mixture distribution in practical engines should be developed. Instantaneous fuel concentration measurements in production engines will greatly aid in engine design and optimisation.

REFERENCE

[1] Glassman I. Combustion. Orlando, FL: Academic Press, Inc.; 1987.

[2] Heywood JB. Internal combustion engine fundamentals. McGraw-Hill; 1988.

[3] Morley C. GASEQ, a chemical equilibrium program for windows.

[4] Perry RH, Green DW, editors. Perry's chemical engineers' handbook. McGraw-Hill; 1997.

[5] Molnarne M, Schendler T, Schroeder V. Explosionsbereiche von Gasgemischen. In: Sicherheitstechnische Kenngroessen, Band 2. Wirtschaftsverlag NW –Verlag fuer neue Wissenschaft; 2003.

[6] Schroeder V, Holtappels K. Explosion characteristics of hydrogen–air and hydrogen–oxygen mixtures at elevated pressures. International Conference on Hydrogen Safety, Pisa, Italy, Paper No. 120001 (2005).

[7] Mohammadi A, Shioji M, Nakai Y, Ishikura W, Tabo E. Performance and combustion characteristics of a direct injection SI hydrogen engine. Int J Hydrogen Energy 2007; 32(2):296–304.

[8] Duan J, Liu F, Sun B. Backfire control and power enhancement of a hydrogen internal combustion engine. Int J Hydrogen Energy 2014;39(9):4581e9.

[9] Oikawa M, Ogasawara Y, Kondo Y, Sekine K, Takagi Y, Sato Y. Optimization of hydrogen jet configuration by single hole nozzle and high speed laser shadowgraphy in high pressure direct injection hydrogen engines. Int J AutomotEng 2012;3:1-8.

[10] Roy MK, Nobuyuki K, Tomita E, Fujitani T. Jet-guided combustion characteristics and local fuel concentration measurements in a hydrogen direct-injection spark-ignition engine. Proc Combust Inst 2013;34:2977-84.

[11] Yamane K, Nogami M, Umemura Y, Oikawa M. Development of high pressure H2 gas injectors, capable of injection at large injection rate and high response using a common-rail type actuating system for a 4-cylinder, 4.7-liter total displacement, spark ignition hydrogen engine. 2011. SAE Paper No. 2011-01-2005.

[12] J. Romm, "The car and fuel of the future", Energy Policy, 34 (2006); pp. 2609–2614

[13] Kawamura A, Yanai T, Sato Y, Naganuma K, Yamane K, Takagi Y. Summary and progress of the hydrogen ICE truck development project. SAE International; 2009. SAE paper no. 2009-01-1922.

[14] Naganuma K, Honda T, Yamane K, Takagi Y, Kawamura A, Yanai T, et al. Efficiency and emissions-optimized operating strategy of a high-pressure direct injection hydrogen engine for heavy-duty trucks. SAE International; 2009. SAE paper no. 2009-01-2683.

[15] Kawamura A, Sato Y, Naganuma K, Yamane K, Takagi Y. Development project of a multi-cylinder DISI hydrogen ICE system for heavy duty vehicles. SAE International; 2010. SAE paper no. 2010-01-2175.

[16] Oikawa M, Ogasawara Y, Kondo Y, Sekine K, Naganuma K, Takagi Y, et al. Optimization of hydrogen jet configuration by single hole nozzle and high speed laser shadowgraphy in high pressure direct injection hydrogen engines. SAE International; 2011. SAE paper no. 2011-01-2002.

[17] Iwasaki H, Shirakura H, Ito A. A study on suppressing abnormal combustion and improving the output of hydrogen fueled internal combustion engines for commercial vehicles. SAE International; 2011. SAE paper no. 2011-01-0674.

[18] Kaiser S, White C. PIV and PLIF to evaluate mixture formation in a direct-injection hydrogen-fuelled engine. SAE International; 2008. SAE paper no. 2008-01-1034.

[19] Wallner T, Scarcelli R, Nande A, Naber J. Assessment of multiple injection strategies in a direct injection hydrogen research engine. SAE International; 2009. SAE paper no. 2009- 01-1920.

[20] Salazar V, Kaiser S, Halter F. Optimizing precision and accuracy of quantitative PLIF of acetone as a tracer for hydrogen fuel. SAE International; 2009. SAE paper no. 2009- 01-1534.

[21] Salazar V, Kaiser S. An optical study of mixture preparation in a hydrogen-fueled engine with direct injection using different nozzle designs. SAE International; 2009. SAE paper no. 2009-01-2682.

[22] Scarcelli R, Wallner T, Salazar V, Kaiser S. Modeling and experiments on mixture formation in a hydrogen directinjection research engine. SAE International; 2009. SAE paper no. 2009-24-0083.

[23] Salazar V, Kaiser S. Influence of the in-cylinder flow field (tumble) on the fuel distribution in a DI hydrogen engine using a single-hole injector. SAE International; 2010. SAE paper no. 2010-01-0579.

[24] Obermair H, Scarcelli R, Wallner T. Efficiency improved combustion system for hydrogen direct injection operation. SAE International; 2010. SAE paper no. 2010-01-2170.

[25] Scarcelli R, Wallner T, Obermair H, Salazar V, Kaiser S. CFD and optical investigations of fluid dynamics and mixture formation in a DI-H2ICE. In: Proceedings of the ASME 2010 internal combustion engine division fall technical conference 2010. Paper no. ICEF2010e35084.

[26] Salazar V, Kaiser S. Interaction of intake-induced flow and injection jet in a direct-injection hydrogen-fueled engine measured by PIV. SAE International; 2011. SAE paper no. 2011-01-0673.

[27] Scarcelli R, Wallner T, Matthias N, Salazar V, Kaiser S. Numerical and optical evolution of gaseous jets in direct injection hydrogen engines. SAE International; 2011. SAE paper no. 2011-01-0675.

[28] Salazar V, Kaiser S. Influence of the flow field on flame propagation in a hydrogen-fueled internal combustion engine. SAE International; 2011. SAE paper no. 2011-24-0098.

[29] Scarcelli R, Wallner T, Matthias N, Salazar V, Kaiser S. Mixture formation in direct injection hydrogen engines: CFD and optical analysis of single- and multi-hole nozzles. SAE International; 2011. SAE paper no. 2011-24-0096.

[30] HyICE: optimization of the hydrogen internal combustion engine. URL, http://ec.europa.eu/research/transport/projects/items/_hyice_optimising_hydrogen_powered_ engines_en.htm; 2007.

[31] Huyskens P, Van Oost S, Goemaere P, Bertels K, Pecqueur M. The technical implementation of a retrofit hydrogen PFI system on a passenger car. SAE International; 2011. SAE paper no. 2011-01-2004.

[32] Sainz D, Dieguez P, Sopena C, Urroz J, Gandia L. Conversion of a commercial gasoline vehicle to run bi-fuel (hydrogengasoline). Int J Hydrogen Energy 2012;37:1781-9.

[33] Hydrogen region Flanders - South Netherlands. URL, http://www.waterstofnet.eu/english.html; 2013.

[34] Welch A, Mumford D, Munshi S, Holbery J, Boyer B, Younkins M, et al. Challenges in developing hydrogen direct injection technology for internal combustion engines. SAE Paper No. 2008-01-2379 (2008).

[35] D'Errico G, Onorati A, Ellgas S. 1d Thermo-fluid dynamic modelling of an SI single-cylinder H2 engine with cryogenic port injection. Int J Hydrogen Energy 2008;33:5829-41.

[36] Hallmannsegger M, Fickel H-C. The mixture formation process of an internal combustion engine for zero CO2-emission vehicles fueled with cryogenic hydrogen. IFP International Conference (Rueil-Malmaison, France, 2004).

[37] Hallmannsegger M. Potentials of the four-stroke Otto engine with PFI of cryogenic hydrogen. PhD thesis, Graz University of Technology (2005).

[38] Heller K, Ellgas S. Optimisation of a hydrogen internal combustion engine with cryogenic mixture formation. Proceedings 1st international symposium on Hydrogen Internal Combustion Engines 49–58 (2006).

[39] Ellgas S. Simulation of a hydrogen internal combustion engine with cryogenic mixture formation. PhD thesis, University of Armed Forces Munich (2008).

[40] Boretti A, Watson H. Numerical study of a turbocharged, jet ignited, cryogenic, port injected, hydrogen engine. SAE Paper No. 2009-01-1425 (2009).

[41] H. Eichlseder, T. Wallner, R. Freymann, J. Ringler, "The Potential of Hydrogen Internal Combustion Engines in a Future Mobility Scenario", SAE paper 2003-01- 2267.

[42] H. Li and G. A Karim, "Hydrogen fuelled spark ignition engines: predictive and experimental performance", ASME Spring Technical Conference, Paper number ICES2003-548, Salzburg, Austria, 2003.

[43] Smith J.R., Aceves S., and Van Blarigan P. Series hybrid vehicle and optimized hydrogen engine design. SAE, paper nr 951955, 1995.

[44] Yi H.S., Min K., and Kim E.S. The optimised mixture formation for hydrogen fueled engines. Int. J. Hydrogen Energy 2000;25:685-690.

[45] Stockhausen W.F. et al. Ford P2000 hydrogen engine design and vehicle development program. SAE, paper nr 2002-01-0240, 2002.

[46] Verhelst S, Maesschalck P, Rombaut N, Sierens R. Increasing the power output of hydrogen internal combustion engines by means of supercharging and exhaust gas recirculation. Int J Hydrogen Energy 2009;34:4406–12.

[47] ETEC hydrogen internal combustion engine full-size pickup truck conversion. Hydrogen ICE truck brochure.

[48] Kirchweger W, Eichlseder H, Gerbig F, Gerke U. Optical measurement methods for the optimization of the hydrogen DI combustion. 7th International Symposium on Internal Combustion Engines Diagnostics (Baden- Baden, Germany, 2006).

[49] Eichlseder H, Wallner T, Freyman R, Ringler J. The potential of hydrogen internal combustion engines in a future mobility scenario. SAE paper 2003; 2003-01-2267.

[50] Homan HS, DE Boer PCT, McLean WJ. The effect of fuel injection on NO*x* emissions and undesirable combustion for hydrogen-fuelled piston engines. Int J Hydrogen Energy 1983;8:131–46.

[51] Glasson ND, Green RK. Performance of a spark-ignition engine fuelled with hydrogen using a high-pressure injector. Int J Hydrogen Energy 1994;19:917–23.

[52] Tomita E, Hamamoto Y, Yoshiyama S, Toda H. Measurement of fuel concentration distribution of transient hydrogen jet and its flame using planar laser induced fluorescence method. JSAE Rev 1998;19(4):329-35.

[53] Smith JD, Sick V. Quantitative, Dynamic Fuel Distribution Measurements in Combustion Related Devices Using Laser-Induced Fluorescence Imaging of Biacetyl in Iso-Octane. Proceedings of the Combustion Institute 2007;31:747-55.

[54] Schulz C, Sick V. Tracer-LIF Diagnostics: Quantitative Measurement of Fuel Concentration, Temperature and Fuel/Air Ratio in Practical Combustion Systems. Progress in Energy and Combustion Science 2005;31:75-121.

[55] Hall MJ, Koenig M. A fiber-optic probe to measure precombustion in-cylinder fuel-air ratio fluctuations in production engines. Proc Combust Inst 1996;26(2):2613-8.

[56] Koenig M. and Hall MJ. Measurements of Local In-Cylinder Fuel Concentration Fluctuations in a Firing SI Engine. SAE Paper No.971644. 1997.

[57] Koenig M. and Hall MJ. Cycle-Resolved Measurements of Pre-Combustion Fuel Concentration Near the Spark Plug in a Gasoline SI Engine. SAE Paper No.981053. 1998.

[58] K. Kawamura, T. Suzuoki, A. Saito, T. Tomoda, M. Kanda, Development of instrument for measurement of air–fuel ratio in vicinity of spark-plug (application to DI gasoline engine), JSAE Rev. 19 (1998) 305–310.

[59] S. Yoshiyama, Y. Hamamoto, E. Tomita, K. Minami, Measurement of hydrocarbon fuel concentration by means of infrared absorption technique with 3.39 μm He–Ne Laser, JSAE Rev. 17 (1996) 339-345.

[60] E. Tomita, N. Kawahara, M. Shigenaga, A. Nishiyama, R.W. Dibble, In Situ measurement of hydrocarbon fuel concentration near a spark plug in an engine cylinder by 3.392 μm

infrared laser absorption method: discussion of applicability with a homogeneous methane–air mixture, Meas. Sci. Technol. 14 (2003) 1350–1356.

[61] E. Tomita, N. Kawahara, A. Nishiyama, M. Shigenaga, In Situ measurement of hydrocarbon fuel concentration near a spark plug in an engine cylinder by 3.392 μm infrared laser absorption method: application to actual engine, Meas. Sci. Technol. 14 (2003) 1357-1363.

[62] E. Tomita, N. Kawahara, S. Yoshiyama, A. Kakuho, T. Itoh, Y. Hamamoto, In-Situ fuel concentration measurement near spark-plug in spark-ignition engines by 3.39 μm infrared laser absorption method, Proc Combust Inst 2002;29(1):735-741.

[63] A. Nishiyama, N. Kawahara, E. Tomita, In-Situ Fuel Concentration Measurement near Spark Plug by 3.39 μm Infrared Absorption Method (Application to Spark Ignition Engine). SAE Paper No.2003-01-1109. 2003.

[64] Kawahara N, Tomita E, Kadowaki T, Honda T, Katashiba H. In situ fuel concentration measurement near a spark plug in a spray-guided direct-injection spark-ignition engine using infrared absorption method, Exp Fluids 2010;49(4):925-36.

[65] N. Kawahara, E. Tomita, K. Hayashi, M. Tabata, K. Iwai, R. Kagawa, Cycle-resolved measurements of the fuel concentration near a spark plug in a rotary engine using an in situ laser absorption method, Proc Combust Inst 2007;31(2):3033-3040.

[66] Grunefeld G, Knapp M, Beushausen V. In-Cylinder Measurements and Analysis on Fundamental Cold Start and Warm-up Phenomena of SI Engines. SAE Technical Paper 1995:SAE paper No. 952394.

[67] Rabenstein F, Egermann J. Vapor-Phase Structures of Diesel-Type Fuel Sprays: An Experimental Analysis. SAE Technical Paper 1998:SAE paper No. 982543.

[68] Miles PC, Hinze PC. Characterization of the Mixing of Fresh Charge with Combustion Residuals Using Laser Raman Scattering with Broadband Detection. SAE Technical Paper 1998:SAE paper No. 981428.

[69] Egermann J, Koebcke W, Ipp W, Leipertz A. Investigation of the Mixture Formation Inside a Gasoline Direct Injection Engine by Means of Linear Raman Spectroscopy. Proceedings of the Combustion Institute 2000;28:1145–52.

[70] F. Ferioli, P.V. Puzinauskas, S.G. Buckley, Laser-induced breakdown spectroscopy for on-line engine equivalence ratio measurements. Appl Spectro 2003;57(9):1183-1189.

[71] Phuoc TX. Laser-induced spark for simultaneous ignition and fuel-to-air ratio measurements. Opt Lasers Eng 2006;44(6):520-34.

[72] Shudo T, Oba S. Mixture distribution measurement using laser induced breakdown spectroscopy in hydrogen direct injection stratified charge. Int J Hydrogen Energy 2009;34(5):2488-93.

[73] N. Kawahara, J.L. Beduneau, T. Nakayama, E. Tomita, Y. Ikeda, Spatially, temporally and spectrally resolved measurement of laser induced plasma in air. Appl. Phys., B Laser Opt. 2007;86(4):605-614.

[74] Y. Ikeda, A. Nishiyama, N. Kawahara, T. Nakayama, E. Tomita, Local Equivalence Ratio Measurement of CH4/air and C3H8/air Laminar Flames With and Without Flame Front by LIBS. Sect. 5, LIBS2006, 2006.

[75] R.M. Merer, J.S. Wallace, Spark Spectroscopy for Spark Ignition Engine Diagnostics. SAE Paper No. 950164. 1995.

[76] K. Kuwahara, H. Ando, Diagnostics of in-cylinder flow, mixing and combustion in gasoline engines. Meas. Sci. Technol. 2000;11:95-111.

[77] T.D. Fansler, B. Stojkovic, M.C. Drake, M.E. Rosalik, Local fuel concentration measurements in internal combustion engines using spark-emission spectroscopy. Appl. Phys., B Laser Opt. 2002;75(4):577-590.

[78] Letty C, Pastore A, Mastorakos E, Balachandran R, Couris S. Comparison of Electrical and Laser Spark Emission Spectroscopy for Fuel Concentration Measurements. Experimental Thermal and Fluid Science 2010;34:338–45.

[79] N. Kawahara, E. Tomita, S. Takemoto, Y. Ikeda. Fuel concentration measurement of premixed mixture using spark-induced breakdown spectroscopy. Spectro Acta Part B 2009;64(10):1085-1092

[80] Roy MK, Nobuyuki K, Tomita E, Fujitani T. Jet-guided combustion characteristics and local fuel concentration measurements in a hydrogen direct-injection spark-ignition engine. Proc Combust Inst 2013;34:2977-84.

[81] Abdul Rahman MT, Kawahara N, Tsuboi K, Tomita E. Visualization and concentration measurement of a direct injection hydrogen jet in a constant-volume vessel using spark-induced breakdown spectroscopy. Int J Hydrogen Energy 2014;39(31):17896-17905.

[82] Abdul Rahman MT, Kawahara N, Tsuboi K, Tomita E. Effect of ambient pressure on local concentration measurement of transient hydrogen jet in a constant-volume vessel using spark-induced breakdown spectroscopy. Int J Hydrogen Energy 2015;40(13):4717-4725

CHAPTER: 3

Investigation of Hydrogen jet in a confined vessel

3.1 Overview of turbulent jet

Whenever a moving fluid enters a quiescent body of the same fluid, a velocity shear is created between the entering and ambient fluids, causing turbulence and mixing. The Jet flow occurs when a stream of one fluid mixes with a surrounding medium, at rest or in motion. Such flows occur in a wide variety of situations, and the geometries, sizes, and flow conditions cover a large range. Fuel gases are generally injected into still air at high speed, usually at Mach number, M_a, greater than 0.3, in order to enhance turbulence and so mixing with the oxidant like oxygen in surrounding air. This implies that generally, the hydrogen jet binary mixture flow would also most probably be expected to be turbulent and compressible. This means that during jet propulsion, the flow gas mixture densities vary greatly with time and space as a result of high injection velocity, temperature changes, intense mixing between fuel gas and air. In the case of hydrogen gas diffusing in air these density variations near the jet boundary mixture are quite large because of the large mass diffusivity of the hydrogen gas in air medium. In addition, the large initial density difference between that of the injected hydrogen gas and ambient surrounding air which can be as high as 1400 % contributes to these large density variations.

3.1.1 Steady jets

Jets are canonical flows that have been widely studied by many researchers, especially steady jets. The basic structure of a steady jet includes a potential core that has not felt the effects of viscosity and, therefore, has a velocity equal to that at the nozzle exit. Next, the flow goes through a transitional development region, and then finally becomes fully developed. Figure 3.1 diagrams these regions of a steady circular jet [1].

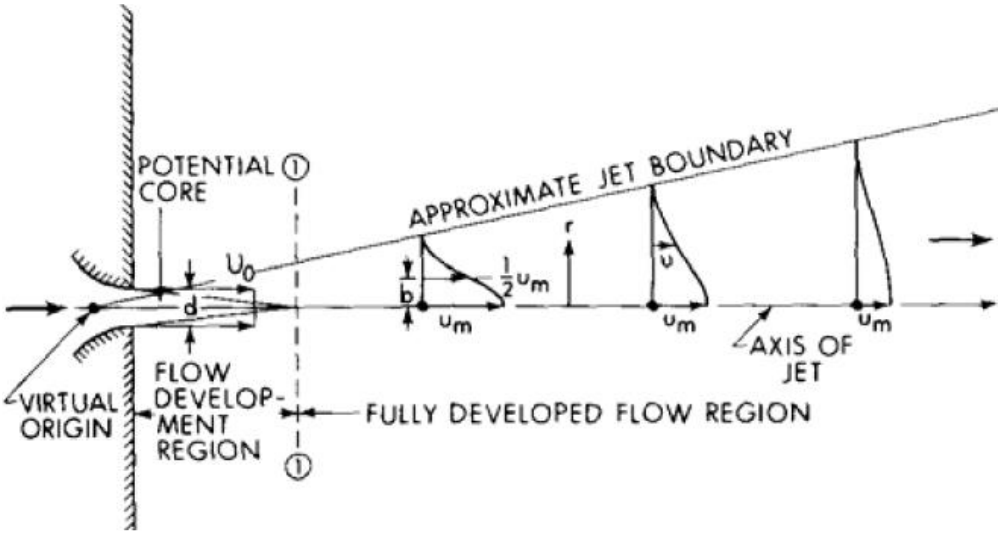

Fig.3.1 Definition sketch of circular turbulent jets [1].

In the fully developed region the flow becomes self-similar and the radial velocity profile, *U(r,z),* normalized by the centerline velocity, U_{CL}, is only a function of the non-dimensional distance, $\eta = 2r / d_n$, where r is the radial position and d_n is the diameter of the nozzle exit.

These relations are represented in equations (3.1) and (3.2).

$$\frac{\mathrm{U(r,z)}}{U_{CL}} = f(\eta) \tag{3.1}$$

and $$\frac{U_{CL}}{u_n} = \frac{k_d}{z/d_n} \quad (3.2)$$

where z is the distance from the exit, u_n is the flow velocity at the nozzle exit, and k_d is a constant that has been experimentally been determined to be approximately 5.0 [2]. As seen in equation (3.2), the centerline velocity scales with the inverse of distance from the exit plane.

In a direct-injection engine, the fuel is injected directly into the chamber through injector and then the subsequent fuel jets spread across the combustion chamber. Understanding physics of the gas jet is necessary to study the behavior of fuel jet and its interaction with the surrounding air in the engine cylinder. Although the main concern with automotive injection is the transient behaviour, fundamental information on steady jets can provide a basis for understanding the structure and scaling of the transient jet.

3.1.2 Transient jets

The structure and properties of incompressible transient jets or impulsively started jets have been studied for a wide range of applications. Turner [3] described the structure of plumes when studying atmospheric mixing in buoyant plumes. A plume was described as consisting of a spherical cap, called a spherical head vortex, which is supplied with additional buoyancy and momentum from a plume below. It was shown that the plume displays self-similarity characteristics throughout its evolution. Figure 3.2 illustrates this initial description of a jet or plume [4]. The jet consists of a spherical vortex flow interacting with a steady-state jet. The vortex of radius moves away from the nozzle at a bulk velocity that decays with the

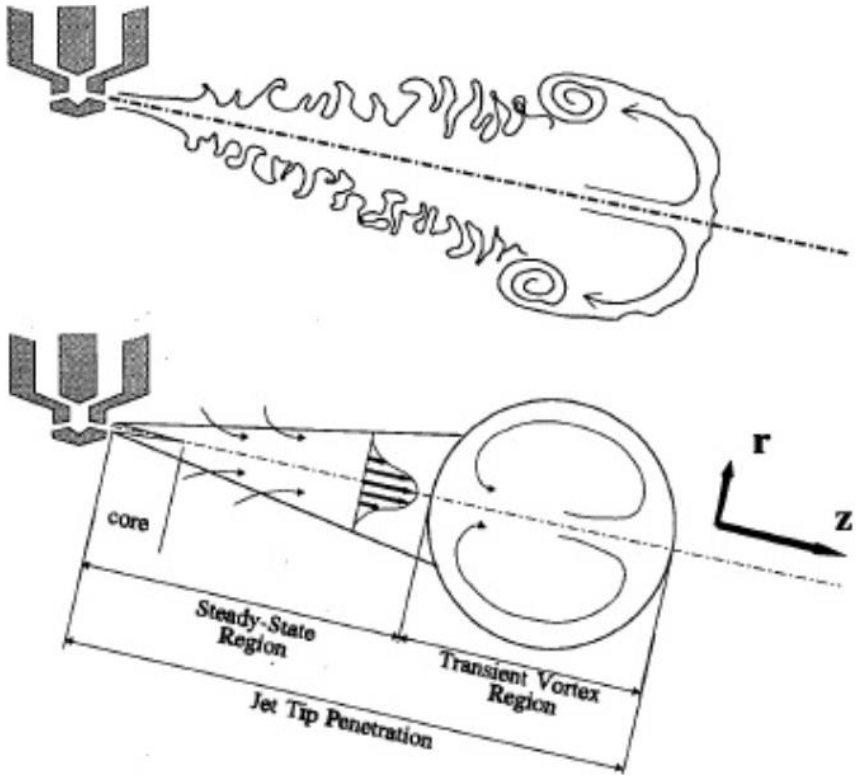

Fig.3.2 Turbulent transient jet model [4]

distance z from the nozzle. The size of the vortex grows continuously due to the entrainment of mass from the steady-state jet which pushes it from behind. The jet behind the vortex is considered to be in a steady state, which is confirmed by the work of Kuo and Bracco [5]. Turner's plume was used as the basic structure of a transient starting jet by many researchers. Abramovich and Solan [6] used this model to develop analytical expressions for the velocity of the spherical vortex in the near and far fields of a liquid jet under laminar conditions with low Reynolds number. It was observed that the velocity of the spherical vortex varies proportional to the distance similar to the axial velocity of a steady state jet only with differing constants. The velocity of the spherical vortex was found to be approximately half that of a fluid element in a steady jet. Abramovich and Solan [6] showed

that the half width and maximum axial velocity show similarity characteristics, both making the jet appear to start from a virtual origin different from the geometric origin. The virtual origin was found to be proportional to the exit diameter and the square root of the Reynolds number.

3.1.2.1 Incompressible transient jets

A steady, incompressible turbulent jet may be defined as a region of finite thickness, formed between two neighbour flows, with a continuous distribution of velocity, temperature and species concentration which result from turbulent disorderly movement of eddies cause by the instability of the tangential separation surface and exchange of matter. The compressibility effects in a flow can be neglected if the maximum Mach number is below 0.3. Incompressible jets have been studied extensively in the past [1,7,8]. As one fluid is injected into another fluid with uniform pressure field, a mixing layer is formed between the two fluids. Mass from the surrounding fluid is entrained in the injected fluid. Experimental investigations by Ricou and Spalding [8] concluded that, the rate of entrainment is proportional to the distance from the nozzle and to the mass injection rate for incompressible air jets issued from the round nozzle into stagnant air. A steady-state jet can be divided into three regions [1]. In the initial region the velocity in the potential core of the jet remains constant and is equal to the initial velocity. The end of the initial region is marked by the disappearance of the potential core because of the thickening of jet boundary layer. The transition region may be defined as the region in which the jet viscosity distribution becomes fully developed. In the fully developed region, the velocity profile is self-similar.

When the densities of the injected fluid and surrounding fluid are different, both the entrainment rate and centerline velocity are different. However, the similarity of the profiles in the jet is still preserved at some distance from the nozzle and has been shown to behave like a jet of similar density as its surroundings when the nozzle diameter is replaced by the equivalent diameter given in equation (3.3) [2]:

$$d_{eq} = d_n \left(\frac{\rho_n}{\rho_{ch}}\right)^{1/2} \tag{3.3}$$

where ρ_n is the density of the injected fluid at the nozzle exit and ρ_{ch} is the density of the chamber fluid. For incompressible jets the nozzle exit density, ρ_n , is density of the injected fluid at the chamber pressure.

3.1.2.2 Compressible transient jets

The propagation of a turbulent jet in any medium is characterized basically by the thickness of the zone of turbulent mixing and by the profiles of velocity, temperature, concentration, and other parameters of the liquid or gas in the cross sections of the flow. When a fluid moves at speeds comparable to its speed of sound, density changes become significant and the flow is termed *compressible*. Probably the two most important and distinctive effects of compressibility on flow are (1) *choking*, wherein the duct flow rate is sharply limited by the sonic condition, and (2) *shock waves*, which are nearly discontinuous property changes in a supersonic flow. An incompressible flow requires only a momentum and continuity analysis. Whereas for compressible flow, if the density change is significant, it follows from the equation of state that the temperature and pressure changes are also substantial. Large

temperature changes imply that the energy equation can no longer be neglected. Therefore, the work is doubled from two basic equations to four- 1. Continuity equation, 2. Momentum equation, 3. Energy equation, 4. Equation of state; to be solved simultaneously for four unknowns: pressure, density, temperature, and flow velocity (p, ρ, T, V).

The Mach number, defined as Ma = V/a, (V is the flow velocity and a is the speed of sound of the fluid) is the dominant parameter in compressible-flow analysis, with different effects depending upon its magnitude. The Mach number is an index that used to define the following flow regimes:

- Ma < 0.3: *incompressible flow*, where density effects are negligible.
- 0.3 < Ma < 0.8: *subsonic flow*, where density effects are important, but no shock waves appear.
- 0.8 < Ma < 1.2: *transonic flow*, where shock waves first appear, dividing subsonic and supersonic regions of the flow. Powered flight in the transonic region is difficult because of the mixed character of the flow field.
- 1.2 < Ma < 3.0: *supersonic flow*, where shock waves are present but there are no subsonic regions.
- 3.0 < Ma: *hypersonic flow* [9], where shock waves and other flow changes are especially strong.

As the Mach number increases above 0.3, compressibility effects have to be taken into account in establishing nozzle exit conditions. The similarity of profiles is still valid in the fully developed region where the local Mach numbers are low. However, the effect of compressibility on the nozzle density and velocity must be incorporated in the scaling.

3.1.2.2.1 Under-expanded jets

When the pressure ratio between the outlet and inlet of an orifice or nozzle is sufficiently dropped to cause the pressure at the exit to be higher than the ambient surroundings, the complex flow that results is termed as under-expanded jet. At the nozzle exit the flow is choked, expands upon leaving the nozzle, and accelerates to supersonic velocities. The jet is expanded radially at the nozzle exit and the jet boundary also forms an expanded shape. A complex pattern of expansion waves result at the outer rim of the exit as shown in Fig.3.3 [10]. The expansion waves originating at the nozzle exit corner are reflected at the jet boundary as compression waves, which coalesce to form the so-called barrel shock that is terminated by a normal shock also called the Mach disk. These barrel shock structures can

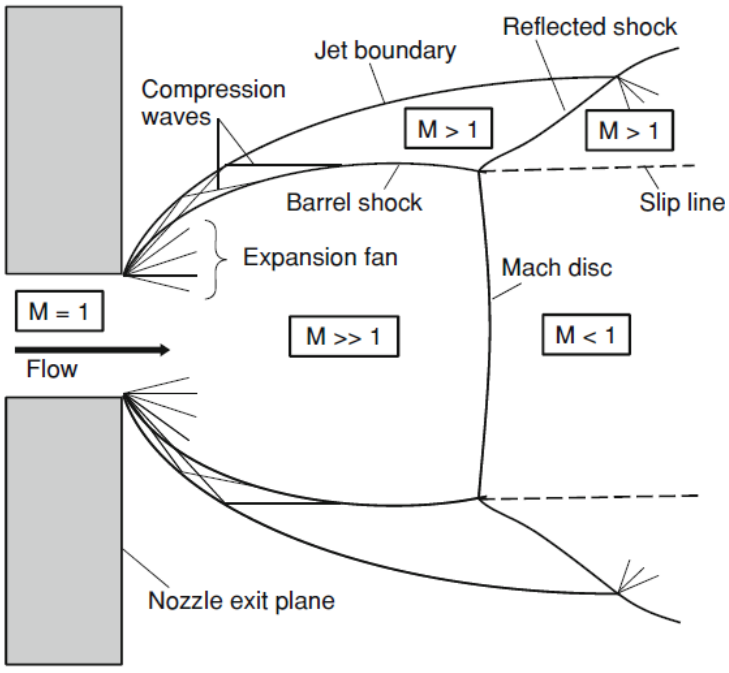

Fig. 3.3 Schematic of under-expanded jets structure [10]

be repeated several times diminishing in strength due to viscous effects. The Mach disk forms if the nozzle exit to chamber pressure ratio is above 2.1 [11]. Flow immediately after the Mach disk is subsonic, whereas flow behind barrel shock is still supersonic. The flow that passes through the barrel shock is again compressed by the reflected shock and separated from the flow behind the Mach disk by the slip line. Along the jet axis, the pressure continuously decreases to values below the ambient pressure value. The pressure is increased to the ambient pressure value by passing through the Mach disk. For moderately under expanded flows with a nozzle to chamber pressure ratio below 2.1, a Mach disk does not form and instead the barrel shock is able to intersect at the flow axis [11]. Experimental investigations usually correlate the location and size of the Mach disk to the nozzle pressure ratio (NPR), NPR = p_0/p_∞; where p_0 is the stagnation pressure at the nozzle entrance and p_∞ the ambient (in-cylinder) static pressure. The ratio of the nozzle total pressure (p_0) to the (p_∞), has a significant effect on the characteristics of a gaseous jet issuing from a circular nozzle. Based on the level of NPR, jets can be classified as subsonic, moderately under-expanded and highly under-expanded [12-14]. Specifically, Donaldson and Snedeker [14] categorized the gaseous jets into three major types based on the NPR (p_0/p_∞) and under-expansion ratio (p_1/p_∞) as subsonic ($1.893 > p_0/p_\infty > 1$, $p_1/p_\infty = 1$), moderately under-expanded ($3.8 > p_0/p_\infty > 2.08$, $1.1 < p_1/p_\infty \leq 2$) and highly under-expanded ($p_0/p_\infty > 3.84$, $p_1/p_\infty > 2$). For NPR above ~4 the jet is considered to be highly under-expanded. As illustrated in Fig.3.4 [14], at such condition, infinite number of Mach waves, namely the Prandtl-Meyer expansion fan, form at the nozzle lip that spread out to the jet boundary and reflect as weak compression waves

which form the intercepting oblique shock that is ended by a slightly curved strong normal shock so-called Mach disk [12]. For higher degrees of under-expansion, e.g. NPR = 8, the subsonic core behind the Mach disk rapidly accelerates and becomes supersonic once more, which then shapes a second shock cell that may resemble the first shock cell and even include a normal shock comparable to the Mach disk [14]. At extremely high levels of NPR, a very large Mach disk forms at the nozzle exit, with no additional normal shocks downstream, and the jet then decays resembling a subsonic jet [14].

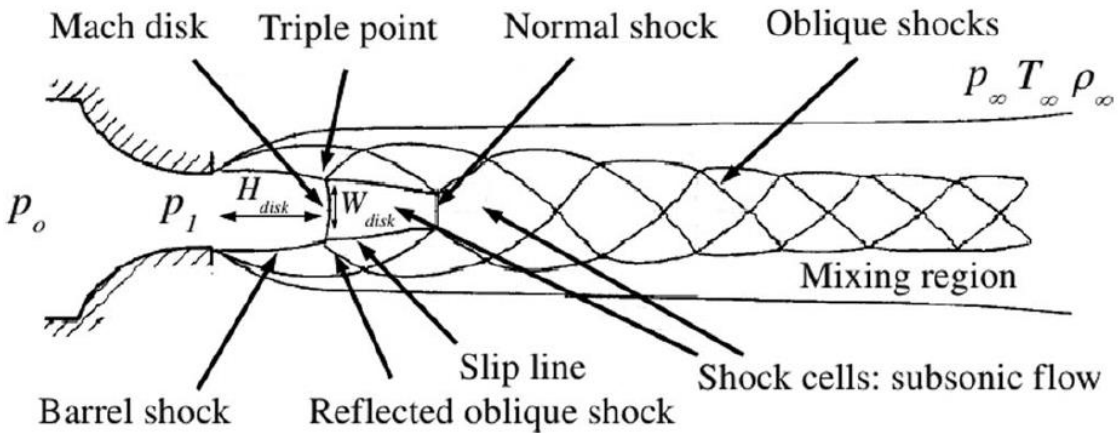

Fig. 3.4 The classical structure of a highly under-expanded jet [14]

3.2 Experimental set-up and Methodology

3.2.1 Constant volume vessel (CVV)

Visualization of hydrogen jet was performed by supplying high pressure hydrogen into a constant volume vessel (CVV) through an injector. The vessel was developed to provide a quiescent, pressurized environment for various flows to propagate into. CVV was a steel

cylinder with a base height of 145-mm and width of 120-mm (Fig. 3.5). For this experiment, the three walls of the chamber were designed to locate and hold the circular quartz windows (diameter: 80mm) to allow full line-of-sight optical access to the chamber. A pressure accumulating-type hydrogen injector actuated by an electromagnetic valve, was mounted on the top of the chamber head so that the jet was directed downward into the cylinder. The ambient gas was nitrogen, and introduced into the vessel from a N_2 cylinder by a pressure-regulated inlet valve. Hydrogen was supplied from an H_2 cylinder, and a fuel accumulator (see Fig. 3.6) was used to maintain constant fuel feed pressure to the injector.

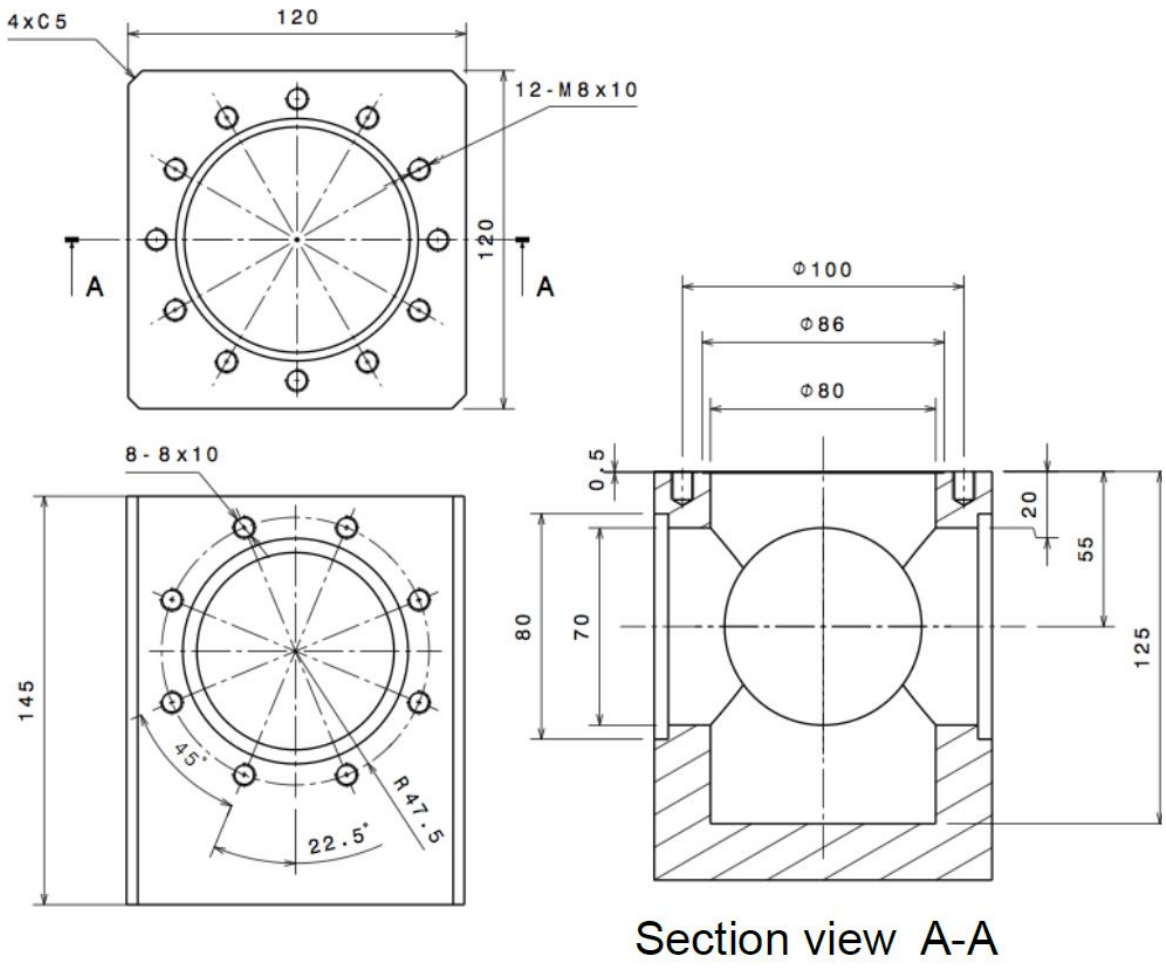

Fig.3.5 Design of the constant volume vessel (CVV)

3.2.2 Hydrogen injector

Figure 3.6 shows the injector used in the experiment for direct visualization of hydrogen jet. A solenoid-driven DI injector used as a fuel injector developed by Mitsubishi Electric Co. Ltd is shown in Fig. 3.4. The fuel injector was a swirl-type DI injector and the H_2 was introduced through a single orifice. The injector had a nominal cone angle of 60° and an orifice diameter of 1.0 mm. The injection signal was controlled by an electric injector driver requiring a high-voltage power source and external trigger input to control the pulse width.

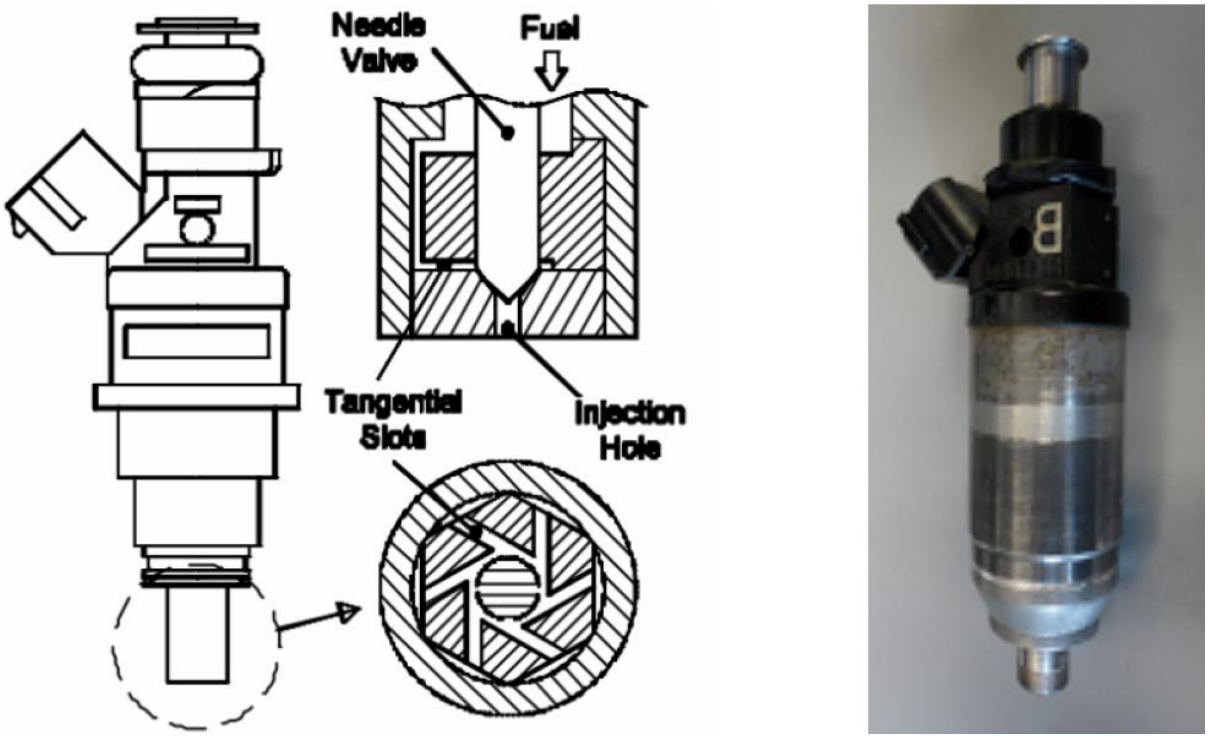

Fig.3.6 Mitsubishi DI injector

3.2.3 High-Speed camera

Figure 3.7 shows the high-speed CMOS (complementary metal-oxide semiconductor) video camera (nac Image Technology Inc., MEMRECAM GX-1) that was used in the experiment to visualize the hydrogen jet in the constant volume vessel. The Memrecam GX-1 uses the latest CMOS sensor and meets the imaging requirements of the most demanding applications in research and development due to its unrivalled sensitivity, speed and resolution. This camera can capture images at maximum resolution of 1280 x 1024 pixels at speed of 2,078 fps and frame rates in excess of 245,098 fps at reduced resolutions. In this experiment frame resolution was set to 256 x 256 pixels with recording speed of 25,000 frames per second. The onset of the high-speed camera recording was synchronized to the H_2 injection. Figure 3.8 shows the viewable area through the constant volume chamber window, the dimensions of each flame image are 70 mm × 70 mm, which is also the case for all of the subsequent images. Stability, distance, relative position between high-speed camera and constant volume chamber are very important and should be maintain same for all the observations to ensure that camera is focused toward same plane along hydrogen jet.

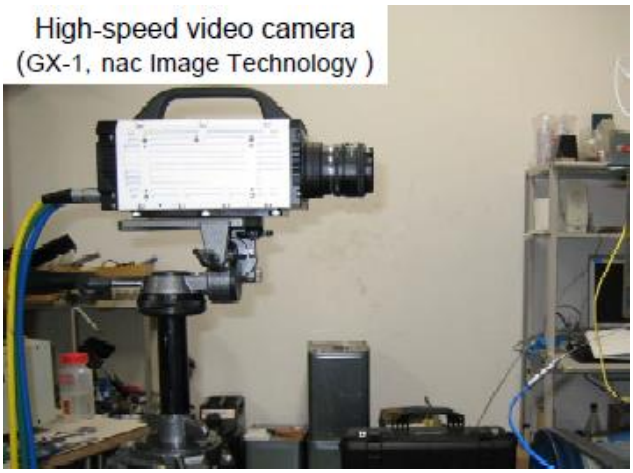

Fig.3.7 High-speed CMOS video camera (nac Image Technology, GX-1)

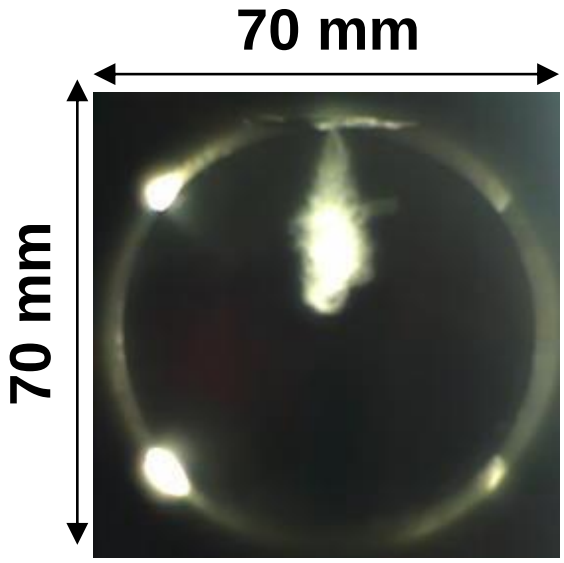

Fig.3.8 Viewable area through the constant volume chamber window

3.2.4 Measurement technique

Constant volume chamber was filled with nitrogen gas and the hydrogen jet was injected into the chamber. An Argon-ion laser beam (Spectra-physics, Stabilite 2017) with an output power of 6W was used as one of the light sources. The thickness of the laser light sheet was approximately 2 mm. The laser beam was focused on the hydrogen jet, and the visualization region was approximately 20×20 mm^2 near the nozzle tip. A fine particle of spherical porous silica (God Ball B-6C, Suzuki Yushi Co. Ltd.) with a nominal diameter of 2.5 μm was seeded into the intake flow (choosing the appropriate size of the flow field visualization tracer was very important to accurately track the airflow). In addition to Argon-ion laser light, we have also used metal halide lamp as alternate light source to illuminate the tracer particle present

in the hydrogen jet. The underlying reasons for this is, with laser light sheet we can illuminate the tracer particle in a fixed 2-D plane of thickness 2 mm whereas using metal halide lamp it is possible to capture the jet structure that resemble more to the 3-D pattern of the hydrogen jet. The high-speed images provided qualitative information of the jet structure, as well as quantitative information of the jet penetration and cone angle.

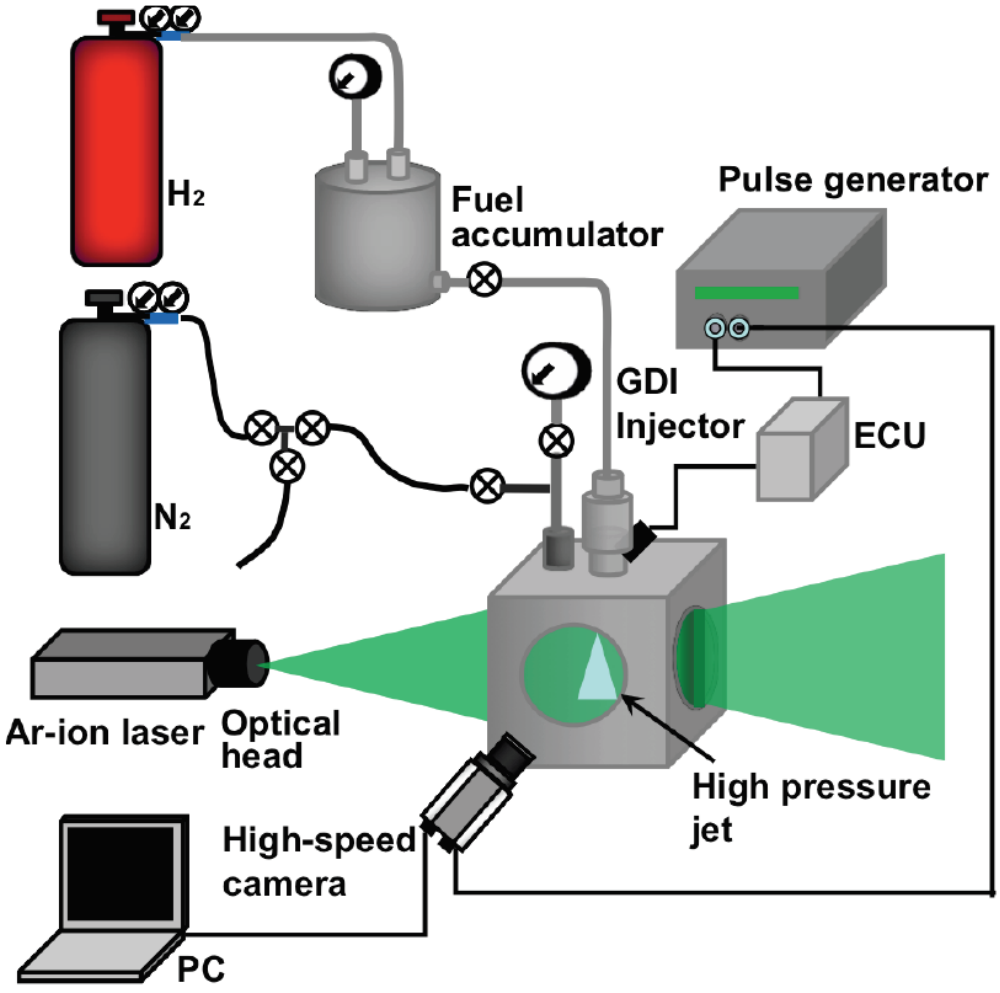

Fig.3.9 Experimental setup for hydrogen jet visualization

3.2.5 Operating condition

The CVV is filled with nitrogen at first with four different ambient pressure starting from 0.5 MPa, up to 2.0 MPa with a uniform interval of 0.5 MPa. Two different injection pressures of 5MPa and 7MPa is considered for introducing hydrogen directly into CVV chamber which was already filled with quiescent nitrogen. The pulse width for hydrogen injection was set at 4ms and 8ms. For each condition, the tests were repeated for 5 times and averaged data were presented for discussions. Operating conditions and characteristics of the constant-volume chamber are summarized in Table 3.1.

Table 3.1 Operating condition for visualization experiments

<table>
<tr><td colspan="2">Chamber volume (cm^3)</td><td colspan="4">675</td></tr>
<tr><td colspan="2">Chamber wall temperature (K)</td><td colspan="4">298</td></tr>
<tr><td colspan="2">Orifice diameter (mm)</td><td colspan="4">1.0</td></tr>
<tr><td colspan="2">Injection duration (ms)</td><td colspan="4">4,8</td></tr>
<tr><td colspan="6">Fuel injection pressure with ambient condition</td></tr>
<tr><td rowspan="2">Fuel</td><td rowspan="2">Fuel Injection pressure, MPa</td><td colspan="4">Chamber pressure, MPa</td></tr>
<tr><td>N_2</td><td>N_2</td><td>N_2</td><td>N_2</td></tr>
<tr><td>H_2</td><td>5</td><td rowspan="2">0.5</td><td rowspan="2">1.0</td><td rowspan="2">1.5</td><td rowspan="2">2.0</td></tr>
<tr><td>H_2</td><td>7</td></tr>
</table>

3.3 Visualization of jet and selection of light source

Jet visualization was the main experimental focus here and was used to investigate the flow structures of gaseous jets produced by injecting hydrogen under a wide range of conditions. Image processing techniques (by MATLAB) were performed on high-speed time-series images of the gaseous jets in order to estimate jet tip penetration and jet angle as functions of time. The raw images were converted to grayscale images, and then binary images of the jet were obtained by thresholding the grayscale images. For image binarization we followed the adaptive thresholding technique as presented by Sauvola et al. [15]. The method works quite well with presence of degradations, such as variable illumination and noise. Jet patterns were imaged both vertically and end-on or directly towards the tip of the injector. Figure 3.10 shows the time-series images of the hydrogen jet evolution over time captured with laser beam as light source whereas images in Fig.3.11 were illuminated by metal halide lamp. Both of these figures correspond to the hydrogen injected with a pressure of 5 MPa into the vessel filled by N_2 with ambient pressure of 1.0 MPa. The images show that jet diameter expands rapidly both in axially and radially, just downstream from the nozzle exit. Here binarized images were processed to estimate the jet tip penetration and jet cone angle. Figure 3.12 illustrates a comparison of jet tip penetration whereas Fig.3.13 compares jet cone angle between the measurements made through ar-ion laser and metal halide lamp. It is evident from these two observations that light source has some remarkable effects on

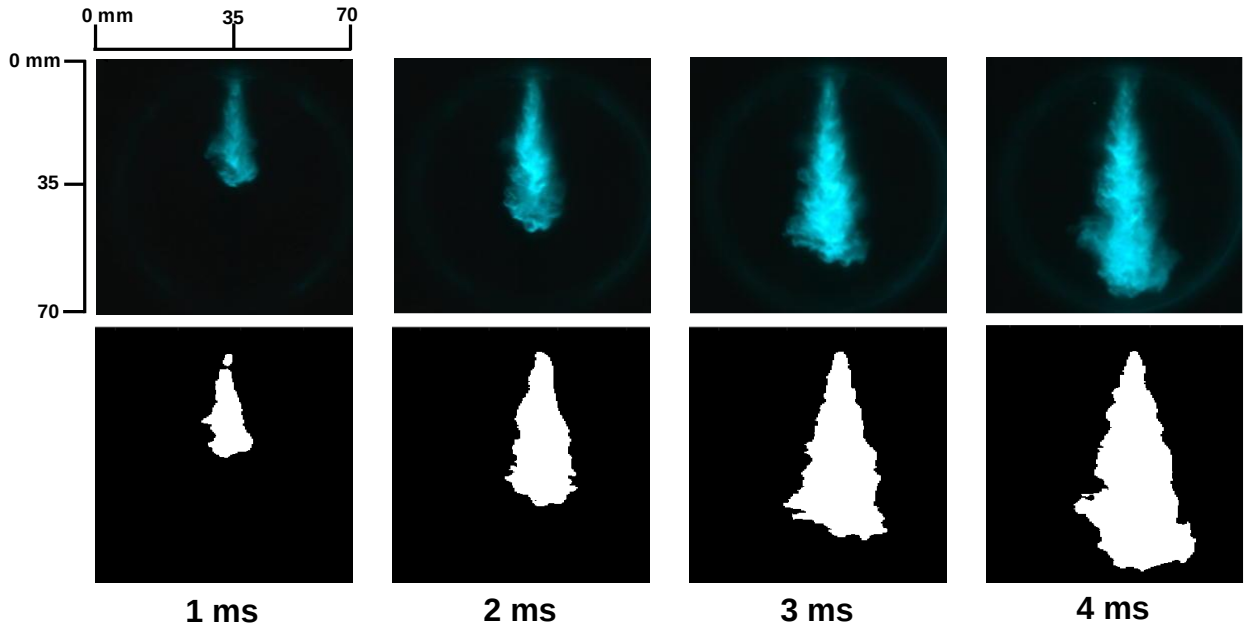

Fig.3.10 Time-series images of hydrogen jet evolution. P_{inj} = 5MPa; P_{amb} = 1.0MPa; light source: Ar-Ion Laser

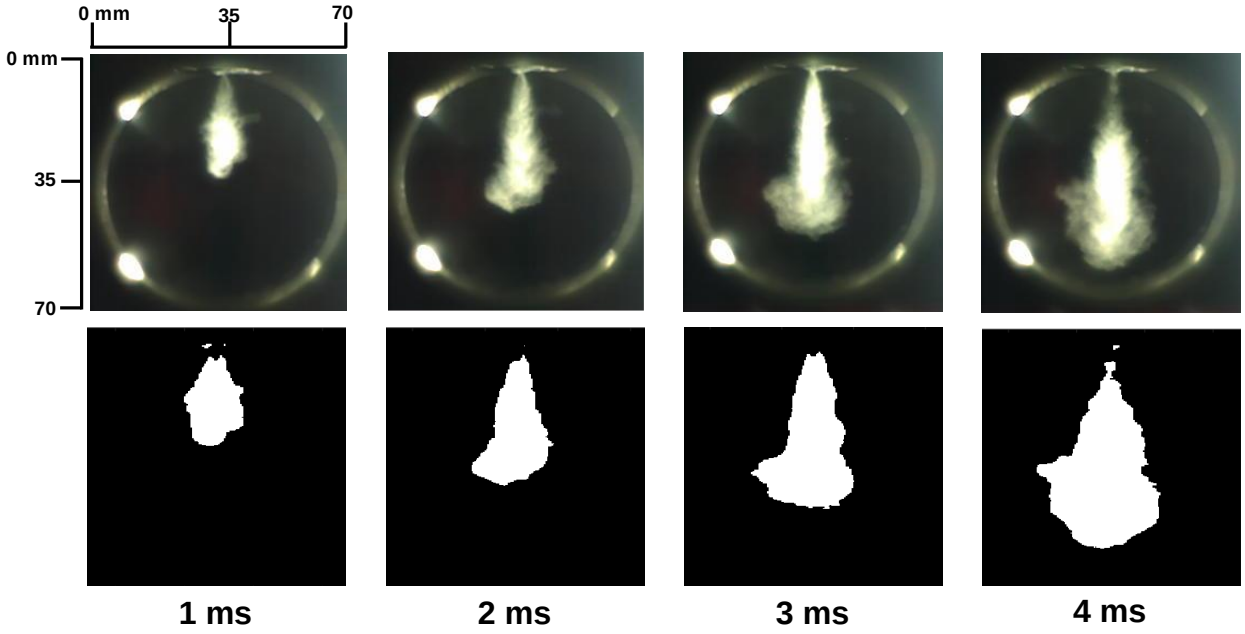

Fig.3.11 Time-series images of hydrogen jet evolution. P_{inj} = 5MPa; P_{amb} = 1.0MPa; light source: Metal Halide Lamp

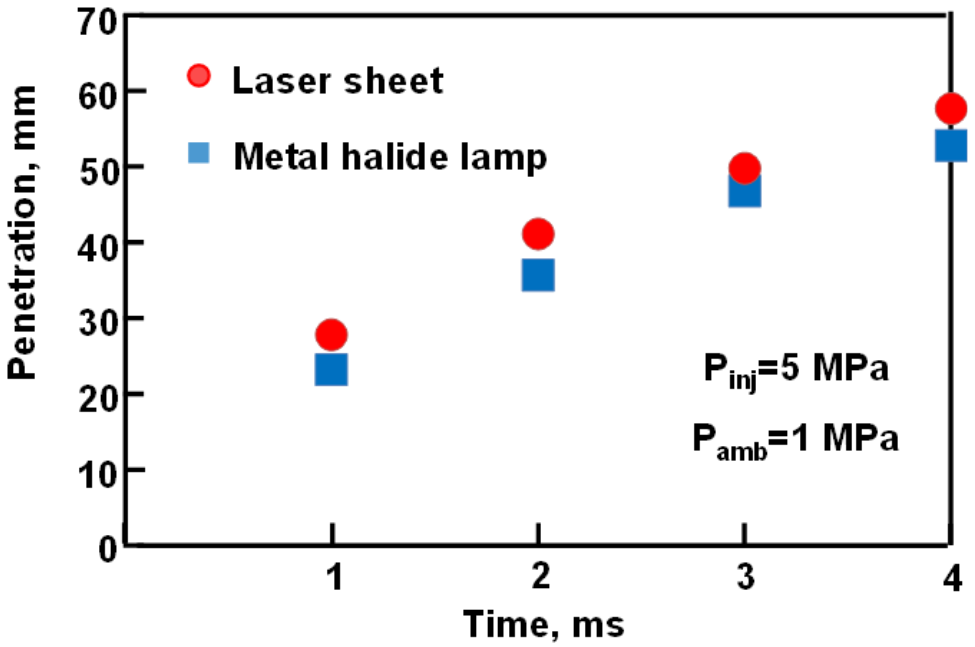

Figure 3.12 Comparison of Jet tip penetration for two different light sources

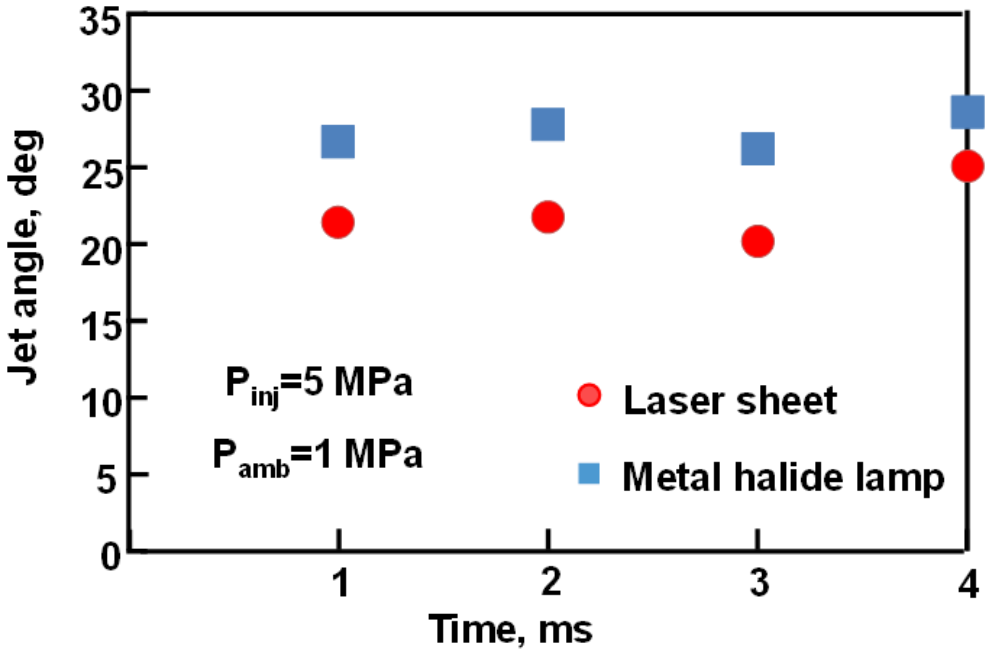

Figure 3.13 Comparison of Jet cone angle for two different light sources

visualization of hydrogen jet structure. For visualization with Ar-ion laser, a light sheet optics with cylindrical lens was used to generate a light sheet of thickness approximately 2 mm. This thin light sheet can illuminate only a portion of scattered tracer particles present in that narrow plane of 2 mm thickness during hydrogen jet formation. Therefore, the captured images represent a 2-D cross-sectional view of the hydrogen jet. On the other hand, light from metal halide lamp could possibly illuminate the entire 3-D structure of the hydrogen jet consisting a spherical head vortex. Taking into consideration these differences, appropriate choice of light source seems very important and as a consequence metal halide lamp is considered to obtain a more complete and qualitative picture of the jet pattern; further discussion on this topic is presented in the next section.

3.4 Jet pattern and penetration measurements

3.4.1 Effect of injection pressure and ambient pressure

The first condition included a range of injection and chamber pressures indicative of hydrogen engine cylinder conditions. The injection pressures along with chamber pressures and gases for these conditions are shown in Table 3.1. In ICEs, penetration depth and jet cone angle are two important factors to obtain better fuel air mixing. Figure 3.14 (a) – (d) show the development of the hydrogen jet for an injection pressure of 5 MPa over various constant-volume chamber (filled with N_2) pressures ranging from 0.1 MPa to 2.0 MPa. The image shows that the jet diameter expands rapidly just downstream from the nozzle exit. At t = 3.0ms, for case (a) P_{inj}= 0.5MPa jet plume appears to penetrate faster compared to higher ambient pressures cases. This is also evident in Fig.3.15 which compares the penetration

rate for various ambient pressures. The hydrogen jet dispersed slightly more in low ambient density than in high ambient density as expected which implies that higher ambient pressure resulted in considerably shorter jet tip penetration. This is caused by the higher inertia of the fluid elements that the injected fluid must accelerate and push aside. Comparison of Fig.3.14 and Fig.3.16 shows that increasing the injection pressure resulted in a significant difference in the jet structure in the initial part of the injection for all the different ambient pressures. In both figures, a spherical head vortex which grew over time could be observed though the light intensity was quite strong. Here air-entrainment which is caused by the shear induced turbulence and momentum exchange between fuel and air is the dominant factor for gas jet mixing process. The main mechanism for entrainment is through engulfment of ambient air along the upstream edge of the large-scale structures. Subsequent mixing occurs as the interface formed between the entrained ambient air and the jet gas is stretched, and both jet and entrained air come into contact at ever smaller scales until the fluid from the two streams becomes molecularly mixed at the Kolmogorov scale. During the gas injection, the jet tip pushes out the still ambient nitrogen, and then the vortex structure is formed by the interaction between the jet and the ambient nitrogen. both the vortex formation and vortex broken are quite useful for fuel-air mixing and the mixture diffusion. The flow induced by the vortex was squeezed out the fuel from the jet tip, which is thought to cause the entrainment of the fuel to the surrounding nitrogen. The symmetry of the vortex may account for the slower spreading of the jet. From Fig.3.17 and Fig.3.18, it is observed that higher injection pressure resulted in faster growth of the hydrogen plume than for the lower injection pressure due to the additional momentum that is supplied to the jet at the injector exit.

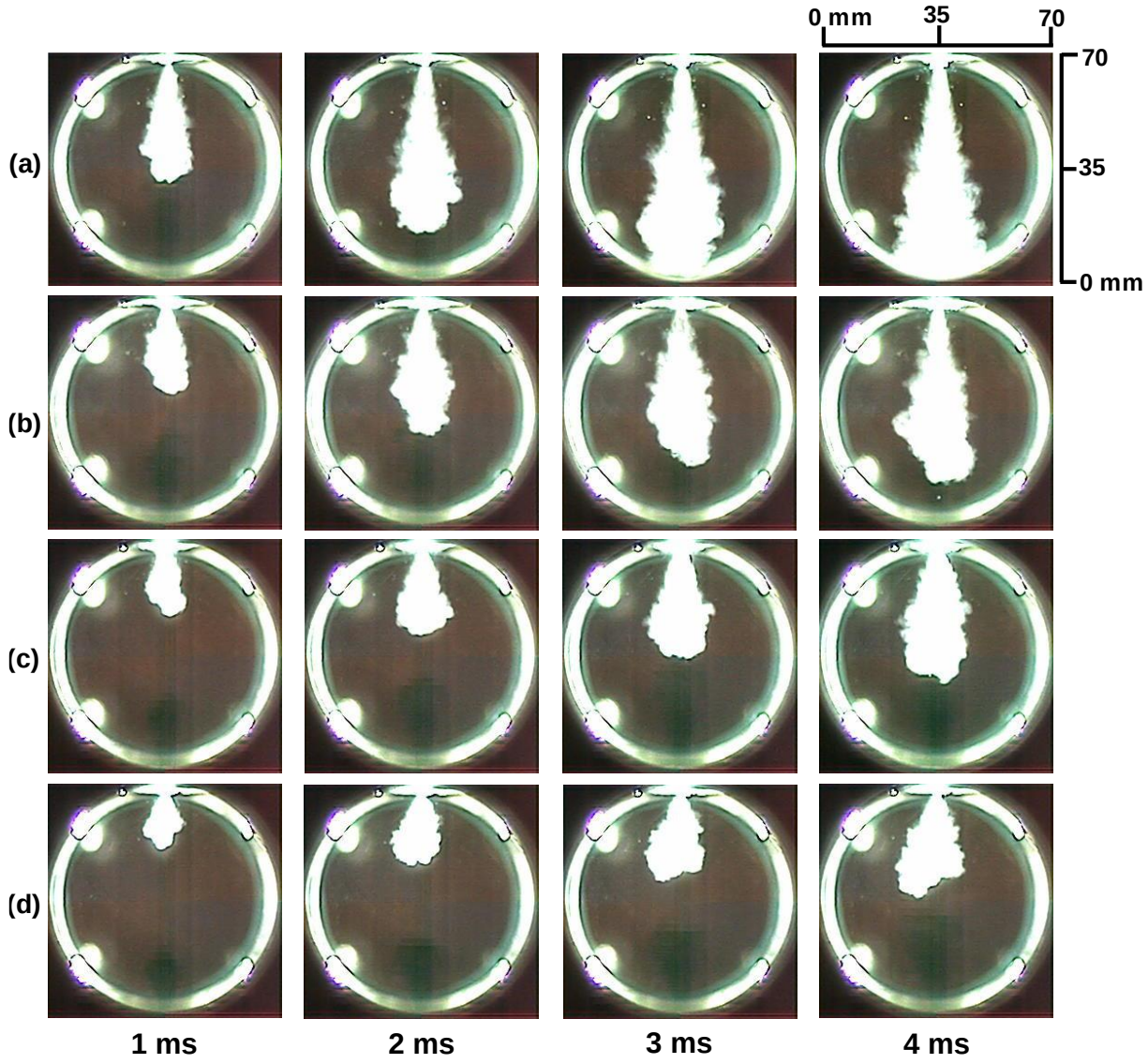

Fig.3.14 Time-series images of hydrogen jet evolution. P_{inj} = 5MPa; (a) P_{amb} = 0.5 MPa; (b) P_{amb} = 1.0 MPa; (c) P_{amb} = 1.5 MPa; (d) P_{amb} = 2.0 MPa; light source: Metal Halide Lamp

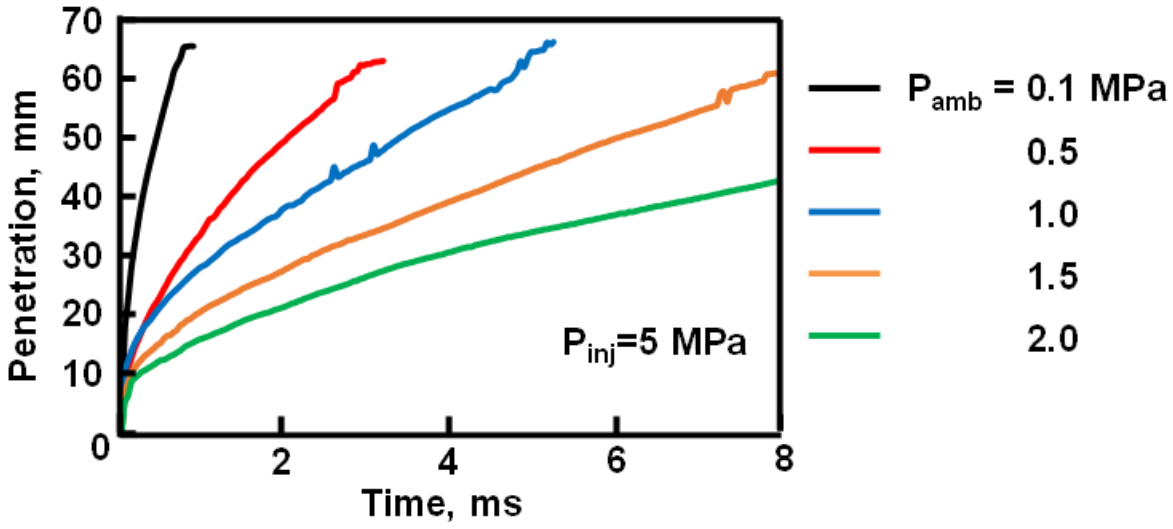

Figure 3.15 Jet tip penetration for P_{inj} = 5MPa; and different ambient pressures

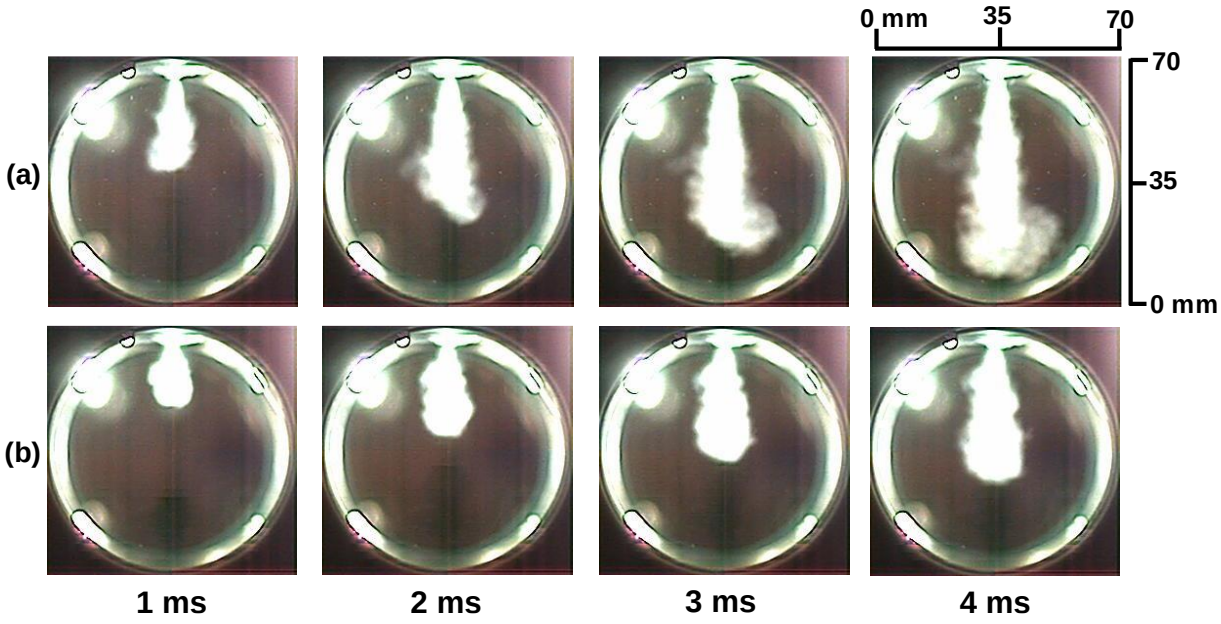

Fig.3.16 Time-series images of hydrogen jet evolution. P_{inj} = 7MPa; (a) P_{amb} = 1.0 MPa; (b) P_{amb} = 2.0 MPa; light source: Metal Halide Lamp

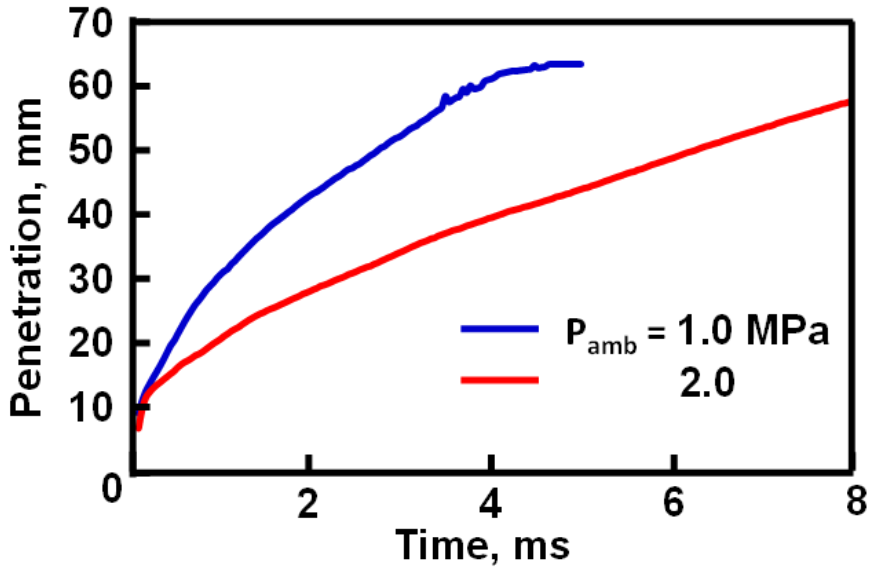

Figure 3.17 Jet tip penetration for P_{inj} = 7MPa; and different ambient pressures

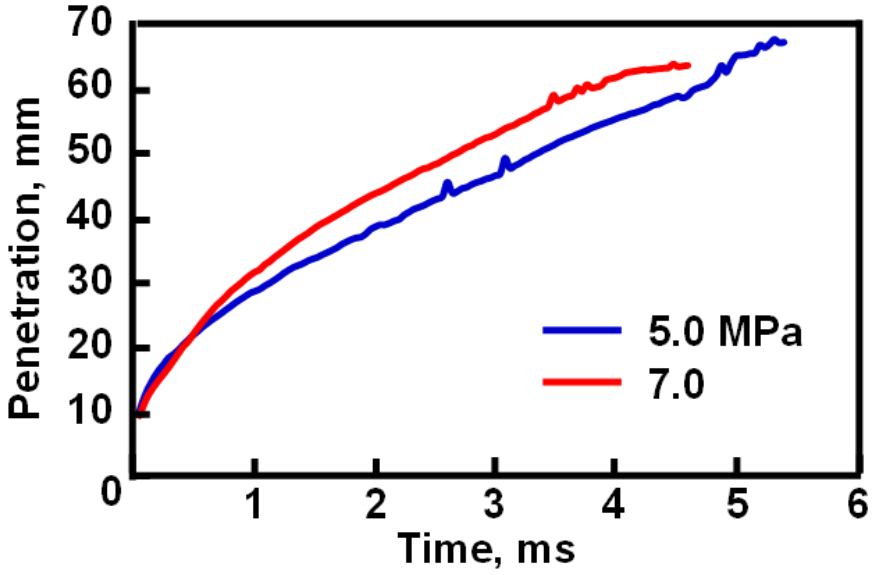

Figure 3.18 Comparison jet tip penetration for different injection pressures at P_{amb} = 1.0MPa

3.5 Jet cone angle measurement

3.5.1 Effect of injection pressure and ambient pressure

Several factors such as the jet inlet velocity profile, nozzle geometry, jet Reynolds number and fluid temperature at the inlet, affect the jet spread. The jet cone angle is most commonly used to describe spray or jet distribution, and is important as it affects the axial and radial distribution of the fuel. The jet angle, θ, is calculated by measuring the projected area, A_p, Z_p, contained within the jet taken at different times during jet flow development and approximating the jet as a triangle in this initial region before the head vortex. The relation for calculating θ is illustrated in Fig.3.19 and is given in equation 3.4.

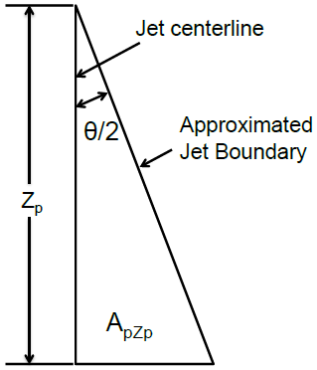

$$\frac{\theta}{2} = \tan^{-1}\left(\frac{A_p Z_p}{Z_p}\right) \qquad (3.4)$$

Figure 3.19 Determination of jet angle

The cone angle was characterized by measuring the angle generated by a triangle connecting the center of the nozzle tip and the widest horizontal span of the gas jet. Here jet cone angle

was measured at 20-mm distance from the nozzle tip. Figure 3.20 (a) – (b) show the effect of the injection pressure on the jet angle as a function of time after the onset of injection event. The jet cone angle is higher at early times due to the development of the head vortex and then drops to a relatively steady value. It should be noted that data presented here were the average of five observations/runs conducted for each condition. From Fig.3.20 and Fig.3.21, for t = 2 ms, it could be observed that an increase in the ambient pressure resulted wider jet angle along with slower penetration of the fuel jet (Fig.3.15 and Fig.3.17) in the downstream region indicating greater entrainment or higher mass of ambient fluid (N_2) into the jet. From conservation of momentum, a greater mass of air in the fuel jet results in lower overall jet velocities at axial direction, and thus slower jet tip penetration [16]. Naber and Siebers [17] studied the effects of ambient gas density on the penetration and dispersion of diesel sprays and developed non-dimensional parameters that included the effects of dispersion or spray angle. Their data showed that as the ambient gas density is increased the spray or jet angle also increases. The increased spray/jet angle is a result of additional entrainment of ambient fluid mass. Moreover, the ambient air moves nearly perpendicular to the jet boundary and is entrained into the jet, and a change in the direction of the jet axis in the upstream region has been reported [18]. Figure 3.22 shows that increasing the injection pressure lead to smaller initial jet angle and higher jet tip penetration (Fig.3.18) as velocity of the jet or total momentum supplied in the fuel was higher for increasing the injection pressure. Therefore, the injected fluid with additional momentum could accelerate more readily by pushing aside the ambient fluid though density of chamber medium was considerably higher than the injected gas.

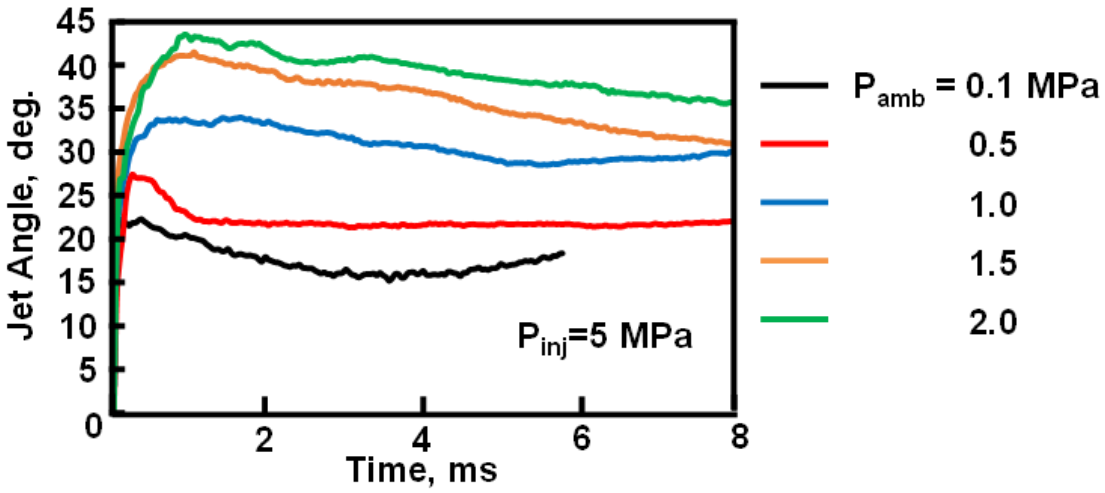

Figure 3.20 Jet cone angle for P_{inj} = 5MPa; and different ambient pressures

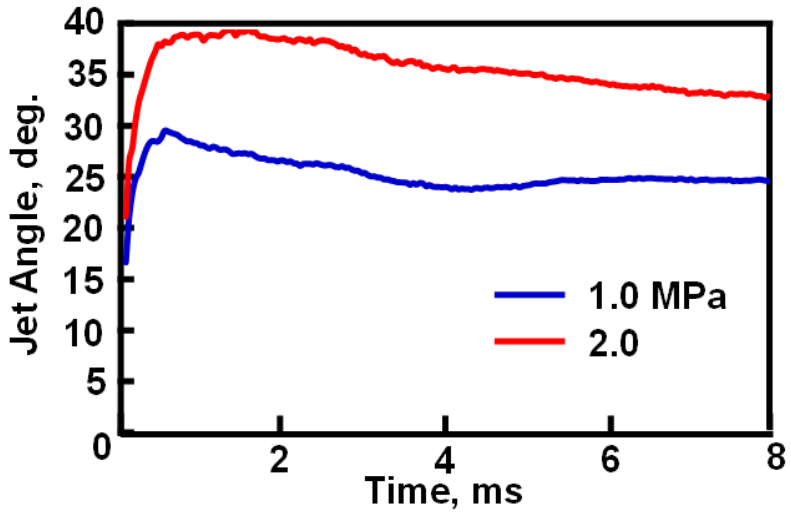

Figure 3.21 Jet cone angle for P_{inj} = 7MPa; and different ambient pressures

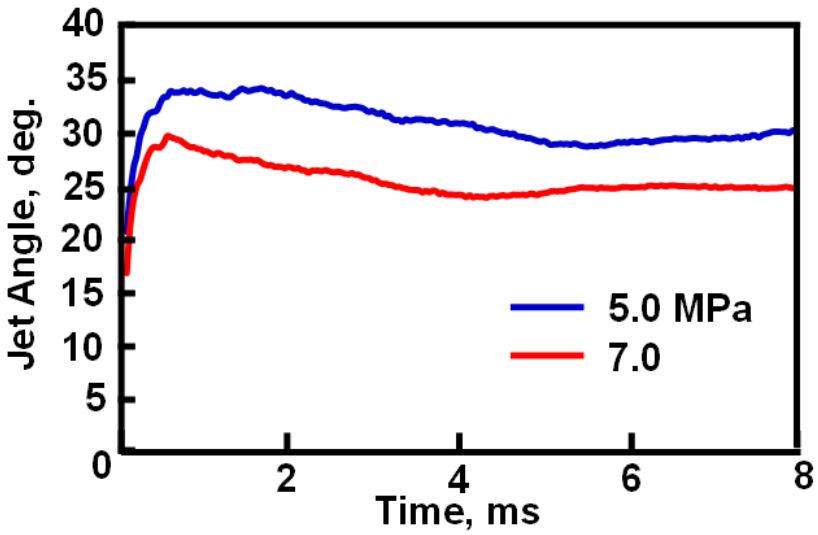

Figure 3.22 Comparison jet cone angle for different injection pressures

at P_{amb} = 1.0MPa

3.6 Summary

Understanding physics of the gas jet is necessary to study the behavior of fuel jet and its interaction with the surrounding air in the engine cylinder. Visualization of hydrogen jet was performed by supplying high pressure hydrogen into a constant volume vessel (CVV) through an injector. The vessel was developed to provide a quiescent, pressurized environment for various flows to propagate into. A high-speed camera, able to capture the evolution of hydrogen jet over time, was used along with an Ar-ion laser and metal halide lamp as the light sources. Time-series images show that jet plume appears to penetrate faster when hydrogen is injected with higher injection pressure into a chamber of comparatively lower ambient pressure as velocity of the jet or total momentum supplied to the fuel jet at

the injector exit was higher for increasing the injection pressure. Therefore, the injected fluid with additional momentum could accelerate more readily by pushing aside the ambient fluid though density of chamber medium was considerably higher than the injected gas. On the other hand, higher ambient pressure resulted in considerably shorter jet tip penetration along with wider jet angle which is caused by the higher inertia of the fluid elements that the injected fluid must accelerate and push aside.

REFERENCE

[1] Rajaratnam N. Turbulent jets. Journal of Fluid Mechanics 1976;82:605–8.

[2] Ouellette, P., 1996, "Direct Injection of Natural Gas for Diesel Engine Fueling," Ph.D. thesis, Department of Mechanical Engineering, University of British Columbia.

[3] J.S. Turner, The starting plume in neutral surroundings, J. Fluid Mech, 13, (1962);356-368.

[4] D. A. Andersion, J.C. Tannehill, R.H. Pleetcher, " Computational Fluid Mechanics and Heat Transfer", (1985), McGraw-Hill.

[5] Kuo T, Bracco F. On the Scaling of Transient Laminar, Turbulent, and Spray Jets. SAE Technical Paper 1982:SAE paper No. 820038.

[6] S. Abramovich, A. Solan, The initial development of a submerged laminar round jet, J Fluid Mechanics, 59, (1973);791-801.

[7] Abramovich G. The Theory of Turbulent Jets. The MIT Press; 1984.

[8] Ricou FP, Spalding DB. Measurements of Entrainment by Axisymmetrical Turbulent Jets. Journal of Fluid Mechanics 2006;11:21–32.

[9] J. D. Anderson, *Hypersonic and High-Temperature Gas Dynamics*, McGraw-Hill, New York, 1989.

[10] Hatanaka K, Saito T. Influence of Nozzle Geometry on Under-expanded Axisymmetric Free Jet Characteristics. Shock Waves 2012;22:427–34.

[11] Cumber P. Predictions of The Structure of Turbulent, Highly Underexpanded Jets. Journal of Fluids Engineering 1995;117:599–604.

[12] Crist S, Sherman PM, Glass DR. Study of the highly under-expanded sonic jet. AIAA J 1966;4:68-71.

[13] Abbett M. The mach disk in under-expanded exhaust plumes. AIAA J 1971;9:512-4.

[14] Donaldson CDuP, Snedeker RS. A study of free jet impingement. Part 1. Mean properties of free and impinging jets. J Fluid Mech 1971;45:281-319.

[15] J. Sauvola and M. Pietikainen, Adaptive document image binarization, Pattern Recognition 33 (2000) 225-236.

[16] D. L. Siebers, "Recent Development on Diesel Fuel Jets under Quiescent Conditions." Flow and Combustion in Reciprocating Engines, Sprringer-Verlag Berlin Heidelberg 2009, 257-308.

[17] Naber, J.D. and Siebers, D.L. "Effects of gas density and vaporization on penetration and dispersion of diesel sprays," SAE Paper 960034, 1996.

[18] T. Wallner, A. Nande and J. Naber, "Study of Basic Injection Configurations Using a Direct-Injection Hydrogen Research Engine", SAE Paper 2009-01-1418

chniques in X-ray photoelectron spectroscopy. Anal Chem Jan. 1982;54(1):13e9.

[20] M K Roy. Investigation of Different Injection Strategies and Local Mixture Concentration for Jet-guided Combustion in a Hydrogen Direct Injection Spark-Ignition Engine. PhD Thesis, 2013.

[21] Abdul Rahman MT. Mixture Formation Measurement of Transient Hydrogen Jet in Constant-Volume Vessel Using Spark Induced Breakdown Spectroscopy (SIBS). PhD Thesis, 2015.

[22] Abdul Rahman MT, Kawahara N, Tsuboi K, Tomita E. Visualization and concentration measurement of a direct injection hydrogen jet in a constant-volume vessel using spark-induced breakdown spectroscopy. Int J Hydrogen Energy 2014;39(31):17896-17905.

CHAPTER: 4

Mixture Formation Process in a Compression-Expansion Machine (CEM)

4.1 Fundamental physics of spark discharge in IC engine

The electrical spark is the most common way to initiate combustion and has been very widely studied, mostly in terms of the minimum ignition energy necessary to ignite a given mixture as a function of the spark parameters such as electrode material, shape, distance, spark duration and electrical circuitry (e.g. capacitor or self-inductance), and as a function of flow parameters such as equivalence ratio, velocity, turbulence level, pressure, and temperature [1-3].

The creation of a spark in a gas may result in flame ignition, if the spark is strong enough and the gas mixture falls within the flammability limits. The energy deposited by the spark results in plasma formation that generates radicals and ionised species which can then trigger chemical reactions and further heat release, in the case of flammable mixture. Even in the case of mixtures that would not normally allow self-sustaining combustion, a spark will result in a short-lived concentration of various intermediates, such as fuel fragments (e.g. CN*) and hydroxyl radicals (OH*) [4].

Ignition by an electrical discharge is a surprisingly complex process. The fundamental physics of spark ignition and its use in internal combustion engines has been reviewed by Maly [5]. For coil-type ignition systems, evolution of an electrode spark can be characterized

by four phases: pre-breakdown, breakdown, arc, and glow discharge [2]. Initially the gas between the electrodes is a perfect isolator. In the pre-breakdown phase, if a voltage is applied between the electrodes, the electrons in the spark gap accelerate from the cathode and the anode. Collisions with gas molecules ionize these, new electrons are produced. If the number of electrons increases sufficiently to make the discharge self-sustainable, breakdown takes place and the pre-breakdown phase is closed. A very small conductive path is formed between the electrodes with a high pressure ~around 20 MPa and temperature ~around 60,000 K [5-7].

The breakdown phase, responsible for the majority of the observed emission characteristics, occurs in less than 10 ns and includes a rapid current rise followed by a decrease in the electrode voltage, seen as the trailing edge of the initial voltage spike in Fig.4.1. Initially, the spark energy is stored in the dissociation, excitation and multiply ionized states of the atoms of the gas molecules in the discharge, creating a plasma. During the breakdown and arc phases, high energy radiation (wavelength < 250 nm) is almost completely reabsorbed by the plasma, although between 1 and 5% of energy escapes as visible radiation [5]. The spark is always associated with some form of light emission, especially the initial breakdown phase results in strong emission. A summary of the evolution of the spark light emission is presented as Fig.4.2. Extensive dissociation and ionization occur during the breakdown phase. Chemical reactions are spectroscopically visible in the gas a few nanoseconds after breakdown at the colder fringes of the plasma where the temperature is on the order of a few thousand K. At this time the plasma centre has a temperature of up to 60 000 K and a diameter on the order of 40 μm. After breakdown, the system relaxes, and the energy is

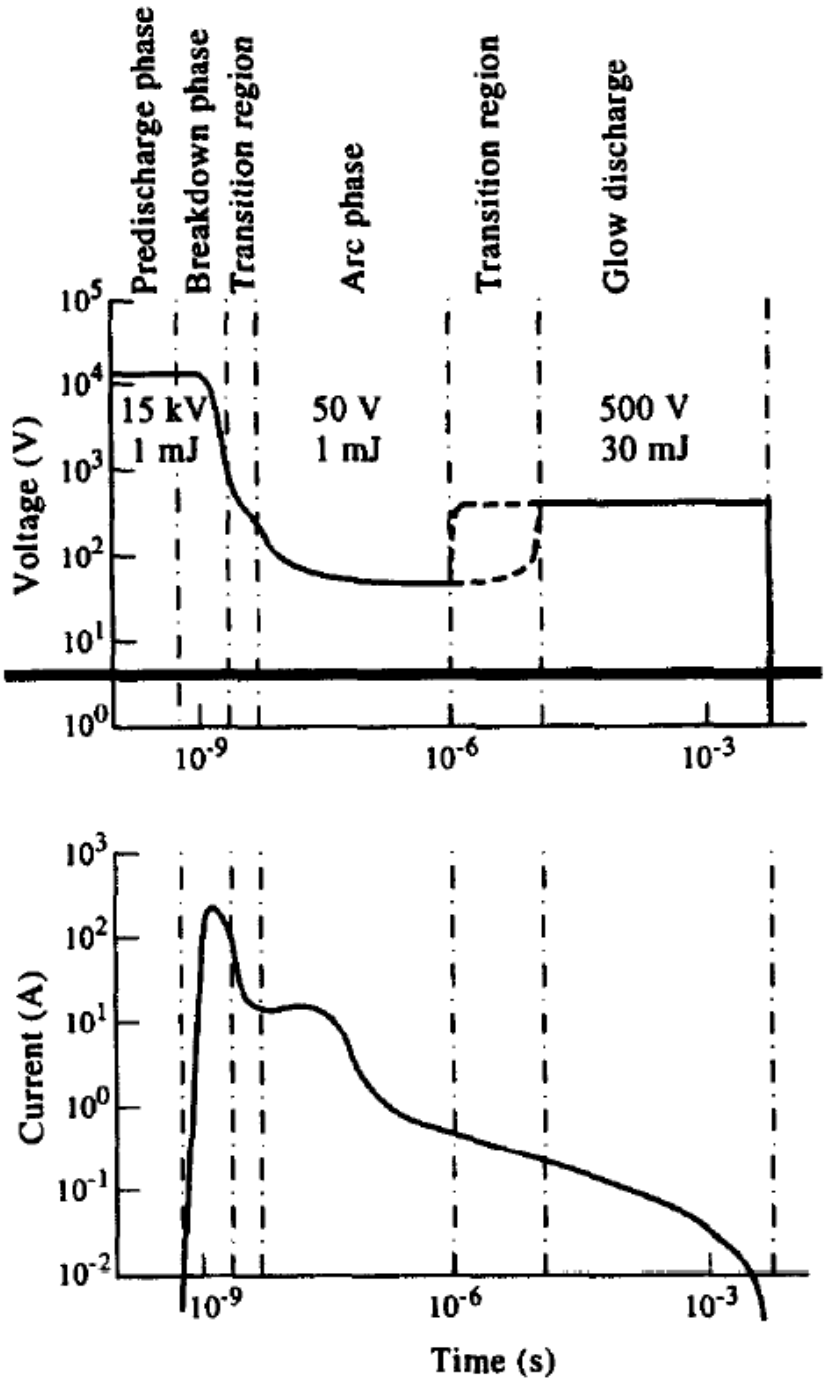

Fig.4.1 Schematic of voltage and current variation with time for convention coil-spark ignition engines

converted into kinetic energy, initially expanding the plasma channel radially at velocities over 5 000 m/s [5]. The rapid expansion of the plasma leads to cooling and recombination of atomic species into new molecules within 5 μs. The nitrogen containing molecules CN, NO and NH, also visible in hot flames, are then spectroscopically dominant [5]. After 10 – 20 μs, the kernel cools to flame temperatures and the expansion velocity falls below 100 m/s, allowing chemical reactions to initiate combustion. Consequently, emissions from molecules such as OH and CH are visible [5]. The breakdown phase is most efficient in transferring energy to the gas and in inflaming the fuel–air mixture, although because of its brevity, it typically accounts for only 1–2% of the energy dissipated in the spark event. In contrast, the glow discharge phase is least efficient in transferring energy to the gas, but because of its long duration accounts for about 90% of the total energy dissipated in the spark. The subsequent glow discharge phase, during which most of the energy is usually deposited, also results in light emission, although this is now less strong.

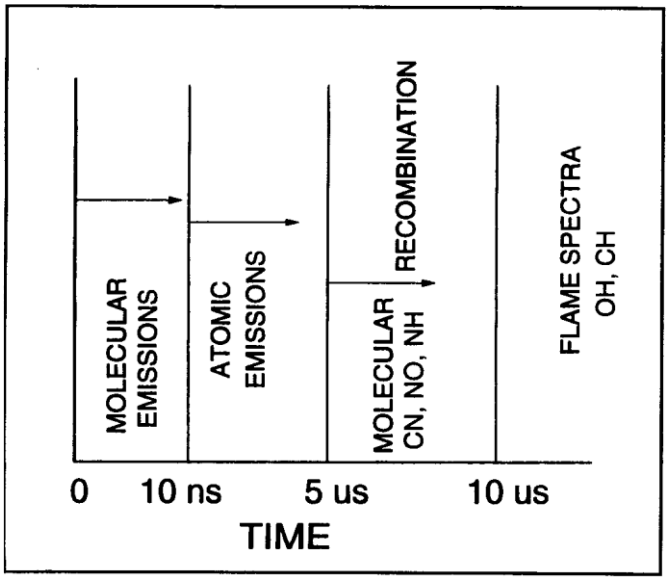

Fig.4.2 Evolution of Spark Light Emissions

Study of spark light emissions up to 10 μs after discharge in a gasoline fired SI engine [8] found that breakdown voltage (Vs) and total light emission (represented by the sensor voltage output, Vo, and referred to as the spark shot intensity) increase with increasing pressure, and decrease with increasing temperature and Ø. Peterson et al. [9] conducted PIV experiments to characterize spark behaviour under extreme high-velocity (0–8m/s) and multiphase fuel concentrations in an optical SG-SIDI engine. They reported that, onset of a spark began when the spark voltage and current values both became negative and the duration of the spark event lasted until the spark current value was no longer negative (Fig.4.3).

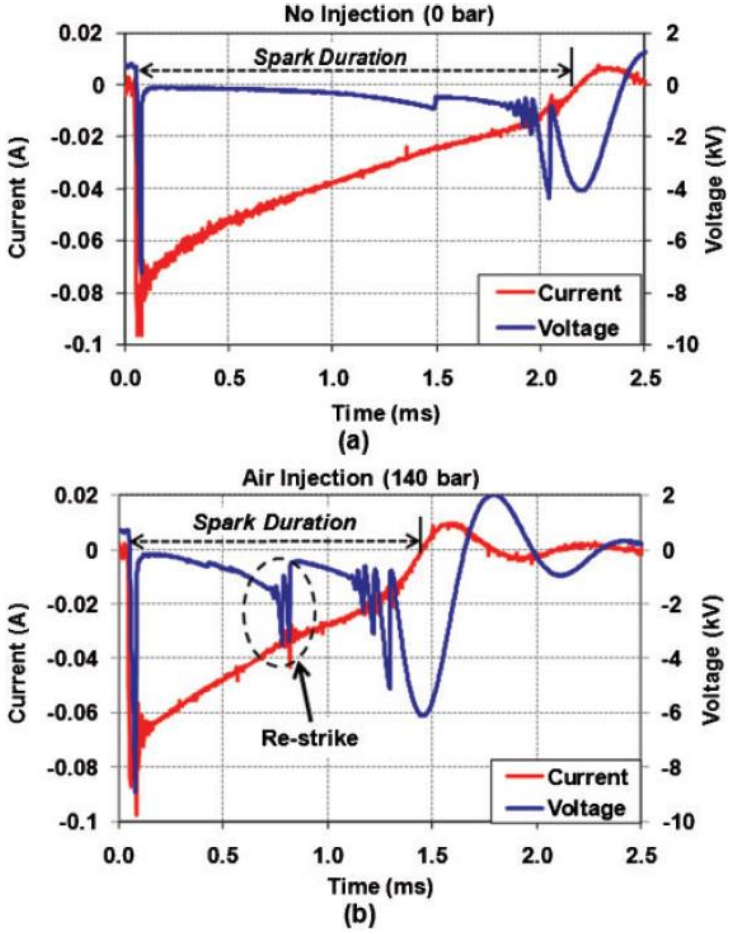

Fig.4.3 Spark voltage and current traces for the non-injection and air injection cycles

The onset of a spark began when the spark voltage and current values both reach to the peak. After the peak voltage value, the voltage drops to a level in the order of 200 V, indicating the discharge has transitioned to either the arc or glow discharge phase [10]. As demonstrated by Lee et al. [11] at the 12bar pressure attained here, a transition from the arc to glow phase cannot always be resolved. The spark voltage trace for the air injection cycle shows a continual voltage increase during the arc and glow phase and is associated with the lengthening of the plasma channel. The voltage increases to a value in which the available coil voltage can no longer sustain the plasma channel, resulting in the re-strike shown in Fig.4.3. This restrike is associated with a new breakdown event and is indicated by a sharp increase in voltage magnitude.

4.2 Development of Spark Plug Sensor

4.2.1 Basic structure of spark plug

Changes in engine design and fuel operating conditions place increased demands on spark plugs and the electrical system. The performance of the spark plug may determine the engine efficiency of the modern engine. The spark plug provides an electrode gap for the spark that is necessary to ignite the compressed fuel-air mixture under compression in each cylinder. It must also provide a gas-tight conducting path from the high-tension lead wire to the electrode gap. Basically, a spark plug consists of three parts: the insulator, electrode, and a threaded metal shell. These parts are assembled together with cement or dry powder to form an operational leak-proof unit. The insulator tip will determine the heat range of the plug

(hot or cold). Spark plug fouling is due to combustion products which collect on the plug's insulator. These products may cause misfiring at high speeds; thus, it is aggravated by rich idle mixtures and excessive oil consumption that may bypass the rings or valve guides. Figure 4.4 demonstrates the basic design and construction of a commercially available standard spark plug which will be used as a SIBS sensor for local fuel concentration measurements in DISI engine. The top of the spark plug contains a terminal to connect to the ignition system. The exact terminal construction varies depending on the use of the spark plug. The physical shape of the ribs function to improve the insulator and prevent electrical energy from leaking from the terminal to the metal case along the side of the insulator. The disrupted and longer path makes the electricity encounter more resistance along the surface of the spark plug. The insulator is typically made from an aluminium oxide, ceramic as is designed to withstand 550° C and 60,000 V. It extends from the metal case into the combustion chamber. The exact composition and length of the insulator partly determines the heat range of the plug. As the spark plug also seals the combustion chamber of the engine when installed, the seals ensure there is no leakage from the combustion chamber. The seals are generally made of copper in the form of washer so that it can get compressed to give a good seal. The metal case of the spark plug bears the torque of tightening the plug, serves to remove heat from the insulator and pass it on to the cylinder head. It also acts as the ground for the sparks passing through the center electrode to the side electrode to body. The tip of the insulator surrounding the center electrode is within the combustion chamber and directly affects the spark plug performance, particularly the heat range. The ground electrode is made from high nickel steel and is welded to the side of the metal case. The ground electrode also runs very hot, especially on projected nose plugs. The center electrode

is connected to the terminal through an internal wire and commonly a ceramic series resistance to reduce emission of radio noise from the sparking. The tip can be made of a combination of copper, nickel, iron, chromium, or precious metals. The center electrode is usually the one designed to eject the electrons (the cathode) because it is the hottest (normally) part of the plug; it is easier to emit electrons from a hot surface, because of the same physical laws that increase emissions of vapor from hot surfaces. In addition, electrons are emitted where the electrical field strength is greatest; this is from wherever the radius of curvature of the surface is smallest, i.e. from a sharp point or edge rather than a flat surface. It would be easiest to pull electrons from a pointed electrode, but a pointed electrode would erode after only a few seconds. Instead, the electrons emit from the sharp edges of the end of the electrode; as these edges erode, the spark becomes weaker and less reliable. The development of precious metal high temperature electrodes (using metals such as yttrium, iridium, platinum, tungsten, or palladium, as well as the relatively prosaic silver or gold) allows the use of a smaller center wire, which has sharper edges but will not melt or corrode away. The smaller electrode also absorbs less heat from the spark and initial flame energy. Spark plugs are typically designed to have a spark gap which can be adjusted manually before installing the spark plug, by the simple mechanism of bending the ground electrode slightly to bring it closer to or further from the center electrode.

Fig.4.4 Basic structure of a standard spark plug

4.2.2 SIBS sensor: optical fibre-embedded spark plug

In the previous spark plug sensor (Fig.4.5), the ground electrode was modified with a sharp-edged electrode for stable ionic initiation and made separable from the thread reach, which could be attached again using screws. This design was adopted initially to make cleaning of the sapphire window and other maintenance easier, because the spark plug sensor was developed for use in the combustion of hydrocarbon fuels [12], in which deposits or fouling of the sapphire window occurred frequently. However, these modifications led to unstable spark formation outside of the measurement area, especially for high ambient pressures

(Fig.4.6). To overcome this issue, a new SIBS sensor was developed without modification to the thread reach or electrodes [13]. In addition, the deposit on the sapphire window was minimal, because the plug was used only for the combustion of hydrogen fuel. In addition, this SIBS sensor is applicable to a production SI engine because it does not require any engine modifications.

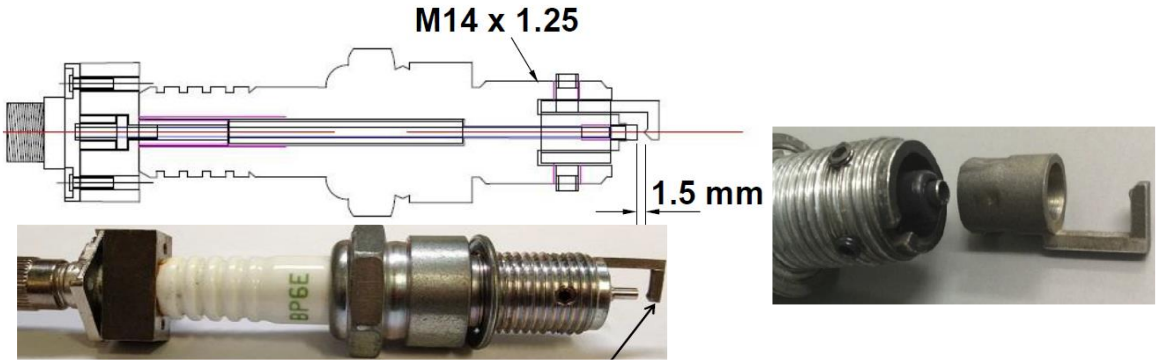

Fig.4.5 Previously designed fibre optic spark plug sensor with separable ground electrode

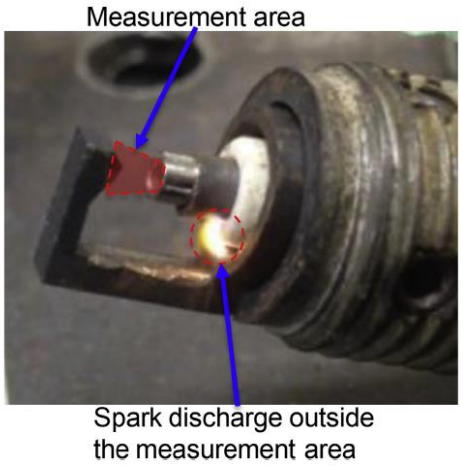

Fig.4.6 Spark discharge occurring outside of measurement area in case of previous design

Figure 4.7 shows the new fibre optic plug sensor developed from a commercially available spark plug (M-12 type) in which a 1.5-mm-diameter hole was drilled centrally along the spark plug body to accommodate the optical fibre and sapphire window assembly. The electrode tip where sapphire window was housed could be attached with centre electrode through threads cut on the both electrode tip and centre electrode. In initial design of the plug sensor, a 200-μm UV-grade quartz fiber was used for investigating a laminar premixed flame in a CH4/air mixture [12]. Further improvement was made by using larger core diameter of the UV-grade quartz fiber up to 600 μm to enhance the capability to collect light from spark plasma [14]. Newly developed spark plug sensor is the outcome of continuous effort to attain improvement in measurement accuracy. For current research, an optical ultraviolet (UV)-grade quartz fibre (core diameter: 1000 mm; outer diameter: 1250 mm) was housed along the centre electrode to collect light from the spark discharge. Sapphire window that could be used safely under high-pressure conditions, was mounted at the tip of the centre electrode to provide passage for light from spark emission. Spark plug gap was maintained at 1.5 mm to generate a stable spark discharge. Optical fibre had a numerical aperture (NA) of 0.20, and covered the area around the ground electrode. A small projection towards the centre electrode was made to facilitate spark discharge initiation; this also acted as the starting point of the ionic streamer during breakdown and arc phases. The discharge voltage and current were supplied to the fibre optic spark plug through a high-voltage power source and a coil-type ignition system.

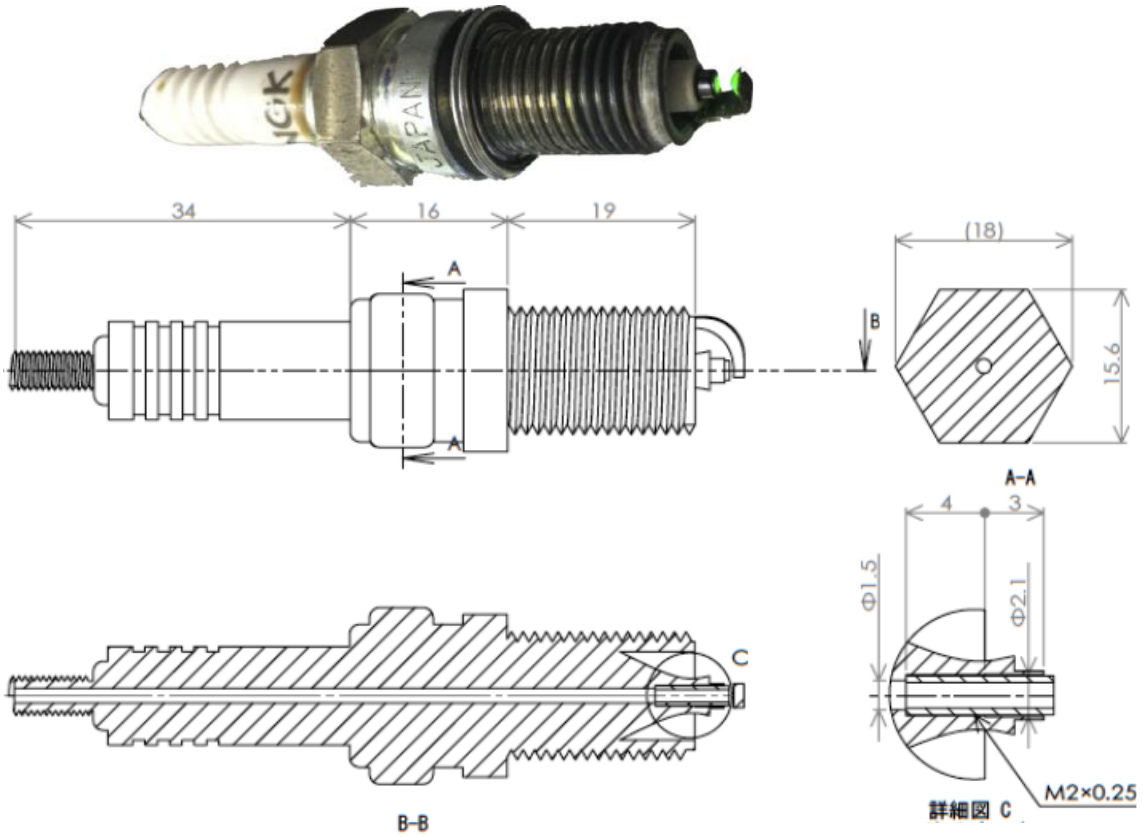

Fig.4.7 Newly developed spark plug sensor (top: laser light passing through the optical fibre housed in the center electrode) [13]

4.3 Experimentation for SIBS Measurement in a CEM

4.3.1 Compression Expansion Machine

A single-cylinder engine (Compression-expansion machine), specially designed to fire only once (single cycle combustion) in one experimental run, was used in this experiment. A schematic diagram of the engine geometry with optical access is shown in Fig.4.8.

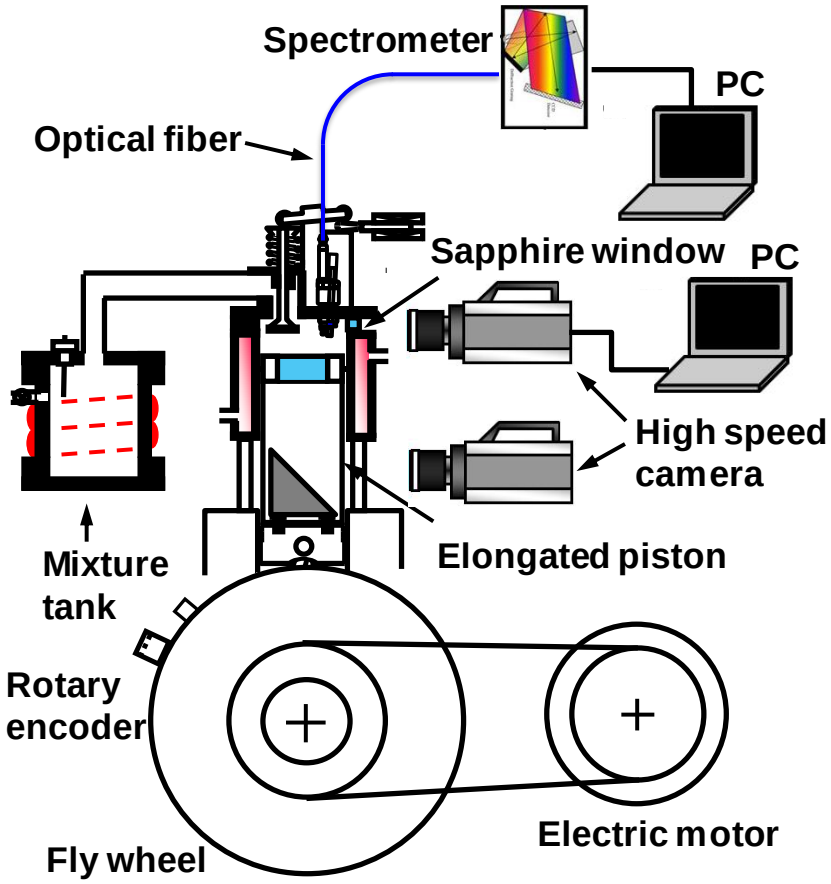

Fig.4.8 Schematic diagram of the engine experimental setup

Table 4.1 Engine (CEM) specifications

Bore x Stroke (mm x mm)	78 x 67
Compression ratio	7
Engine speed, rpm	600
Intake Valve Closing, IVC	BDC
Charge motion	Jet guided
Fuel (H_2) injection pressure, MPa	5
Spark timing	TDC

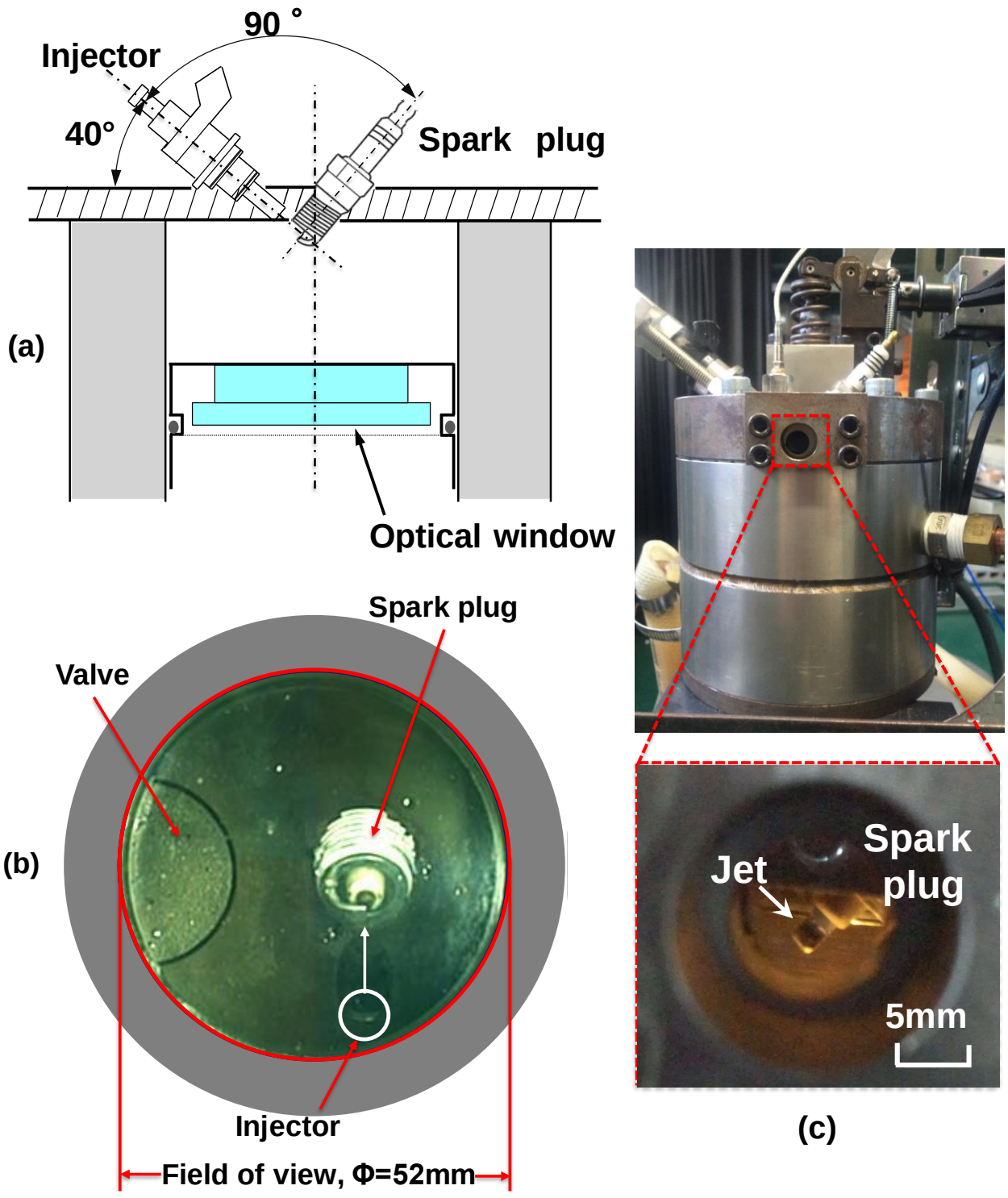

Fig.4.9 (a) Orientation of injector and spark plug; (b) Field of view through bottom window; (c) Arrangement for side window

A summary of engine specifications is presented in Table 4.1. This engine had only one intake valve through which in-cylinder exhaust gas was drawn out by a vacuum pump after each experimental run. A 52 mm-diameter sapphire window was attached to the crown of Bowditch elongated flat piston to get optical access inside the combustion chamber. Initially air was introduced into the cylinder through inlet valve at a pressure of 101 kPa and a temperature of 300 K. An electric motor drove the engine starting from piston position at TDC. Control circuit was triggered when engine reached desired speed of 600 rpm, and solenoid driven intake valve was closed for piston location at bottom dead center (BDC). Fuel accumulator was used to maintain stable fuel (supplied from a H_2 cylinder) feed pressure to the injector. A single-hole injector, developed by Mitsubishi Electric Co. Ltd, had an orifice diameter of 1.0 mm and was located close to the spark plug (see Fig.4.9 (a)) on the central part of the cylinder head in order to form a jet guided combustion system. The inclined injector geometry directed the injected fuel toward the spark plug. Distance between injector nozzle tip and spark plug was around 17.4 mm. Direct photography of the combustion flame was acquired through a mirror mounted at 45^o in the extended piston and using a high-speed CMOS camera (GX-8, nac Image Technology) and field of view was depicted in Fig.4.9 (b). Simultaneous visualization of spark behavior with different fuel concentration and flow field was also performed through the side window in the cylinder head using another high-speed CMOS camera (GX-1, nac Image Technology) as illustrated in Fig.4.9(c). For visualization through bottom view, frame resolution were 320 x 320 pixels at 3,000 frames per second whereas to capture spark discharge frame resolution were 208 x 156 pixels at 60,000 frames per second. Kistler piezoelectric transducer installed on the cylinder head could trace in-cylinder pressure history and facilitated subsequent pressure-

based analysis. Synchronization of the various trigger signals with high-speed video recording and the data acquisition system were achieved by using a time-generator control circuit.

4.3.2 Spectrometer with CCD

A spectrometer is used in spectroscopy for producing spectral lines and measuring their wavelengths and intensities. The spectrometer converted incoming light into voltage across a charge-coupled device (CCD), wherein each pixel of the CCD represented a pre-calibrated wavelength. For SIBS analysis, emission spectra from the spark-induced plasma were led to the spectrometer (Ocean Optics USB2000+) with CCD detector as shown in Fig.4.10. Ocean Optics USB2000+, can measure optical emission spectrum over a range from 250 and 800 nm with a resolution of 0.3 nm and a minimum integration time of 1 ms. Data analysis was performed using the Ocean Optics Spectra Suite software package. The USB 2000+ spectrometer is a simple optical instrument based on a diffraction grating and a one-dimensional CCD detector array. The CCD array has 1 × 2048 pixels, so the spectrum reads out as a list of 2048 data numbers.

Figure 4.11 shows a schematic of the USB 2000+ spectrometer. Light from a fiber enters the optical bench through the SMA connector (1). Light from the fiber passes through a slit (2), which acts as the entrance aperture. An optical filter (3) is installed between the slit and the aperture in the SMA connector. This filter blocks light that would be diffracted in the second- and third-orders by the grating. A collimating mirror (4) matches to the 0.22 numerical aperture (F/2.3) of the optical fiber. Light reflects from this mirror, as a collimated beam, toward the grating. The grating (5) is installed on a rotating platform that selects wavelength

range. After assembly, the grating platform is fixed to eliminate mechanical shifts or drift. A mirror (6) focuses the first-order spectra on the detector plane. A cylindrical lens (7) is fixed to the detector to focus the light from the tall slit onto the shorter detector element (14 μm × 200 μm pixels), increasing light-collection efficiency. A 2048-element Sony ILX511 linear CCD array detector (8) pixel responds to the wavelength of light that strikes it.

The corresponding 'Absolute efficiency' of the CCD photocathode for groove density of 600line/mm was shown in Fig.4.12. and properties for different grating numbers are summarize in Table 4.2. For SIBS measurements, Grating#03 was selected which set the spectral range within 350-850 nm. The detector used for the USB2000+ is a charge transfer device (CCD) that has a fixed well depth (capacitor) associated with each photodetector (pixel). Charge transfer, reset and readout initiation begin with the integration time clock going HIGH. At this point, the remaining charge in the detector wells is transferred to a shift register for serial transfer. This process is how the array is read. The reset function recharges the photodetector wells to their full potential and allows for nearly continuous integration of the light energy during the integration time, while the data is read out through serial shift registers. At the end of an integration period, the process is repeated. When a well is fully depleted by leakage through the back-biased photodetector, the detector is considered saturated and provides the maximum output level. The CCD is a depletion device and thus the output signal is inversely proportional to the input photons. The electronics in the USB2000+ invert and amplify this electrical signal.

Each pixel on the CCD represents a specific wavelength of light, and the more photons absorbed, the more electrical signal generated. Therefore, the electrical signal output by the CCD at each pixel is proportional to the light intensity at each corresponding wavelength.

Fig.4.10 The Ocean Optics USB2000+ spectrometer

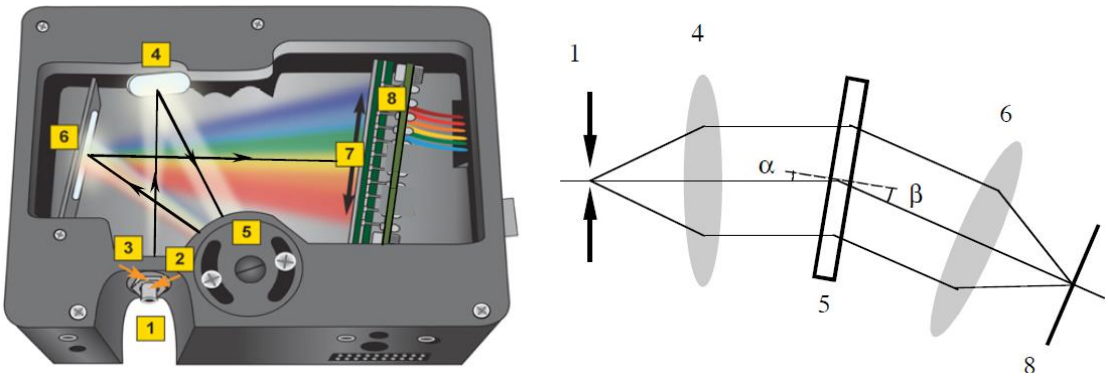

Fig.4.11 Interior of USB 2000+ spectrometer

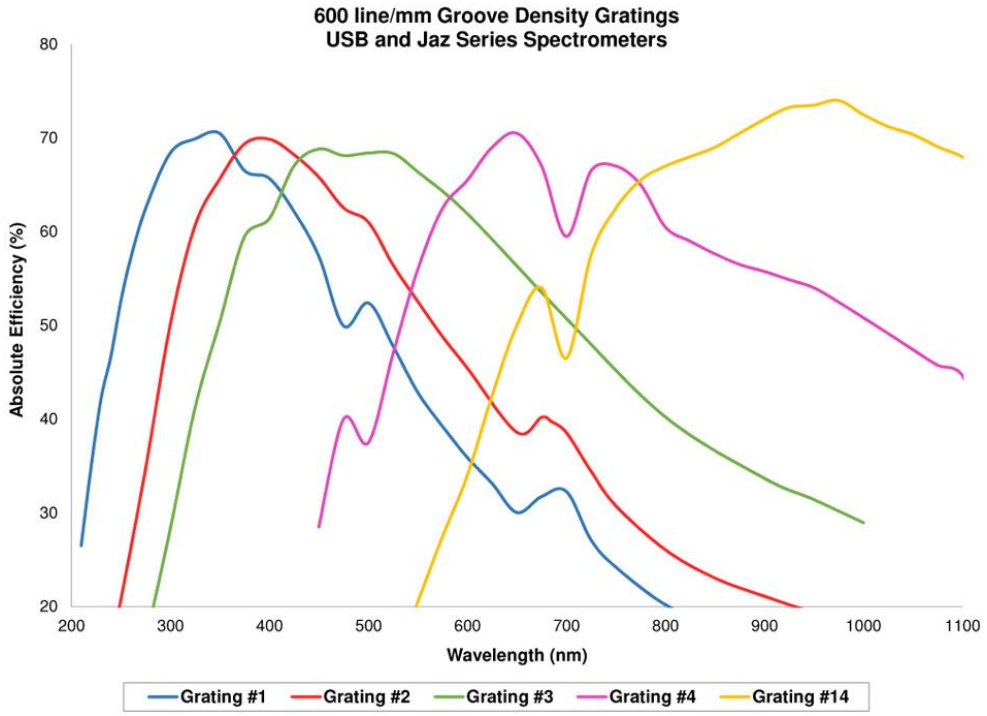

Fig.4.12 Efficiency for groove density of 600 lines/mm

Table 4.2 Spectral range and other properties for different grating numbers

Grating Number	Intended Use	Groove Density	Spectral Range	Blaze Wavelength	Best Efficiency (>30%)
1	UV	600	650 nm	300 nm	200-575 nm
2	UV-VIS	600	650 nm	400 nm	250-800 nm
3	VIS-Color	600	650 nm	500 nm	350-850 nm
4	NIR	600	625 nm	750 nm	530-1100 nm
5	UV-VIS	1200	300 nm	Holographic UV	200-400 nm
6	NIR	1200	200-270 nm	750 nm	500-1100 nm
7	UV-VIS	2400	100-140 nm	Holographic UV	200-500 nm
8	UV	3600	50-75 nm	Holographic UV	290-340 nm
9	VIS-NIR	1200	200-270 nm	Holographic VIS	400-800 nm
10	UV-VIS	1800	100-190 nm	Holographic UV	200-635 nm
11	UV-VIS	1800	120-160 nm	Holographic VIS	320-720 nm
12	UV-VIS	2400	50-120 nm	Holographic VIS	260-780 nm
13	UV-VIS-NIR	300	1700 nm	500 nm	300-1100 nm
14	NIR	600	625 nm	1000 nm	650-1100 nm
31	UV-NIR	500	200-1025 nm	250 nm	200-450 nm

4.3.3 Opticle fiber

The optical fiber used in this research to collect spark emission spectra is known as a step index (SI) and refers to the fact that the refractive index of the fiber core (n core) is a constant. The fiber (Fig.4.13) is manufactured by Mitsubishi Cable Industries Ltd. (STU1000H) which has a core diameter 1000 μm and fiber diameter of 1250 μm. A summary of the major specification is shown in Table 4.3. Optical fiber consists of several elements which are core, cladding, coating buffer, strength member and outer jacket. The optic core is the light carrying element at the center. This pure silica core fibers feature high light transmission efficiency and is suitable for a wide range of applications. The optical fiber had a numerical aperture (NA) of 0.20±0.02, which covered the area around the ground electrode as indicated in Fig.4.14. Numerical aperture (NA) of fiber optic is the measurement of the acceptance angle of an optical fiber, which is the maximum angle at which the core of the fiber will take in light that will be contained within the core.

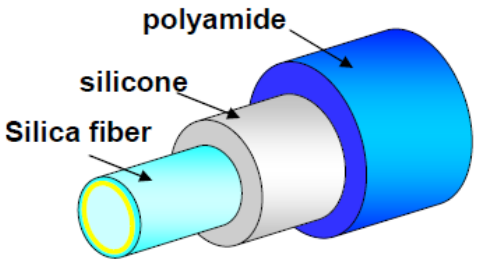

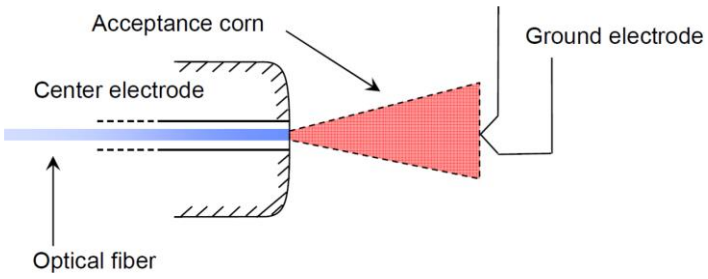

Fig.4.13 Optical fiber structure

Fig.4.14 Diagram of light collecting area of optical fiber

Table 4.3 Specifications of the Optical fiber

Type	NA	Core diameter, μm	Fiber diameter, μm	Allowable bending radius, mm	Optical transmission loss (dB/km)
STU 1000H	0.2±0.02	1000	1250	250	<600

4.3.4 Pressure sensor with charge amplifier

For the measurement of pressure inside the chamber during the combustion of hydrogen, a piezo-electric pressure transducer (Kistler-6052C) as shown in Fig.4.14 (a) is used in this experiment with charge amplifier (Kistler 5011B) shown in Fig.4.14 (b). The sensor is installed with front sealing in an M5x0.5 bore. This pressure sensor uses a piezoelectric crystal which achieves high sensitivity in conjunction with an extremely small sensor structure. The front end of the crystal is exposed through a diaphragm to the chamber pressure; as the chamber pressure increases during the combustion, the crystal is compressed and generates an electric charge which is proportional to the pressure. The output electric charge from the sensor is fed to the charge amplifier through a rugged cable with steel braiding. Finally, the charge amplifier (Type 5011B) converts the electrical charge produced by piezoelectric sensors into a proportional voltage signal. This sensitivity varies by not more than ±1,0 % in the operating temperature range. The passive acceleration compensation patented by Kistler keeps the influence of engine vibrations to a minimum.

Fig.4.14 (a) Piezo-electric pressure sensor (Kistler 6052C), (b) Charge amplifier (Kistler 5011B)

4.4 Spark behavior and mixture formation for different fuel concentration

4.4.1 Early injection case; SOI=180°BTDC

It is possible to conduct a fundamental investigation of mixture formation near spark plug in compression-expansion machine (CEM) using SIBS technique. For different preset air-excess ratio (air excess ratio can be defined as the ratio of the actual air-to-fuel ratio to the stoichiometric air-to-fuel ratio i.e. simply the inverse of fuel/air equivalence ratio), varying from λ_{preset} =1.0 to λ_{preset} = 5.0, spark behavior was studied by the help of high speed visualization through optical window mounted at the side of the CEM head (Fig.4.9-c). Spark-induced breakdown spectroscopic measurements were performed simultaneously using the

SIBS sensor. In order to avoid abnormal combustion such as knocking, hydrogen was injected into the nitrogen atmosphere field at a pressure of 101 kPa. The injection timing was set to SOI = 180 ° BTDC, just at the time of intake valve closing to ensure a premixed state of the mixture while onset of spark discharge occurred at TDC. For SIBS measurements, integration time used here was 150 μs from the onset of spark discharge; as this is found to be optimum duration to record strong atomic emission line of Hα, N(I) and O(I) within the spark duration of around 2 ms.

There have been a few studies that investigated spark behaviour under various levels of fuel concentration [10, 15-18]. Merer and Wallace [16] demonstrated that spark properties, such as breakdown voltage, were affected by fuel concentration. Figure 4.15 shows the time-series images of the spark discharge for λ_{preset} = 5.0 and λ_{preset} = 1.0, whereas voltage and current traces are shown in Fig.4.16. In these figures, it is apparent that for lean mixture (λ_{preset} = 5.0), the glow discharge appears to persist up to 2000 μs, whereas for stoichiometric mixture (λ_{preset} = 1.0), spark event lasted only up to 1000 μs. The spark voltage was measured at the top of the spark plug by a high-voltage probe (Tektronix model P6015A), while the spark current was measured using a current monitor (Pearson Model 110). The spark energy, *E* (energy dissipated throughout the duration of the spark event) was evaluated by integrating the product of the measured spark current, *i(t)* and voltage, *v(t)* over the appropriate time using the following relation,

$$E = \int_0^\infty v\,(t) i(t) dt \tag{4.1}$$

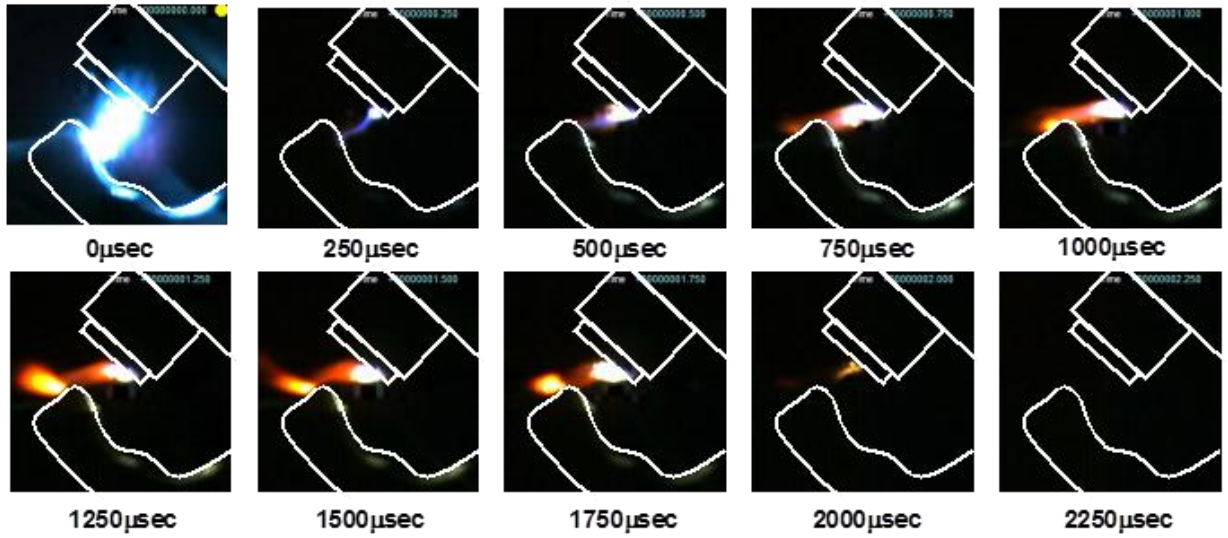

(a) λ_{preset} = 5.0

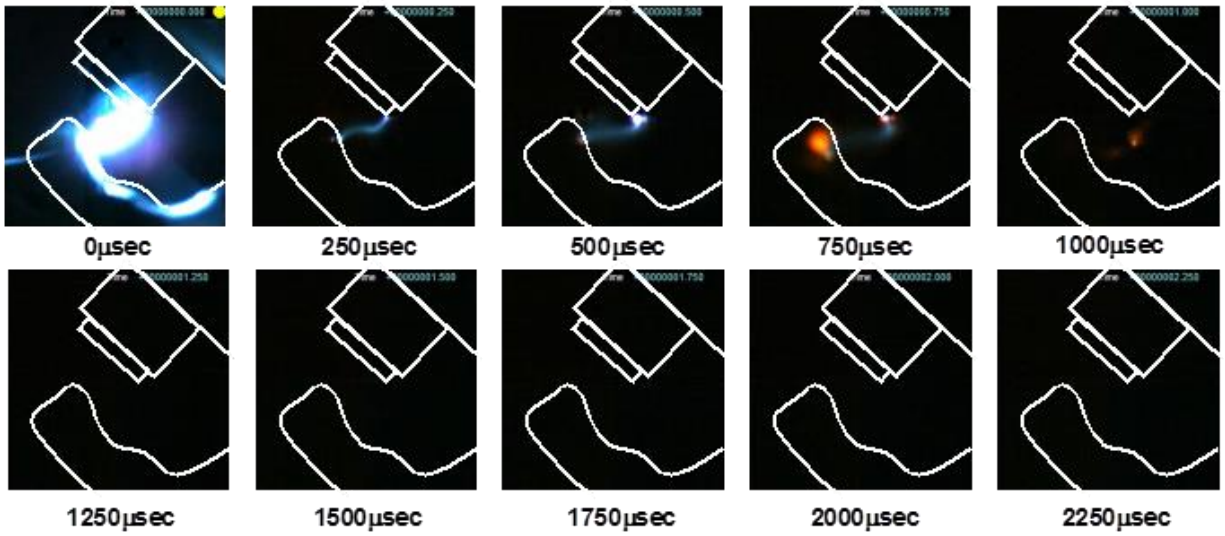

(b) λ_{preset} = 1.0

Fig.4.15 Time -series images of spark discharge behavior for different fuel concentration

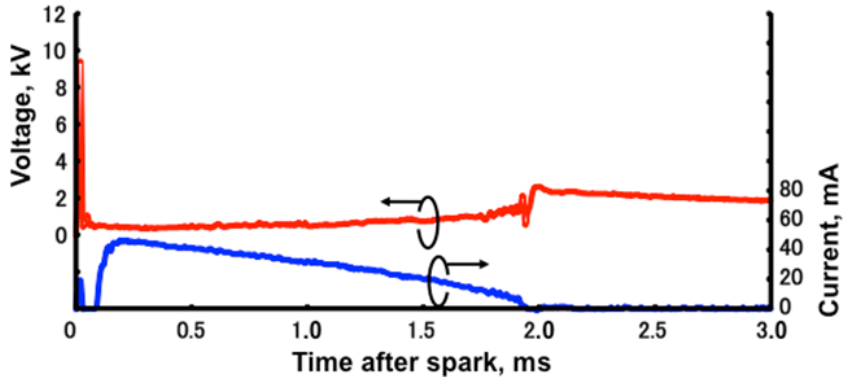

(a) λ_{preset} = 5.0

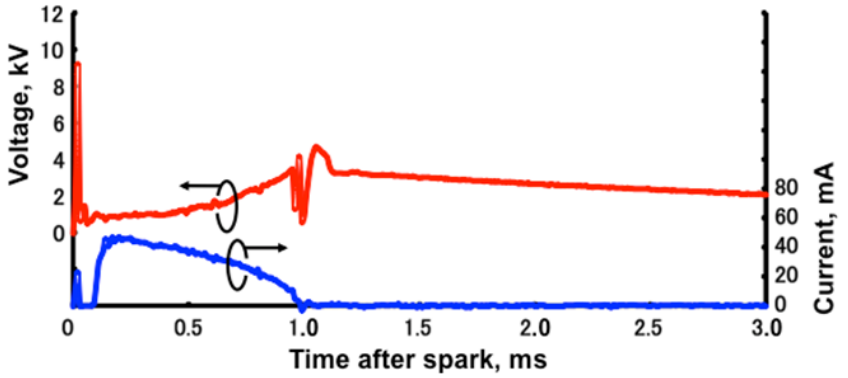

(b) λ_{preset} = 5.0

Fig.4.16 Spark voltage and current traces for different fuel concentration

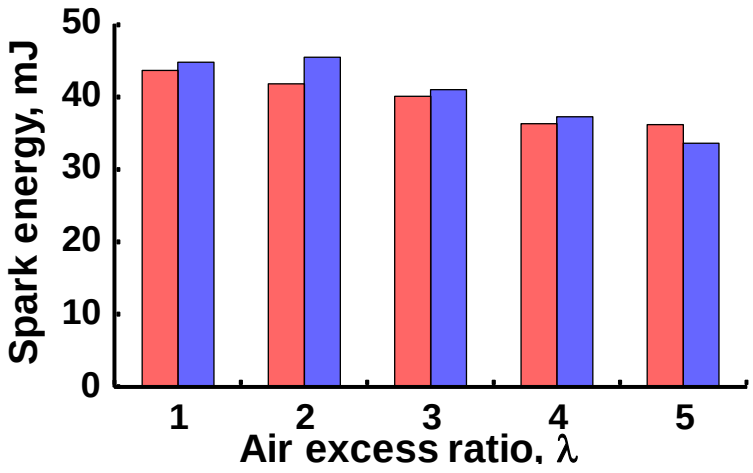

Fig.4.17 Spark discharge energy for different fuel concentration

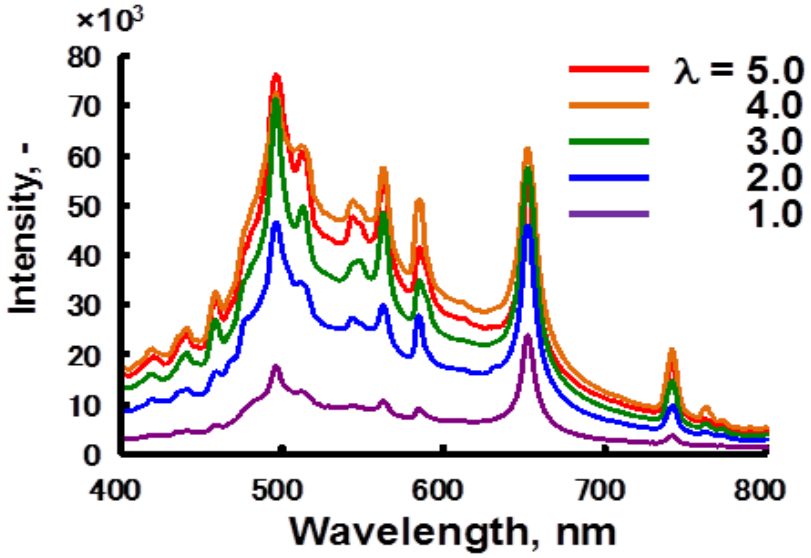

Fig.4.18 Spectral distribution for different fuel concentration

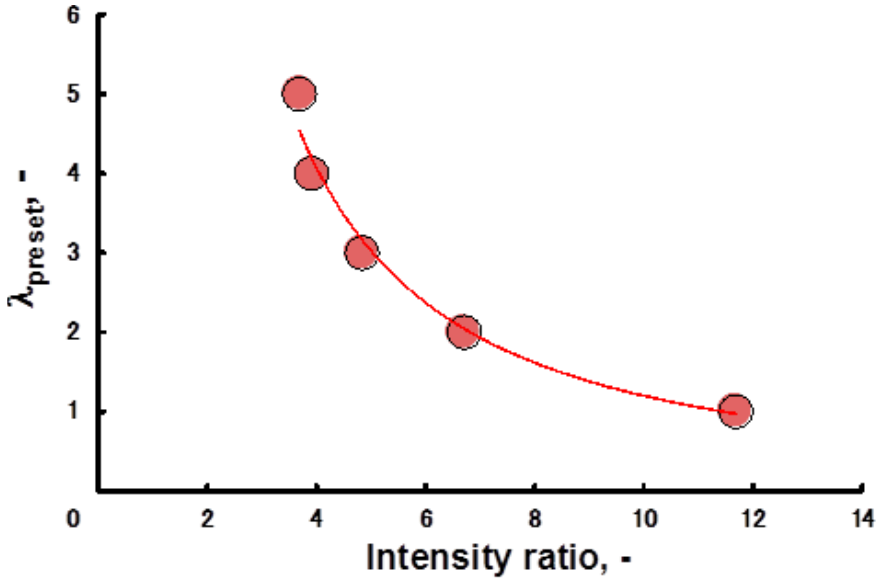

Fig.4.19 Correlation of preset air excess ratio, λ_{preset} with atomic intensity ratio of Hα to N

Influence of fuel concentration on spark discharge energy was plotted in Fig.4.17 which clearly indicates that presence of higher fuel concentration in the vicinity of spark gap leads

to higher discharge energy as the magnitude of both breakdown voltage and current increase though duration of spark event becomes shorter with lower air excess ratio.

Spectral distribution for corresponding preset air-excess ratio is shown in Fig.4.18, where the atomic emission lines of H_α at 656 nm, N(I) at 501 nm and at 745 nm were clearly recorded. The intensity of the Hα line was due to electronically excited hydrogen dissociated from the fuel (H2) molecules, while the emissions of N(I) lines was obtained from electronically excited nitrogen dissociated from ambient. In spectroscopic measurements and analyses, it is important to subtract the background from the raw spectrum data, especially when the intensities of some elements become the subject of interest. Here, background was subtracted from the raw spectra following the method suggested by Proctor and Sherwood [19] to obtain the background-corrected intensities for H_α, and N(I) emission lines. Details of the calibration and background subtraction methods can be found in the previous works conducted at Heat Power Engineering Laboratory of Okayama University, Japan [20-23].

In Fig.4.18, it is evident that, increasing λ_{preset} (i.e. higher hydrogen concentration) resulted in decreased signal intensities (i.e. line emissions), as well as weaker background emissions (i.e. plasma or arc emission). This is probably because when hydrogen concentration was relatively higher, breakdown voltage became higher which made spark discharge difficult to sustain over a long time (see Fig.4.15 and 4.16) and both continuum background emission (i.e. emission from spark plasma) and atomic emission intensity of the spectral distribution declines. An exponential relationship was observed between preset air-excess ratio (λ_{preset}) and emission intensity ratio of Hα (656 nm) to N (745 nm) as shown in Fig.4.19. As expected,

lower the preset air excess ratio, resulted in higher intensity ratio of Hα/N due to presence of higher concentration of hydrogen fuel compared to that of nitrogen. However, with a hydrogen density above a certain level, it is considered that the emission intensity ratio does not show a linear relationship because there is a limit to the amount of hydrogen atoms that can be excited. Therefore, a change in the discharge energy lead to a corresponding change in the relationship between atomic emission intensity ratio and excess air ratio.

4.4.2 Late injection case; EOI=70°BTDC ~ 0°BTDC

In order to investigate the mixture formation process around the spark plug for different injection strategies, injection timing was varied from EOI (End of Injection) = 70 to 0 ° BTDC, for a preset global air-excess ratio of λ_{preset} = 12.6, and fixed ignition timing at TDC. Exposure time for spectroscopic analysis (i.e. SIBS measurement), was set at 150 μs from onset of spark event. In addition, simultaneous visualization of hydrogen flames was performed using high speed camera, GX-8 at a frame speed of 3000 fps with frame resolution of 320 × 320 pixels.

For each operating condition, experiment was repeated for ten times and average values of 10 cycles are presented for discussion. The average in-cylinder pressure history and corresponding rate of heat release (ROHR) for hydrogen combustion are shown in Fig.4.20. Here, it is evident that cylinder pressure and heat release rate rise rapidly with retarded injection timing. This may be attributed to the fact that with direct injection condition the mixture became locally fuel-rich and the degree of richness increased with delayed start of

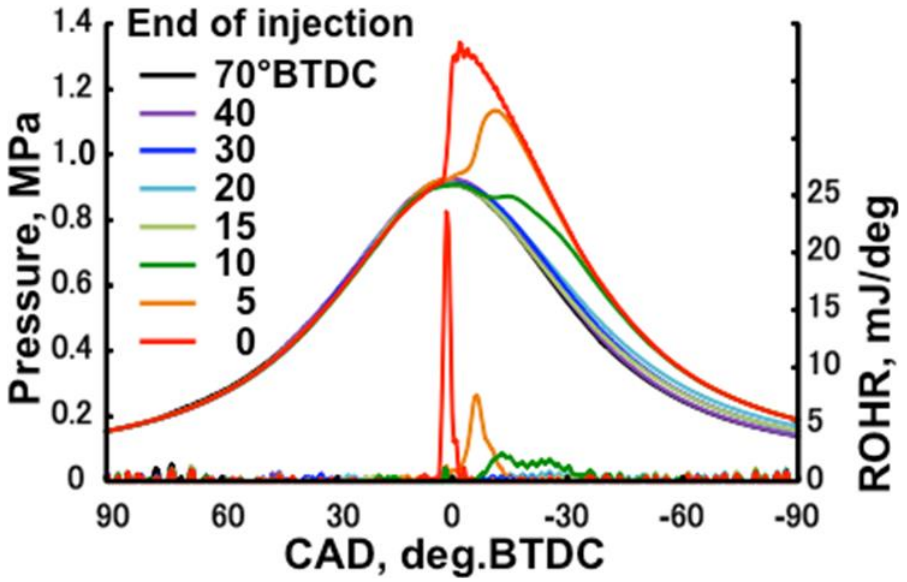

Fig.4.20 In-cylinder pressure history and rate of heat release (ROHR) for injection timing, EOI = 70 to 0°BTDC

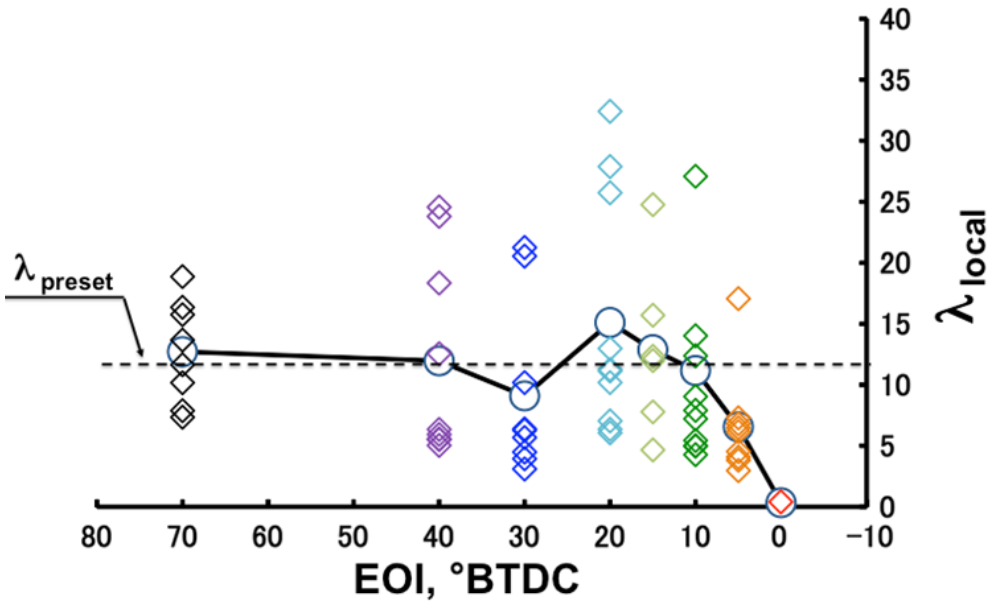

Fig.4.21 Variation local air-excess ratio with injection timing, EOI = 70 to 0°BTDC

injection (or end of injection) leading to rapid burning of the mixture. To confirm this local stratification of the fuel mixture during ignition, SIBS measurements were carried out and the local air excess ratios was plotted against varying end of injection (Fig.4.21). With retarded injection timing, i.e. when the EOI was delayed from 70°BTDC to 0°BTDC, the mixture in the vicinity of the spark gap location became successively richer during spark timing at TDC and this phenomenon is evident in Fig.4.21 because the average local air excess ratio (indicated by empty circle in the figure) decreased gradually with retarded EOI. However, for some observations, local air excess ratio (λ_{local}) was higher compared to preset air-excess ratio. In addition, cyclic variation in λ_{local} was significant and more pronounced for EOI = 70 to 20°BTDC than EOI = 10 to 0°BTDC. It is surmised that, for EOI = 10 to 0°BTDC hydrogen jet was less effected by in-cylinder flow, could retain its structure and just passing through the spark plug during the spark event at TDC. On the other hand, for EOI = 70 to 15°BTDC, behavior of the hydrogen jet was greatly influenced by the swirl flow and in-cylinder turbulence before ignition event could take place.

To have a close look in mixture formation process, EOI = 10 to 0°BTDC was considered with increments of 1 CAD. It can be seen that (Fig.4.22), as the injection timing retards, even for a small increment, combustion becomes more abrupt. Partial combustion can be observed for EOI = 10 to 5°BTDC, correlating with the fact that λ_{local} in each cycle fall below the lean limit of flammability (λ = 10) for hydrogen. As shown in Fig.4.23, for EOI = 5 to 0 ° BTDC, as the injection timing retarded, cyclic variation in λ_{local} decreased and lead lower average value of λ_{local}, indicating that a dense fuel-air mixture is formed near the spark plug region and very

dense portion of the hydrogen jet was ignited. For EOI = 0°BTDC, rapid combustion occurred along with peak pressure oscillation. This can be attributed to the fact that, presence of high fuel concentration with huge jet velocity lead to re-striking or multiple spark channels between the electrodes. As a consequence, several localized flame kernels might have developed and contributed to the pressure oscillation.

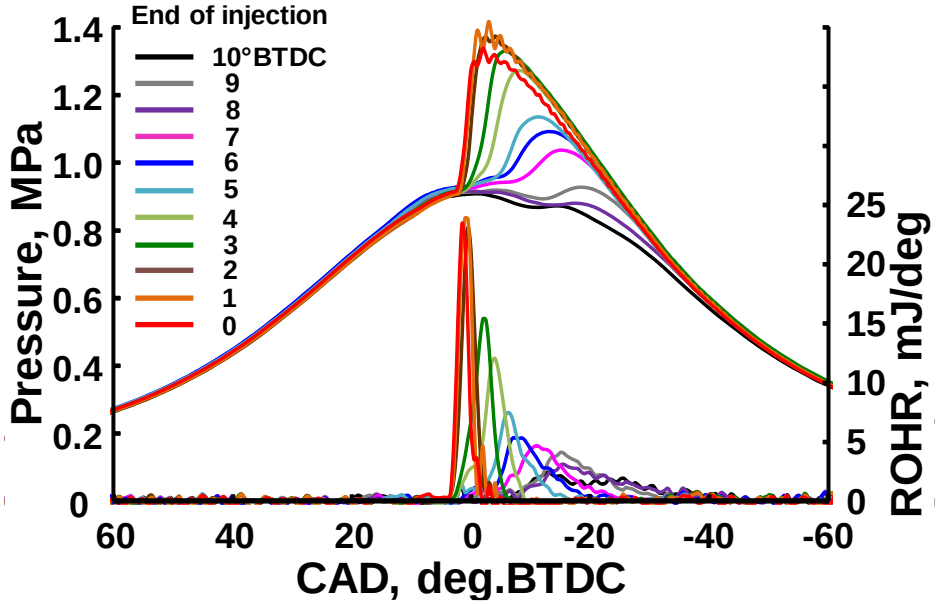

Fig.4.22 In-cylinder pressure history and rate of heat release (ROHR) for injection timing, EOI = 10 to 0°BTDC

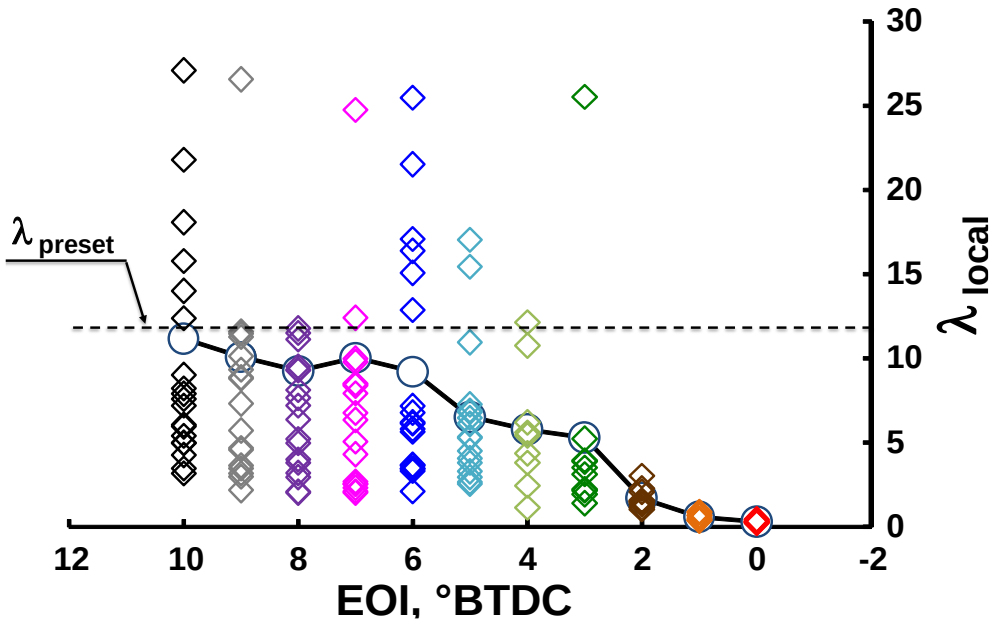

Fig.4.23 Variation local air-excess ratio with injection timing, EOI = 10 to 0°BTDC

4.5 Summary

A new sensor with an optical fibre housed in the centre electrode of the spark plug was developed from a commercially available M12-type spark plug with no major modification to the electrodes, leading to stable spark formation. Spectroscopic analysis of spark-plasma emission and high-speed visualization of spark behavior with different air-excess ratio was studied simultaneously in a compression expansion machine (CEM). Results clearly indicates that presence of higher fuel concentration in the vicinity of spark gap leads to higher discharge energy as the magnitude of both breakdown voltage and current increase though duration of spark event becomes shorter with lower air excess ratio. Exposure duration for

spectroscopic measurement of spark plasma is optimized to obtain better atomic emission intensity of Hα (656nm) and N (745nm). When hydrogen concentration was relatively higher, breakdown voltage became higher which made spark discharge difficult to sustain over a long time and both continuum background emission (i.e. emission from spark plasma) and atomic emission intensity of the spectral distribution declines. As expected, lower the preset air excess ratio, resulted in higher intensity ratio of Hα/N due to presence of higher concentration of hydrogen fuel compared to that of nitrogen. However, with a hydrogen density above a certain level, it is considered that the emission intensity ratio does not show a linear relationship because there is a limit to the amount of hydrogen atoms that can be excited. Therefore, a change in the discharge energy lead to a corresponding change in the relationship between atomic emission intensity ratio and excess air ratio.

REFERENCE

[1] B. Lewis, G. von Elbe, Combustion Flames and Explosion of Gases, third ed., Academic Press, Orlando, Florida, 1987.

[2] S.F.AhmedE. Mastorakos, Spark ignition of lifted turbulent jet flames, Combustion and Flame 146 (2006) 215–231.

[3] T. Marchione, S.F. Ahmed, E. Mastorakos, Ignition of turbulent swirling nheptane spray flames using single and multiple sparks, Combustion and Flame 180 (2009) 156–166.

[4] L. Beduneau, N. Kawahara, T. Nakayama, E. Tomita, Y. Ikeda, Laser-induced radical generation and evolution to a self-sustaining flame, Combustion and Flame 156 (2009) 642–656

[5] R.R. Maly: 'Spark Ignition: Its Physics and Effect on the Internal Combustion Engine'. In: *Fuel Economy: Road Vehicles Powered by Spark Ignition Engines*, ed. by J.C. Hilliard, G.S. Springer (Plenum, New York 1984) Ch. 3

[6] G.T. Kalghatgi: Soc. Autom. Engrs. Paper 870163 (1987)

[7] J.D. Dale, M.D. Checkel, P.R. Smy, Application of high energy ignition systems to engine, Progress in Energy and Combustion Science 23 (1997) 379–398. [3] B. Lewis, G. von Elbe, Combustion Flames and Explosion of Gases, third ed., Academic Press, Orlando, Florida, 1987

[8] Y. Ohyama, M. Ohsaga and H. Kuraiwa, "Study on Mixture Formation and Ignition Process in Spark Ignition Engines using Optical Combustion Sensor", SAE Paper No. 901712, 1990

[9] B. Peterson and V. Sick, "High-speed flow and fuel imaging study of available spark energy in a spray-guided direct-injection engine and implications on misfires", Int. J. Engine Res. (11):313-329

[10] Maly, R. and Vogel, M. Initiation and propagation of flame fronts in lean CH4-air mixtures by the three modes of the ignition spark. In Proceedings of the Seventeenth International Symposium on Combustion, Leeds, UK, August 1978, (The Combustion Institute, Pittsburgh, PA), 821-831

[11] Lee, M. J., Hall, M., Ezekoye, O. A., and Matthews, R. Voltage, and energy deposition characteristics of spark ignition systems. SAE paper 2005-01-0231,2005

[12] Kawahara N, Tomita E, Takemoto S, Ikeda Y. Fuel concentration measurement of premixed mixture using spark-induced breakdown spectroscopy. Spectrochim Acta Part B 2009;64(10):1085-92.

[13] Rahman K.M., Kawahara N., Matsunaga D., Tsuboi K., Tomita E., Takagi Y. and Mihara Y. Local fuel concentration measurement through spark-induced breakdown spectroscopy in a direct-injection hydrogen spark-ignition engine. Int J Hydrogen Energy 41 (2016) 14283-14292.

[14] Roy MK, Kawahara N, Tomita E, Fujitani T. Jet-Guided Combustion Characteristics and Local Fuel Concentration Measurements in a hydrogen Direct-Injection Spark-Ignition Engine. Proceedings of the Combustion Institute 2013;34:2977-84.

[15] Ballal, D. R. and Lefebvre, A. H. A general model of spark ignition for gaseous and liquid fuel-air mixtures. In Proceedings of the 18th International Symposium on Combustion, Waterloo, Canada, August 1981, (The Combustion Institute, Pittsburgh, PA) pp. 321–328.

[16] Merer, R. M. and Wallace, J. S. Spark spectroscopy for spark ignition engine diagnostics. SAE paper 950164, 1995.

[17] Ziegler, G. F. W., Wagner, E. P., and Maly, R. R. Ignition of lean methane–air mixtures by high pressure glow and arc discharges. In Proceedings of the 20th International Symposium

on Combustion, Ann Arbor, MI, August 1984 (The Combustion Institute, Pittsburgh, PA) pp. 1817–1824.

[18] Arcoumanis, C. and Bae, C.-S. Correlation between spark ignition characteristics and flame development in a constant-volume combustion chamber. SAE paper 902413, 1992.

[19] Proctor A, Sherwood PMA. Data analysis techniques in X-ray photoelectron spectroscopy. Anal Chem Jan. 1982;54(1):13e9.

[20] M K Roy. Investigation of Different Injection Strategies and Local Mixture Concentration for Jet-guided Combustion in a Hydrogen Direct Injection Spark-Ignition Engine. PhD Thesis, 2013.

[21] Abdul Rahman MT. Mixture Formation Measurement of Transient Hydrogen Jet in Constant-Volume Vessel Using Spark Induced Breakdown Spectroscopy (SIBS). PhD Thesis, 2015.

[22] Abdul Rahman MT, Kawahara N, Tsuboi K, Tomita E. Visualization and concentration measurement of a direct injection hydrogen jet in a constant-volume vessel using spark-induced breakdown spectroscopy. Int J Hydrogen Energy 2014;39(31):17896-17905.

[23] Abdul Rahman MT, Kawahara N, Tsuboi K, Tomita E. Effect of ambient pressure on local concentration measurement of transient hydrogen jet in a constant-volume vessel using spark-induced breakdown spectroscopy. Int J Hydrogen Energy 2015;40(13):4717-4725.

CHAPTER: 5

Mixture Formation Process in a DISI Hydrogen Engine

5.1 Introduction

The local equivalence ratio near the spark plug at the time of the spark discharge is particularly important for successful ignition, because the jet-guided system generates a stratified fuel concentration near the spark plug in a DISI engine. Spark-emission spectroscopy has been applied to measure the equivalence ratio in a DISI engine [1-3]. Ando and Kuwahara [2], and Fansler et al. [3] reported individual measurements of the equivalence ratio at the spark gap using the ratio of CN (388 nm) emission intensity and OH (306 nm) radical intensity from the spark that initiates combustion. They determined the cycle-resolved local fuel–air ratio in the spark gap, controlled the large-scale stratification, and evaluated the utility of SIBS as an engine diagnostic tool. However, it is difficult to detect the equivalence ratio under lean mixture conditions due to lack of the linearity of CN/OH emission intensity ratio. All of these studies require engine modification for optical access to the combustion chamber from outside. Kawahara et al. [4] used the SIBS technique to measure the local equivalence ratio in a laminar premixed flame of a CH4/air mixture. Spectrally resolved emission spectra of plasma generated by a spark plug were investigated for their potential to measure local fuel concentrations in a premixed mixture. The spectrum was measured through an optical fibre housed in the centre electrode of the spark plug, which makes this technique suitable for measuring the equivalence ratio in the spark gap at

ignition timing, in production engines without engine modification. Roy et al. [5] further improved the spark-plug sensor to measure the local fuel–air concentration in the spark gap at the time of ignition in a fired, jet-guided hydrogen SI-engine operated under stratified-charge conditions using SIBS. Tasyrif et al. [6] investigated the mixing process of a hydrogen jet in a constant-volume vessel and characterised the spatial distribution of the equivalence ratio across the jet and along its axis. Later, they reported the effects of the ambient pressure on fuel concentration measurements for a jet of hydrogen injected into a nitrogen environment with different ambient pressures; also, local concentrations were measured at various spark locations in a constant-volume vessel [7].

5.2 Plume ignition combustion concept (PCC)

Optimisation of spark timing, injection timing, and injection pressure, are important aspects of the development of hydrogen DISI engines and can suppress backfiring and knocking, especially at higher engine loads. Oikawa et al. reported a “plume ignition combustion concept” (PCC) for hydrogen DISI engines, denoting the ignition of a rich mixture plume during or right after an injection event [8]. In their study, the injector was mounted close to the spark plug to achieve jet-guided combustion with the jet being directed towards the spark plug using high injection pressures (200 bar). This PCC combustion with late injection strategy was shown to substantially reduce NOx emissions at high speed and under high load conditions while maintaining high thermal efficiency and power. A major challenge in the use of H2-DI is in-cylinder hydrogen-air mixing. It is critical to understand the physical process of mixing between the injected fuel and the air within the cylinder to optimize the overall performance of the direct injection engine. The high-pressure injector used for the

direct-injection engines usually have multiple holes in the nozzle tip to ensure an even distribution of fuel and promote proper mixing. This results in the formation of multiple under-expanded jets in the cylinder, which interact with each other and with the in-cylinder boundaries to form the fuel-air mixture before combustion. Almost in all cases, fluid fuel injection flow is three-dimensional and turbulent. This flow can be measured and calculated to some limited degree of accuracy using reasonable assumptions. In continuous system whose combustion chamber are usually large, fuel injection may be assumed to be represented by a turbulent free gas jet discharging into surrounding air. In this experiment PCC (Plume Ignition Combustion Concept) was successfully employed in a direct injection hydrogen spark-ignition research engine at Tokyo City University and quantitative measurements of local fuel concentrations were performed using the spark-induced breakdown spectroscopy (SIBS) technique.

5.3 SIBS Measurement in a production engine

5.3.1 Experimental set-up

The engine experiments were conducted using a single cylinder production engine (Nissan diesel engine, FD1), modified and redesigned by Tokyo City University (TCU) [8] for using it as a hydrogen direct injection spark-ignition engine. The major specifications of the engine are presented in Table 5.1. The combustion chamber geometry, orientation of the injector, and spark plug are shown in Fig.5.1 and Fig.5.2. A bowl-shaped piston was used to achieve better fuel-air mixing and improved combustion performance. Spark plug was located 20 mm away from the injector, and the hydrogen jet was aimed towards the spark plug gap,

forming a jet-guided combustion system. Hydrogen fuel was introduced from a high-pressure cylinder with a maximum pressure of 20 MPa and the flow rate was measured with a hot-wire type mass flowmeter (OVAL corporation, F-133M). A lamina air flow meter (Tsukasa Sokken Co. Ltd., LFE-25B) was used for measuring the intake air amount. Surge tanks were installed downstream of the hot wire mass flowmeter and air flow meter to eliminate the measurement error due to pressure oscillation.

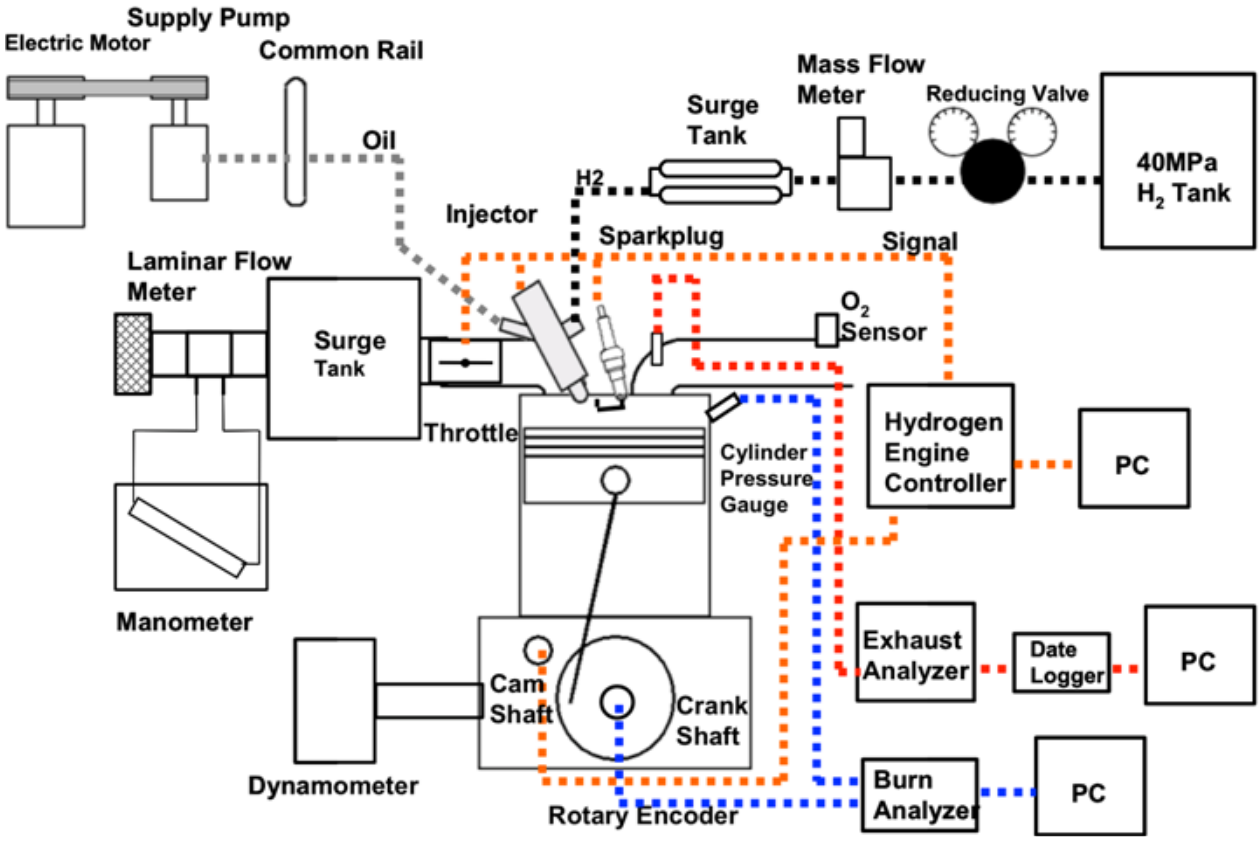

Fig.5.1 Schematic diagram of the engine experimental setup

Table 5.1 Major specifications of the research engine

Bore x Stroke (mm x mm)	108 x 115
Compression ratio	13:1
Engine displacement, cc	1054
Engine speed, rpm	1000
Combustion chamber type	Bowl
Throttle opening	50%, 100%
Swirl ratio	2.2
Injection system	PFI, DI
Cooling system	Water
Ignition system	Spark ignition

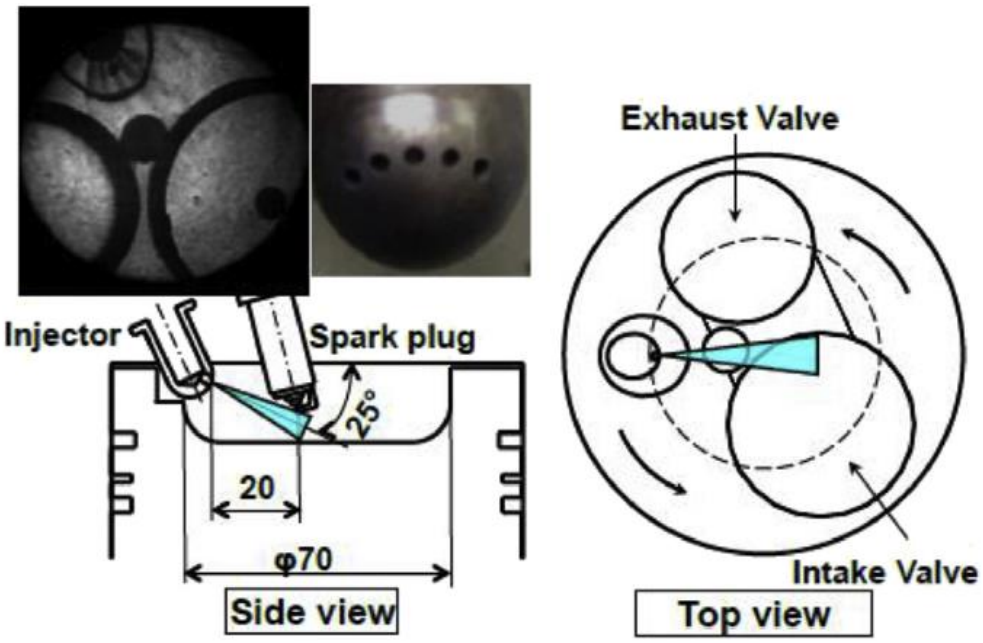

(a) (b)

Fig.5.2 (a) Combustion chamber geometry, orientation of injector and spark plug; (b) Field of view (dotted circle)

For measuring hydrogen concentration in exhaust gas, a magnetic sector type hydrogen gas analyzer (MSHA-1000W, Horiba Ltd.) was used whereas an automobile exhaust gas analyzer (NBY-401, Best Instruments Co. Ltd.) measured other exhaust gas components. Fuel injection timing, injection duration and ignition timing were synchronized by a control device (Controller Type II, Serizawa System Research Co. Ltd.) which can be set arbitrarily based on the crank angle of the engine. In-cylinder pressure was measured using a water-cooled piezoelectric pressure sensor (6067C, Kistler) and charge amplifier (5010, Kistler); and then combustion characteristics were evaluated by using a combustion analyzer (DS-9110, Ono Sokki Co. Ltd.)

5.3.2 Development of a high pressure common-rail injector

A high-pressure injector with a five-hole arrangement capable of producing a flat cone jet was developed by the researchers at TCU and used in this study (see Fig.5.3). Specifications for this newly developed injector are given in Table 5.2. The needle valve of this common rail injector was driven by oil pressure, enabling hydrogen to be injected at a pressure of 20 MPa and providing fast response. This injection system is capable of injecting maximum amount of required fuel into the combustion chamber for injection duration of 30 crank angle degrees at an engine speed of 3000 rpm. Injection timing and duration were adjusted by controlling the timing and quantity of spill oil in the common rail injector drive line. Details of this newly developed high-pressure injector can be found in the reference [9].

Table 5.2 specifications of the high-pressure injector

Nozzle type	Hole nozzle
Drive method	Oil pressure driven and Back pressure spill control
Max. oil pressure	120 MPa
Max. injection pressure	20 MPa
Max. injection rate (target)	400 Nml/stroke @30 deg. CA, @3000 rpm

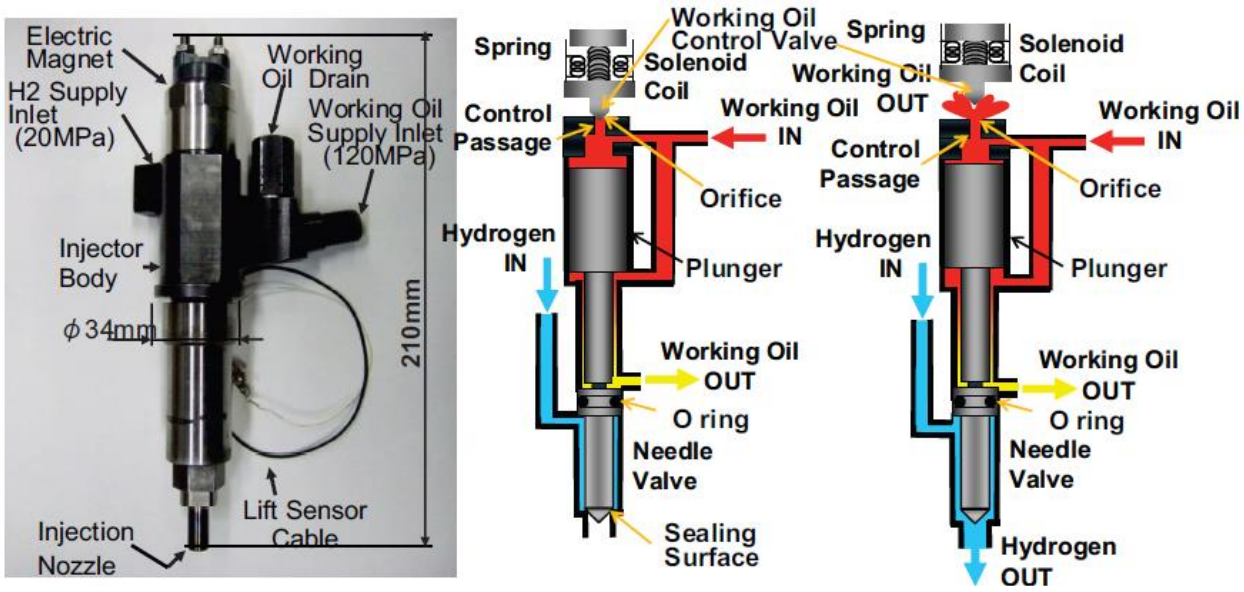

(a) Photograph (b) Close position (c) Open position

Fig.5.3 Structure and Injection mechanism of the newly developed high-pressure injector

5.3.3 Effect of corresponding pressure during spark initiation on spectral calibration: calibration map

Prior to measuring the mixture distribution in the hydrogen engine, SIBS require calibration to determine the correlation between the local air excess ratio and the intensities of the emission lines (i.e. I_H/I_N). To make a calibration curve, port fuel injection was used, which ensured a premixed charge of hydrogen and air. To investigate the effects of the corresponding ambient pressure during ignition (i.e. spark discharge) on the accuracy of fuel concentration measurements; the ignition timing was varied from 20^o to 0^{o}BTDC (before top dead centre) along with different throttle openings (50% and 100%) over a range of preset or overall air excess ratios (i.e. overall relative air/fuel ratio) varying from λ_{preset} =2.0 to λ_{preset} = 4.5. The experiments were repeated for 100 times for each operating condition and all the data presented throughout the study represent the average of 100 engine cycles.

Fig.5.4 shows the in-cylinder pressure history of the port fuel injected hydrogen combustion with different air-excess ratios. For λ_{preset} = 3.0, in-cylinder pressure during onset of spark discharge at (Ig.T. =) 20^{o}BTDC with 50% throttle was 1.03 MPa, whereas it was 2.2 MPa for Ig.T. = 15^{o}BTDC with a throttle opening of 100%, which produced peak combustion pressure of ~4.5 MPa. The durability and functionality of the optical fibre and sapphire window assembly was not affected adversely by this harsh environment, although the pressure variation had a significant effect on emission intensities, as shown in Fig.5.5.

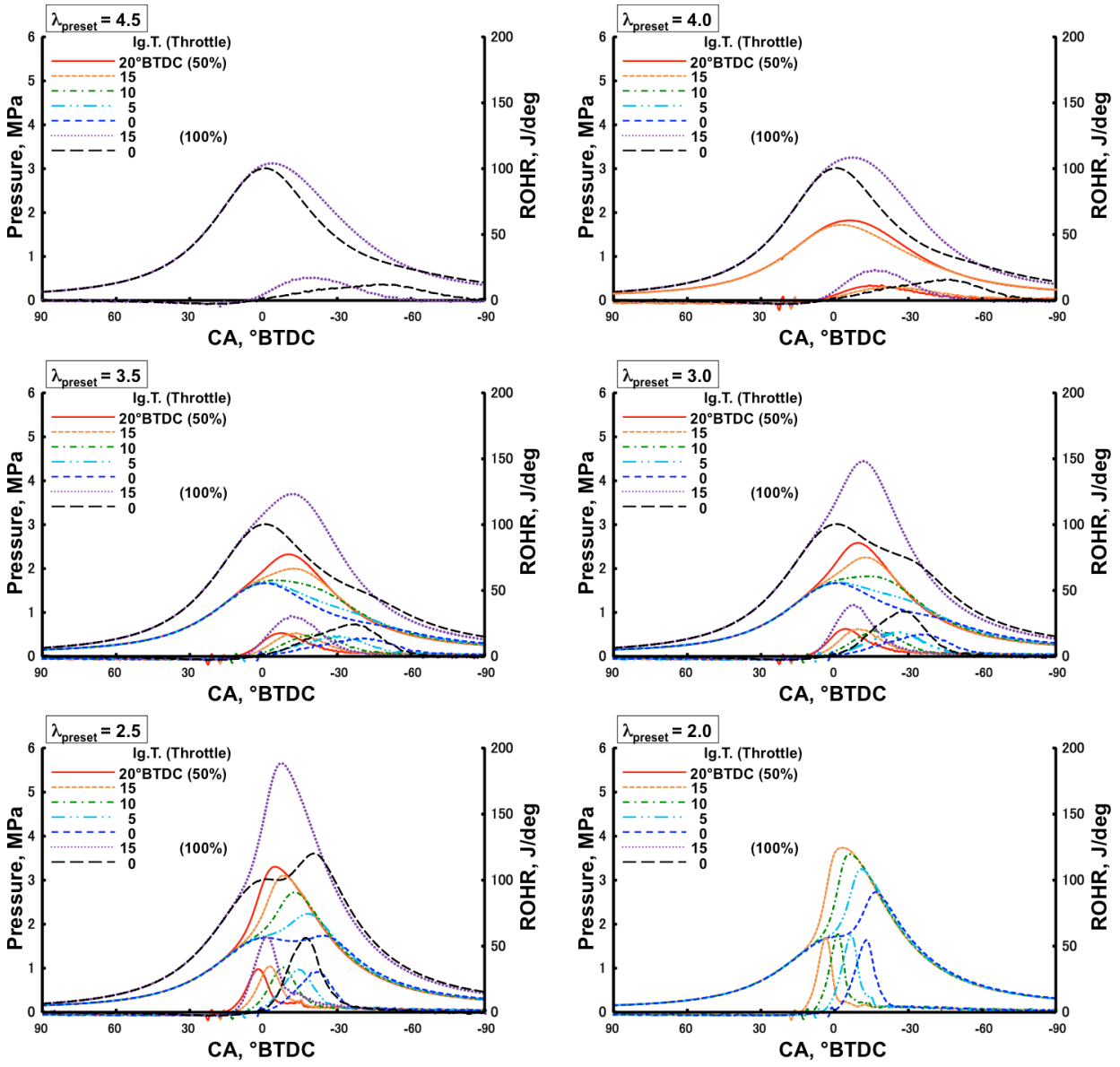

Fig.5.4 In-cylinder pressure history for PCC combustion with different air-excess ratio and throttle opening

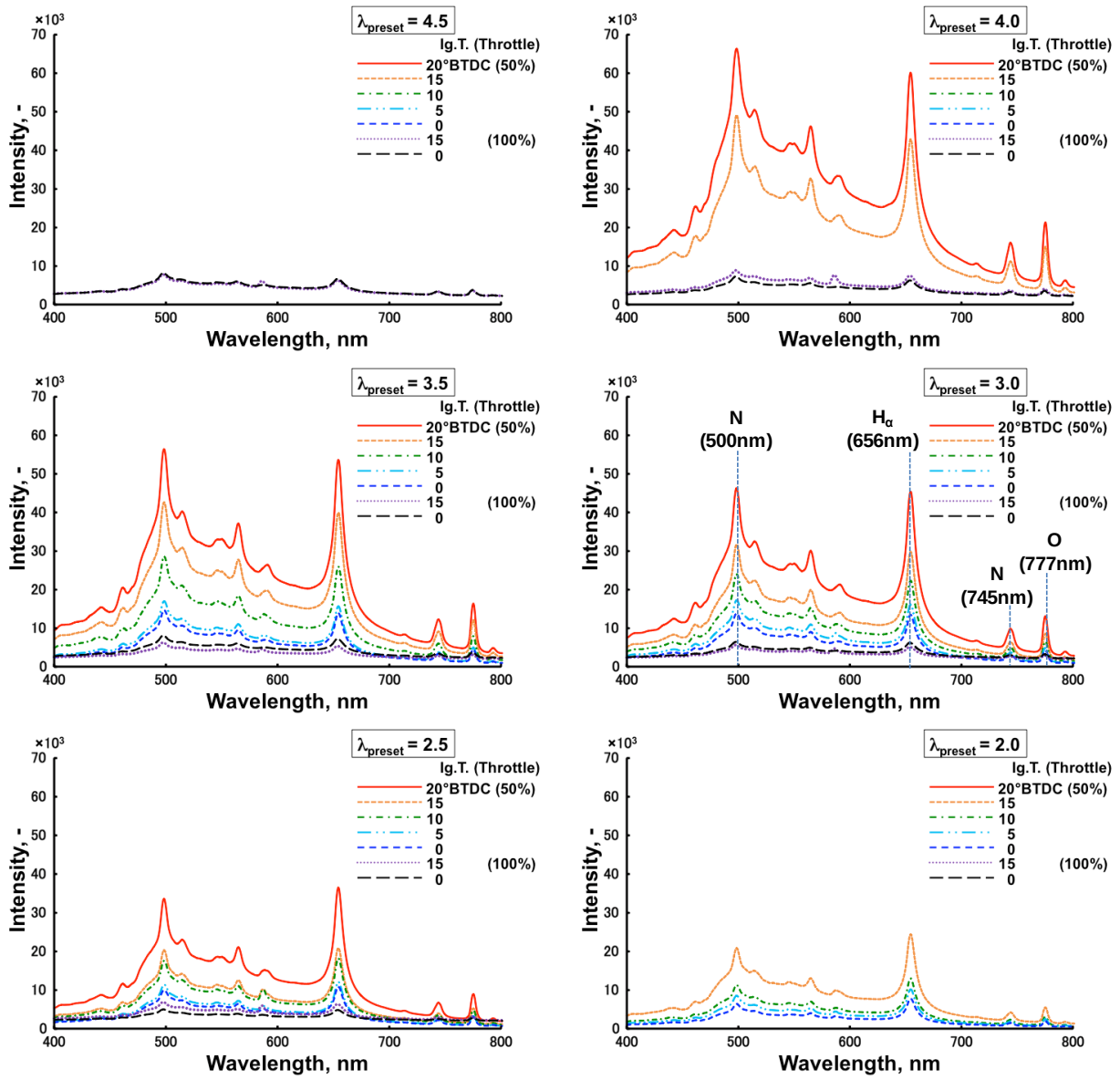

Fig.5.5 Spark emission spectra for PCC combustion with different air-excess ratio and throttle opening

Here, the integration time or the gate width of the spectrometer was 150 ms with no gate delay with respect to the onset of spark discharge. In Fig.5.5, the atomic emission lines of Ha at 656 nm, O(I) at 777 nm, N(I) at 501 nm and at 745 nm were clearly recorded. The intensity of the H_{α} line was due to electronically excited hydrogen dissociated from the fuel (H_2) molecules, while the emissions of N(I) and O(I) lines were obtained from electronically excited nitrogen and oxygen, respectively, dissociated from air. It can be seen in Fig.5.5 that retarded spark timing (i.e. higher ambient pressure at ignition timing) resulted in decreased signal intensities (i.e. line emissions), as well as weaker background emissions (i.e. plasma or arc emission). This indicates that variations in ambient pressure inside the engine cylinder during different sparks lead to variation in spark discharge behaviour and plasma formation.

Fig.5.6 shows the effect of ambient pressure during spark initiation on background-corrected atomic emission intensities of H_{α}, N(I), and O(I). Here, background was subtracted from the raw spectra following the method as previously mentioned in Chapter-4, section 4.3.4 to obtain the background-corrected intensities for H_{α}, N(I), and O(I) emission lines. From Fig.5.5, it can be observed that the intensity of background emission was considerably higher underneath the atomic emission of N(I) at 501 nm compared to that of N(I) at 745 nm which will lead to greater inaccuracy when calculating background corrected peak intensity. Besides; N(I) at 745 nm was considered to be free of interference from other nearby emissions unlike N(I) at 501 nm. As a consequence, for atomic emission intensity of nitrogen N(I), emission line at 745 nm was chosen for further analysis throughout the study. Significant effect of in-cylinder pressure at ignition timing could be observed on the atomic

emissions of H_α, N(I), and O(I) as demonstrated in Fig.5.6. Especially, the spectral line intensity of H_α (656 nm) decreased more rapidly with pressure compared to N (745 nm) and O (777 nm), indicating H_α has greater degree of pressure dependency compared to others. It is known that with higher pressure and density of atoms or molecules, interactions between atoms or molecules increase, which produces a higher collision probability and intensified collisions. The decay time of atoms becomes shorter when excited atoms collide with and are knocked down from excited levels by other atoms before radiating spontaneously. A decrease in the decay time of the atoms or the molecules and higher collision probability reduce the line intensities and broaden the line widths.

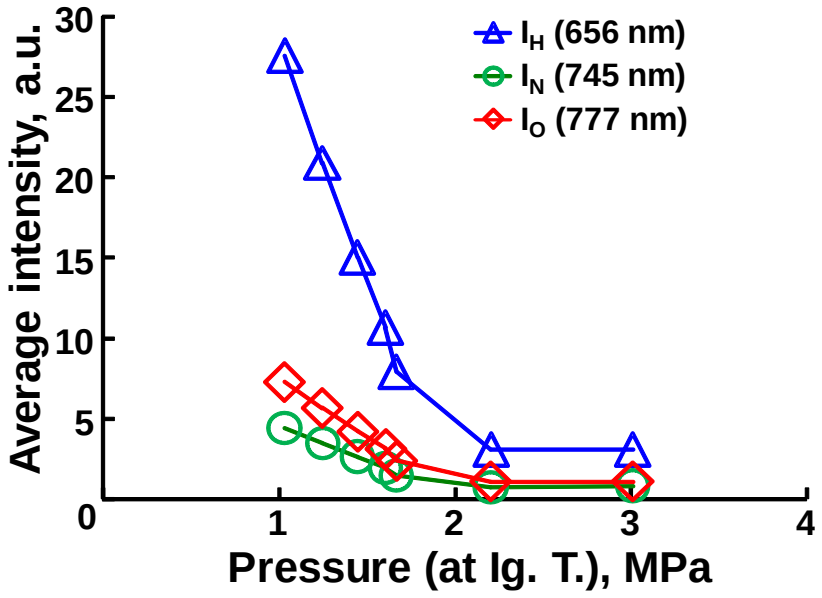

Fig.5.6 Variation in atomic emission intensities of H_α, N(I) and O(I) with in-cylinder ambient pressure at spark timing, λ_{preset} = 3.0

Fig.5.7 shows the correlation of the air excess ratio with background-corrected atomic emission intensity ratio (also known as a calibration curve) as a function of pressure at different ignition timings with different throttle openings (50% and 100%) over a range of preset or overall air excess ratios (i.e. overall relative air/fuel ratio) varying from λ_{preset} =2.0 to λ_{preset} = 4.0. A linear relationship was demonstrated between the air excess ratio and the intensity ratio for both I_H/I_N and I_H/I_O over all pressure values. In Fig.5.7(a) the black thick line, which is a linear regression line for all the data sets, represents the correlation of air excess ratio with intensity ratio of H/N, regardless of the pressure dependency of the atomic emission. The standard deviation of the mean value of intensity ratios were calculated and all the values of standard deviation found to lie within σ = 0.5967. Higher intensity ratios for both I_H/I_N and I_H/I_O could be observed with a lower air excess ratio, as the electronically excited hydrogen dissociated from the fuel (H_2) molecules increased with higher fuel concentration. Fig.5.7 shows that the calibration lines became steeper (i.e. absolute slopes became greater) when the pressure at spark discharge increased and also effect of pressure on atomic emission was less pronounced as the mixture became leaner (i.e. when air excess ratio was increasing). A comparison between Fig.5.7 (a) and (b) reveals that the pressure dependence characteristics of I_H/I_N differ from those of I_H/I_O. Absolute slope or gradient of each calibration line was calculated and plotted against the pressure at ignition timing, as shown in Fig.5.8. An increasing trend in absolute slope with pressure, P_{ig} at ignition timing was observed though this pressure effect or the pressure dependency of spectral line intensity was found to be less significant at comparatively higher pressure (P_{ig} beyond 2 MPa). Here the absolute slopes of calibration lines for I_H/I_O showed greater values than that

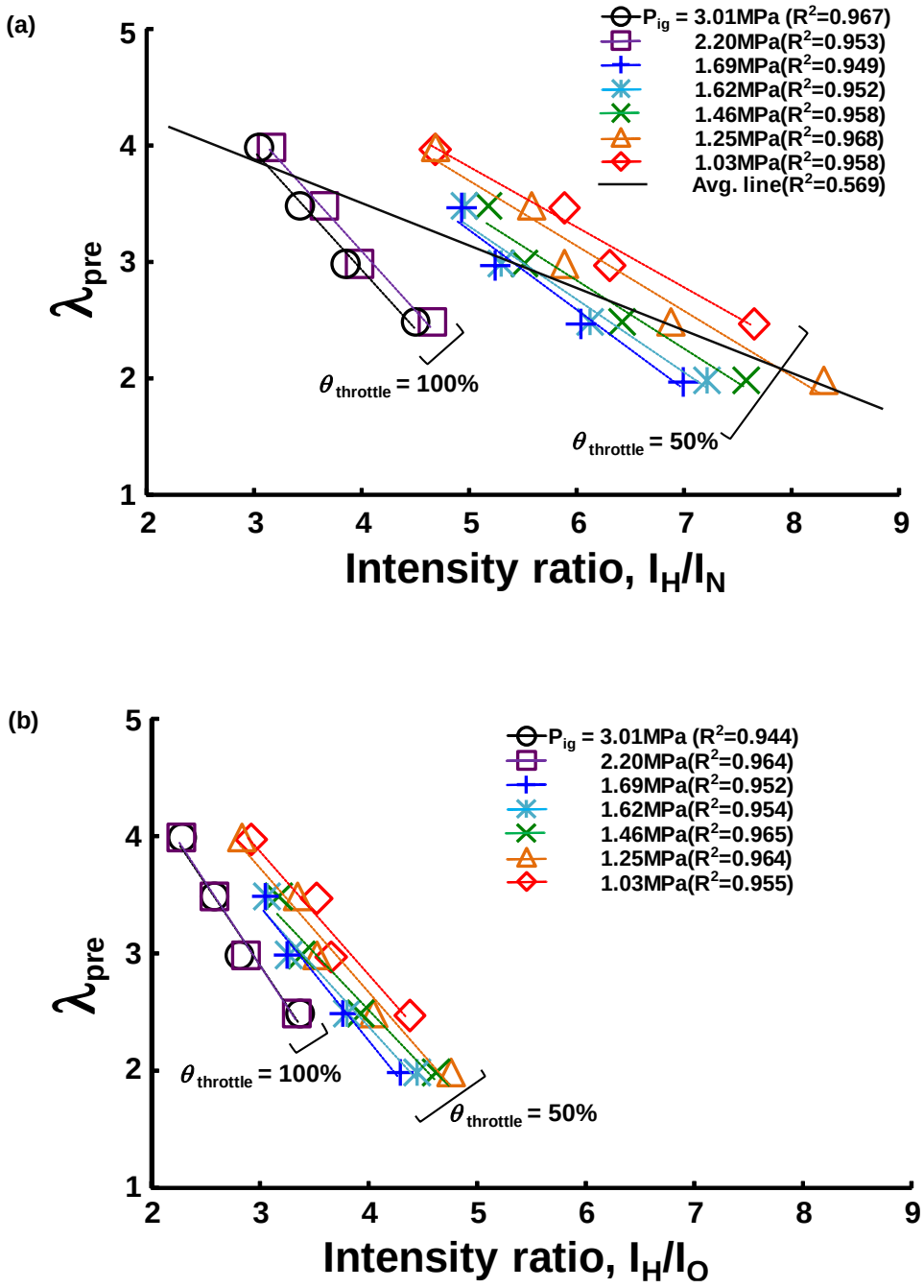

Fig.5.7 Correlation of the air excess ratio with atomic intensity ratio (a) of H_α to N, (b) with that of the H_α to O for different in-cylinder ambient pressure at spark timing

for I_H/I_N which imply that, for a fixed value of pressure, P_{ig} or ignition timing a small difference in measured intensity ratio of I_H/I_O will produce a comparatively large deviation between local air excess ratio (λ_{local}) and preset or overall air excess ratio (λ_{preset}). Therefore, only the correlation between the air excess ratio λ_{preset} with intensity ratio of I_H/I_N was considered as the calibration line for measuring the local fuel concentration in hydrogen direct injection case.

In the previous sections, a significant effect of pressure at ignition timing was observed on spark-induced breakdown spectroscopic measurements and emission line characteristics under port injection conditions. Retarded spark timing (i.e. higher ambient pressure at the ignition site) resulted in lower spectral line intensities as well as weaker background emissions. These results are consistent with those from the literature (e.g. Phuoc [10] and Zhang et al. [11]). As reported in the literature, at relatively higher pressures the expanding plasma is cooled quickly by the surrounding gas through enhanced collisional processes, leading to both a weak broadband continuum and spectral line intensities.

A calibration map which represents the correlation of air excess ratio with both intensity ratio and pressure at ignition timing was developed as shown in Fig.5.9, by taking into account the pressure dependency of spectral line intensity. This calibration map and calibration line (i.e. the black thick line in Fig.5.7 (a), that did not consider the effect of pressure at ignition timing on atomic emissions) were used for SIBS measurements.

Fig.5.10 shows a comparison of mean local air excess ratio measured with the use of the calibration map (Fig.5.9) with that measured using the calibration line (black thick line in

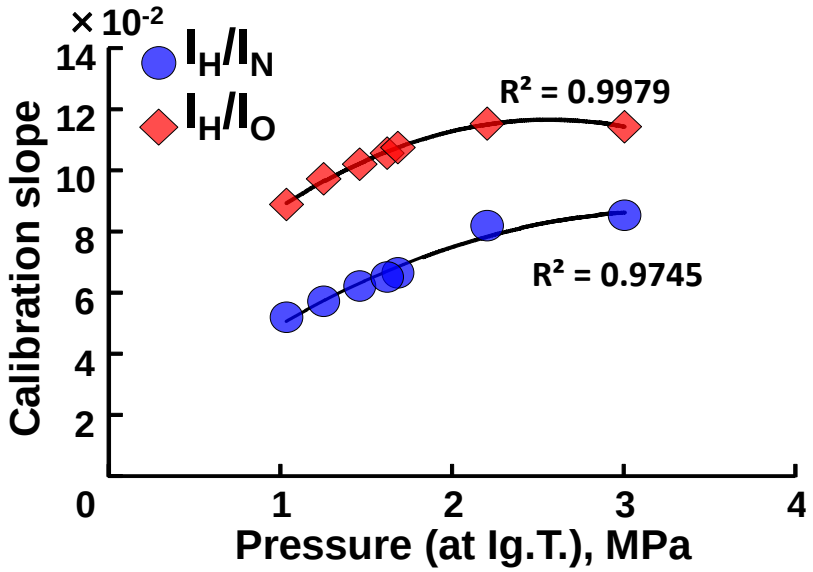

Fig.5.8 Effect of pressures at ignition timing on slope of the calibration lines

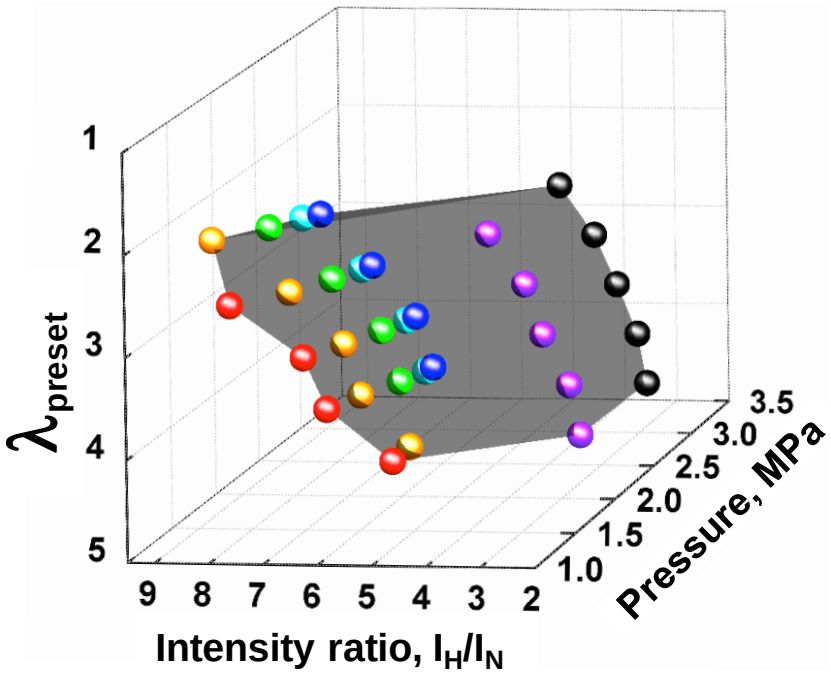

Fig.5.9 Calibration map or correlation of air excess ratio with intensity ratio and pressure at ignition timing

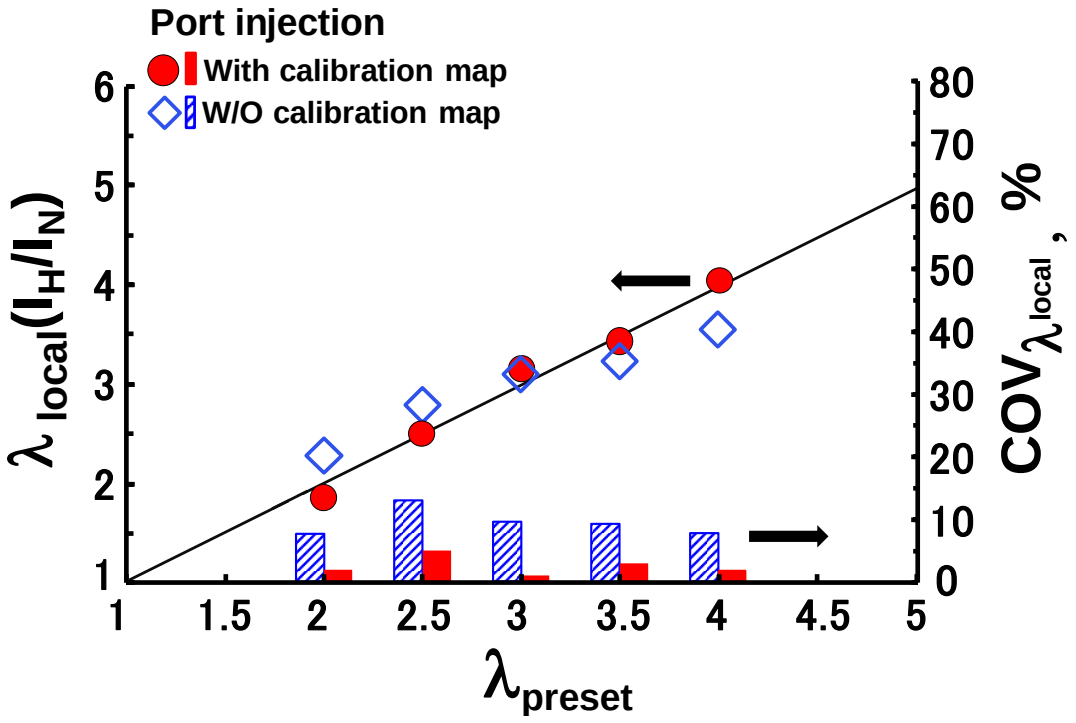

Fig.5.10 Improvement in accuracy of SIBS measurement through the use of calibration map under port injection condition

Fig.5.7 (a)) under port injection conditions. Here, for a fixed/ preset air excess ratio, local air excess ratios were measured for different spark or ignition timing, varying from 20^0 to 0^0 BTDC along with different throttle openings (50% and 100%) over a range of air excess ratios from 2.0 to 4.0 and mean local air excess ratios were plotted against the preset value (λ_{preset}) in the figure. Although for a fixed ignition timing, the SIBS measurements made with calibration line produced completely different λ_{local} from fixed/preset air excess ratio but averaging the values over ignition pressures P_{ig} (i.e. mean λ_{local} for Ig.T. = 20^0 - 0^0 BTDC) diminished this difference remarkably. Despite, it can be clearly observed from Fig.5.10 that the deviation in λ_{local} from fixed/preset air excess ratio (λ_{preset}) was comparatively large for

measurement made without using calibration map whereas λ_{local} obtained with calibration map leads to higher degree of closeness of local air excess ratios to the preset air excess ratios (true values). Furthermore, the coefficient of variation in local air excess ratio (COV $_{\lambda local}$) was significantly smaller for measurements made with the calibration map. For example, in the case of λ_{preset} = 3.0, the COV $_{\lambda local}$ for measurements made with the calibration map was ~1% whereas this increased to ~10% for data obtained using calibration line. This indicates that the quantitative measurement of fuel concentration through SIBS technique is strongly dependent on the strategy to generate calibration curve and the measurement accuracy can be improved significantly when the pressure dependency of atomic emissions is taken into account.

5.3.4 Local air excess ratio measurement for hydrogen direct-injection

Quantitative measurements of fuel concentration around the spark gap location at the time of ignition in a jet-guided direct-injection hydrogen research engine were conducted for both PI and DI strategies using the same spark plug sensor. The experiments were performed with different air excess ratio varying from 2.5 to 4.5; and to achieve an axially stratified charge, the start of injection (SOI) was varied from120^0 BTDC to 35^0 BTDC while MBT (minimum advance for best torque) timing was considered as an ignition strategy. The in-cylinder pressure history and rate of heat release (ROHR) for hydrogen combustion (PCC) with varying air excess ratio and different injection timing are shown in Fig.5.11. Here, it is

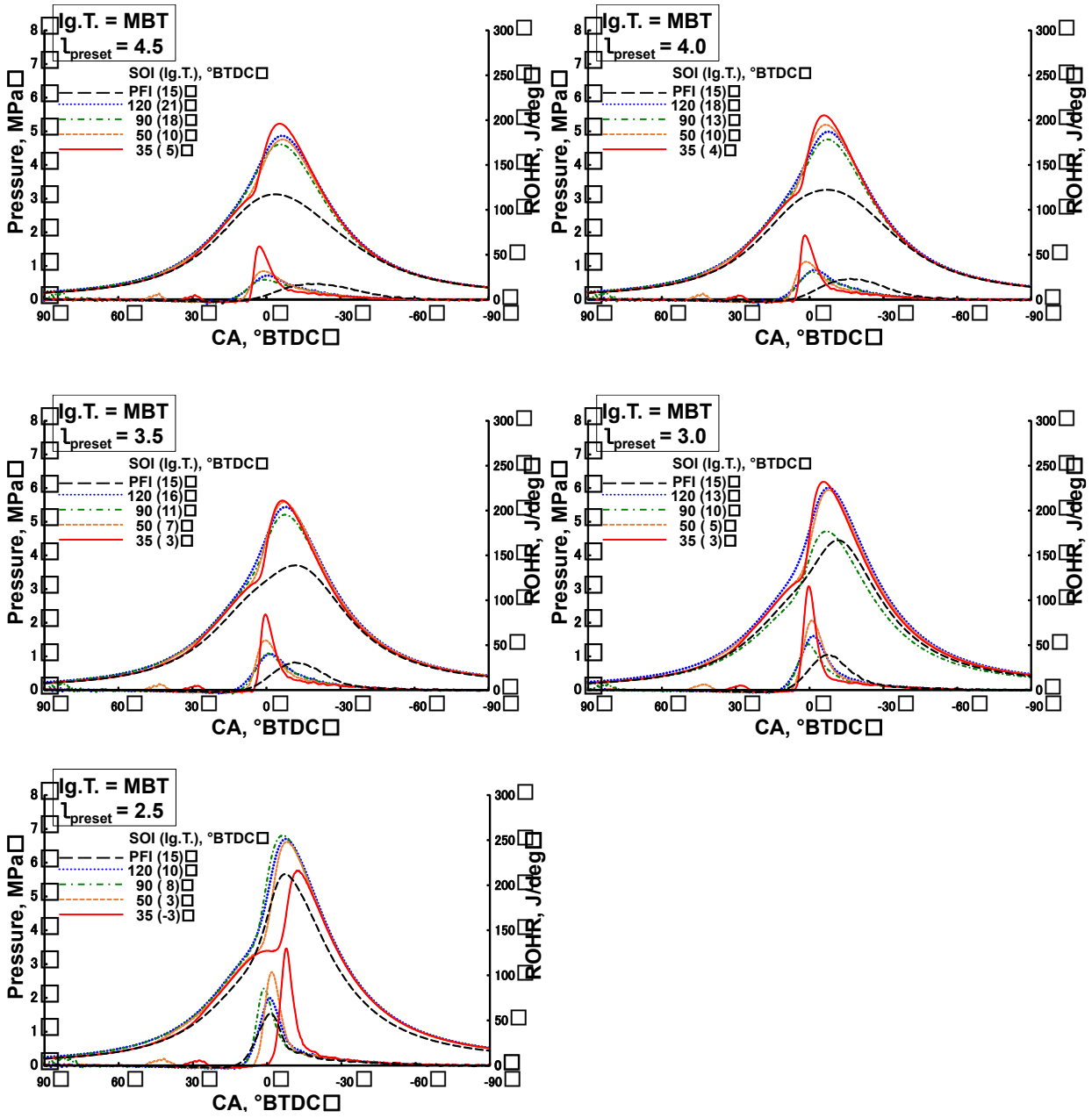

Fig.5.11 In-cylinder pressure history and rate of heat release (ROHR) with varying injection timing and air excess ratio

evident that in-cylinder combustion pressure and heat release rate rise rapidly with retarded injection timing.

This may be attributed to the fact that with direct injection condition the mixture became locally fuel-rich and the degree of richness increased with delayed start of injection leading to rapid burning of the mixture. It can be seen in Fig.5.12 that retarded SOI (i.e. higher degree of fuel stratification) resulted in greater signal intensities (i.e. line emissions), as well as strong background emissions (i.e. plasma or arc emission). This indicates that variations in fuel concentration inside the engine cylinder lead to variation in spark discharge behaviour and plasma formation. To confirm this local stratification of the fuel mixture during ignition timing, SIBS measurements were carried out and the local air excess ratios was plotted against varying injection timing (Fig.5.13). With retarded injection timing, i.e. when the SOI was delayed from 120^0 BTDC to 35^0 BTDC, the mixture in the vicinity of the spark gap location became successively richer during spark timing at MBT. This phenomenon is evident in both Fig.5.13 (a) and (b) because the local air excess ratio (λ_{local}) decreased gradually with retarded SOI. However, direct injection (DI) conditions generated a higher local air excess ratio (λ_{local}) compared with port injection (PI) conditions when the pressure dependency of the spectral emissions was ignored (Fig.5.13 (a)). This measurement inaccuracy can be eliminated by taking into account the effect of ambient pressure on atomic emission intensity, as shown in Fig.5.13 (b). Fig.5.14 (a) shows the results for local air excess ratios obtained without considering the pressure dependency of atomic emissions, whereas Fig.5.14 (b) shows the results obtained using the calibration map. It can be seen from Fig.5.14 (a) that the mixture at the spark gap

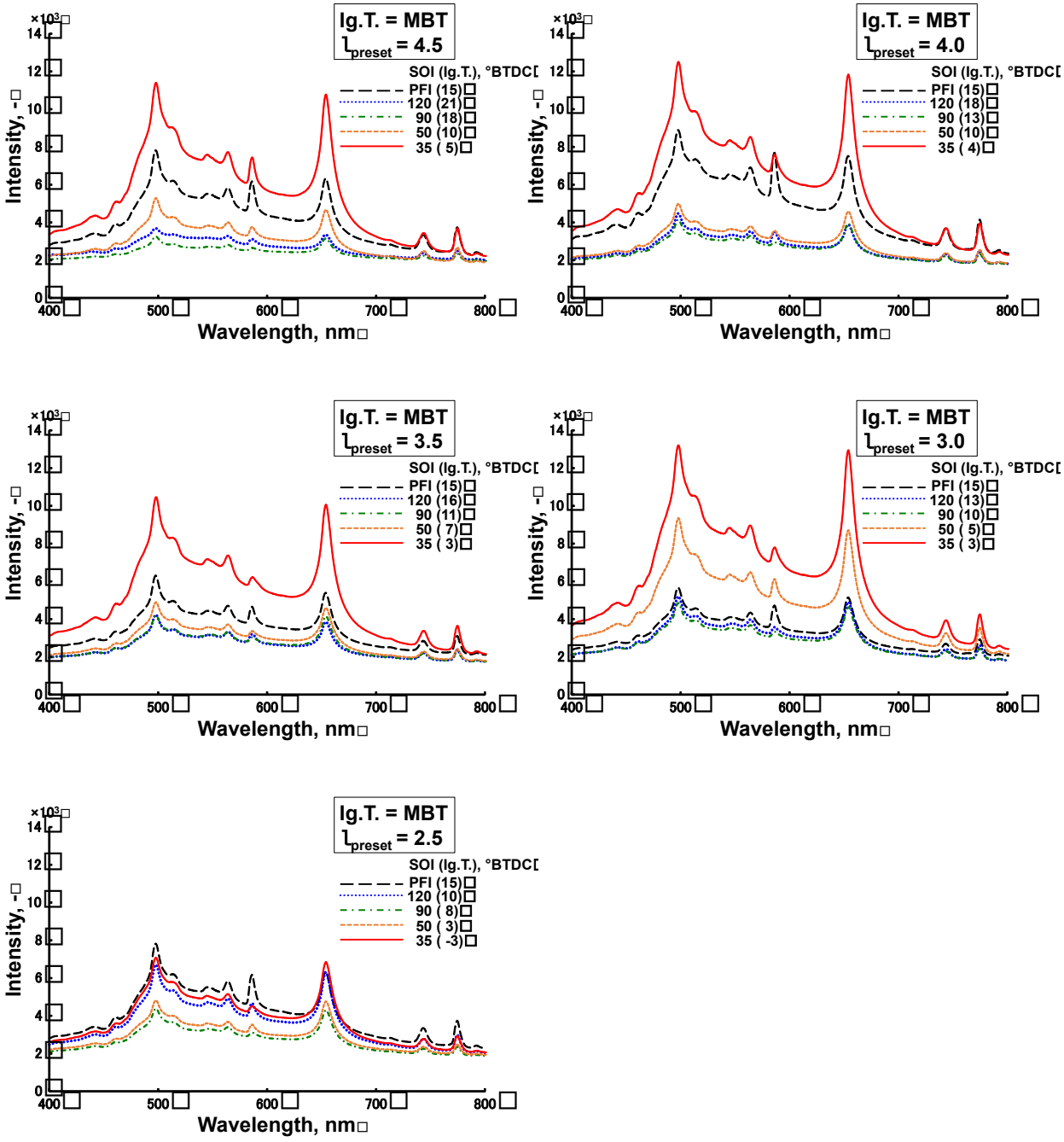

Fig.5.12 Spark emission spectra for PCC combustion with varying air-excess ratio and different start of injection

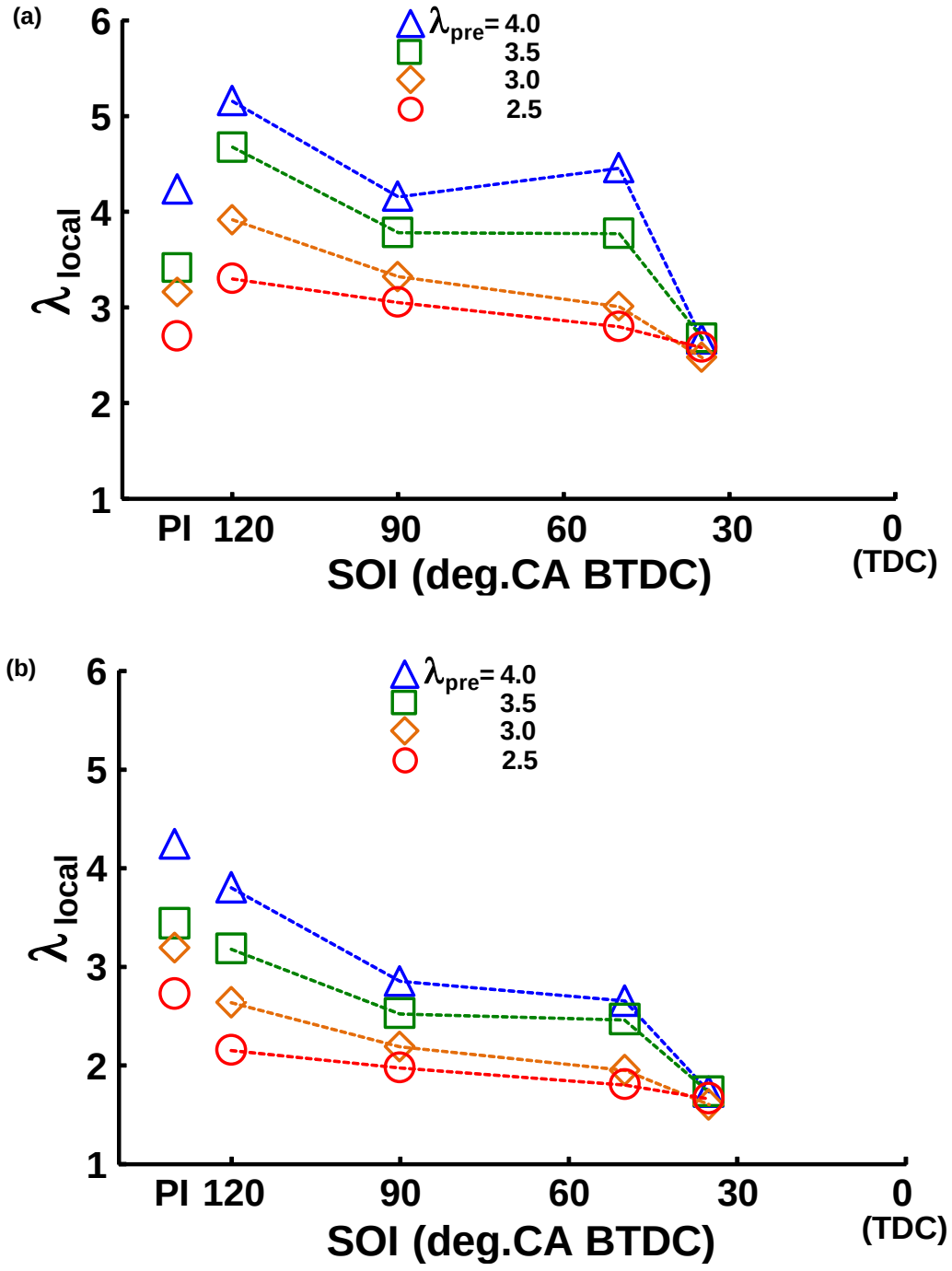

Fig.5.13 Variation of local air excess ratio (λ_{local}) with injection timing; (a) without considering pressure dependency, (b) SIBS measurements through calibration map

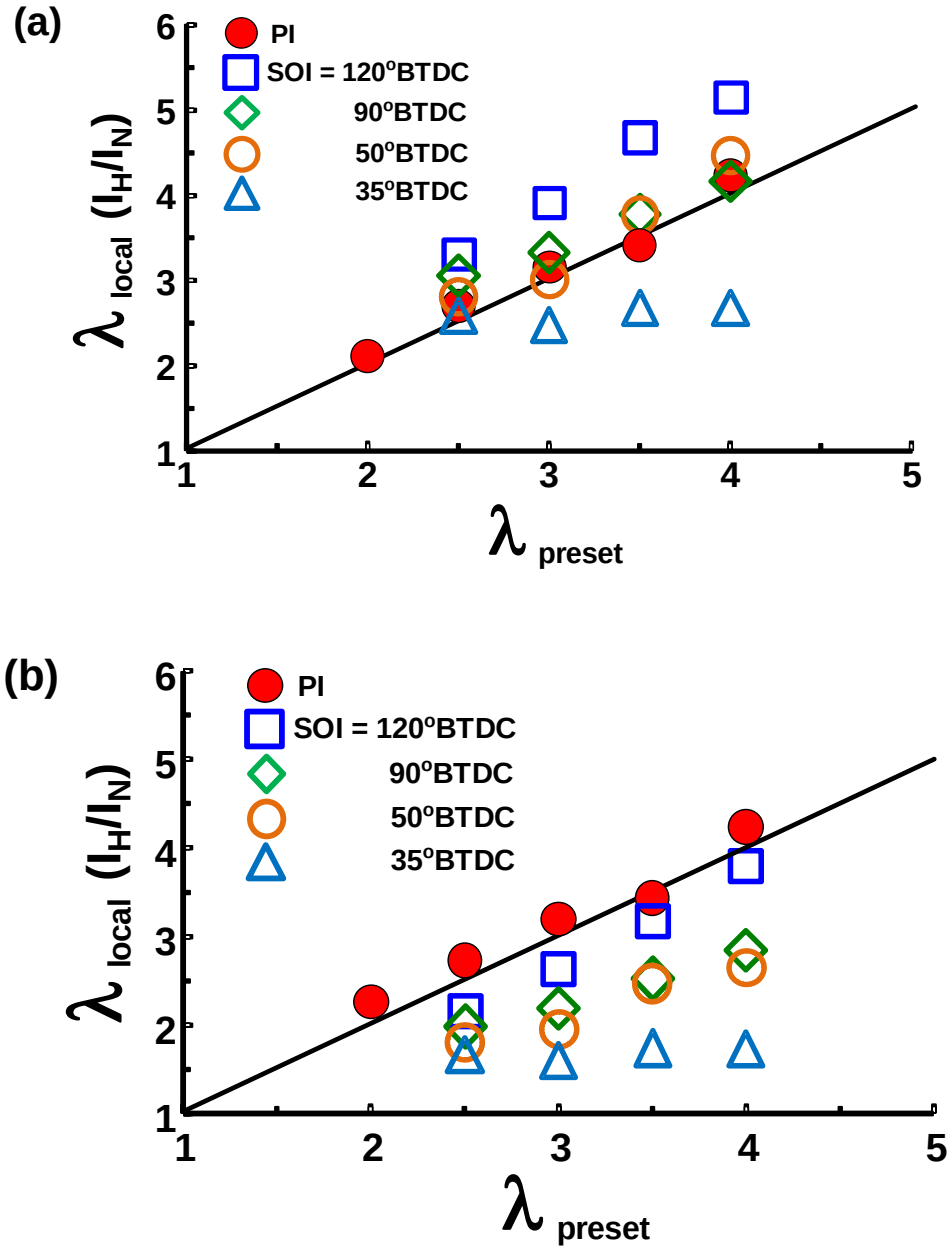

Fig.5.14 Effect of pressure dependency of spectral emission on SIBS measurements of local air excess ratio with different injection strategies

seems to be comparatively leaner for the direct injection strategy with SOI = 120^0 - 50^0 BTDC compared with that for PI conditions. This is quite unlikely and impractical because local air excess ratio (λ_{local}) around the spark gap region for the jet-guided stratified operation of the engine should be lower (as the mixture was stratified and became locally rich) than the local air excess ratio (λ_{local}) for port injection conditions. This discrepancy demonstrates that ignoring the pressure dependency of atomic emissions i.e. measurements made through average calibration line (the black thick line in Fig.5.7 (a)), the value of local air excess ratio (λ_{local}) would be greater than the actual. In Fig.5.14 (b), local air excess ratio (λ_{local}) for direct injection condition found to be lower than that for PI for all the values of preset air-excess ratios, λ_{preset} , indicating formation of a richer mixture around the spark gap region with the jet-guided stratified operation. This result is consistent and indicates improvement in measurement accuracy due to taking into account the effects of in-cylinder ambient pressure at ignition timing on the spectral line emissions.

5.4 Summary

Quantitative measurements of fuel concentration were conducted for the first time in a direct-injection hydrogen spark-ignition research engine through spark-induced breakdown spectroscopy (SIBS) technique. A new sensor with an optical fibre housed in the centre electrode of the spark plug was developed from a commercially available M12-type spark plug with no major modification to the electrodes, leading to stable spark formation. The main focus of this study was to characterise the effects of ambient pressure at ignition timing on atomic emissions and to improve the accuracy of the SIBS measurements by taking into

account the pressure dependency of atomic emissions. Summarising the results, the following conclusions can be drawn:

1. The newly developed fibre optic spark plug sensor was used successfully in a DISI research engine. The plug sensor had better durability and required less maintenance when applied to hydrogen combustion.

2. A linear relationship (calibration line) was demonstrated between air excess ratio and intensity ratio for both IH/IN and IH/IO over all pressure values. A significant effect of the corresponding pressure at ignition timing was observed on SIBS measurements and emission line characteristics. Retarded spark timing (i.e. higher ambient pressure at the ignition site), resulted in lower spectral line intensities as well as weaker background emissions. This indicates the variation in spark discharge behaviour and plasma formation with variation in ambient pressure inside the engine cylinder during spark timing variation. At relatively higher pressures, cooling process of the expanding plasma was quicker due to collisional processes with the surrounding gas, leading to both a weaker broadband continuum and atomic emissions.

3. A calibration map, representing the correlation of air excess ratio with both intensity ratio and pressure at ignition timing, was developed by taking into account the effect of the corresponding pressure at ignition timing on spectral line intensity for quantitative measurements of local air excess ratio in a research engine. Local stratification of the fuel mixture in the vicinity of the spark gap location associated with direct injection was confirmed through SIBS measurements using newly developed spark plug sensor. The COV of local air excess ratio was considerably smaller for measurements made through the

calibration map. This indicates that the accuracy of measurements of local air excess ratio through SIBS technique can be improved significantly when the pressure dependency of atomic emissions is taken into account.

REFERENCE

[1] R.M. Merer, J.S. Wallace, Spark Spectroscopy for Spark Ignition Engine Diagnostics. SAE Paper No. 950164. 1995.

[2] K. Kuwahara, H. Ando, Diagnostics of in-cylinder flow, mixing and combustion in gasoline engines. Meas. Sci. Technol. 2000;11:95-111.

[3] T.D. Fansler, B. Stojkovic, M.C. Drake, M.E. Rosalik, Local fuel concentration measurements in internal combustion engines using spark-emission spectroscopy. Appl. Phys., B Laser Opt. 2002;75(4):577-590.

[4] N. Kawahara, E. Tomita, S. Takemoto, Y. Ikeda. Fuel concentration measurement of premixed mixture using spark-induced breakdown spectroscopy. Spectro Acta Part B 2009;64(10):1085-1092

[5] Roy MK, Nobuyuki K, Tomita E, Fujitani T. Jet-guided combustion characteristics and local fuel concentration measurements in a hydrogen direct-injection spark-ignition engine. Proc Combust Inst 2013;34:2977-84.

[6] Abdul Rahman MT, Kawahara N, Tsuboi K, Tomita E. Visualization and concentration measurement of a direct injection hydrogen jet in a constant-volume vessel using spark-induced breakdown spectroscopy. Int J Hydrogen Energy 2014;39(31):17896-17905.

[7] Abdul Rahman MT, Kawahara N, Tsuboi K, Tomita E. Effect of ambient pressure on local concentration measurement of transient hydrogen jet in a constant-volume vessel using spark-induced breakdown spectroscopy. Int J Hydrogen Energy 2015;40(13):4717-4725.

[8] Oikawa M, Ogasawara Y, Kondo Y, Sekine K, Takagi Y, Sato Y. Optimization of hydrogen jet configuration by single hole nozzle and high speed laser shadowgraphy in high pressure direct injection hydrogen engines. Int J Automot Eng 2012;3:1-8.

[9] Yamane K, Nogami M, Umemura Y, Oikawa M. Development of high pressure H2 gas injectors, capable of injection at large injection rate and high response using a common-rail type actuating system for a 4-cylinder, 4.7-liter total displacement, spark ignition hydrogen engine. 2011. SAE Paper No. 2011-01-2005.

[10] Phuoc TX. Laser-induced spark for simultaneous ignition and fuel-to-air ratio measurements. Opt Lasers Eng 2006;44(6):520e34.

[11] Zhang S, Yu X, Li F, Kang G, Chen L, Zhang X. Laser induced breakdown spectroscopy for local equivalence ratio measurement of kerosene/air mixture at elevated pressure. Opt Lasers Eng 2012;50(6):877-82.

CHAPTER: 6

CFD Modeling of Mixture Formation Process in Hydrogen IC Engine

6.1 Introduction

For the past few decades, in addition to experimental investigations, Computational Fluid Dynamics (CFD) has become an essential tool to gain a better knowledge about the mixture formation and combustion processes inside the engine cylinder. CFD is developed and employed in many fields of internal combustion engine application and offers successful assessment of new technologies, e. g. new combustion concepts, and/or alternative fuels. With the recent advancement in computer processors and expansion of allowable memory, researchers are now able to integrate detailed chemical kinetics with a computational fluid dynamics (CFD) code to simulate IC engines. Many statistical studies have focused on using three-dimensional computational fluid dynamics (CFD) tools to understand the in-cylinder flow field and mixing process [1-10]. Rakopoulos et al. [1,4-5] have recently developed combustion model for simulation of a hydrogen spark-ignition engine. They have investigated the combustion processes inside cylinder, especially with varying equivalence ratios. Kosmadakis et al. [6] have reported reduction in exhaust nitrogen oxides emissions through variation of EGR rates using the same model. However, only a few investigations may be found in the literature that carried out simulation of hydrogen engines, specially mixture formation process.

For internal combustion (IC) engines, in-cylinder reacting flows are compressible and highly turbulent. In order to modeling the in-cylinder mixture formation process and hydrogen combustion, ANSYS FORTE CFD that is specially designed for internal combustion engine applications, was employed in the current study. This code is based on the Reynolds Averaged Navier-Stokes (RANS) equations and primary governing equations are the conservation of mass, momentum, and energy. The ANSYS Forte CFD Package introduces important breakthroughs in chemistry-solution techniques that greatly enhance the accuracy achievable by engine simulation within commercial design time lines. Detailed chemical kinetic reactions for hydrogen oxidation were considered in the code. These techniques reduce simulation time by as much as two orders of magnitude when compared to conventional CFD. Chemistry models that were previously thought of as only practical for 0-D simulations now become practical for full 3-D engine simulations with moving pistons and valves. Better handling of chemistry with multi-component fuel representation makes predictive simulation possible within the schedule constraints of the concept phase of design. ANSYS Forte builds on models and sub-models that have been well validated against experimental data over a broad range of conditions and over many years by engine-simulation experts.

6.2 Conservation Equations for Turbulent Reacting Flows

6.2.1 Species Conservation Equation

In ANSYS Forte's turbulent reacting flow representation, the basic fluid dynamics are governed by the Navier-Stokes equations. Model transport equations represent the

turbulent nature of the flow. Beyond these models, the main assumptions made in the derivation of the governing equations are the use of the ideal gas law for the gas-phase equation of state, the use of Fick's law for mass diffusion, and the use of Fourier's law for thermal diffusion. For a high diffusible gas like hydrogen which mixes faster with air at the molecular level than conventional fuels, the question arises whether preferential diffusion of hydrogen should be introduced into the CFD model for hydrogen/air mixture formation simulation. Colin [11] carried out a study to preferential diffusion modelling for RANS mixture formation simulations in hydrogen combustion engines. He concluded that for relatively high turbulent Reynolds numbers ($Re_t >> 1$), as occur in internal combustion engines, preferential diffusion effects can be neglected in comparison to turbulent fluxes. Regarding mean species diffusion fluxes, turbulent diffusion largely exceeds molecular diffusion, so that preferential diffusion effects do not have to be taken into account in the investigation of mixture formation.

The aim of the turbulent combustion modeling approach is to remove the necessity of resolving all the smallest structures and fluctuations associated with turbulence, while retaining the main effects of turbulence on the flow and combustion characteristics. To accomplish this, the Favre average is employed to represent an instantaneous quantity, such as the flow velocity vector **u**, into an average **ũ** and a fluctuating part **ű** as **u = ũ + ű**. In this approach, the average **ũ** part is defined as a conventional average by $\tilde{\mathbf{u}} = \overline{\boldsymbol{\rho}\mathbf{u}} / \overline{\boldsymbol{\rho}}$ while the fluctuation **ű** is defined to satisfy $\overline{\boldsymbol{\rho}\ddot{\boldsymbol{u}}} = \mathbf{0}$, where the over-bar represents an averaging operator. The governing equations in ANSYS Forte all follow this convention.

The ***conservation equation*** for species *k* is:

$$\frac{\partial \bar{\rho}_k}{\partial t} + \nabla \cdot (\bar{\rho}_k \tilde{\boldsymbol{u}}) = \nabla \cdot \left[\bar{\rho} D_T \nabla \left(\frac{\bar{\rho}_k}{\bar{\rho}}\right)\right] + \dot{\bar{\rho}}_k^{\,c} + \dot{\bar{\rho}}_k^{\,s} \quad (k = 1, \ldots\ldots K), \tag{6.1}$$

where $\boldsymbol{\rho}$ is the density, subscript $\boldsymbol{k}$ is the species index, $\boldsymbol{K}$ is the total number of species, **u** is the flow velocity vector. Application of Fick's Law of diffusion results in a mixture averaged turbulent diffusion coefficient$\boldsymbol{D_T}$, $\dot{\bar{\boldsymbol{\rho}}}_{\boldsymbol{k}}^{\,\boldsymbol{c}}$ and $\dot{\bar{\boldsymbol{\rho}}}_{\boldsymbol{k}}^{\,\boldsymbol{s}}$ are source terms due to chemical reactions and spray evaporation, respectively.

6.2.2 Fluid Continuity Equation

The summation of Equation 6.2 over all species gives the ***continuity equation*** for the total fluid:

$$\frac{\partial \bar{\rho}}{\partial t} + \nabla \cdot (\bar{\rho} \tilde{\boldsymbol{u}}) = \dot{\bar{\rho}}^{s} \tag{6.2}$$

6.2.3 Momentum Conservation Equation

The ***momentum equation*** for the fluid is

$$\frac{\partial \bar{\rho} \tilde{\boldsymbol{u}}}{\partial t} + \nabla \cdot (\bar{\rho} \tilde{\boldsymbol{u}} \tilde{\boldsymbol{u}}) = -\nabla \bar{p} + \nabla \cdot \bar{\sigma} - \frac{2}{3} \bar{\rho} \tilde{k} I + \bar{F}^{s} + \overline{\rho \mathrm{g}}, \tag{6.3}$$

where $\boldsymbol{p}$ is the pressure, **I** is the identity tensor, $\bar{\boldsymbol{F}}^{\boldsymbol{s}}$ is the rate of momentum gain per unit volume due to the spray, **g** is the specific body force.

$\bar{\boldsymbol{\sigma}}$ is molecular momentum transport due to the total viscous stress tensor (laminar plus turbulent) given by

$$\bar{\sigma} = (\mu + \mu_T)[\nabla\tilde{\boldsymbol{u}} + \nabla\tilde{\boldsymbol{u}}^{\boldsymbol{T}} - \tfrac{2}{3}(\nabla \cdot \tilde{\boldsymbol{u}})I], \tag{6.4}$$

μ is the laminar dynamic viscosity, $\boldsymbol{\mu_T}$ is the turbulent dynamic viscosity, superscript **T** means vector transpose, $\widetilde{\boldsymbol{k}}$ is the turbulent kinetic energy, defined by

$$\tilde{k} = \frac{\mathbf{1}}{\mathbf{2}}\widetilde{\mathbf{\acute{u}} \cdot \mathbf{\acute{u}}}, \tag{6.5}$$

The turbulent dynamic viscosity $\boldsymbol{\mu_T}$ is related to the turbulent kinetic energy $\widetilde{\boldsymbol{k}}$ and its dissipation rate $\boldsymbol{\varepsilon}$ by

$$\mu_T = c_\mu \bar{\rho}\frac{\tilde{k}^2}{\tilde{\varepsilon}}, \tag{6.6}$$

where $\boldsymbol{c_\mu}$ is a model constant that varies in different turbulence model formulations. By definition, $\boldsymbol{\mu_T}$ is related to the turbulent thermal diffusivity $\boldsymbol{\alpha_T}$ and mass diffusivity $\boldsymbol{D_T}$ by

$$\alpha_T = \frac{V_T}{Pr_T} = \frac{\mu_T}{\bar{\rho}Pr_T}, \tag{6.7}$$

$$D_T = \frac{V_T}{Sc_T} = \frac{\mu_T}{\bar{\rho}Sc_T}, \tag{6.8}$$

where $\boldsymbol{V_T}$ is the turbulent kinematic viscosity, $\boldsymbol{Pr_T}$ and $\boldsymbol{Sc_T}$ are the turbulent Prandtl and Schmidt numbers, respectively. Based on Equation 6.4, the stress contribution due to turbulence, called the Reynolds stress tensor $\bar{\boldsymbol{\tau}}$, is defined as

$$\bar{\tau} = -\bar{\rho}\widetilde{\acute{\mathbf{u}}\cdot\acute{\mathbf{u}}} = \mu_T[\nabla\tilde{\boldsymbol{u}} + \nabla\tilde{\boldsymbol{u}}^{\boldsymbol{T}} - \tfrac{2}{3}(\nabla\cdot\tilde{\boldsymbol{u}})I] - \tfrac{2}{3}\bar{\rho}\tilde{k}I \quad (6.9)$$

6.2.4 Internal Energy Conservation Equation

The ***internal energy transport equation*** is:

$$\frac{\partial\bar{\rho}\tilde{I}}{\partial t} + \nabla\cdot(\bar{\rho}\tilde{u}\tilde{I}) = -\bar{p}\nabla\cdot\tilde{u} - \nabla\cdot\tilde{J} + \bar{\rho}\tilde{\varepsilon} + \dot{\tilde{Q}}^{c} + \dot{\tilde{Q}}^{s}, \quad (6.10)$$

where $\tilde{\boldsymbol{I}}$ is the specific internal energy, $\tilde{\boldsymbol{I}}$ is the heat flux vector accounting for contributions due to heat conduction and enthalpy diffusion,

$$\tilde{J} = -\lambda\nabla\tilde{T} - \bar{\rho}D_T\sum_k \tilde{h}_k\nabla\left(\frac{\bar{\rho}_k}{\bar{\rho}}\right), \quad (6.11)$$

λ is the turbulent thermal conductivity, $\tilde{\boldsymbol{T}}$ is the fluid temperature, and $\tilde{\boldsymbol{h}}_{\boldsymbol{k}}$ is the specific enthalpy of species *k*. $\dot{\tilde{\boldsymbol{Q}}}^{\boldsymbol{c}}$ and $\dot{\tilde{\boldsymbol{Q}}}^{\boldsymbol{s}}$ are source terms due to chemical heat release and spray interactions, respectively. By definition, $\boldsymbol{\lambda}$ is related to the turbulent thermal diffusivity $\boldsymbol{\alpha_T}$ and heat capacity $\boldsymbol{c_p}$ by

$$\lambda = \bar{\rho}c_p\alpha_T \quad (6.12)$$

6.3 Turbulence modeling

Instead of turbulence modelling in terms of RANS, computation may be performed in terms of Large Eddy Simulation (LES). In this method, the largest structures of the flow field are explicitly computed, and only smallest eddies are modelled. Consequently, a higher

predictability of turbulent quantities is reported for this approach. Due to the increased numerical expense compared to RANS, this modelling technique was not investigated in the present work. Reynolds-Averaged Navier-Stokes (RANS) models decompose the instantaneous flow variables into their steady and fluctuating components. Both advanced RNG (Re-Normalized Group Theory) *k*-ε model and standard *k*-ε model formulations are evaluated and compared. These consider velocity dilatation in the ε-equation and jet-induced source terms for both *k* and ε equations. The standard Favre-averaged equations for *k* and ε are given in equation 6.13 and 6.14:

$$\frac{\partial \bar{\rho}\tilde{k}}{\partial t} + \nabla \cdot \left(\bar{\rho}\tilde{\boldsymbol{u}}\tilde{k}\right) = -\frac{2}{3}\bar{\rho}\tilde{k}\nabla \cdot \tilde{\boldsymbol{u}} + \sigma : \nabla\tilde{\boldsymbol{u}} + \nabla \cdot \left[\frac{(\mu + \mu_T)}{Pr_k}\nabla\tilde{k}\right] - \bar{\rho}\tilde{\varepsilon} + \dot{\widetilde{W}}^s, \qquad (6.13)$$

$$\frac{\partial \bar{\rho}\tilde{\varepsilon}}{\partial t} + \nabla \cdot (\bar{\rho}\tilde{\boldsymbol{u}}\tilde{\varepsilon}) = -\left(\frac{2}{3}c_{\varepsilon 1} - c_{\varepsilon 3}\right)\bar{\rho}\tilde{\varepsilon}\nabla \cdot \tilde{\boldsymbol{u}} + \nabla \cdot \left[\frac{(\mu + \mu_T)}{Pr_\varepsilon}\nabla\tilde{\varepsilon}\right] + \frac{\tilde{\varepsilon}}{\tilde{k}}(c_{\varepsilon 1}\sigma : \nabla\tilde{\boldsymbol{u}} -$$

$$c_{\varepsilon 2}\bar{\rho}\tilde{\varepsilon} + c_s\dot{\widetilde{W}}^s), \qquad (6.14)$$

In these equations, $\mathbf{Pr_k}$, $\boldsymbol{Pr_\varepsilon}$, $\boldsymbol{c_{\varepsilon 1}}$, $\boldsymbol{c_{\varepsilon 2}}$ and $\boldsymbol{c_\mu}$ are model constants, which are listed and described in *Table 6-1*.

The source terms involving $\dot{\widetilde{\boldsymbol{W}}}^{\boldsymbol{s}}$ are calculated based on the droplet probability distribution function [12]. Physically, $\dot{\widetilde{\boldsymbol{W}}}^{\boldsymbol{s}}$ is the negative of the rate at which the turbulent eddies are doing work in dispersing the spray droplets. $\boldsymbol{c_s} = 1.5$ was suggested by Amsden [12] based on the postulate of length scale conservation in spray/turbulence interactions. The advanced version of the *k*-ε model is derived from Re-Normalized Group (RNG) theory, as first proposed by Yakhot and Orszag [13]. The *k* equation in the RNG version of the model is the

same as the standard version, but the ε equation is based on rigorous mathematical derivation rather than on empirically derived constants. The RNG ε equation is written as

$$\frac{\partial \bar{\rho}\tilde{\varepsilon}}{\partial t} + \nabla \cdot (\bar{\rho}\tilde{\boldsymbol{u}}\tilde{\varepsilon}) = -\left(\frac{2}{3}c_{\varepsilon 1} - c_{\varepsilon 3}\right)\bar{\rho}\tilde{\varepsilon}\nabla \cdot \tilde{\boldsymbol{u}} + \nabla \cdot \left[\frac{(\mu + \mu_T)}{Pr_\varepsilon}\nabla\tilde{\varepsilon}\right] + \frac{\tilde{\varepsilon}}{\tilde{k}}(c_{\varepsilon 1}\sigma : \nabla\tilde{\boldsymbol{u}} - c_{\varepsilon 2}\bar{\rho}\tilde{\varepsilon} + c_s\dot{\widetilde{W}}^s) - \bar{\rho}R, \tag{6.15}$$

where the $\boldsymbol{R}$ in the last term of the right-hand side of the equation is depends on the model. For standard *k*-ε model, $\boldsymbol{R}$ = 0 and for RNG *k*-ε, $\boldsymbol{R}$ is described as

$$R = \frac{c_\mu(\eta)^3\,(1-\eta/\eta_0)}{1+\beta\eta^3}\frac{\tilde{\varepsilon}^2}{\tilde{k}}, \tag{6.16}$$

with

$$\eta = S\,\frac{\tilde{k}}{\tilde{\varepsilon}}, \tag{6.17}$$

$$S = (2\bar{S}\cdot\bar{S})^{1/2}, \tag{6.18}$$

and $\bar{\mathbf{S}}$ is the rate of strain tensor,

$$\bar{S} = \frac{1}{2}(\nabla\tilde{\boldsymbol{u}} + \nabla\tilde{\boldsymbol{u}}^T) \tag{6.19}$$

Compared to the standard ε equation, the RNG model has one extra term, which accounts for non-isotropic turbulence, as described by Yakhot and Orszag [13]. Values of the model constants, $\boldsymbol{Pr_k}$, $\boldsymbol{Pr_\varepsilon}$, $\boldsymbol{c_{\varepsilon 1}}$, $\boldsymbol{c_{\varepsilon 2}}$ and $\boldsymbol{c_\mu}$ used in the RNG version are also listed in *Table 6-1*. In the ANSYS Forte implementation, the RNG value for the variable $\boldsymbol{c_{\varepsilon 3}}$ is based on the work of Han and Reitz [14], who modified the constant $\boldsymbol{c_{\varepsilon 3}}$ to take the compressibility effect into account. According to Han and Reitz [14],

$$c_{\varepsilon 3} = \frac{-1+2\,c_{\varepsilon 2}-3m(n-1)+(-1)^{\delta}\sqrt{6c_{\mu}c_{\eta}}}{3}, \quad (6.20)$$

where m=0.5, n=1.4 for an ideal gas. The value of $c_{\varepsilon 3}$ varies in the range of -0.9 to 1.726 [14], and in ANSYS Forte is determined automatically, based on the flow conditions and specification of other model constants, η_0 and β. In previous studies on engine CFD, Han and Reitz [14] applied their version of the RNG k-ε model to engine simulations and observed large-scale structures in the results compared to the standard k-ε model. In hydrogen DI engines large-scale structures are generated by the hydrogen jet during injection. Therefore, RNG k-ε model might be favourable for computation of mixture formation process in hydrogen direct-injection engine. In ANSYS Forte, the RNG k-ε model is the default and recommended turbulence model.

Table 6.1 Constants in the standard and RNG k-ε models [15]

	c_{μ}	$c_{\varepsilon 1}$	$c_{\varepsilon 2}$	$c_{\varepsilon 3}$	$1/\mathrm{Pr_k}$	$1/Pr_{\varepsilon}$	η_0	β
Standard k-ε	0.09	1.44	1.92	-1.0	1.0	0.769		
RNG k-ε	0.0845	1.42	1.68	Eq-6.20	1.39	1.39	4.38	0.012

6.4 Initial and Boundary Conditions

In numerical methods, different boundary condition may result in distinct solutions. Some of them may introduce non-physical influences on the domain. Arranging a correct set of boundary condition is important for physical stability inside the domain. For transient simulations, initial conditions for all variables and fluid properties are required. Fluid

properties are used to determine the initial values of the state variables and to initialize other terms in the governing equations. Initial fluid properties include initial pressure, temperature, species composition, initial turbulence kinetic-energy density (TKEI) and turbulence length scale (TLS) for each computational region. In this work for in-cylinder engine simulations, initial and boundary conditions of the computational model are derived from experimental results of engine measurements; turbulent law-of-the-wall velocity condition with fixed-temperature walls are employed. Fluid momentum boundary conditions on rigid walls are introduced by imposing a value of the velocity at the wall. On turbulent law-of-the-wall boundaries the normal gas velocity is set equal to the normal wall velocity and the two tangential components of the wall stress are explicitly specified by matching to a logarithmic profile. The wall heat transfer model of Han and Reitz [16] is used to calculate the gas-phase wall heat transfer. In the near wall region of wall-confined in-cylinder engine flows, the following assumptions hold:

1. Gradients normal to the wall are much greater than those parallel to the wall;

2. The flow velocity is directed parallel to the flat wall;

3. Pressure gradients are neglected;

4. Viscous dissipation and enthalpy diffusion effects on energy flux are neglected;

5. Radiation heat transfer is neglected.

6.5 Spark-Ignition Model

Spark-ignition engines are characterized by flame initiation near the spark location followed by flame propagation into the engine cylinder. The initial formation and development of the flame kernel caused by spark discharge in internal combustion engines is a very complex phenomenon which has a non-negligible influence on the subsequent combustion process. The high electrical potential difference across the spark-plug electrodes causes breakdown, creates a strong pressure wave and establishes a partially ionized plasma channel at high temperature [17,18]. Heat conduction and diffusion allow the kernel to expand before the combustion reactions take over and the combustion becomes self-sustainable [19]. Due to the high requirements in terms of mesh resolution associated with the use of Eulerian models [18], Lagrangian models are generally employed: a set of particles is placed in the vicinity of the spark plug, each of them representing a part of the ignited kernel and evolves in time. Several models have been proposed, namely: DPIK (Discrete Particle Ignition Kernel) model [20], further improved version, which accounts for spark discharge energy and effects of flow turbulence on kernel growth [21,22], AKTIM (Arc and Kernel Tracking Ignition Model) proposed by Duclos and Colin [23], and more recent Spark-CIMM model introduced to predict combustion in stratified-charge direct-injection engines, where mixture distribution, flow field and turbulence play a very important role in combustion process [24,25]. AKTIM model introduces marker particles to represent both the spark and flame kernels that advect and diffuse in response to the turbulent flow field after the spark discharge ignites the gas–air mixture. In the DPIK model by Fan,Tan and Reitz [20,21], a spherical-shaped kernel is initialized (and remains) centered on the spark gap while the

flame front position is marked (or tracked) by Lagrangian particles as it grows by spark-energy input and flame propagation until it is large enough for a G-equation simulation. The flame surface density is obtained from the number density of these particles in each computational cell as shown in Fig.6.1.

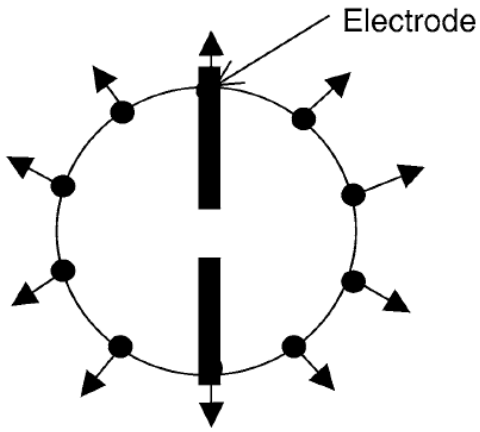

Fig.6.1 Discrete particle ignition kernel

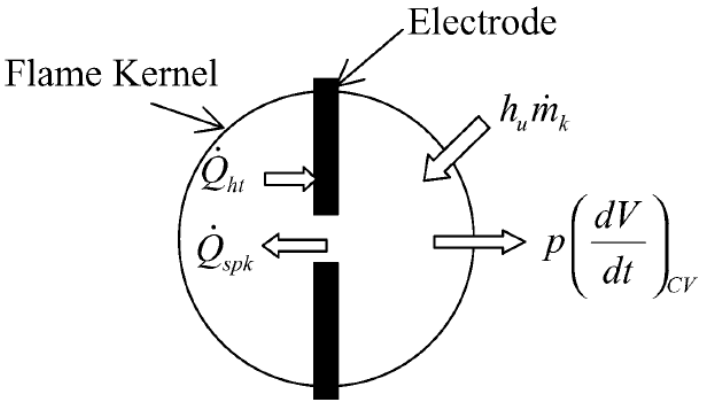

Fig.6.2 Thermodynamic system for the ignition kernel

With this method, even when the kernel size is smaller than the computational cell size, kernel growth can still be tracked accurately. Thus, the use of a very fine numerical mesh to predict the spark ignition process is not needed. This model is a phenomenological one, and the great advantage of this Lagrangian method lies in the reduction of model sensitivity to grid size effects, which are unavoidable during the early stage of the ignition process when the flame kernel is really smaller than the same grid size. ANSYS Forte tracks the growth of the ignition kernel by using the Discrete Particle Ignition Kernel Flame (DPIK) model. A thermodynamic system model of the ignition kernel region was used to analyze the flame kernel growth rate. The system is schematically shown in Fig.6.2. It is assumed that

1. The calculation starts after the breakdown period (e.g., after 1 μs), and the ignition kernel is spherical with a radius of 0.5 mm, as suggested by experiments [26].
2. The ignition kernel flame is very thin and separates the burned and unburned gas. The kernel flame structure is not resolved, and the temperature and all reactive scalars jump from their values in unburned mixture to the corresponding equilibrium values in the burned gas.
3. The ignition kernel surface (defined by marker particles positions) is located just in front of the flame, and thus, there is no heat transfer between the kernel and unburned gas.
4. The pressure is uniform inside and outside the kernel.
5. The temperature inside the kernel is uniform.

Assuming the temperature inside the kernel to be uniform, the kernel growth rate is:

$$\frac{dr_k}{dt} = \frac{\rho_u}{\rho_k}(S_{plasma} + S_T) \tag{6.21}$$

where r_k is the kernel radius, ρ_u is the local unburnt gas density, and ρ_k is the gas density inside the kernel region. The above equation is used to calculate the movement of the kernel particles.

The plasma velocity S_{plasma} is given as:

$$S_{plasma} = \frac{\dot{Q}_{spk} \cdot \eta_{eff}}{4\pi r_k^2[\rho_u(u_k - h_u)] + P\frac{\rho_u}{\rho_k}} \tag{6.22}$$

where ρ_u and h_u are the density and enthalpy of the unburned mixture. ρ_k and u_k are the density and internal energy of the mixture inside the kernel. $\dot{Q}_{spk}$ is the electrical energy discharge rate, η_{eff} is the electrical energy transfer efficiency due to heat loss to the spark-plug. A typical value of η_{eff} is 0.3, as suggested by Heywood [17].

6.6 G-equation Model for Turbulent Flame Propagation

One of the most promising methods to simulate turbulent combustion in spark-ignition (SI) engines is the G-equation combustion model [27]. The G-equation concept has been successfully applied to model Bunsen flames [28,29], homogeneous charge SI engines [21, 30,31], and lifted turbulent flames [32,33]. The modeling of early flame propagation after spark initiation is, however, a field of active academic and industrial research and presents a particular challenge for SG-SIDI engines. The G-equation combustion model is based on the turbulent premixed combustion flamelet theory of Peters [27]. This theory addresses two regimes of practical interest:

1. The corrugated flamelet regime where the entire reactive-diffusive flame structure is assumed to be embedded within eddies of the size of the Kolmogorov length scale η;
2. The thin reaction zone regime where the Kolmogorov eddies can penetrate into the chemically inert preheat zone of the reactive-diffusive flame structure but cannot enter the inner layer where the chemical reactions occur.

For application of the G-equation model to IC engine applications, this theory was further developed by Tan et al. [21] and by Liang et al. [34, 35]. For the current work, G-equation model is employed to track the propagation of fully developed turbulent flames. The G-equation model consists of a set of Favre-averaged level-set equations. This includes the equations for the Favre mean, $\widetilde{\boldsymbol{G}}$, and its variance, $\widetilde{\boldsymbol{G''^2}}$, as well as a model equation for the turbulent/laminar flame surface area ratio $\boldsymbol{\sigma_T}$. Application of the equation for the turbulent/laminar flame surface area ratio results in an explicit expression for the turbulent flame speed $\boldsymbol{S_T^0}$. Together with the Reynolds-averaged Navier-Stokes equations and the turbulence modeling equations, these provide a complete set of equations to describe premixed turbulent flame-front propagation. The equation set used is:

$$\frac{\partial \tilde{G}}{\partial t} = \tilde{\bar{u}} - \bar{u}_{vertex} \cdot \nabla \tilde{G} = \frac{\bar{\rho}_u}{\bar{\rho}_b} S_T^0 \, |\nabla \tilde{G}| \; - \; D_T \widetilde{K} \, |\nabla \tilde{G}|, \tag{6.24}$$

$$\frac{\partial \widetilde{G''^2}}{\partial t} + \tilde{\bar{u}} \cdot \nabla \widetilde{G''^2} = \nabla\| \cdot \left(\frac{\bar{\rho}_u}{\bar{\rho}_b} \, D_T \nabla\| \, \widetilde{G''^2}\right) \tilde{G}| \; + 2 D_T (\nabla \tilde{G})^2 - c_s \frac{\tilde{\varepsilon}}{\tilde{k}} \widetilde{G''^2}, \tag{6.25}$$

where $\nabla||$ denotes the tangential gradient operator; $\bar{\boldsymbol{u}}$ is the fluid velocity; $\bar{\boldsymbol{u}}_{\boldsymbol{vertex}}$ is the velocity of the moving vertex; $\boldsymbol{\rho_u}$ and $\boldsymbol{\rho_b}$ are the average densities of the unburned and burned mixtures, respectively; $\boldsymbol{D_T}$ is the turbulent diffusivity; $\widetilde{\boldsymbol{K}}$ is the Favre mean flame front curvature; $\boldsymbol{c_s}$, $\boldsymbol{a_4}$, $\boldsymbol{b_1}$, and $\boldsymbol{b_3}$ are modeling constants (cf. ref. [50]); $\widetilde{\boldsymbol{k}}$ and $\tilde{\boldsymbol{\varepsilon}}$ are the Favre mean turbulent kinetic energy and its dissipation rate from the RNG k-ε; $\boldsymbol{u'}$ is the turbulence intensity.

Here the flame front is represented by level-set surface $\widetilde{\boldsymbol{G}}\ (\boldsymbol{x}, \boldsymbol{t}) = \boldsymbol{0}$. This interface divides the flow field into unburned region, $\widetilde{\boldsymbol{G}} < 0.0$, and a burned gas region, $\widetilde{\boldsymbol{G}} > 0.0$. It is assumed that the instantaneous flame front always falls in those computational cells where the mean flame front is located, as depicted in Fig.6.3.

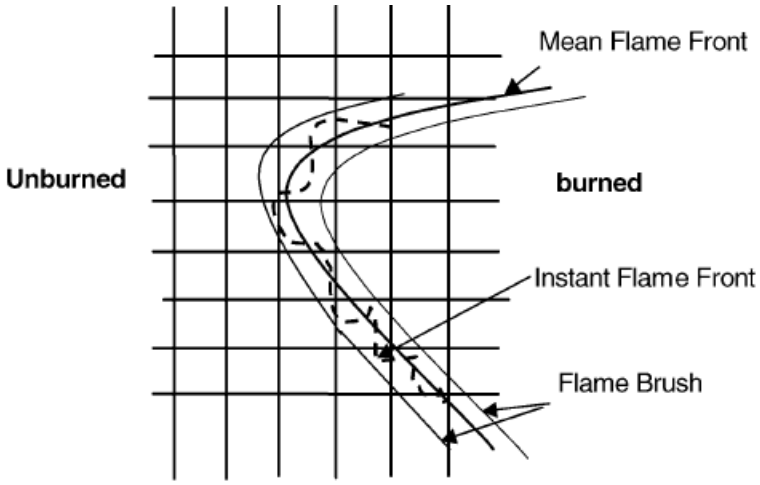

Fig.6.3 Schematic diagram of turbulent flame structure (mean flame front, flame brush)

When the flame is initiated by the spark, the ignition-kernel flame has a structure that is typically smaller than the average grid size in the computational mesh. During this time, then, the kernel flame front is first tracked by a group of discrete "particles". The calculation switches from this kernel flame model to the G-equation model after the flame structure grows bigger than a characteristic flow length scale. The transition from the kernel model to the turbulent G-equation model is controlled by a comparison of the kernel radius with a critical size that is proportional to the locally averaged turbulence integral length scale, viz.,

$$r_k \geq C_{ml} \cdot l = C_{ml} \cdot 0.16 \frac{k^{3/2}}{\varepsilon} \tag{6.23}$$

where C_{ml} is a model constant. C_{ml} is provided as a user input (Kernel Flame to G-equation Switch Constant) in ANSYS Forte with typical value 2.0 ANSYS Forte checks two criteria: critical temperature and size of the ignition kernel. After the ignition kernel is formed, the flame propagation model is activated. Computational cells with temperatures greater than the critical temperature become ignition sites. For each of these cells, if the ignition kernel radius is greater than the TLS (turbulent length scale), a $\widetilde{G}(x,t) = 0$ surface is initialized. This surface divides the areas where the gas temperature is lower or higher than the critical temperature. The area inside the surface is the area of ignition.

6.7 Model development and Mesh generation

Figure 6.4 provides a high-level view of the Simulation tasks. ANSYS Forte provides several options for defining the computational mesh, which allows much flexibility in creating a workflow that best suits the needs of a particular simulation. There are three options to define the computational mesh: 1). load in just the definitions of the geometric surfaces that bound the system from a Fluent, CGNS, or other mesh surface file, and then use the automatic mesh-generation option, or 2). load in a pre-defined, structured body-fitted mesh, 3). generate a body-fitted sector mesh from basic piston-bowl profile information. In this study, for CFD simulation, model development and mesh generation started by importing basic geometry information in a CAD software- generated STL format, splitting the geometry and defining various elements/parts of engine and then defining the computational mesh (i.e. creating a full 360° mesh) by employing automatic, on-the-fly mesh generation option in ANSYS Forte. Fig.6.5 and Fig.6.6 show the CAD geometry and corresponding mesh for both

CEM and research engine respectively. The global grid size of the immersed-boundary meshes for CEM case was set to 3 mm whereas for research engine case it was only 2 mm in order to achieve greater accuracy in the calculation results. Mesh refinement around the key geometric features such as valves, piston, walls, and open boundaries ("continuative outflows") in terms of Point, Surface, Line, or Feature Refinements, or Small Feature Avoidance Controls were also performed. This mesh control found to be useful in allowing certain regions of the domain to remain coarse when refinement is not needed. The mesh format adopted in ANSYS FORTE is block-structured hexahedron as hexahedral cells provide better convergence and accuracy than tetrahedral cells. In addition, hexahedral cells were preferred when dealing with moving meshes and boundaries.

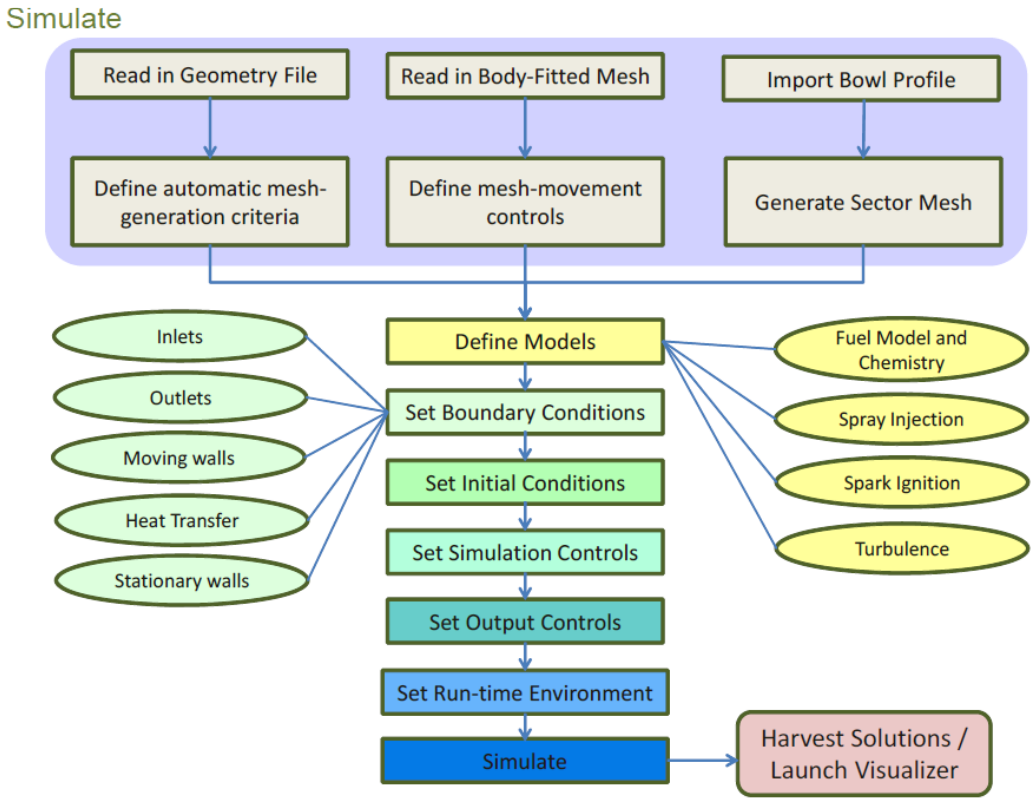

Fig.6.4 ANSYS Forte Simulate: Workflow overview

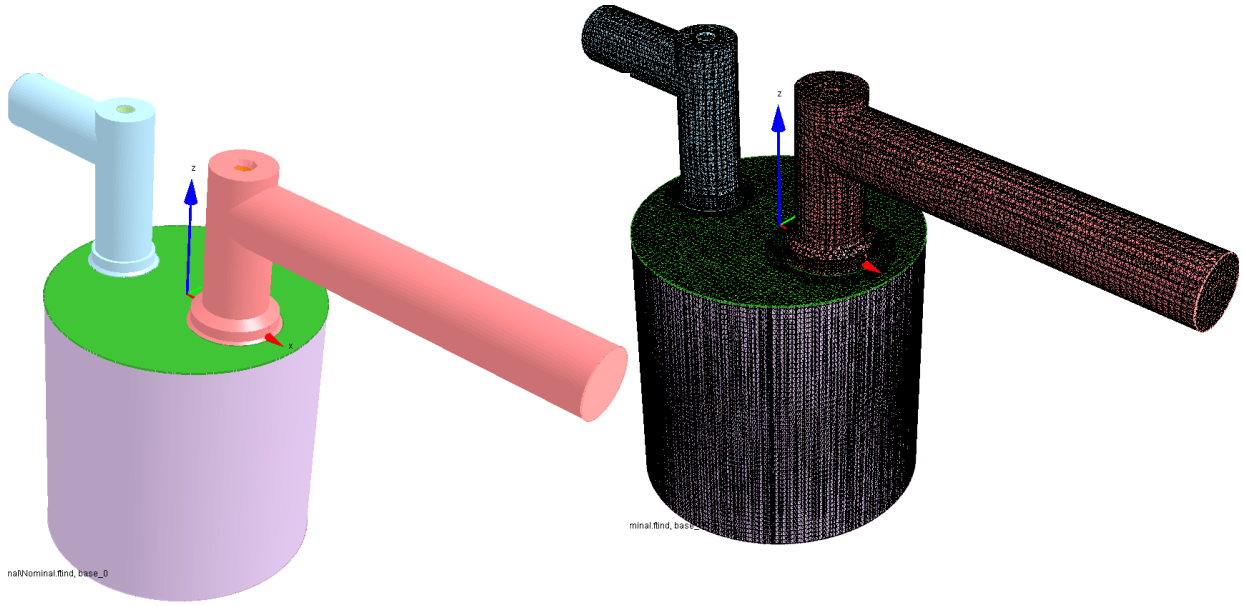

Fig.6.5 CEM: CAD geometry and Corresponding Mesh

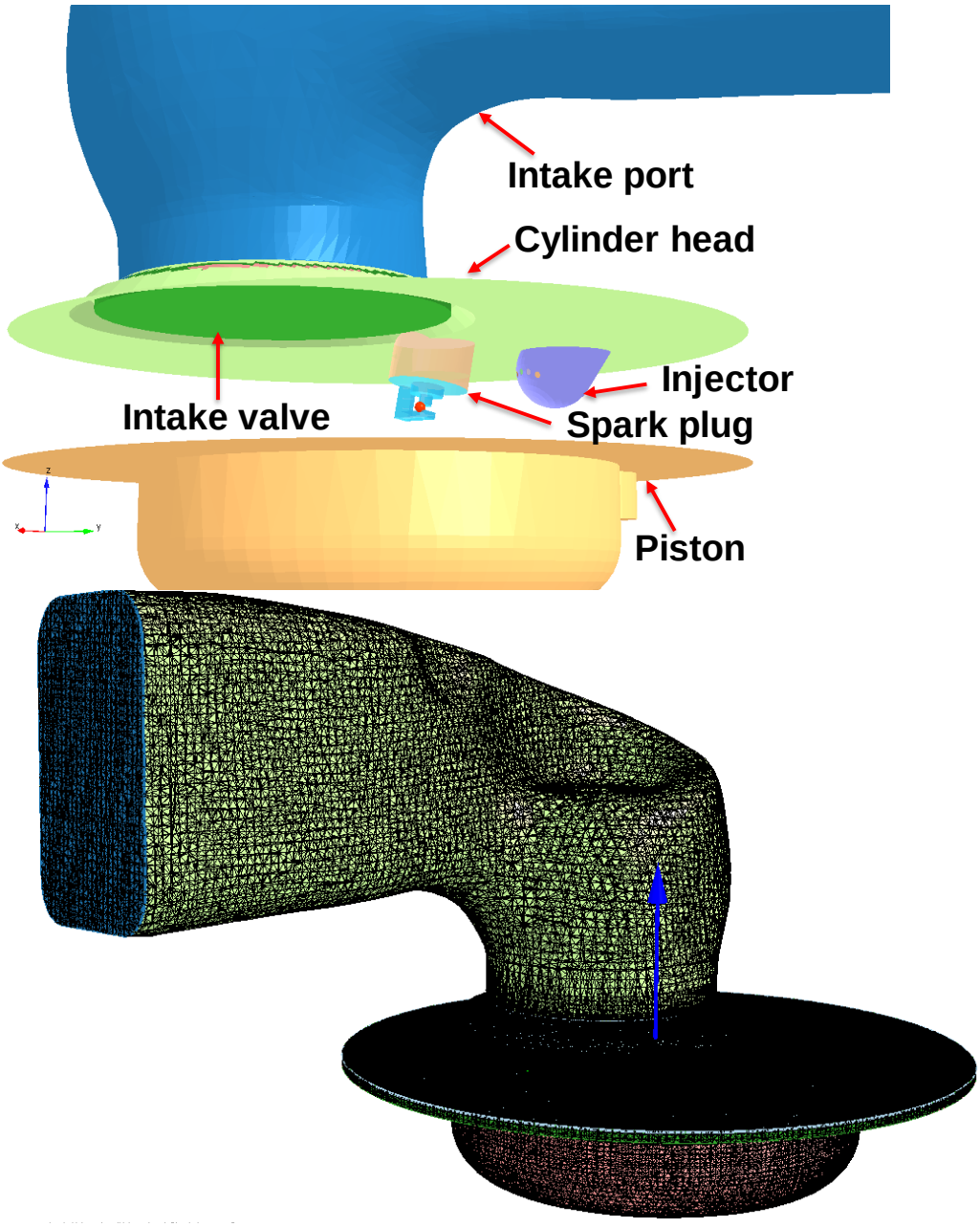

Fig.6.6 Research engine (TCU): CAD geometry and Corresponding Mesh

6.8 Concept of Inflow Boundary Condition

Basically, ANSYS FORTE CFD is designed for simulating IC engine operating in either PFI mode, or liquid fuel direct injection (GDI, Diesel CI etc.) mode. For PFI operation one has to just specify mixture concentration at inlet boundary whereas for DI operation user has to choose the appropriate spray model and specify the nozzle characteristics. As our main focus was to simulate direct injection spark-ignition engine with gaseous fuel like Hydrogen; it is not possible to introduce hydrogen directly into the combustion chamber with existing spray model found in the user interface. Therefore, we opted to utilize the concept of inflow boundary condition at the nozzle exit so that gaseous hydrogen can be introduced into the simulated domain. In a typical direct-injection engine, the injector tip extrudes from the cylinder head surface so that the nozzle exit is exposed to the in-cylinder gas. In the geometry of both CEM and research engine, injector tip was added as an integrated part of the cylinder head surface. In Fig.6.7., the integrated cylinder head and injector tip surface is shown as a solid black curve, and the nozzle exit is marked by the blue. The integrated surface of cylinder head and injector tip was then specified as a solid wall boundary condition, except for the nozzle exit area. The geometric area of the nozzle exit was explicitly marked out of the injector tip surface, and a velocity inflow boundary condition was specified on it. Correspondingly, in Forte Simulate setup, we need to set up meshing controls such that the volume mesh near the nozzle exit (inflow boundary) is refined to a similar or smaller

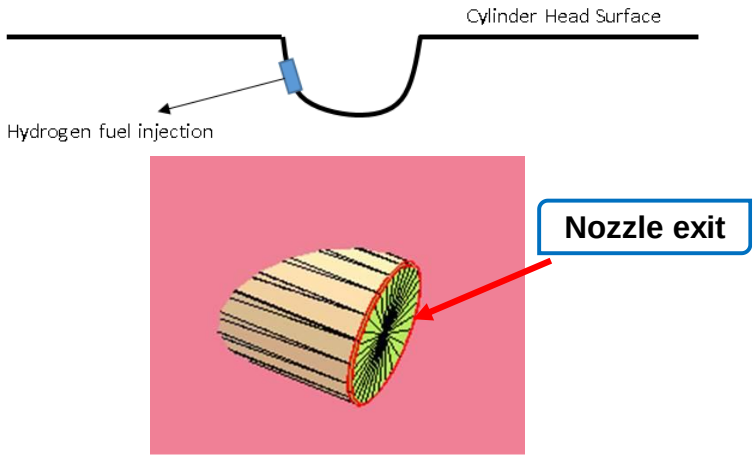

Fig.6.7 Concept of velocity inflow boundary condition

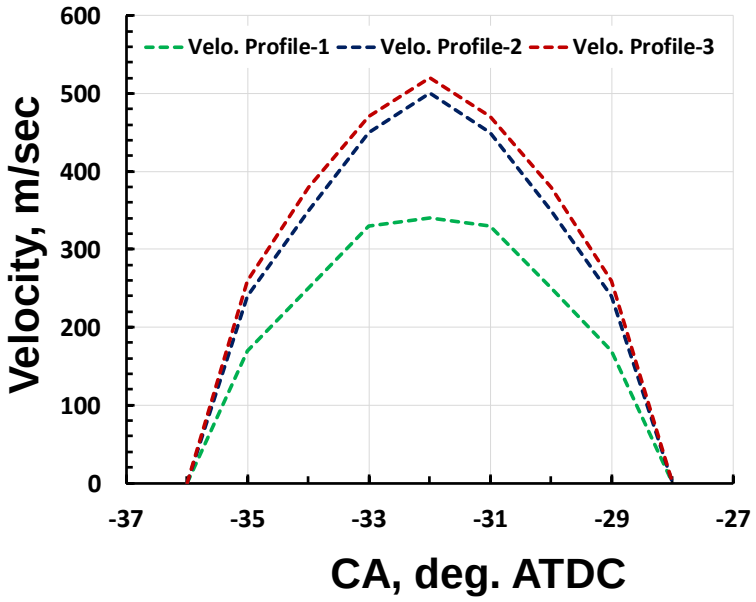

Fig.6.8 Velocity profiles for hydrogen injection

length scale than the nozzle size, in order to capture the hydrogen jet structure and mass diffusion more accurately. Jet cone angle is to be predicted by Forte CFD solution. The predicted turbulent diffusion of hydrogen upon its exit from the nozzle will affect the jet cone angle. Forte allows specification of inflow boundary condition using the option of "velocity,

time varying". Therefore, velocity profiles varying with crank angle were predicted in order to specify the both start of injection (SOI) and end of injection (EOI) as illustrated in Fig.6.8.

6.9 Intake Flow Characteristics

The research engine has intake port with helical geometry that generates in-cylinder swirl. The valve lift profiles are set using experimentally measured valve lift values. The fine grid arrangement is necessary during the valve movement to obtain the stability and convergence criteria. The mesh for intake ports of both engine configurations have been created using a similar topology, where the cells are oriented in the flow direction and joined with a cylindrical structured mesh in the zone upstream of the valves.

Simulations are started from intake TDC to 80°ATDC during expansion. This encompasses the full intake, compression stroke and part way through the expansion stroke, after combustion has completed. The intake stroke is computed to account for realistic thermal stratification and in-cylinder velocity profiles in the premixed intake gas. Chemistry is computed only for cells with temperatures in excess of 600 K and is not computed in the intake or exhaust ports while the respective valves are closed. This helps reduce the computational cost of the simulations, as the time computing chemistry accounts for a large fraction of the total computational effort. The initial pressure and temperature within engine cylinder need to be defined to provide the initial conditions of governing equations to be solved. The initial pressure of 0.09MPa while initial temperature of 300 K was set for both CEM and research engine.

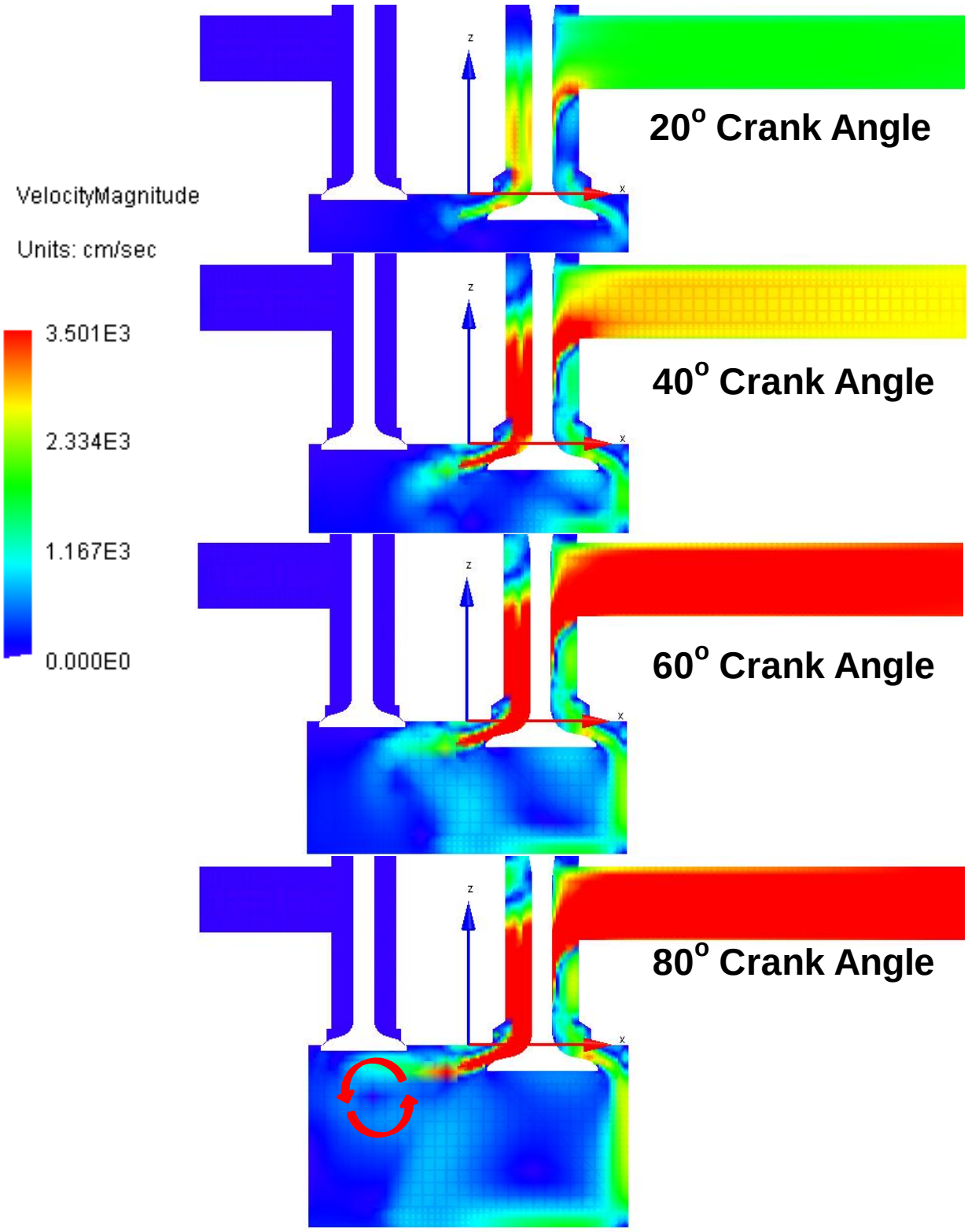

Fig.6.9 Velocity plot for air flow during intake stroke in CEM case (continue)

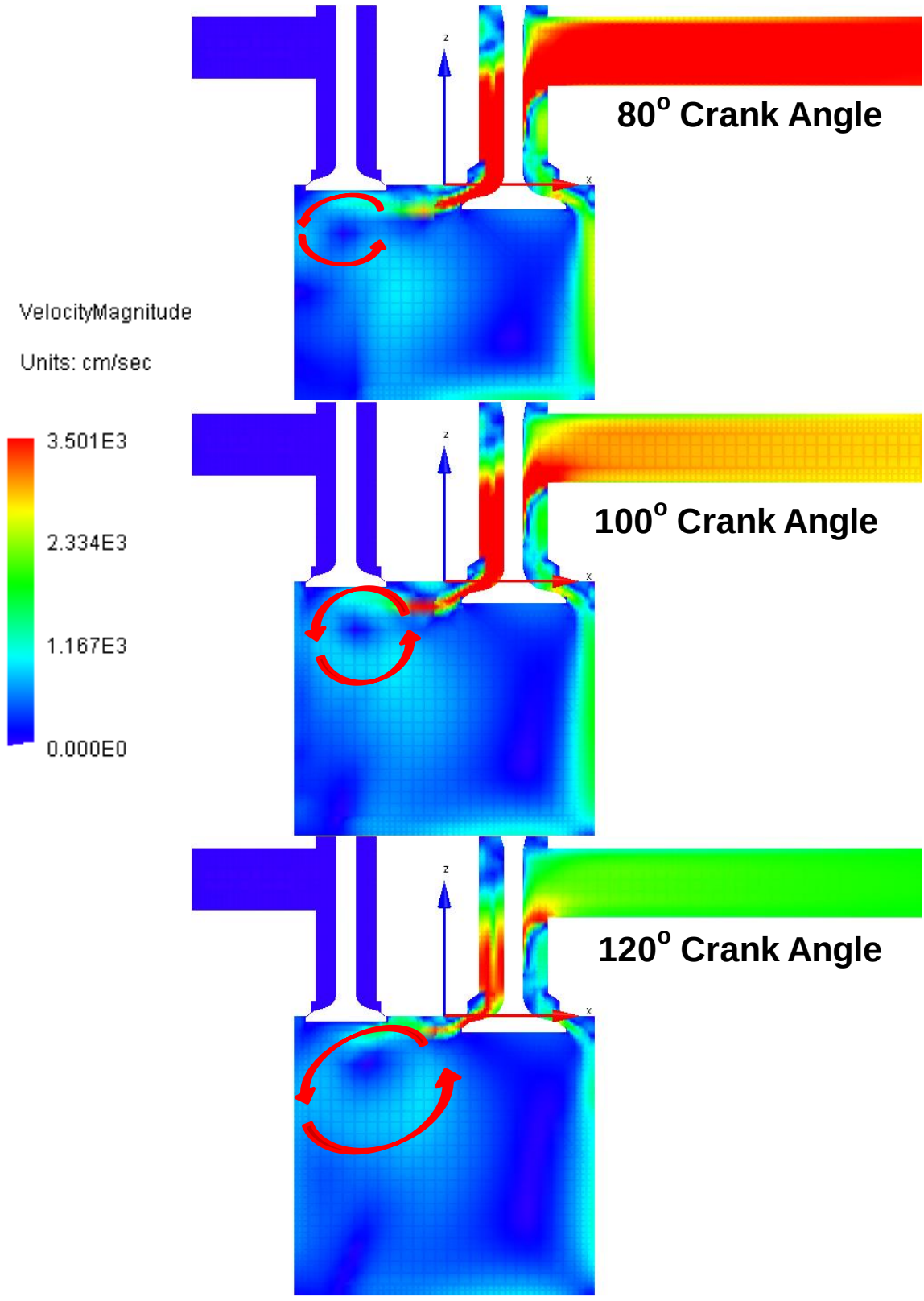

Fig.6.9 Velocity plot for air flow during intake stroke in CEM case

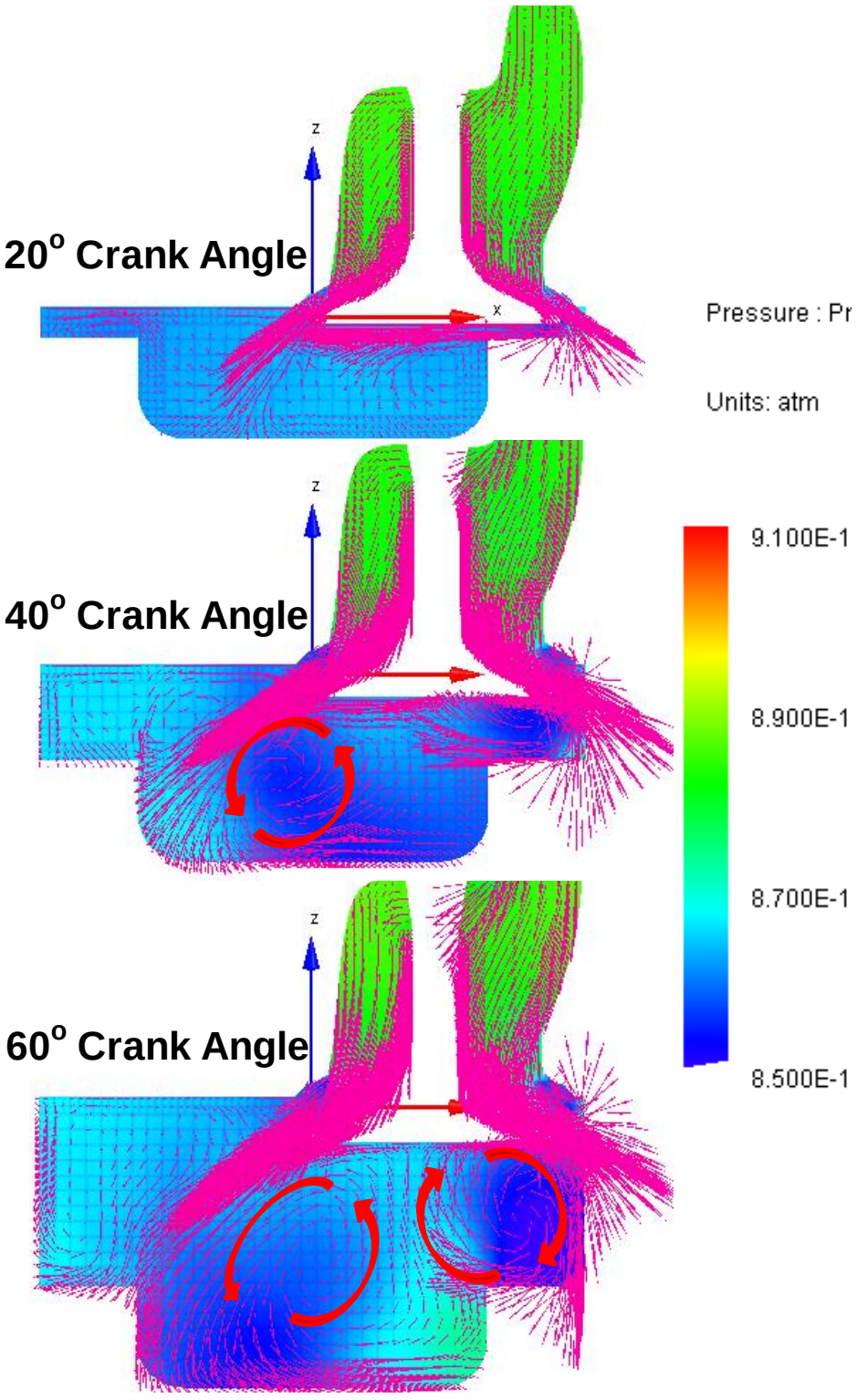

Fig.6.10 Velocity field with pressure plot for air flow during intake stroke in research engine case (continue)

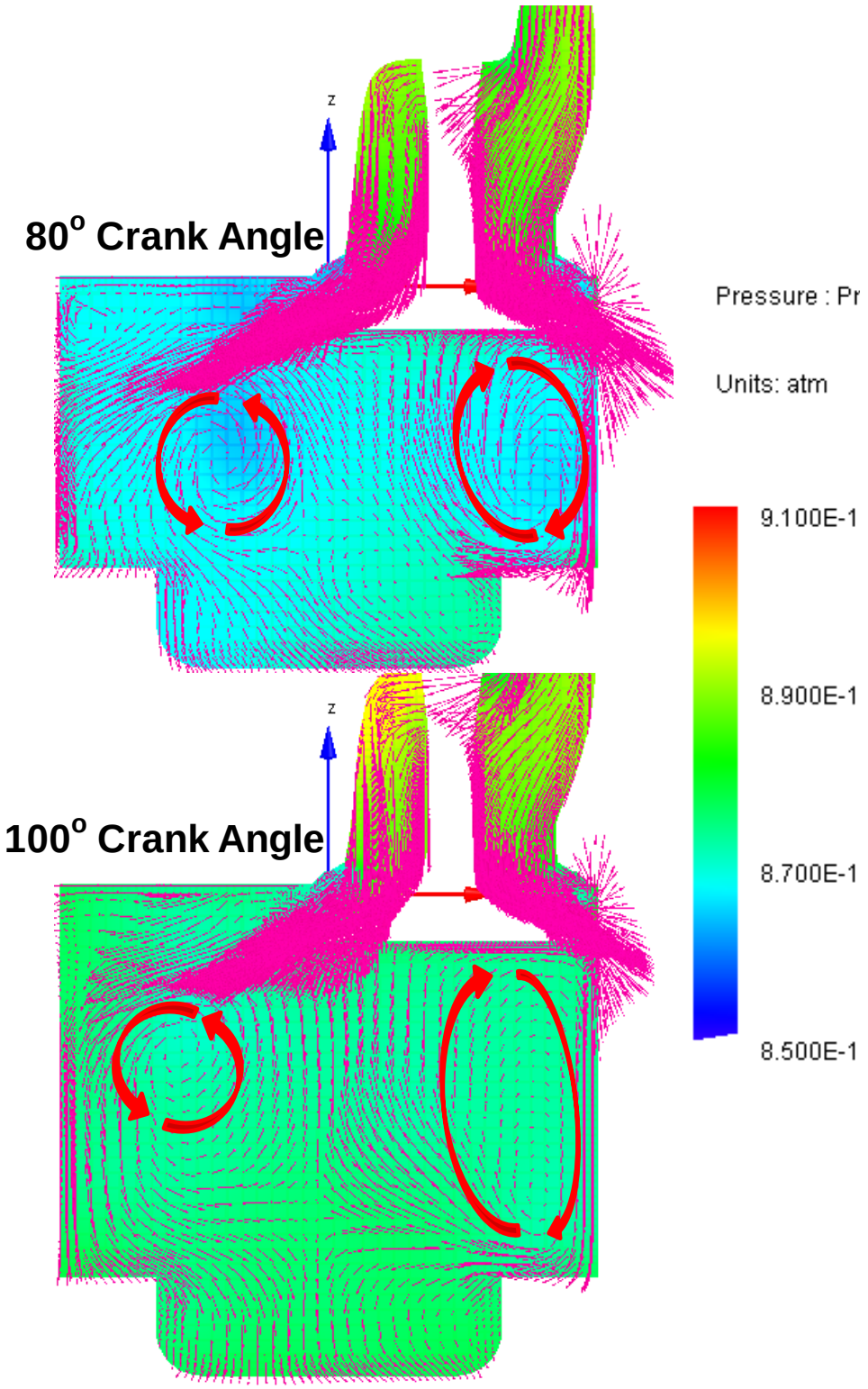

Fig.6.10 Velocity field with pressure plot for air flow during intake stroke in research engine case

Fig.6.9 shows the velocity plot in a vertical cut plane for air intake into the CEM at the time of maximum intake valve lift, whereas pressure plot with velocity vector in a vertical cut plane for air intake into the hydrogen research engine is shown in Fig.6.10. Very strong annular jet flows can be observed in both of engine configuration. As the flow velocity was quite high during the entry into the cylinder, vortex regions formed later on when the high-speed air interact with fixed wall of the cylinder and piston bowl. These toroidal vortices gradually become stronger and expanded over time. For research engine case, air swirl generated with a magnitude of 2.2 (measured experimentally) due to the helical shape of intake port; consequently, vortices appeared to be much stronger compared to that in RCEM case.

6.10 Hydrogen Injection and jet characteristics

In order to capture the hydrogen jet with higher spatial resolution and to overcome the mesh dependence, a very fine mesh is required in the region where the jet is present. This is achieved using “line refinement” feature available in the mesh control (see Fig.6.11). This particular mesh refinement was activated only during the injection event which caused the number of cells in the computational domain to become 1.7 million and 0.7 million, for research engine and CEM, respectively. To run simulation for such a huge number of cells, therefore, a high-performance computer (HPC) with Intel XEON processor including 32 cores was used to reduce the computational time.

Fig.6.12 shows the jet structure in vertical cut plane through nozzle exit and spark-plug geometry for hydrogen direct injection into CEM with start of injection (SOI) =10^{o}BTDC and

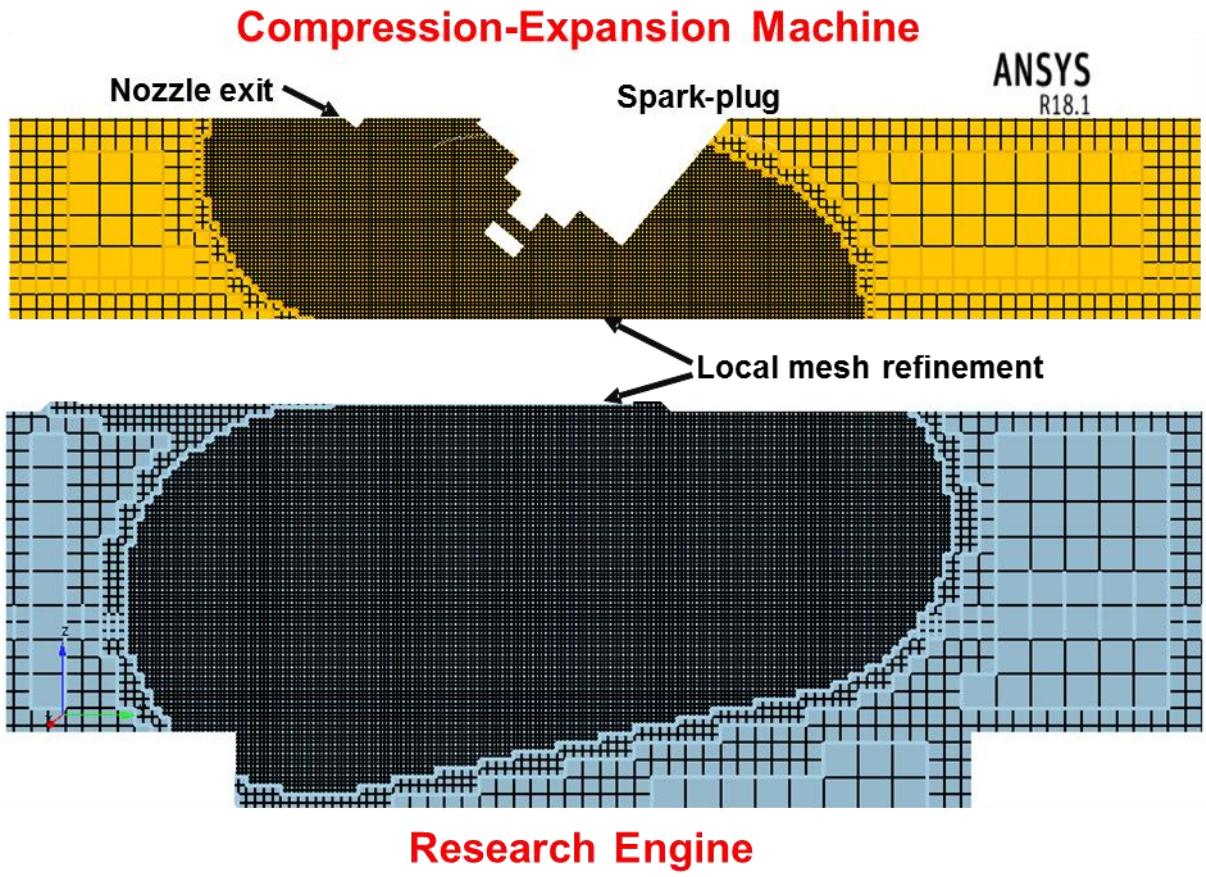

Fig.6.11 Local mesh refinement along jet direction for air flow during intake stroke

global air-excess ratio, λ = 10. Here, end of injection (EOI) = 0°BTDC and spark timing coincide with EOI (i.e. at TDC). Fig.6.9 confirms that it is possible to introduce gaseous fuel directly into the combustion chamber using the concept of "velocity inflow boundary" by specifying boundary conditions like pressure, temperature, time varying velocity profile etc. appropriately for the nozzle exit area. This simulation also confirms that the hydrogen jet directed towards the spark gap region forming a jet guided combustion system in accordance with original design of the chamber head.

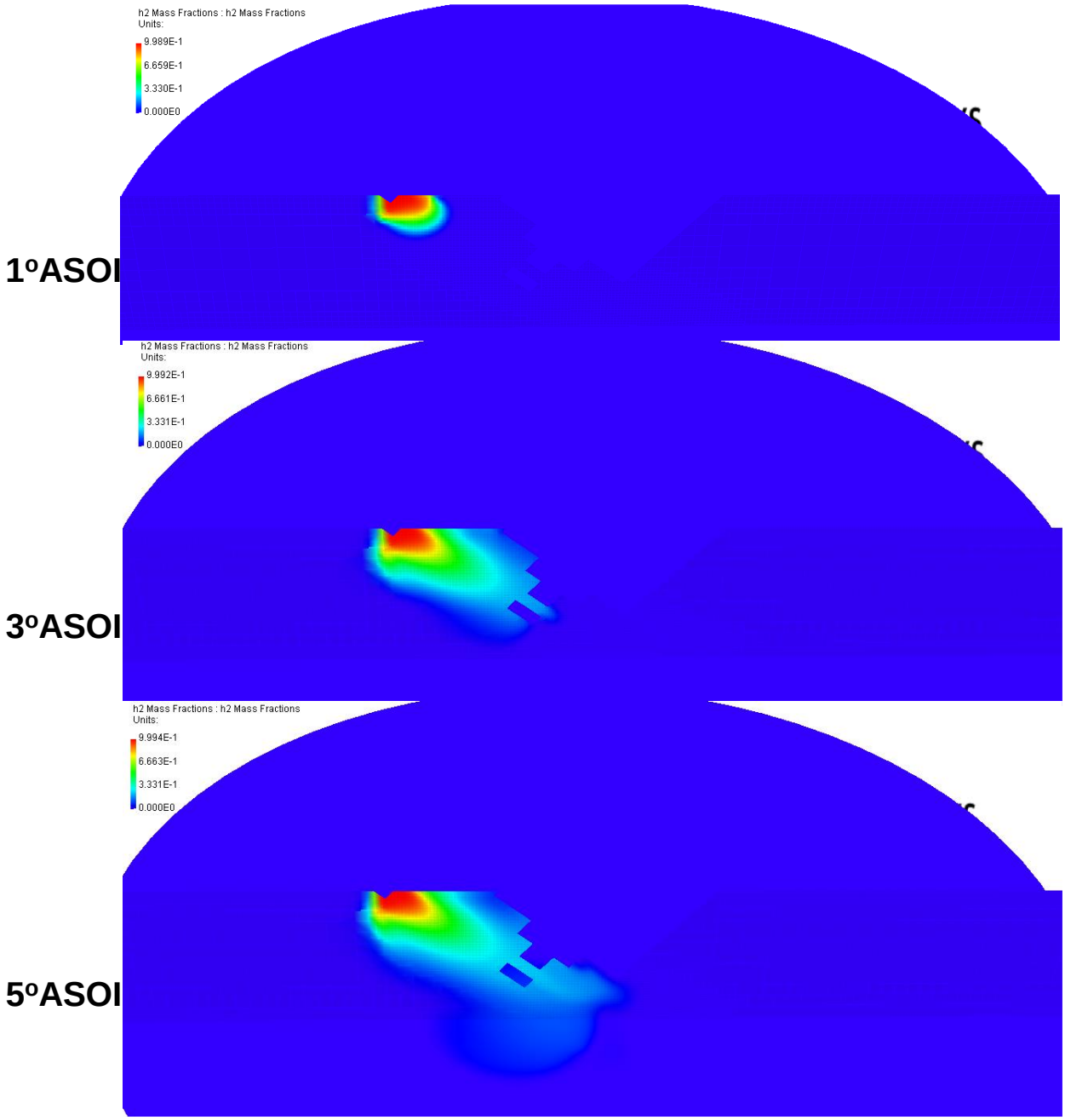

Fig.6.12 Hydrogen jet structure in CEM case for EOI=0ºBTDC and λ = 10 (continue)

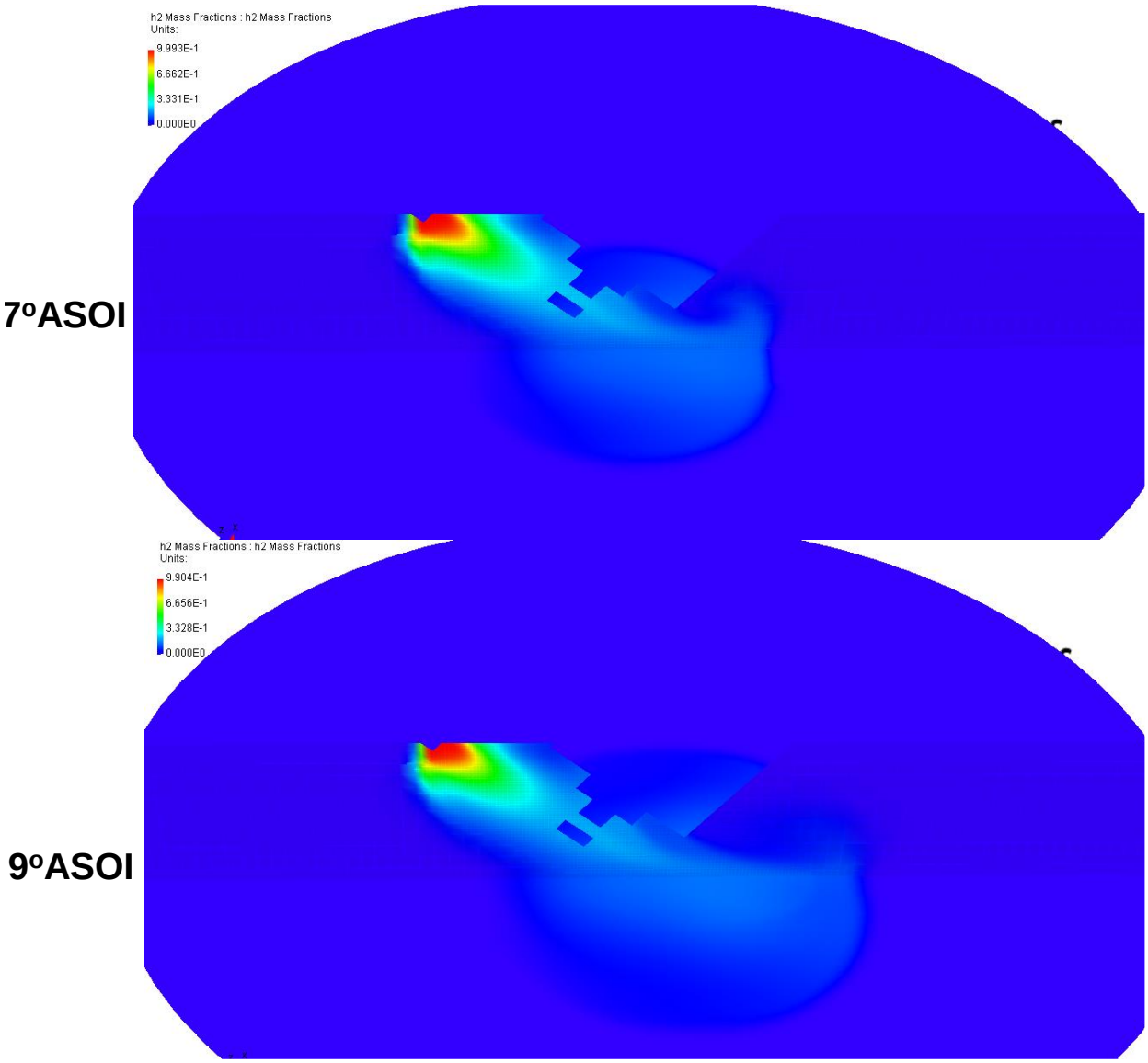

Fig.6.12 Hydrogen jet structure in CEM case for EOI=0°BTDC and λ = 10

Fig.6.13 and Fig.6.14 present hydrogen jet structure at different crank angle after start of injection (ASOI) for different injection timing considered in the experimental works

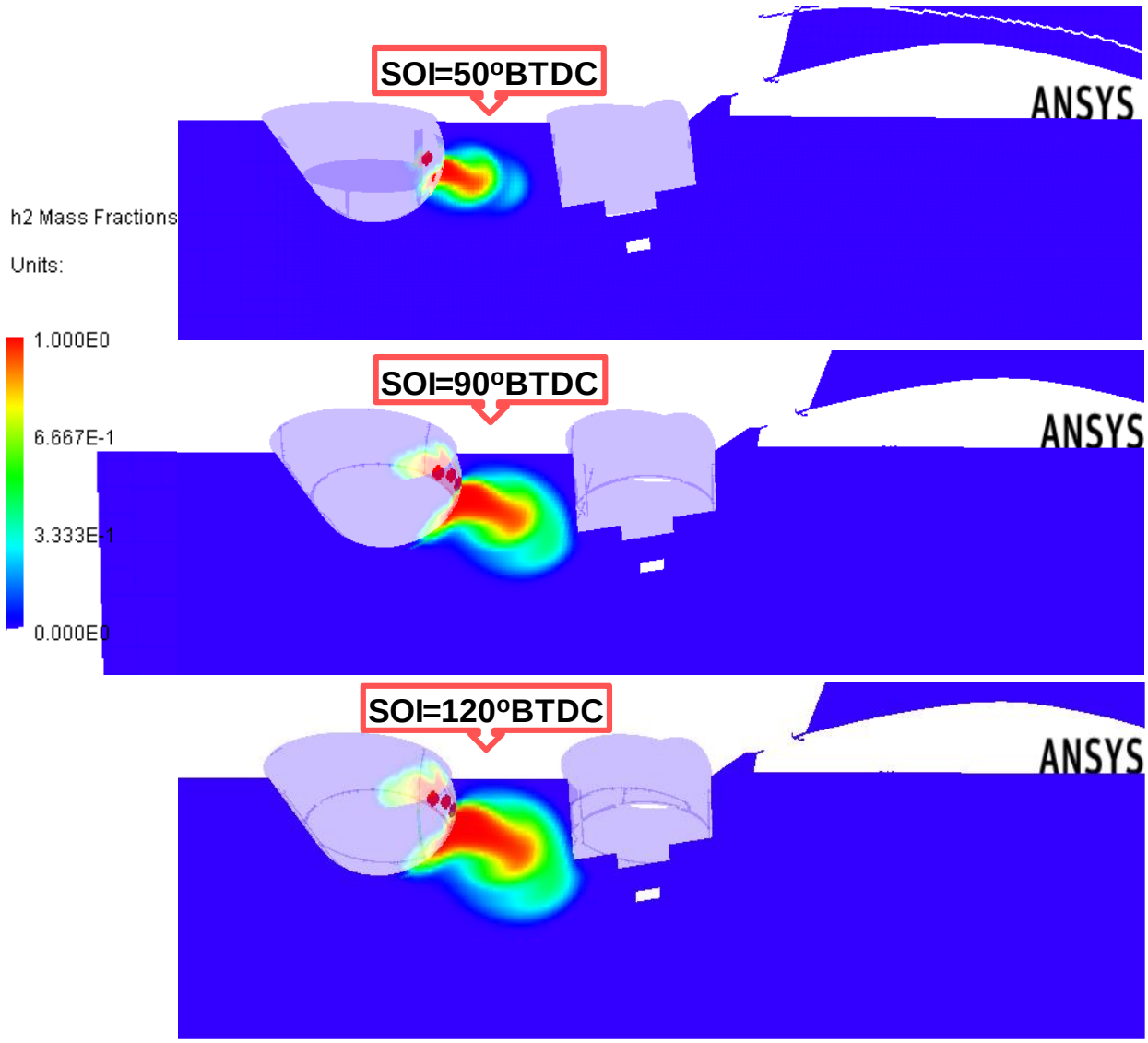

Fig.6.13 Hydrogen jet structure at 1° ASOI for research engine case; λ = 4

conducted in research engine case; here preset air excess ratio was, λ = 4. It is clearly depicted in the figure that when start of injection (SOI) was retarded jet penetration and jet diffusion became slower or reduced. This might be attributed to the fact that in cylinder

pressure getting higher as piston advances during compression stroke; therefore, with retarded injection during compression stroke fuel jet experience higher pressure immediately upon exiting from the nozzle tip. This high ambient pressure hinders the gas diffusion into the ambient air and consequently reduce the jet penetration.

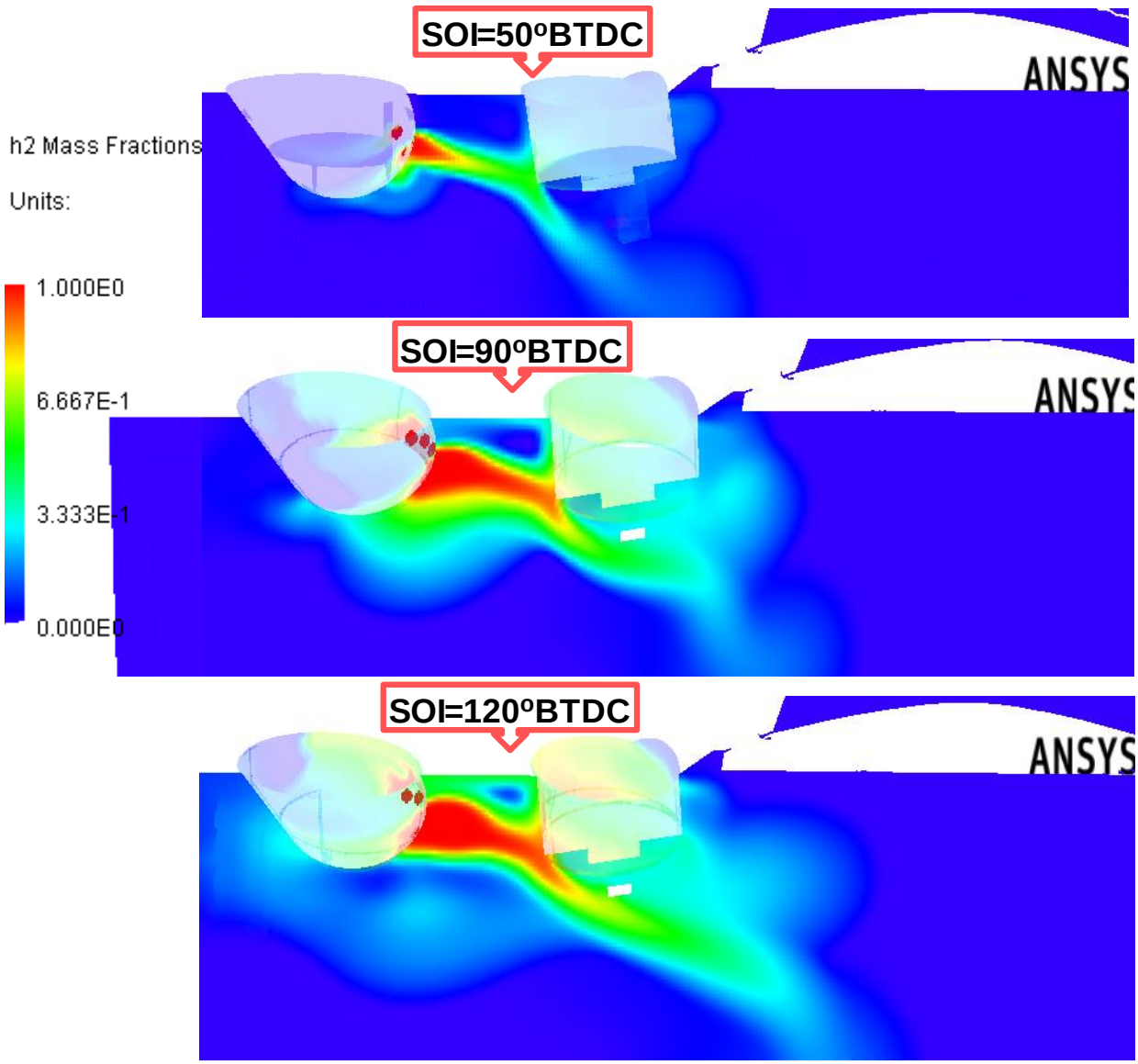

Fig.6.14 Hydrogen jet structure at 6° ASOI for research engine case; λ = 4

For SOI = 120°BTDC, the in-cylinder pressure during the onset of injection was only 0.128 MPa whereas the value increased to 0.556 MPa with SOI = 50°BTDC. This explains the reason why hydrogen molecular diffusion was weaker for SOI = 50°BTDC, as seen in Fig. 6.13 and Fig.6.14 compared to others injection timing.

6.11 Modeling Mixture formation and Combustion in CEM case

6.11.1 Flame front tracking and pressure history

In accordance with the experimental conditions, 3-D CFD simulation were performed for hydrogen direct injection and spark ignition in CEM case. Evolution of hydrogen flames with crank angle position was modeled and depicted in Fig.6.15 whereas simulated in-cylinder pressure history for hydrogen combustion was plotted and compared with experimental result in Fig.6.16. Here, injection event completed at, EOI=0°BTDC and spark discharge occurred at the same instant. Therefore, at TDC, we can presume that the mixture was highly stratified and ignition point might be located somewhere along the hydrogen jet. As a result, flame propagation velocity was so high that 50% heat release occurred within just 1°CA from the onset of spark event, as found in FORTE log file. It took only 2°CA to accumulate 90% of the total heat release. This phenomenon is clearly demonstrated in Fig. 6.12, as the flame front, tracked by G-equation model, engulfed the whole combustion chamber within 2°CA from the onset of spark event. The complex flame motion phenomena can be included when the flame front is tracked accurately. These phenomena would be neglected if only the kinetics within each cell were considered in determining flame location.

Turbulent flame speed cannot be pre-determined in the same way as laminar flame speed, because of the dependence on local and dynamic turbulence parameters and the fact that turbulence scales can vary over several orders of magnitude within the same simulation. However, there are fundamental correlations that allow on-the-fly determination of turbulent flame-speed values using the kinetics-derived laminar flame-speed and the local turbulent kinetic energy and turbulent length scale. ANSYS FORTE accounts for local conditions at each flame front location by accessing pre-established look-up tables that provide laminar flame-speed values dynamically at each location of the flame front. Turbulent flame speeds are derived from the fundamental laminar flame speed and from the local turbulence parameters. In this way the flame propagation at each time step and at each point along the flame surface is determined by the fundamental chemical kinetics relevant to those conditions as well as the turbulence conditions.

Initially full cycle simulation was performed in order to capture more flow structures, eddies and vortices that have significant influences on both mixture formation process and subsequent combustion. But a remarkable deviation in agreement between experiment and simulation can be observed in Fig.6.16. This discrepancy indicates the presence of very small leakage in the RCEM. As an alternative to full cycle modeling, a second simulation carried out from -25o ATDC to 40o ATDC during which all the major events like injection, spark discharge and flame propagation took place. The trend of peak pressure is well captured; and very good agreements are obtained for the injection, ignition and combustion stages.

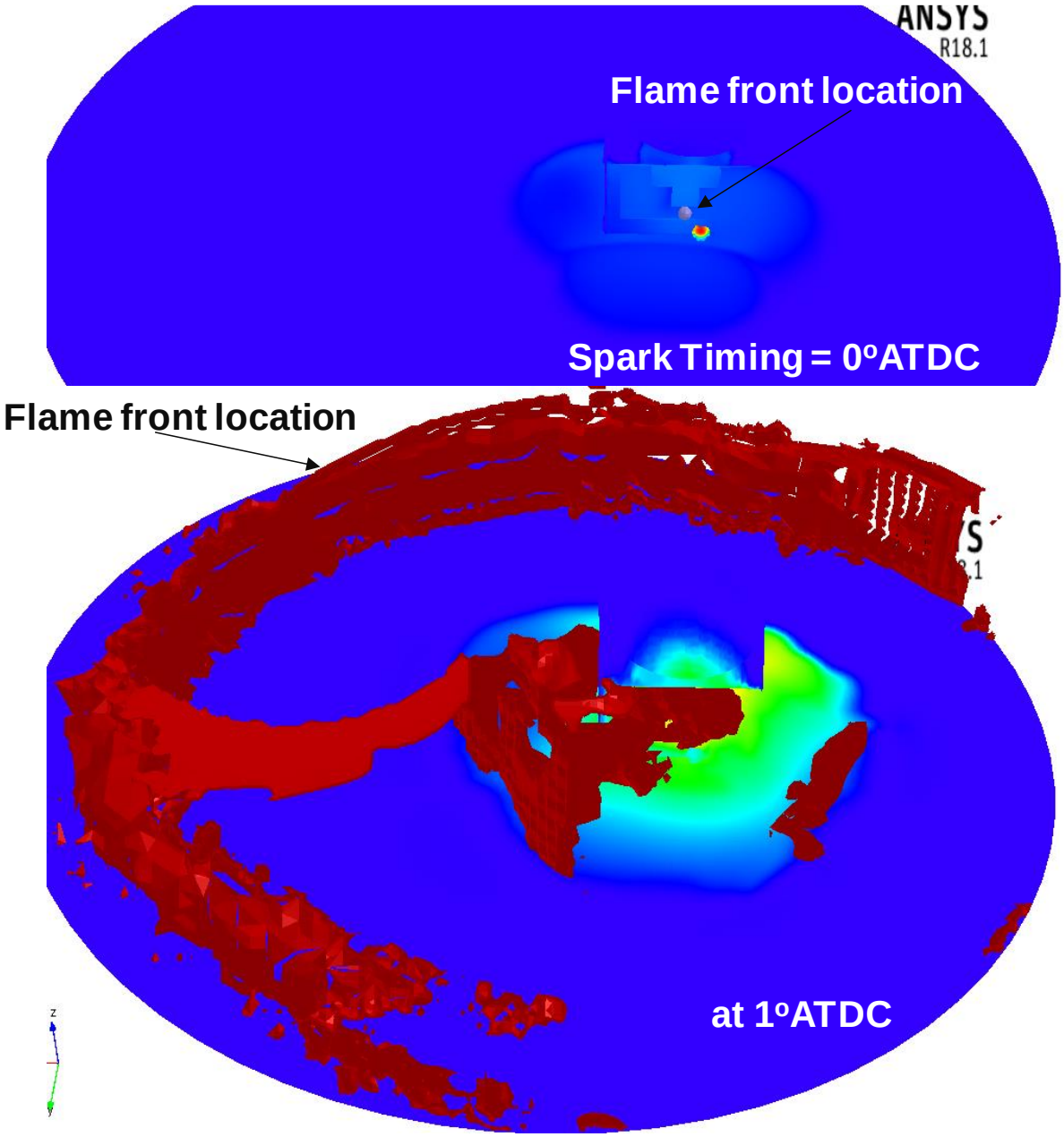

Fig.6.15 Flame front evolution with crank angle for EOI = 0°BTDC in CEM case; λ = 10 (conitue)

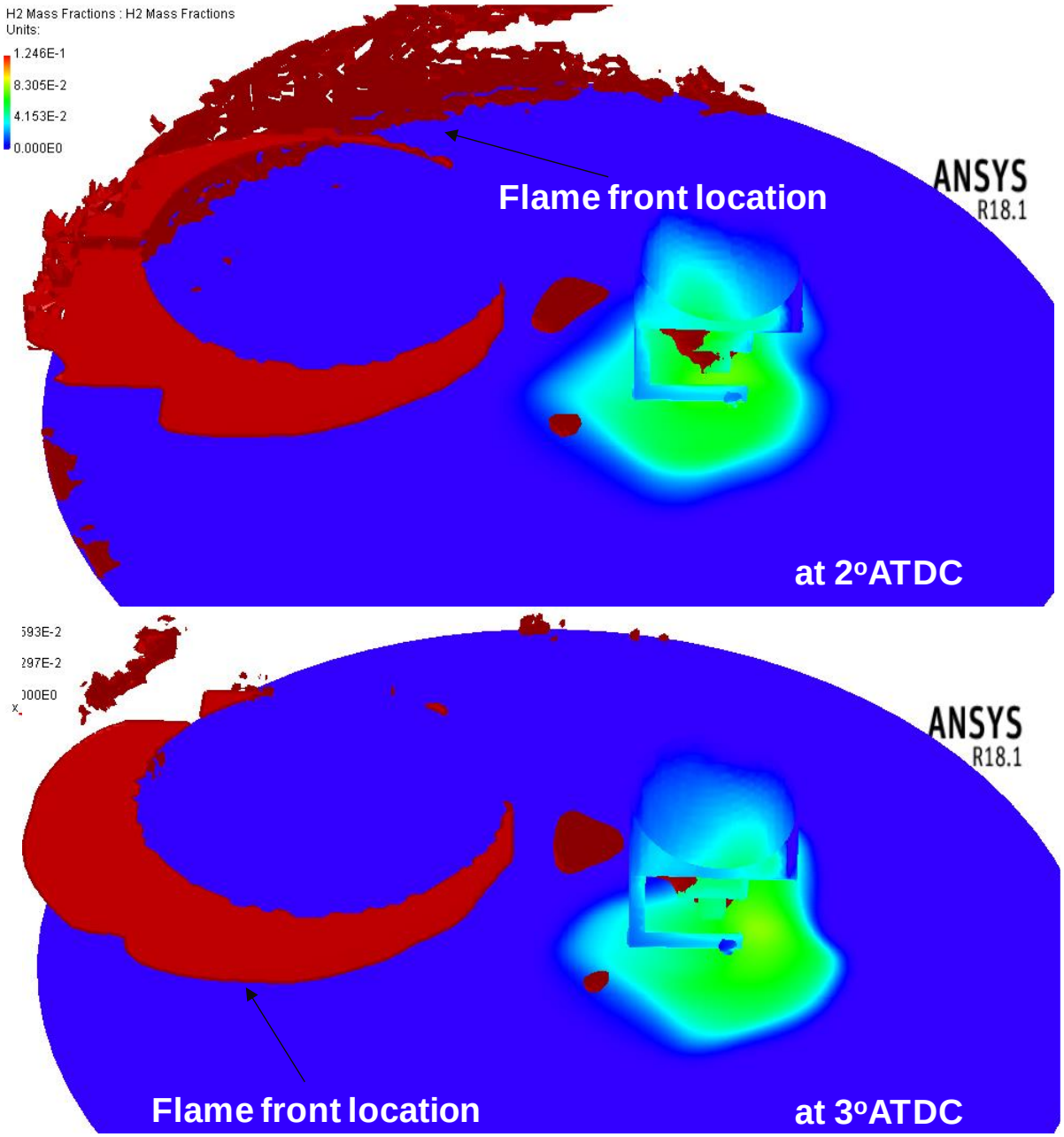

Fig.6.15 Flame front evolution with crank angle for EOI = 0°BTDC in CEM case; λ = 10

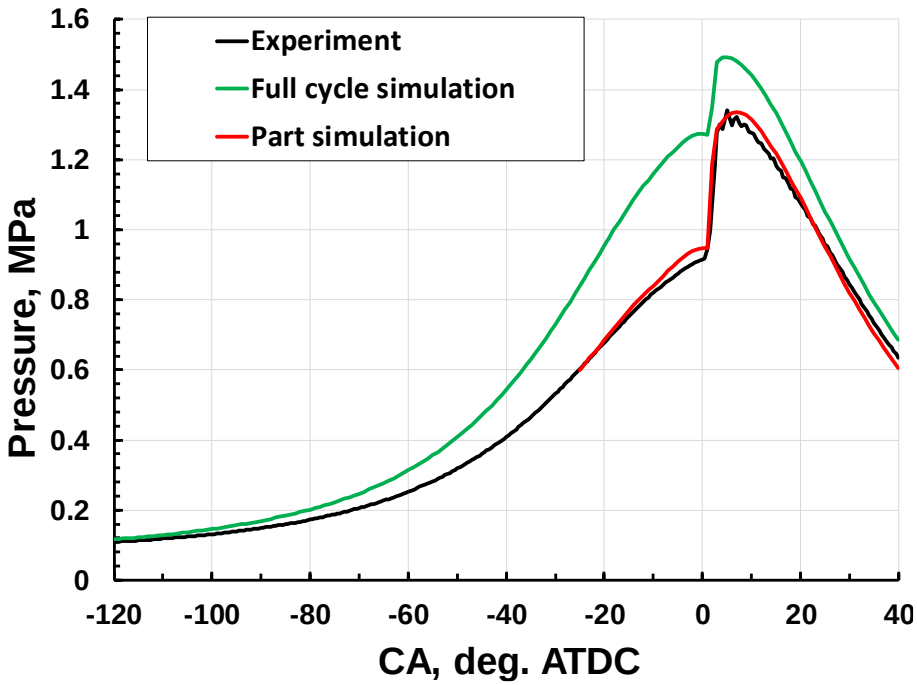

Fig.6.16 Comparing simulated pressure history with experimental data for EOI = 0°BTDC and λ = 10 in CEM case

6.11.2 Comparison of local equivalence ratio

Previously in Chapter-4 it is stated that mixture formation process was investigated experimentally through spark-induced breakdown spectroscopy (SIBS) technique in a compression-expansion machine (CEM). As a consequence, local fuel-air equivalence ratio, ϕ (or local air-excess ratio) near spark gap were measured through SIBS sensor. To validate the experimental results, and to get better insight into mixture formation process, therefore it is quite necessary to accurately estimate the local fuel concentration at electrode gap during ignition timing while performing simulation. In ANSYS FORTE it is possible to use "point probe sampling" feature which is a single sampling point specified in Cartesian

coordinates within the volumetric region of the solution geometry, in order to extract the information of local equivalence ratio at spark timing (see Fig.6.17). Multiples point probe were created at location very close to the spark gap region to estimate average of the local equivalence ratio and plotted against experimental values in Fig.6.18 for validation. Three injection timing were considered here namely, EOI= 10^{o}, 5 ^{o}, and 0 ^{o} BTDC. Though overall agreements seem very reasonable, but CFD simulation slightly overpredicted local fuel-air equivalence ratio, $\boldsymbol{\phi}$ than in experiments, particularly for EOI= 5^{o} BTDC case.

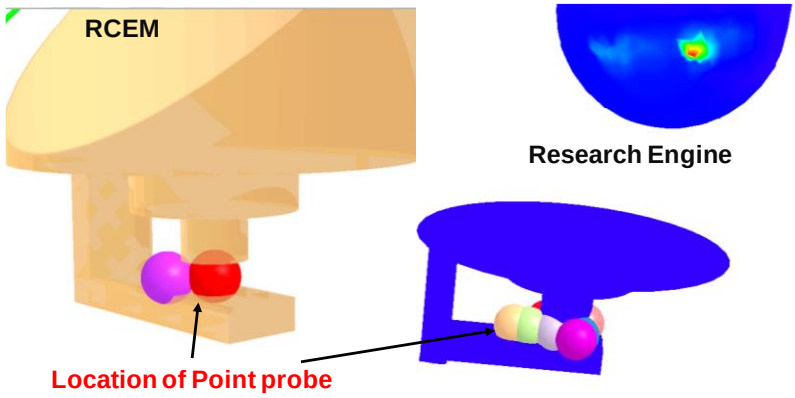

Fig.6.17 Point probe sampling to extract local mixture properties

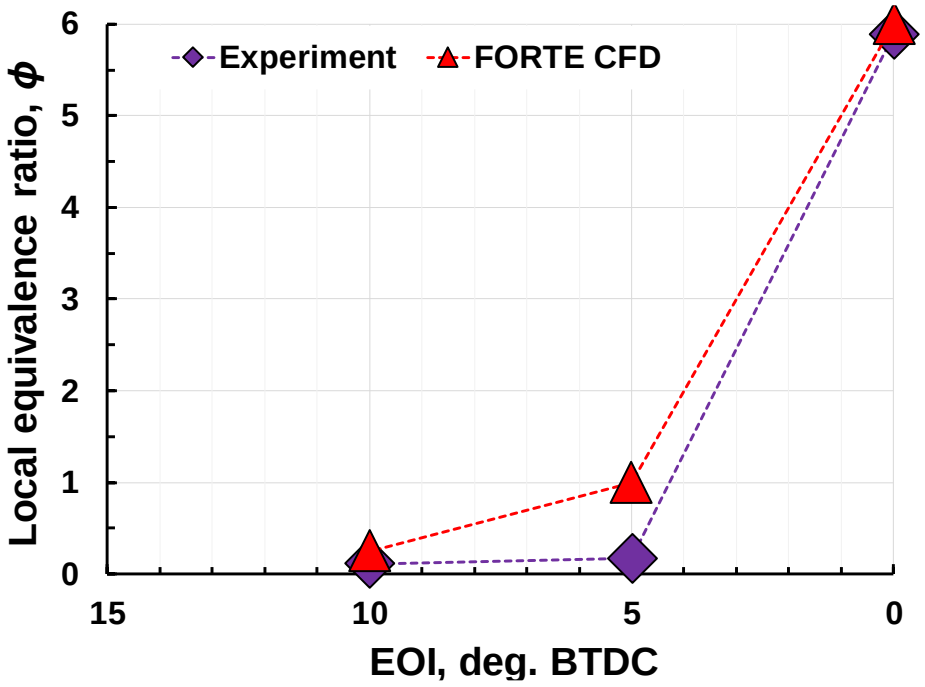

Fig.6.18 Comparison of predicted local equivalence ratio with experimental results for varying injection timing

6.12 Modeling Mixture formation and Combustion in a hydrogen research engine

6.12.1 Hydrogen PFI operation

Operating the engine in PFI (port fuel injection) leads to formation of premixed or homogeneous mixture and after spark event a premixed flame propagate throughout the combustion chamber. Therefore, while modeling the PFI engine operation, initial gas

composition was used to specify the fuel-air mixture in the intake port region and perfect mixing within the port was assumed. Simulations were carried out for global air excess ratio varying from 2.0 to 4.0 and for different spark timing. Fig.6.19 and Fig.6.20 represent the flame propagation for λ=2.5 and λ=4.0, respectively. In both of the cases spark timing was fixed at 15°BTDC.

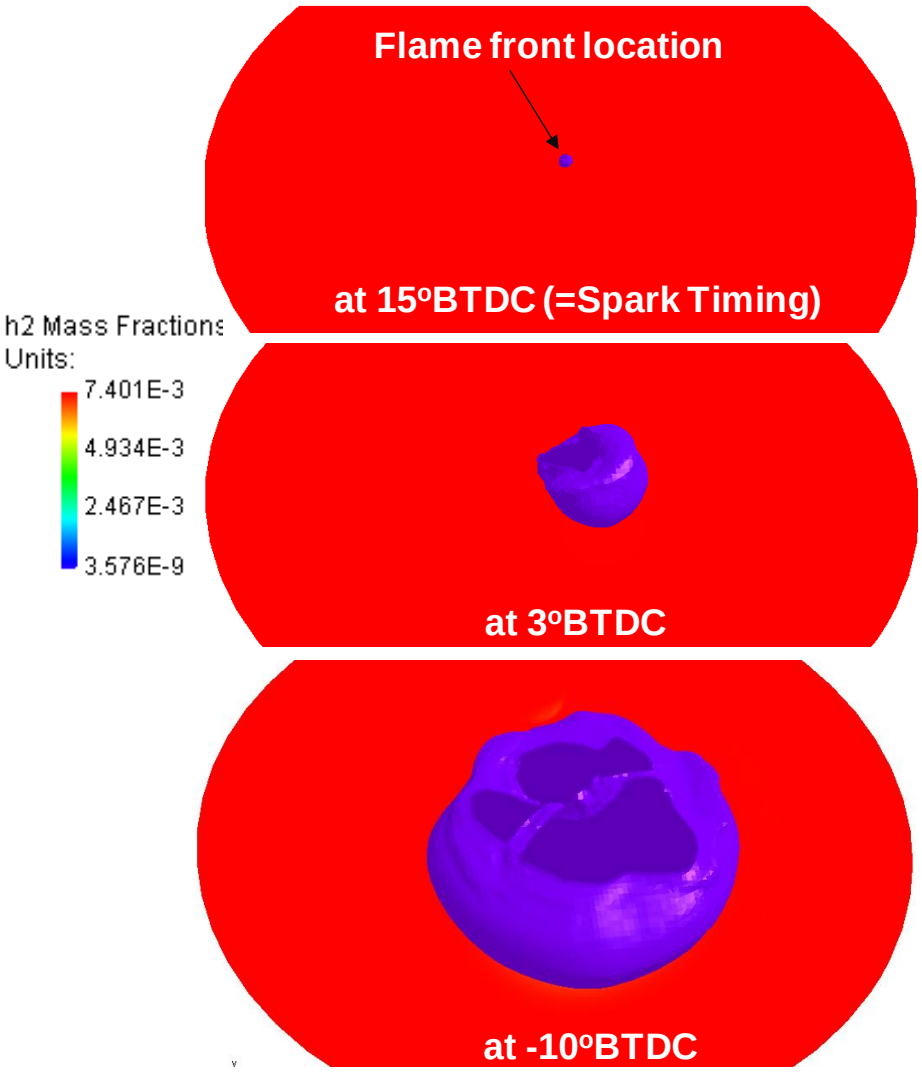

Fig.6.19 Flame front evolution with crank angle for PFI operation; λ = 4

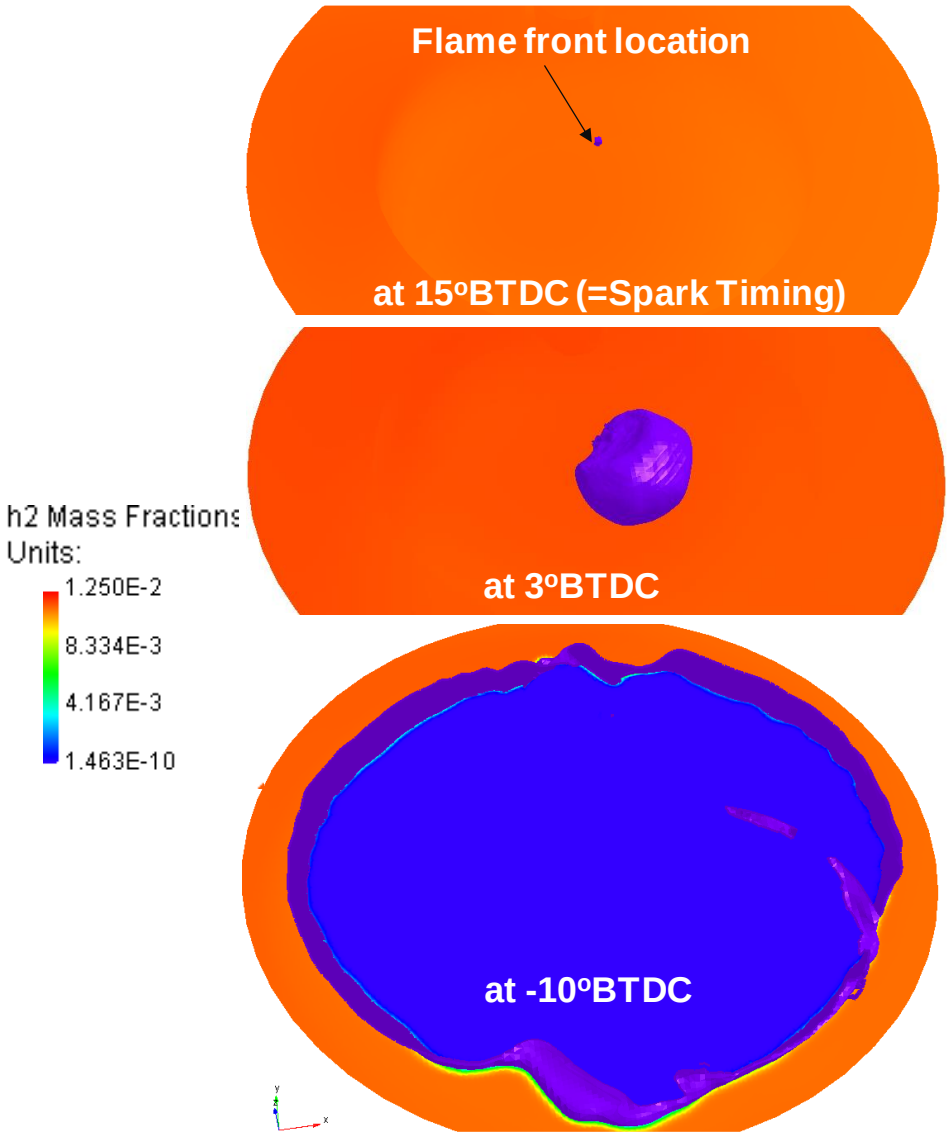

Fig.6.20 Flame front evolution with crank angle for PFI operation; λ = 2.5

Front tracking algorithms for resolving sharp gradients in flow systems are well established in computational mathematics. The G-equation model, mathematically known as the level-set method, was used to track the location of the flame front, independent of mesh resolution, with a highly efficient numerical technique. From the comparison between Fig.6.19 and 6.20

it is quite evident that flame development and propagation was much faster for λ = 2.5 than for λ = 4.0. Here, color bars show that mass fraction of H_2 fuel in combustion chamber is higher for λ = 2.5, as expected. It is generally agreed that the higher fuel concentration or comparatively rich mixture leads to faster kernel development and flame propagation. This characteristics feature is also observed in the pressure history as shown in Fig.6.21.

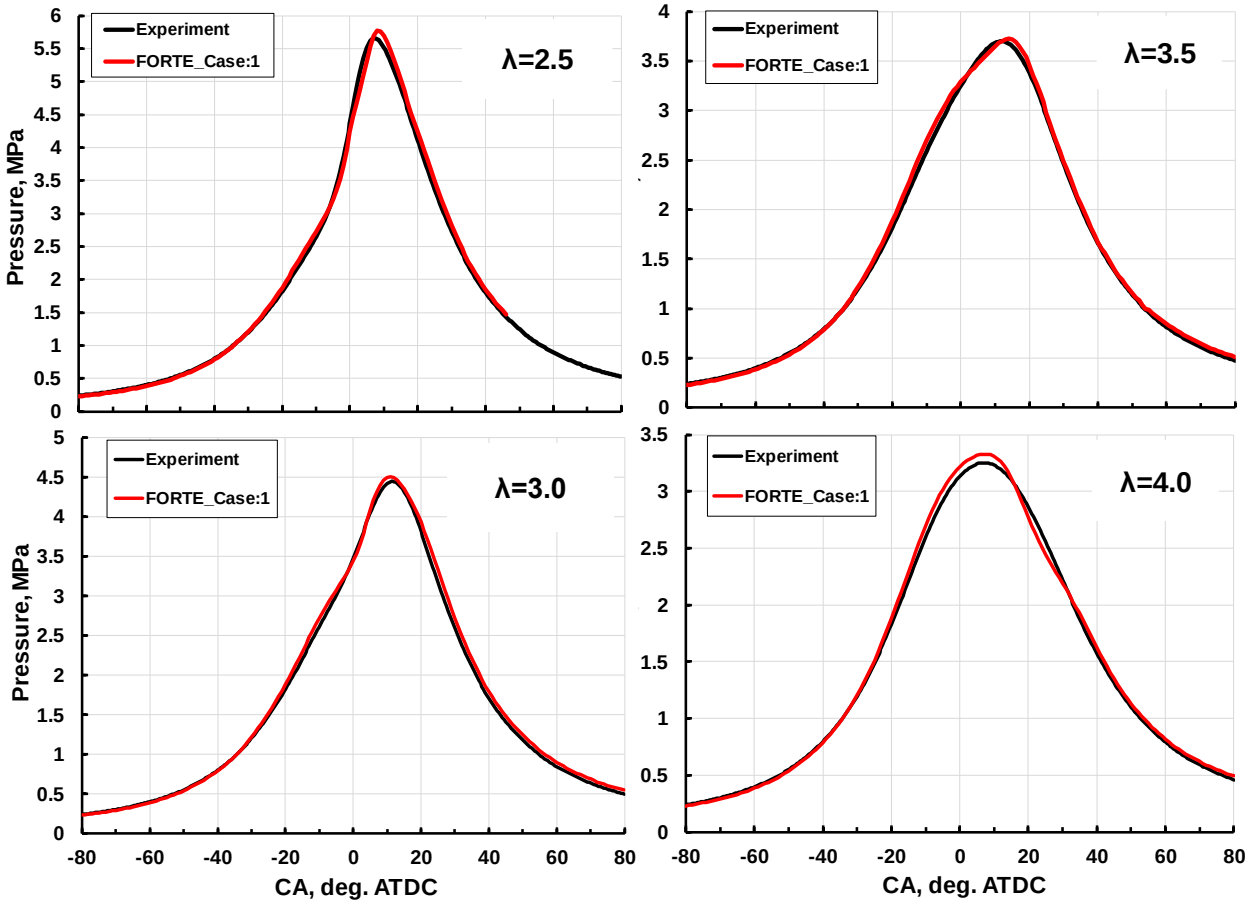

Fig.6.21 Comparing simulated pressure history with experimental data for hydrogen research engine in PFI mode

Very good agreements were achieved between predicted pressure histories with that of experimental data. To reach up-to this level of agreements, it is required to specify initial and

boundary conditions accurately; do very fine tuning of several important parameters namely, turbulent flame speed ratio, flame stretching factor, flame development co-efficient etc. In Fig.6.21, it is found that, with increasing air-excess ratio, pressure rise deaccelerated and produced lower peak values. This is caused by lower heat content in the mixture with higher λ values which ultimately decreased the flame propagation as evident in Fig.6.19 and Fig.6.20 also.

In Chapter-5, mean local air excess ratios (λ_{local}) were plotted against the preset value (λ_{preset}) for port injection conditions, and it was described how accuracy of SIBS measurement can be improved significantly through the "calibration map" that takes into account the pressure dependency of atomic emissions. Here, in Fig.6.22, local fuel

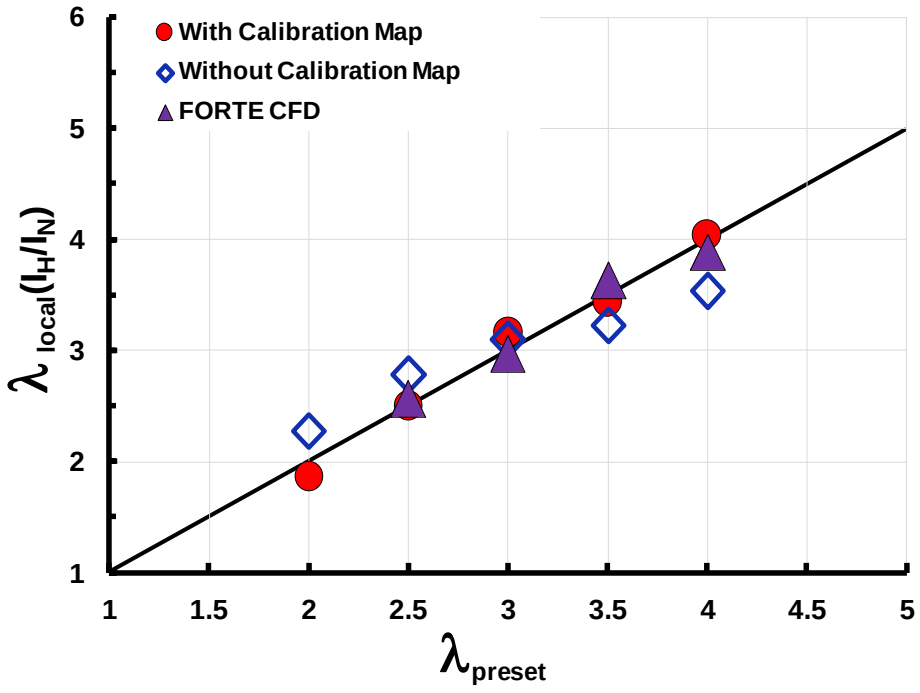

Fig.6.22 Comparison of predicted local air excess ratios with experimental results for varying preset value (λ_{preset})

concentration estimated by ANSYS FORTE simulation was compared with experimentally measured values by using calibration map; and calibration line. The predicted λ_{local} values from simulation matched quite well with experimentally measured values by using calibration map. This demonstrates that simulation carried out in this study was successful in predicting the mixture formation process as well as combustion phenomenon in a hydrogen engine operating in PFI mode.

6.12.2 Hydrogen DI operation

As stated in Chapter-5, experiments were performed with different air excess ratio varying from 2.5 to 4.5; and to achieve an axially stratified charge, the start of injection (SOI) was varied from120^0 BTDC to 35^0 BTDC while MBT (minimum advance for best torque) timing was considered as an ignition strategy. Full cycle simulations were performed operating conditions similar to experiments. Hydrogen flame front movement for different SOI are shown in Fig.6.23As the flame expanded, the flame front rippled, and buckled due to the stratification of the fuel/air mixture and turbulence conditions in the cylinder. From the color bar, representing the hydrogen mass fraction, it can be observed that for SOI= 120^oBTDC and 90^oBTDC hydrogen was diffused throughout chamber forming almost homogeneous mixture whereas for SOI= 50^oBTDC and 35^oBTDC, mixture became highly stratified at spark timing. Therefore, simulation is able to confirm that for late injection cases, combustion occurred with diffusion flame propagation. In Fig.6.23, it seems that the area engulfed by the flame front gradually decreased with retarded injection timing, therefore,

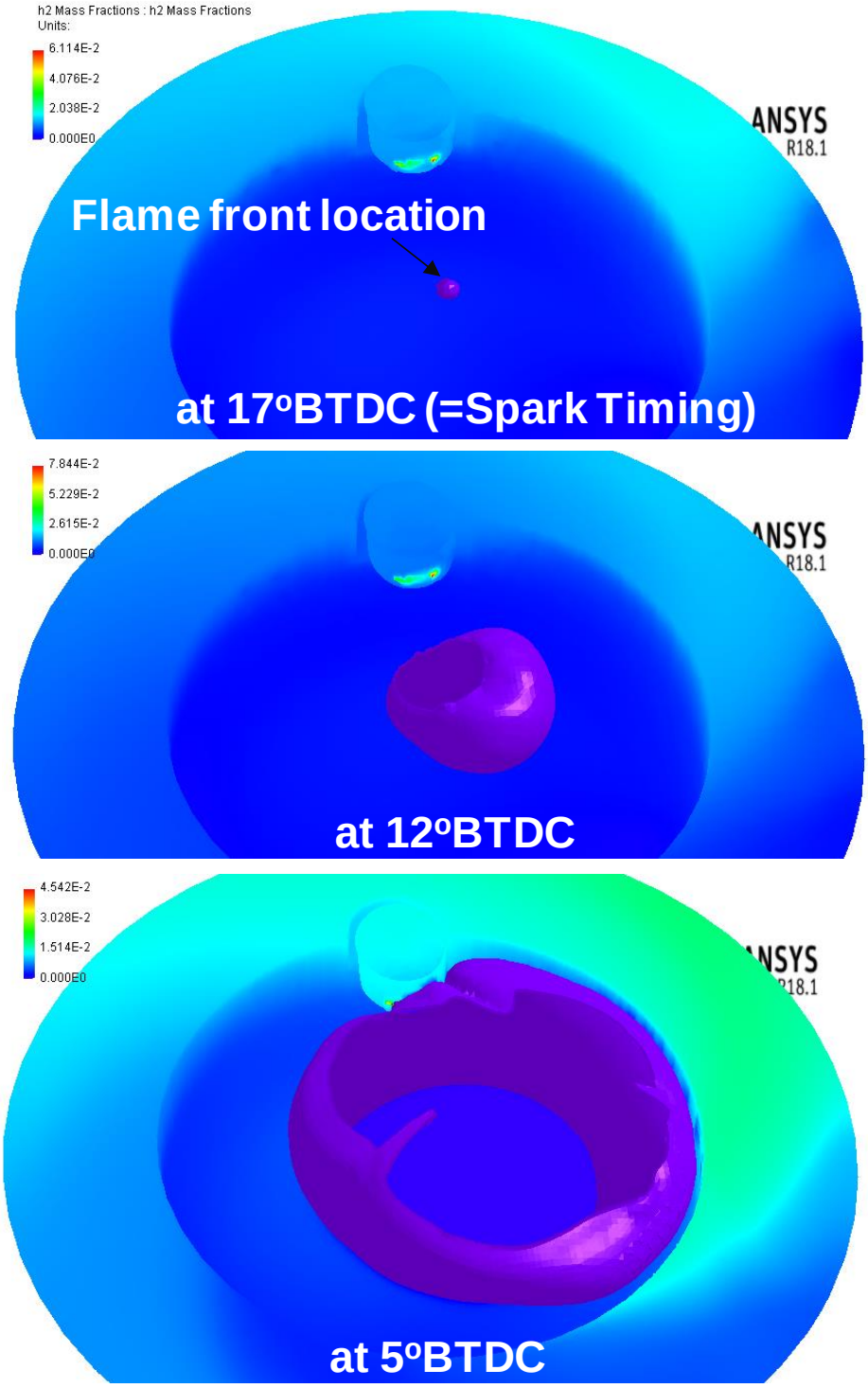

Fig.6.23 (a) Flame front evolution for SOI =120°BTDC; λ = 4.0

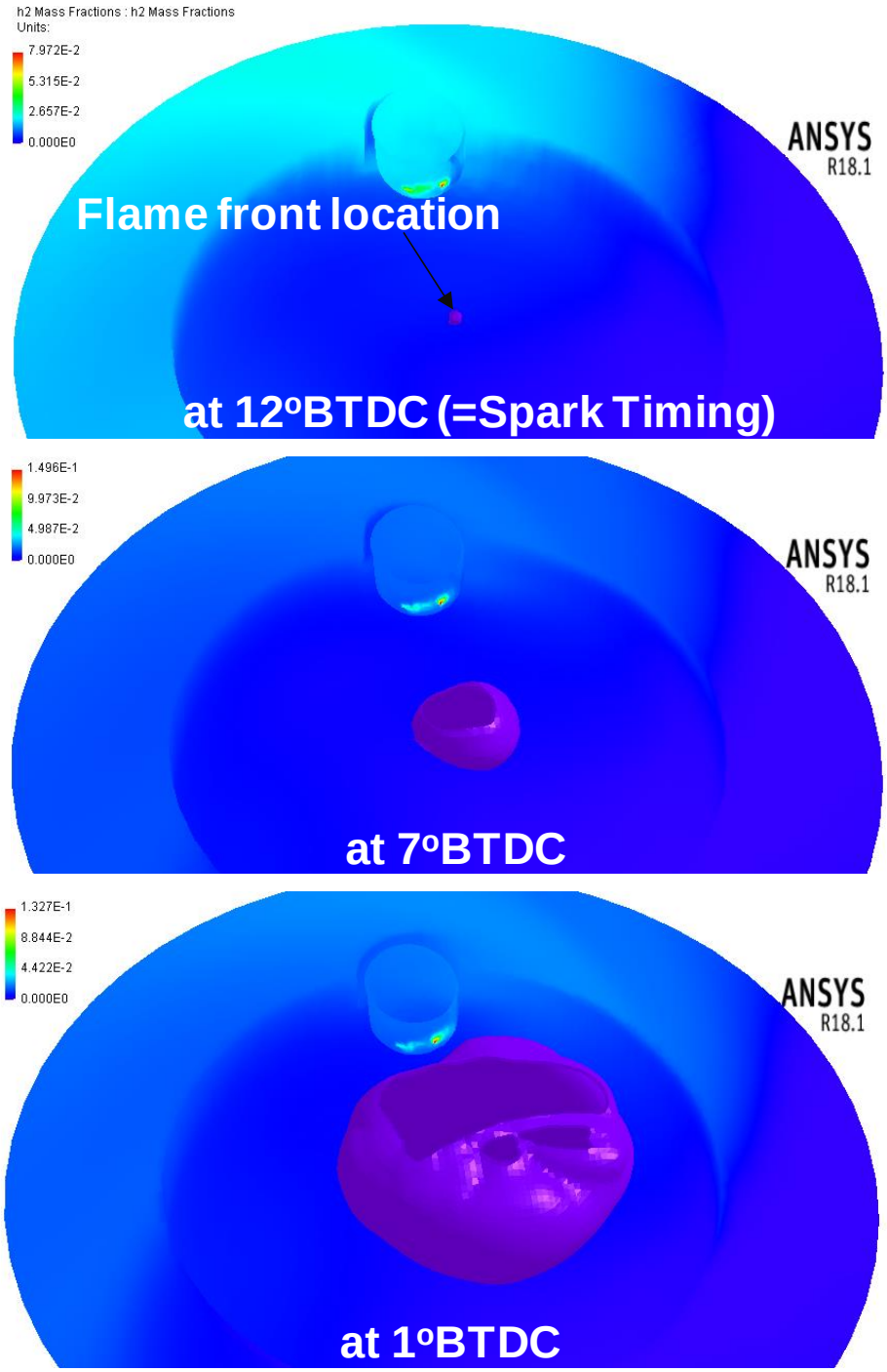

Fig.6.23 (b) Flame front evolution for SOI =90°BTDC; λ = 4.0

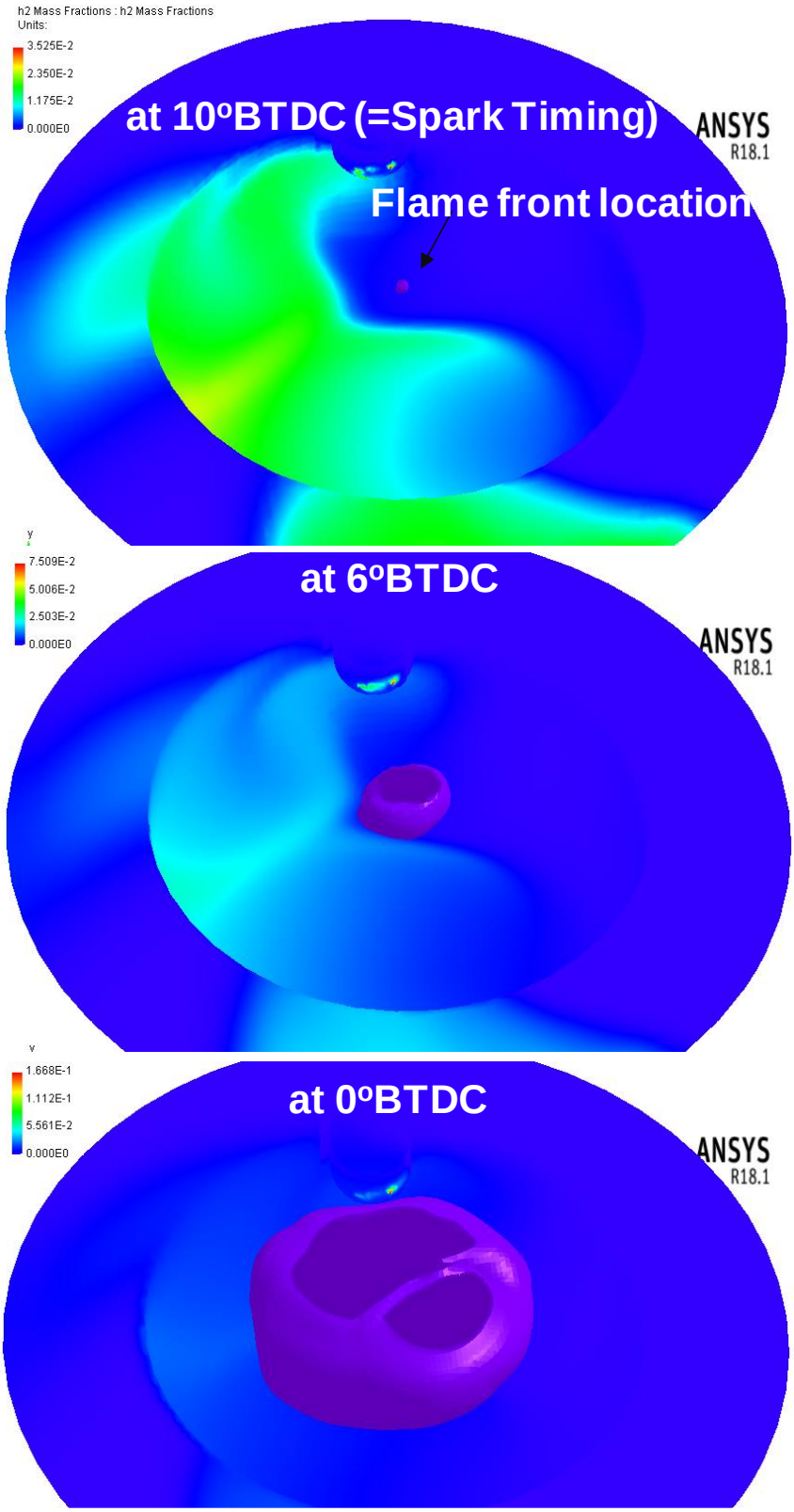

Fig.6.23 (c) Flame front evolution for SOI =50°BTDC; λ = 4.0

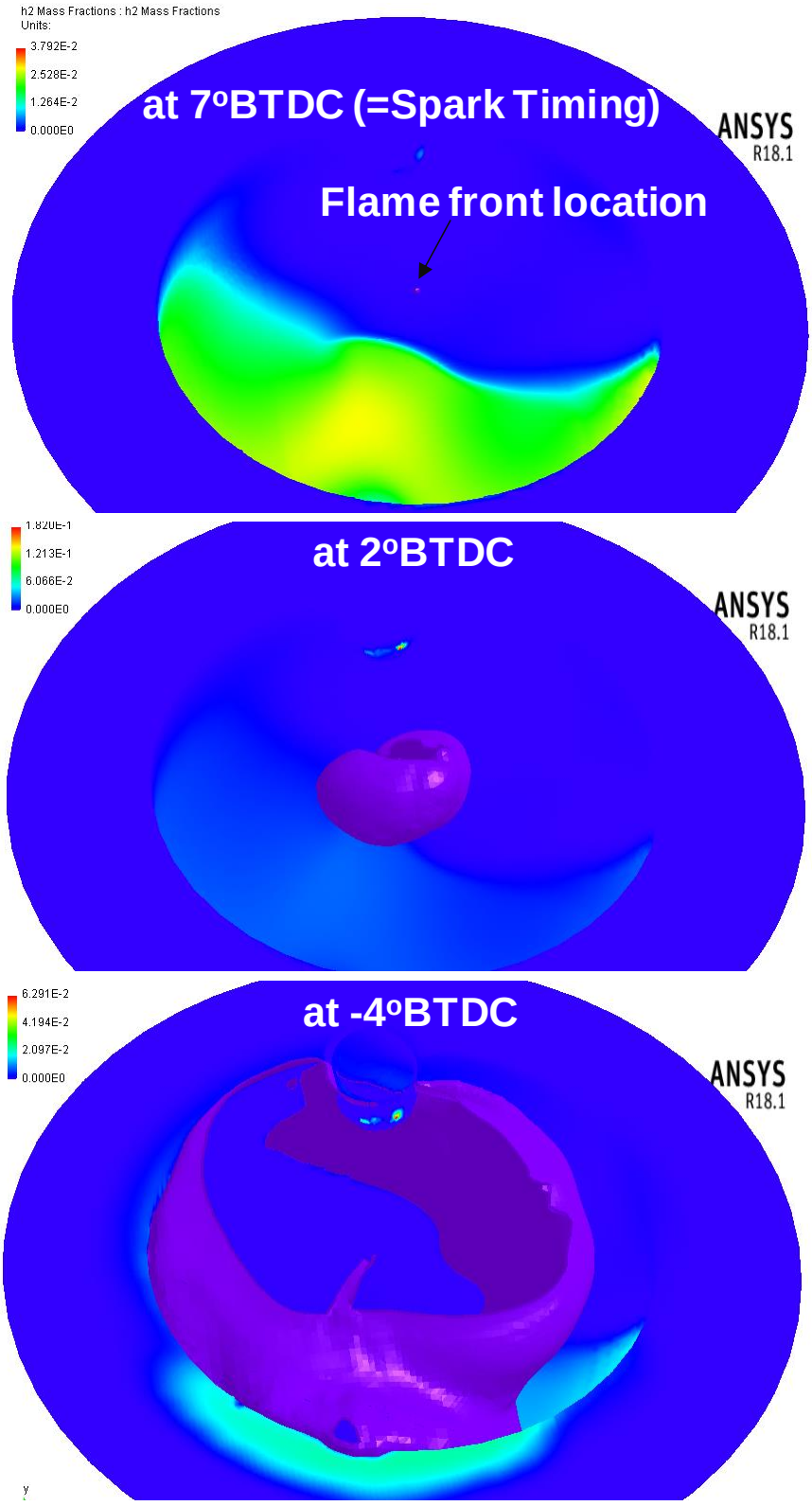

Fig.6.23 (d) Flame front evolution for SOI =35°BTDC; λ = 4.0

one may misunderstand that the combustion with late injection became slower. But this misunderstanding can be eliminated by shedding light on the fact that with late injection most of the fuel mass exist within a small volume (typically near the spark plug region in jet guided combustion system) in space and once the ignition is initiated by the spark-discharge, flame surface rapidly engulfed the fuel-air mass leading to higher mass fraction burned (MFB) and rapid combustion.

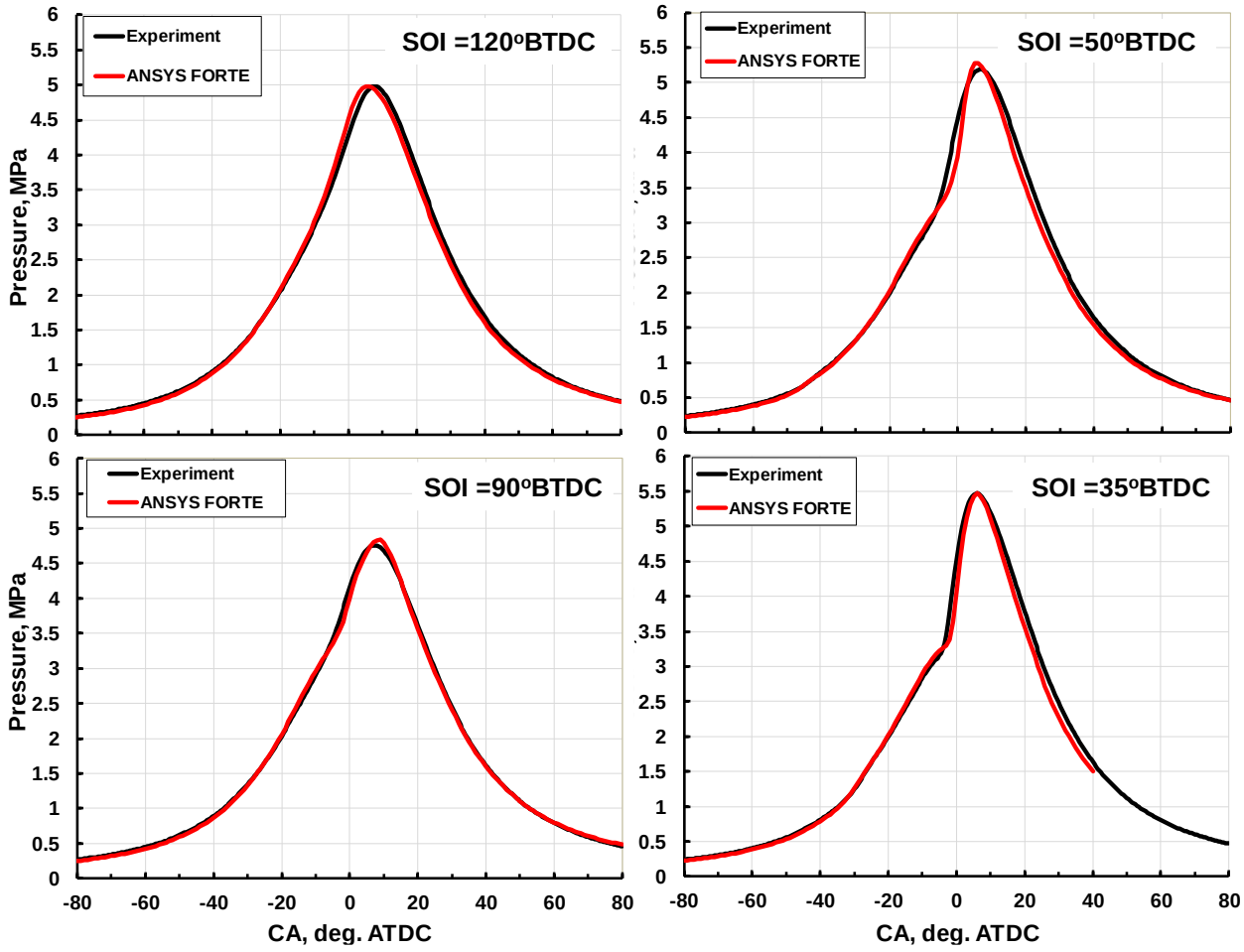

Fig.6.24 Comparing simulated pressure history with experimental data for hydrogen research engine operating in DI mode; λ = 4.0

Fig.6.24 shows a comparison of simulated and measured pressure histories for different injection timing while global equivalence ration was maintained at constant value (λ = 4.0). During this CFD simulation through ANSYS FORTE, three most important parameters that have significant influence on initial kernel development and burning velocity are:

1. Turbulent flame speed ratio, b_1 which is the ratio of fully developed turbulent flame speed over turbulent burning velocity. A larger value increases the turbulent flame speed.
2. Flame development coefficient, C_{m2} which models the increasingly disturbing effect of the surrounding eddies on the flame front surface as the ignition kernel grows from the laminar flame stage into the fully developed turbulent stage. Increasing the value of this variable will expedite the transition from the laminar kernel flame to the fully developed turbulent flame.
3. Flame stretching coefficient which accounts for strain and curvature effects. A larger value will increase the flame strain cause by turbulence and reduce flame speed. Its effect can be large when flame propagation is weak, for example, under high EGR or lean burn conditions.

In Chapter-5, spark-induced breakdown spectroscopic (SIBS) measurements confirmed higher degree of mixture stratification and higher equivalence ratio in spark gap region at the time of ignition with retarded injection timing. Local air-excess ratio, λ_{local} predicted by ANSYS FORTE CFD was compared with measured values by using calibration map and calibration line as shown in Fig.6.25. Very good agreement obtained between simulation and experimental data measured with calibration map for SOI = 120^{o}BTDC, 90^{o}BTDC and

35°BTDC; while for SOI = 50°BTDC, a reasonable agreement achieved. It should be reminded that for each operating condition, experiments were repeated for 100 times and all the data presented throughout the study represent the average of 100 engine cycles, thereby diminishing the cycle to cycle variation. On the other hand, predicted data represents only a single cycle. Furthermore, the velocity profile that adopted in the simulation for introducing hydrogen into the combustion chamber was not measured experimentally rather it was just the assumption though fine tuning was performed to maintain the same equivalence ratio. Therefore, there might be some short fall in accurately predicting the jet movement and molecular diffusion of hydrogen. These factors might have led to the discrepancy between simulation and experimental results.

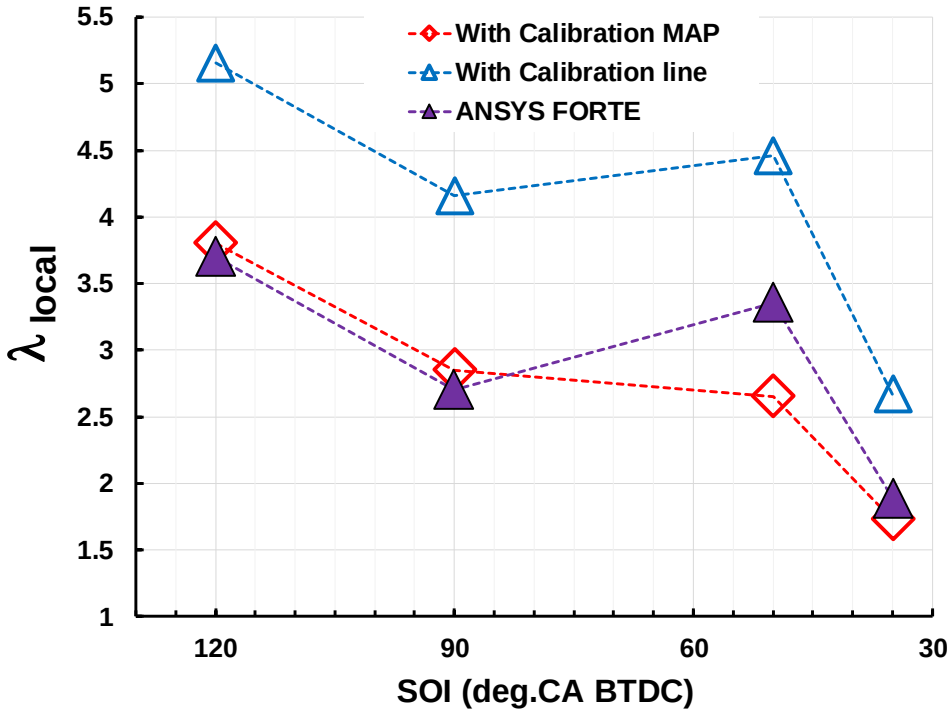

Fig.6.25 Comparison of predicted local air excess ratios with experimental results for varying start of injection (SOI); $\lambda_{preset} = 4.0$

6.13 Summary

In this study, CFD simulations were carried out for different injection strategies and over a range of global air-excess ratio varying from 2.0 to 4.0. Full cycle simulation was performed in order to capture more flow structures, eddies and vortices that have significant influences on both mixture formation process and subsequent combustion. Concept of inflow boundary condition at the nozzle exit was successfully utilized to introduce gaseous hydrogen directly into the combustion chamber. This simulation confirms that the hydrogen jet directed towards the spark gap region forming a jet guided combustion system in accordance with original design of the chamber head. With retarded injection during compression stroke, fuel jet experience higher pressure immediately upon exiting from the nozzle tip. This high ambient pressure hinders the gas diffusion into the ambient air and consequently reduce the jet penetration. The complex flame motion phenomena can be included when the flame front is tracked accurately. These phenomena would be neglected if only the kinetics within each cell were considered in determining flame location. The G-equation model, mathematically known as the level-set method, was used to track the location of the flame front, independent of mesh resolution, with a highly efficient numerical technique. As the flame expanded, the flame front rippled, and buckled due to the stratification of the fuel/air mixture and turbulence conditions in the cylinder. It is generally agreed that the higher fuel concentration or comparatively rich mixture leads to faster kernel development and flame propagation; this characteristics feature was observed in the simulation. It is found that, with increasing air-excess ratio, pressure rise deaccelerated and produced lower peak values. This caused by lower heat content in the comparatively leaner mixture which ultimately decreased the

flame propagation. With late injection most of the fuel mass exist within a small volume (typically near the spark plug region in jet guided combustion system) in space and once the ignition is initiated by the spark-discharge, flame surface rapidly engulfed the fuel-air mass leading to higher mass fraction burned (MFB) and rapid combustion. Very good agreements were achieved between predicted pressure profiles with experimental data.

To validate the experimental results (i.e. SIBS data), and to get better insight into mixture formation process, local fuel concentration at electrode gap during ignition timing was extracted from simulation results. CFD simulation data of local equivalence ratio supported the claim that accuracy of SIBS measurement can be improved significantly by taking into account the pressure dependency of atomic emissions. The predicted λ_{local} values from simulation matched quite well with experimentally measured values by using calibration map. This demonstrates that simulation carried out in this study was successful in predicting the mixture formation process as well as combustion phenomenon in a hydrogen engine. To reach up-to this level of agreements, it is required to specify initial and boundary conditions accurately; do very fine tuning of several important parameters namely, turbulent flame speed ratio, flame stretching factor, flame development co-efficient etc.

REFERENCE

[1] Rakopoulos, CD.; Kosmadakis, GM.; Pariotis, EG. Evaluation of a new computational fluid dynamics model for internal combustion engines using hydrogen under motoring conditions. *Energy* **2009**, 12, 2158-66.

[2] Arash, H.; Pavlos, A. Computational study of hydrogen direct injection for internal combustion engines. *SAE Technical Paper* **2013**-01-2524.

[3] Zhenzhong, Y.; Aiguo, S.; Fei, W.; Nan, G., "Research into the formation process of hydrogen air mixture in hydrogen fueled engines based on CFD. *Int. J. Hydrogen Energy* **2010,** 35, 3051-7.

[4] Rakopoulos, CD.; Kosmadakis, GM.; Pariotis, EG. Evaluation of a combustion model for the simulation of hydrogen spark ignition engines using a CFD code. *Int. J. Hydrogen Energy* **2010**, 35,12545-60.

[5] Rakopoulos, CD.; Kosmadakis, GM.; Demuynck, J.; Paepe, M.; Verhelst, S. A combined experimental and numerical study of thermal processes, performance and nitric oxide emissions in a hydrogen-fueled spark-ignition engine. *Int. J. Hydrogen Energy* **2011,** 36, 5163-80

[6] Kosmadakis, GM.; Rakopoulos, CD.; Demuynck, J.; Paepe, M.; Verhelst, S. CFD modeling and experimental study of combustion and nitric oxide emissions in hydrogen-fueled spark-ignition engine operating in a very wide range of EGR rates. *Int. J. Hydrogen Energy* **2012**, 37, 10917-10934.

[7] Vincent, K.; Adle`ne, B. Modelling of combustion and nitrogen oxide formation in hydrogen-fuelled internal combustion engines within a 3D CFD code. *Int. J. Hydrogen Energy* **2008,** 33, 5083-5097.

[8] Knop, V., Benkenida, A., Jay, S. and Colin, O., "Modelling of combustion and nitrogen oxide formation in hydrogen- fuelled internal combustion engines within a 3D CFD code", *International Journal of Hydrogen Energy*, Vol. 33, pp. 5083-5097, 2008.

[9] Safari, H., Jazayeri, S.A. and Ebrahimi, R., "Potentials of NOX emission reduction methods in SI hydrogen engines: Simulation study", *International Journal of Hydrogen Energy*, Vol. 34, pp. 1015-1025, 2009.

[10] Verhelst, S., T'Joen, C., Vancoillie, J. and Demuynck, J., "A correlation for the laminar burning velocity for use in hydrogen spark ignition engine simulation", *International Journal of Hydrogen Energy*, Vol. 36, pp. 957-974, 2011.

[11] COLIN, O., Hydrogen turbulent mixing modeling. In: *Internal Report, D*3.2.*C, EU integrated project HyICE, No.* 506604

[12] Amsden, A. A., "KIVA-3V: A Block-structured KIVA Program for Engines with Vertical or Canted Valves," *Los Alamos National Laboratory Report LA-13313-MS*, Los Alamos National Laboratory, 1997.

[13] Yakhot, V., and S. A. Orszag, "Renormalization Group Analysis of Turbulence: I. Basic Theory," *Journal of Scientific Computing*, 1:3, 1986.

[14] Han, Z., and R. D. Reitz, "Turbulence Modeling of Internal Combustion Engines Using RNG *k*-ε Models," *Combustion Science and Technology,* 106, pp. 267-295, 1995.

[15] Tan, Z., "Multi-Dimensional Modeling of Ignition and Combustion in Premixed and DIS/CI (Direct Injection Spark/Compression Ignition) Engines." Ph.D. Thesis, University of Wisconsin-Madison, 2003.

[16] Han, Z., and R. D. Reitz, "A Temperature Wall Function Formulation for Variable-density Turbulence Flows with Application to Engine Convective Heat Transfer Modeling," International Journal of Heat Mass Transfer, 40, 3, pp. 613–625, 1997.

[17] J.B. Heywood, Internal Combustion Engine Fundamentals, McGraw-Hill, NewYork, 1988.

[18] M. Thiele, S. Selle, U. Riedel, J.Warnatz, and U. Maas, Numerical simulation of spark ignition including ionization, Proc. Combus. Inst. 28 (2000), pp. 1177–1185.

[19] H. Willems and R. Sierens, Modeling the initial growth of the plasma and flame kernel in SI engines, J. Eng. GasTurbines Power 125 (2003), pp. 479–484.

[20] Fan, L., and Reitz, R. D., "Development of Ignition and Combustion Model for Spark-Ignition Engines, SAE Technical Paper 2000-01-2809," *SAE Technical Paper Series*, 2000.

[21] Tan, Z.; Reitz, R.D., "An Ignition and Combustion Model for Spark Ignition Engine Multi-dimensional Modeling," Combustion and Flame, 145 (2006), 1-15.

[22] S. Falfari and G. Bianchi, Development of an ignition model for S.I. engines simulation, SAE Paper, 2007-01-0148,2007.

[23] J.M. Duclos and O. Colin, Arc and kernel tracking ignition model for 3D spark-ignition engine calculations,Proceedings of COMODIA 2001 Conference, Nagoja, 2001.

[24] R. Dahms, T.D. Fansler, M.C. Drake, T.W. Kuo, A.M. Lippert, N. Peters, Modeling ignition phenomena in spray-guided spark-ignited engines, Proc. Combust. Inst. 32 (2009) 2743–2750.

[25] R.N. Dahms, M.C. Drake, T.D. Fansler, T.-W. Kuo, and N. Peters, Understanding ignition processes in spray-guided gasoline engines using high-speed imaging and the extended spark-ignition model SparkCIMM. Part A: Spark channel processes and the turbulent flame front propagation, Combus. Flame158(11),2011; 2229–2244.

[26] R. Maly, M. Vogel, Initiation and propagation of flame fronts in lean CH4-air mixtures by the three modes of the ignition spark, Proc. Combust. Inst. 17 (1978) 821-833.

[27] N. Peters, Turbulent Combustion, Cambridge University Press: Cambridge, UK, 2000.

[28] M. Herrmann, Numerical simulation of turbulent Bunsen flames with a level set flamelet model, Combust. Flame 145 (2006) 357–375.

[29] M. Herrmann, Numerical Simulation of Premixed Turbulent Combustion Based on a Level Set Flamelet Model, Ph.D. thesis, RWTH Aachen University, Germany, 2001.

[30] J. Ewald, N. Peters, On unsteady premixed turbulent burning velocity prediction in internal combustion engines, Proc. Combust. Inst. 31 (2006) 3051–3058.

[31] R. Dahms, N. Peters, D.W. Stanton, Z. Tan, J. Ewald, Pollutant formation modelling in natural gas SI engines using a level set based flamelet model, Int. J. Eng. Res. 9 (2008) 1–14.

[32] M. Chen, M. Herrmann, N. Peters, Flamelet modeling of lifted turbulent methane/air and propane/air jet diffusion flames, Proc. Combust. Inst. 28 (2000) 167–174.

[33] S.E. Vogel, Simulation of Lifted Diesel Sprays Using a Combined Level-Set Flamelet Model, Ph.D. thesis, RWTH Aachen University, Germany, 2008.

[34] Liang, L. and R. D. Reitz. "Spark Ignition Engine Combustion Modeling Using a Level Set Method with Detailed Chemistry, SAE TEchnical Paper 2006-01-0243," SAE Technical Paper Series, 2006.

[35] Liang, L., Reitz, R.D., Iyer, C.O. and Yi, J., "Modeling Knock in Spark-Ignition Engines Using a G-equation Combustion Model Incorporating Detailed Chemical Kinetics, SAE Technical Paper 2007-01-0165," SAE Technical Paper Series, 2007.

CHAPTER: 7

Conclusions

The primary objective of this study was to investigate mixture formation process in jet guided direct injection hydrogen spark ignition engine through simultaneous application of high speed visualization and spark-induced breakdown spectroscopy (SIBS). The experimental works were conducted in a compression-expansion machine (CEM) designed and fabricated by Heat Power Laboratory, Okayama University; and a direct-injection hydrogen spark-ignition research engine developed at Tokyo City University. Spark-induced breakdown spectroscopy (SIBS) technique was employed as a diagnostic tool for local fuel concentration measurements in a direct-injection hydrogen research engine for the first time. The followings are the key findings obtained from this research:

1) Time-series images of the evolution of hydrogen jet showed that jet plume appears to penetrate faster when hydrogen was injected with higher injection pressure into a chamber of comparatively lower ambient pressure as velocity of the jet or total momentum supplied to the fuel jet at the injector exit was higher for increasing the injection pressure. Therefore, the injected fluid with additional momentum could accelerated more readily by pushing aside the ambient fluid; though density of chamber medium was considerably higher than that of the injected gas.

2) Higher ambient pressure resulted in considerably shorter jet tip penetration along with wider jet angle which was caused by the higher inertia of the fluid elements that the injected fluid must accelerate and push aside.
3) A new sensor with an optical fibre housed in the centre electrode of the spark plug was developed from a commercially available M12-type spark plug with no major modification to the electrodes, leading to stable spark formation.
4) Spectroscopic analysis of spark-plasma emission and high-speed visualization of spark behavior with different air-excess ratio was studied simultaneously in a compression expansion machine (CEM). Results clearly indicates that presence of higher fuel concentration in the vicinity of spark gap leads to higher discharge energy as the magnitude of both breakdown voltage and current increase though duration of spark event becomes shorter with lower air excess ratio.
5) Exposure duration for spectroscopic measurement of spark plasma was optimized to obtain better atomic emission intensity of Hα (656nm) and N (745nm). When hydrogen concentration was relatively higher, breakdown voltage became higher which made spark discharge difficult to sustain over a long time and both continuum background emission (i.e. emission from spark plasma) and atomic emission intensity of the spectral distribution declines. As expected, lower the preset air excess ratio, resulted in higher intensity ratio of Hα/N due to presence of higher concentration of hydrogen fuel compared to that of nitrogen. However, with a hydrogen density above a certain level, emission intensity ratio did not show a linear relationship and it was considered that there was a limit to the amount of hydrogen atoms that can be excited. Therefore, a change in the discharge energy lead to a

corresponding change in the relationship between atomic emission intensity ratio and excess air ratio.

6) Quantitative measurements of fuel concentration were conducted for the first time in a direct-injection hydrogen spark-ignition research engine through spark-induced breakdown spectroscopy (SIBS) technique. The newly developed fibre optic spark plug sensor was used successfully in a DISI research engine and showed better durability and robustness even with very in-cylinder pressure and turbulence. Here the main focus was to characterise the effects of ambient pressure at ignition timing on atomic emissions and to improve the accuracy of the SIBS measurements by taking into account the pressure dependency of atomic emissions.

7) A linear relationship (calibration line) was demonstrated between air excess ratio and intensity ratio for both IH/IN and IH/IO over all pressure values. A significant effect of the corresponding pressure at ignition timing was observed on SIBS measurements and emission line characteristics. Retarded spark timing (i.e. higher ambient pressure at the ignition site), resulted in lower spectral line intensities as well as weaker background emissions. This indicates the variation in spark discharge behaviour and plasma formation with variation in ambient pressure inside the engine cylinder during spark timing variation. At relatively higher pressures, the cooling of the expanding plasma was quicker due to collisional processes with the surrounding gas, leading to both a weaker broadband continuum and atomic emissions.

8) A calibration map, representing the correlation of air excess ratio with both intensity ratio and pressure at ignition timing, was developed by taking into account the effect of the corresponding pressure at ignition timing on spectral line intensity for

quantitative measurements of local air excess ratio in a research engine. Local stratification of the fuel mixture in the vicinity of the spark gap location associated with direct injection was confirmed through SIBS measurements using the newly developed spark plug sensor. The COV of local air excess ratio was considerably smaller for measurements made through the calibration map. This indicates that the accuracy of measurements of local air excess ratio through SIBS technique can be improved significantly when the pressure dependency of atomic emissions is taken into account.

9) Multidimensional CFD simulation was carried out over a range of global air-excess varying from 2.0 to 4.0 and different injection strategies, by using commercial 3D-CFD software ANSYS Forte, to obtain better insight on hydrogen jet characteristics and mixture formation process in hydrogen direct-injection engines.

10) Simulation confirmed that with retarded injection during compression stroke, fuel jet experience higher pressure immediately upon exiting from the nozzle tip. This high ambient pressure hinders the gas diffusion into the ambient air and consequently reduce the jet penetration.

11) The G-equation model, mathematically known as the level-set method, was used to track the location of the flame front, independent of mesh resolution, with a highly efficient numerical technique. As the flame expanded, the flame front rippled, and buckled due to the stratification of the fuel/air mixture and turbulence conditions in the cylinder. It is generally agreed that the higher fuel concentration or comparatively rich mixture leads to faster kernel development and flame propagation; this characteristics feature was observed in the simulation. It is found that, with

increasing air-excess ratio, pressure rise deaccelerated and produced lower peak values. This was caused by lower heat content in the comparatively leaner mixture which ultimately decreased the flame propagation. With late injection most of the fuel mass exist within a small volume (typically near the spark plug region in jet guided combustion system) in space and once the ignition is initiated by the spark-discharge, flame surface rapidly engulfed the fuel-air mass leading to higher mass fraction burned (MFB) and rapid combustion.

12) Very good agreements were achieved between predicted pressure profiles with experimental data.

13) To validate the experimental results (i.e. SIBS data), local fuel concentration at electrode gap during ignition timing was extracted from simulation results. The claim to achieve higher accuracy in SIBS measurement by taking into account the pressure dependency of atomic emissions, was confirmed through CFD simulation data of local fuel concentration. The predicted λ_{local} values from simulation matched quite well with experimentally measured values.

14) To reach up-to this level of agreements, it is required to specify initial and boundary conditions accurately; do very fine tuning of several important parameters namely, turbulent flame speed ratio, flame stretching factor, flame development co-efficient etc.

15) These demonstrate that the simulation carried out in this study was successful in predicting the mixture formation process as well as combustion phenomenon in a hydrogen engine.